UNIVERSITY OF SOUTHAMPTON

FACULTY OF NATURAL AND ENVIRONMENTAL SCIENCES

Ocean and Earth Science

The Seasonal and Interannual Variability of the Ligurian Sea

Author:

Simona Aracri

Thesis for the degree of Doctor of Philosophy

UNIVERSITY OF SOUTHAMPTON

ABSTRACT

FACULTY OF NATURAL AND ENVIRONMENTAL SCIENCES

Ocean and Earth Sciences

Doctor of Philosophy

THE SEASONAL AND INTERANNUAL VARIABILITY OF THE LIGURIAN SEA

by
Simona Aracri

Understanding the variability of the Ligurian Sea is potentially leading to solve the long standing questions about how deep is the Liguro-Provençal Current (LPC)? What drives the circulation across the Corsica Channel? What are the time scales of this variability and how well can geostrophy describe the circulation across the Ligurian basin?

Seven free floating devices called MERMAID have been deployed in the Ligurian Sea from 2012 to 2015, surfacing every 4-5 days on average. The instruments positioning data constituted a valuable source to estimate the LPC depth and speed at 1500 m below the sea surface.

The Corsica Channel is a choke point to monitor the exchanges between the Tyrrhenian Sea and Ligurian Sea. The water flux across the Channel has been monitored for more than 30 years, constituting one of the longest world time series. In the present work the water flux from 1985 to 2010 constitutes the focus to relate atmospheric and marine variables in the Ligurian Sea and Tyrrhenian Sea. The study highlights the permanent influence of the atmospheric Sea Surface Pressure (SSP) on the exchange between the two basins and the crucial role of the Sea Level Anomaly (SLA) on the opposite sides of the Corsica Channel. On a seasonal time scale the water flux variability well relates with SSP, SLA, Ekman transport and meridional wind stress. The interannual variability results instead from changes in SLA.

The novel discoveries about deep LPC velocities and Corsica Channel transport are useful constraints for Inverse Box Model (IBM). The IBM, has been run for the first time incorporating data collected during 9 cruises. The oceanographic cruises took place from 2002 to 2012. The IBM results shed light on the importance of the Capraia Channel, almost completely absent in literature. The inversions also outlined the Western Corsica Channel current variability neglected in literature. Through the IBM technique, a modern estimation of the Ligurian Sea circulation and geostrophic transport has been generated.

This study ultimately contributes to the fundamental knowledge of the Ligurian Sea circulation, implementing state of the art observations and reanalysis data.

Contents

List of Tables

List of Figures

Academic Thesis: Declaration Of Authorship

I, Simona Aracri

declare that this thesis and the work presented in it are my own and has been generated by me as the result of my own original research.

The Seasonal and Interannual Variability of the Ligurian Sea

I confirm that:

1. This work was done wholly or mainly while in candidature for a research degree at this University;
2. Where any part of this thesis has previously been submitted for a degree or any other qualification at this University or any other institution, this has been clearly stated;
3. Where I have consulted the published work of others, this is always clearly attributed;
4. Where I have quoted from the work of others, the source is always given. With the exception of such quotations, this thesis is entirely my own work;
5. I have acknowledged all main sources of help;
6. Where the thesis is based on work done by myself jointly with others, I have made clear exactly what was done by others and what I have contributed myself;
7. Either none of this work has been published before submission, or parts of this work have been published as: [please list references below]:

Signed:

Date: 6th June 2018

1 Acknowledgements

The amount of people that have been accompanying me during this trip is huge. I hope to remember them all.

So without particular order I would love to thank the little Margot and Gabriele, the youngest of my family to have brought an unexpected light in our lives, because thanks to them the distance between me and my home has felt a little shorter and I have found new energies to swim into this incredible Ph.D. adventure.

I am deeply thankful to my friends: Ale, Sara, Davide, because they remind me who I am and where I come from, because they have had the courage to stick to me even when I would have not done it in the first place, because of their constant presence and unbelievable faith and support.

Thank you to Fra because he is just the best, humblest and funniest friend.

I am very grateful to my friends and colleges in Venice: Grazia, Federica, Fer, Elena, Francesco, Francesca, Antonio, Christian, Georg. Thank you to Irene, Claudia, Laura. Thanks to Loïc, for his bright mind and patience whiles answering to all my stupid questions.

I am so thankful to the crews and friends that I met on board: Giuseppe, Andrey, Martin, Miguel, Virna, Stefania. I am thankful to the ship and the cruise that guide us in the remote corners of the ocean. The memories on R/V Navicula, R/V Urania, NR/V Alliance, R/V Minerva, R/V Sonne are amongst the dearest of mine.

I am grateful to have had the chance to be part of the Institute of Marine Sciences in Venice and has been marvellous to be part of the National Oceanography Centre in Southampton.

I feel deeply grateful to Vic, Cris, Giulia, Carolina and Manuel who gave me a place where to stay in Southampton, who advised me and offered me their priceless friendship.

Thanks to Jon for constantly challenging me and pushing me to be a better person, thanks for his strength and confidence.

Many thanks to Mary at the PG Office for her professionalism and patience.

Thanks to my family because they are an inexhaustible source of pure strength, because they are every day a better version of themselves and constantly push me to grow.

I am deeply grateful to my supervisors, Dr Elaine McDonagh, Emeritus Professor Harry Bryden, Dr Jacopo Chiggiato, Dr Katrin Schroeder, Professor Simon Josey, and to the panel chair: David Smeed. They have been constantly supporting me, yet they gave me all the freedom. Their advice have been invaluable, their patience has been immense. Katrin, Harry, Elaine, Simon, Jacopo have been an inspiration personally and out of any doubt professionally.

The thesis, the Ph.D. challenge would not have been possible without any of this people. I feel lucky to have all of them on my side.

Glossary

Abbreviations	
Geographical Names	
CC	Corsica Channel
CCh	Capraia Channel
GoL	Gulf of Lion
GS	Strait of Gibraltar
LPB	Liguro Provençal Basin
LPC	Liguro Provençal Current
LS	Ligurian Sea
NC	Nice-Calví
SC	Sicily Channel
Sch	Sardinia Channel
TYS	Tyrrhenian Sea
WMED	Western Mediterranean Sea
Currents Names	
ECC	Eastern Corsica Current
LPC	Liguro Provençal Current
WCC	Western Corsica Current
Water Masses	
AW	Atlantic Water
DW	WMDW+nWMDW
LIW	Levantine Intermediate Water
nWMDW	new Western Mediterranean Deep Water
WMDW	Western Mediterranean Deep Water
WIW	Winter Intermediate Water
Time Series	
SLA_{grid}	Sea Level Anomaly from gridded satellite products
SLA_{sat}	Sea Level Anomaly from along track satellite products
SSP	Sea Surface Pressure
τ_y	sea surface instantaneous turbulent meridional wind stress

τ_x	sea surface instantaneous turbulent zonal wind stress
Notations	
subscript 'a'	indicates the anomaly of a time series: series minus long term average of the series
'Δ'	indicates difference: Tyrrhenian basin average minus Ligurian basin average
Phenomena	
DWF	Deep Water Formation
EMT	Eastern Mediterranean Transient
IB	Inverse Barometer
WMT	Western Mediterranean Transition
SCV	Submesoscale Coherent Vortices
Instruments	
CTD	Conductivity Temperature Depth
RCM	Rotor Current Meter
MERMAID	Mobile Earthquake Recording in Marine Areas by Independent Divers
Satellite Missions	
Env	Envisat
J2	Jason2
Gyre	
NIG	North Ionian Gyre
Atmospheric Oscillation	
NAO	North Atlantic Oscillation
Tools	
IBM	Inverse Box Model
ALES	Adaptive Leading Edge Subwaveform retracker
PC	Principal Component
EOF	Empirical Orthogonal Function

Table 1: Main abbreviations used in the thesis listed in alphabetical order per group. Each acronym is repeated in the text only at the first occurrence or more often to facilitate the reading flow

2 Introduction

The Mediterranean Sea is a landlocked sea. Its main exchange with the open ocean happens through the Strait of Gibraltar (GS). The Mediterranean is a miniature ocean with its own overturning circulation and Deep Water Formation (DWF) sites (Marshall and Schott, 1999, Chiggiato et al., 2016). As a semi-closed basin, it also constitutes a potentially useful case study to evaluate heat-budget estimation uncertainties (Josey et al., 2013). In contrast to the world ocean, important phenomena, e.g. overturning circulation and thermohaline modification due to climate change or anthropogenic influence, can be observed in a human life time scale in the Mediterranean. This allows us to use this sea as the perfect observatory to understand, model and forecast the phenomena that drive the behaviour of the ocean. The Mediterranean Sea is constituted by two basins: the eastern and the western basins, that are connected through the Sicily Channel (SC), Figure 1. The present work focuses on the Western Mediterranean Sea (WMED), especially on the Ligurian Sea (LS). A brief description of the WMED circulation follows.

The surface circulation in the Mediterranean is generally cyclonic. The northern return branch is more stable than the southern flow, which is characterised by several meanders and eddies (Tanhua et al., 2013, Schroeder et al., 2012), some of which appear to be stable and have a life time of several years (Millot, 1999). The surface circulation is fed by the inflow of fresh and warm Atlantic Water (AW) entering at the Strait of Gibraltar, flowing along the northern African shores, until it splits: a branch goes towards the eastern basin, crossing the Sicily Channel, the other branch skews northwards and enters the Tyrrhenian Sea (TYS) through the Sardinia Channel (SCh). From the Tyrrhenian Sea the AW enters in the Ligurian Sea and joins the Liguro-Provençal Current (LPC), Figure 2, along the north-western shores completing the cyclonic circulation in the western basin. The AW after entering the Ionian Sea in the eastern basin flows along the Libyo-egyptian coast, northern African coast, creating a number of anti-cyclonic eddies. In this basin the surface circulation seems to be influenced by the North Ionian Gyre (NIG), which reverses its rotation approximately on a decadal time scale (Civitarese et al., 2010, Gačić et al., 2013), affecting the Atlantic Water path and therefore its dilution effect on the Levantine Intermediate Water (LIW).

The LIW is a high salinity intermediate water formed in the eastern Mediterranean and observed everywhere throughout the Mediterranean Sea. LIW is known to be formed in the Rhodes gyre in the north-western part of the Levantine Sea, where salty and warm surface waters accumulate and then sink in winter, remaining at intermediate depths. It is through the surface and intermediate circulation cell, dominated by the

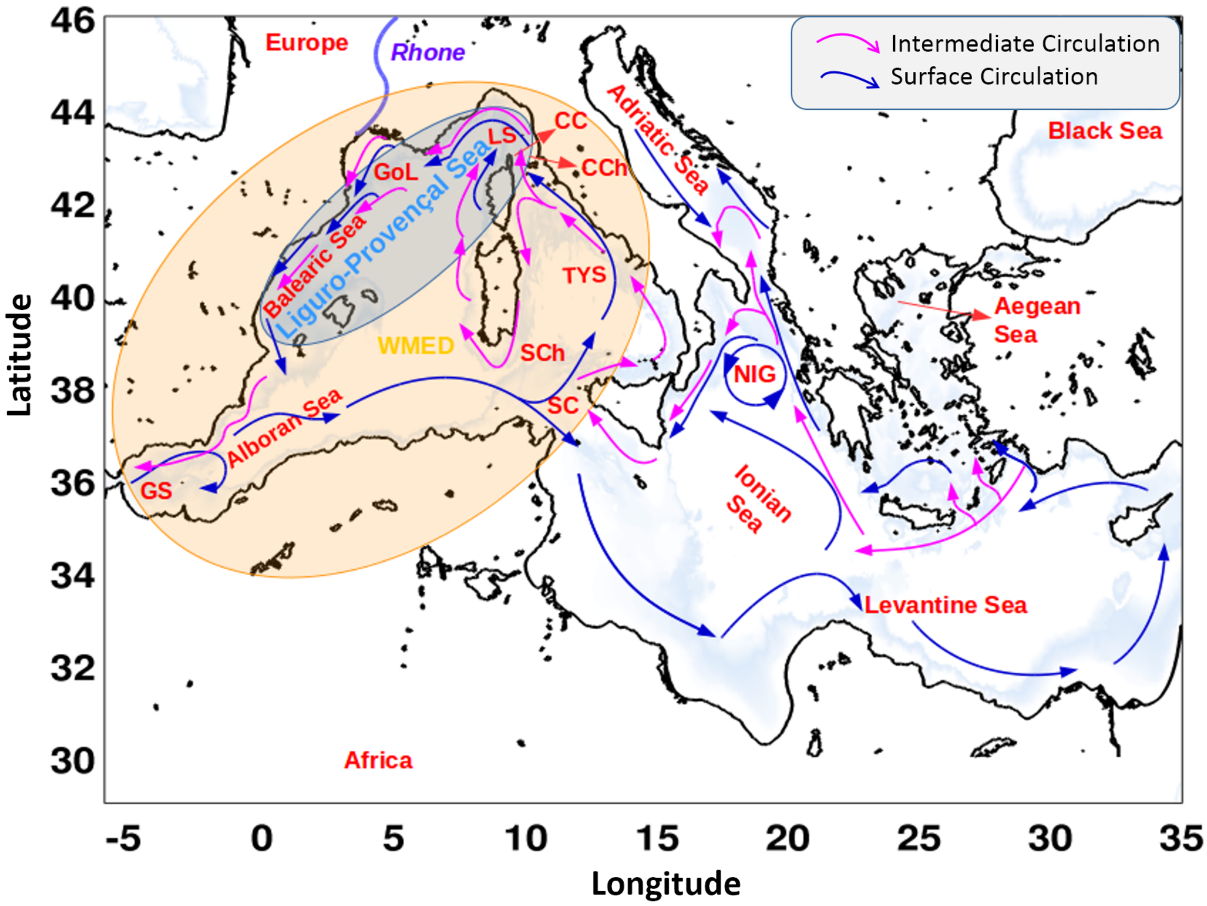

Figure 1: Mediterranean Sea map. Western Mediterranean Sea (WMED), Strait of Gibraltar (GS). Corsica Channel (CC). Capraia Channel (CCh). Gulf of Lion (GoL). Ligurian Sea (LS). Tyrrhenian Sea (TYS). Sardinia Channel (SCh), Sicily Channel (SC). North Ionian Gyre (NIG). The figure shows also a schematic of the main circulation as depicted by Millot and Taupier-Letage (2005). Blue lines represent the surface circulation dominated by Atlantic Water (AW). Magenta arrows show the intermediate circulation, constituted by Levantine Intermediate Water (LIW)

LIW, that the western and the eastern Mediterranean can communicate (Lascaratos et al., 1999). The LIW enters the WMED through the Sicily Channel, skews eastward, into the TYS, where it flows cyclonically. In the TYS the interaction between LIW and deep waters produces salt finger mixing processes (Bryden et al., 2014). When the LIW reaches the Corsica Channel (CC) to the north, a branch enters the Ligurian Sea, the rest continues to flow along the eastern Corsican and Sardinian shores. Once the LIW arrives at the Sardinia Channel, it deviates northward, flowing then on the western side of Corsica and Sardinia islands, until it gets to the LS and joins the LPC all the way to Gibraltar. The LIW constitutes the main contributor to the Mediterranean outflow into the Atlantic (Lascaratos et al., 1999).

The deep circulation cell is nourished in the WMED by the Deep Water Formation processes happening in the Gulf of Lion (GoL) and in the Ligurian Sea, sustaining the Mediterranean overturning circulation. In winter cold northerly/north-westerly

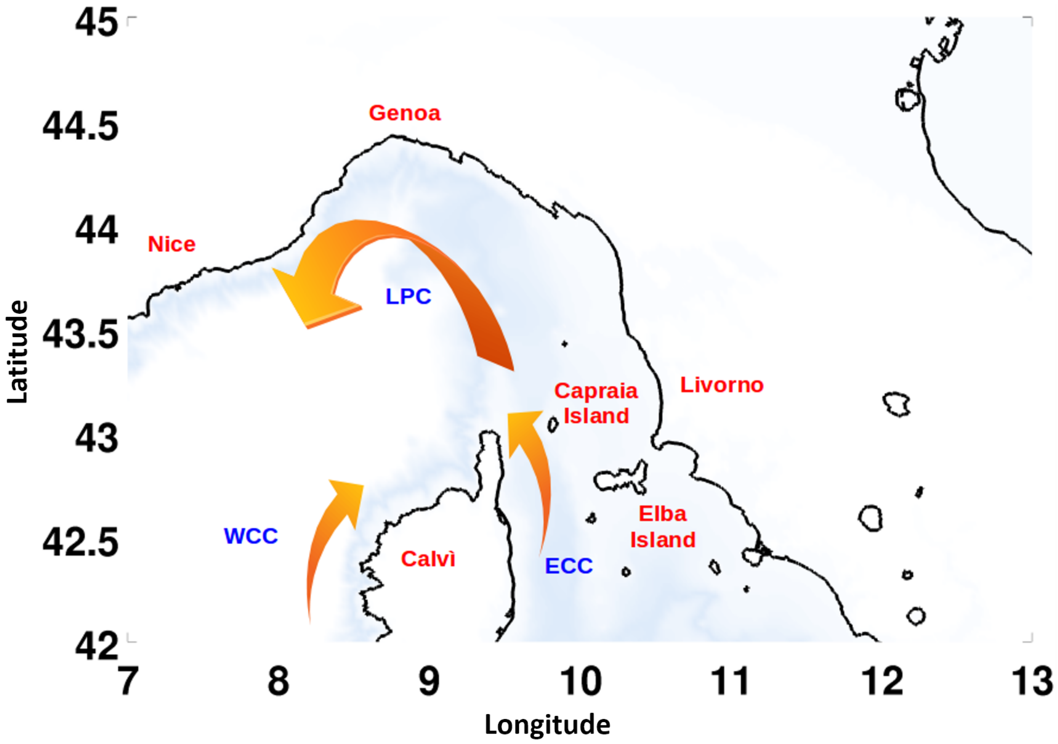

Figure 2: Ligurian Sea circulation. Eastern Corsica Current (ECC). Western Corsica Current (WCC). Liguro-Provençal Current (LPC)

winds, i.e. Mistral and Tramontane, blow on this region, facilitating the cooling and evaporation of the surface waters, which sink until they reach the bottom. Another important role in the DWF events has been recognised as the preconditioning of the water column (Grignon et al., 2010). The saltier the LIW is the easier it is for DWF to occur. Therefore even during average cold winters deep convection can take place. Shelf cascading has also been observed on the continental shelf of the Gulf of Lion (Font et al., 2007, Durrieu de Madron et al., 2013). The new deep water formed by this process results in cooler and fresher deep water than the water mass formed offshore due to the river run-off influence acting in the shelf area, mainly ascribable to the presence of the Rhône delta. Sometimes the buoyancy loss of the surface layer is not enough to erode the stratification from the surface to the bottom, so that cooled water crosses the Atlantic Water layer, but stops above the more dense LIW, forming Winter Intermediate Water (WIW) (Sparnocchia et al., 1995, Gasparini et al., 1999). The first evidence of deep convection in the Ligurian Sea was recorded in February 1969 down to a depth of 1200 m, other events were observed in 1991 (Sparnocchia et al., 1995) and from 2003 to 2006 almost every year. In the LS in 2006 the most saline, warm and dense deep water ever in the Western Mediterranean was recorded (Marty and Chiavérini, 2010). Some of the deep water partially gets dragged by the Liguro-Provençal Current to the Strait of Gibraltar, part of it exits into the Atlantic, another part follows the cyclonic circulation and flows along the northern African shores. From the formation sites some of the deep water spreads into the central WMED (Millot, 1999).

The WMED water column is mainly made up of four water masses: AW, LIW, Western Mediterranean Deep Water (WMDW) and, since winter 2004-2005, new Western Mediterranean Deep Water (nWMDW), see Figure 3. AW and LIW have already been introduced. The deep water deserves special attention.

The WMDW salinity and temperature have been increasing for several decades, then in winter 2004-2005 an exceptional volume of deep water was produced in the GoL and LS, this event set the start of the Western Mediterranean Transition (WMT) (Schroeder et al., 2010, 2016), modifying the vertical structure of the WMED water column. A new denser, saltier and warmer water mass appeared: the nWMDW. The factors that favoured such a massive DWF event were the intense air-sea interaction (Schroeder et al., 2010, Josey et al., 2013), with consequent heat and volume losses, and the preconditioning of the water column (Grignon et al., 2010). Some authors infer that even a normal winter would have led to deep convection, given the preconditioning status of the water column (Grignon et al., 2010). The winter of 2005 was not an average winter in any case, it was the driest and coldest of the last years, moreover more persistent northerly winds and a low river discharge occurred (Font et al., 2007). This event has been also linked to the propagation of the Easter Mediterranean Transient (EMT) signal. The EMT was an event that took place in the early 1990s, during which the deep water formation site in the Easter Mediterranean moved from the Adriatic to the Aegean Sea (Roether et al., 1996), probably modifying the thermohaline properties of the LIW. After 2004-2005 the $\theta - S$ diagram presented a "hook" at the bottom of the water column as the signature of the nWMDW formed after the WMT, which lifted by several meters the old WMDW (CIESM Monographs, 2009). Figure 4 shows the CTD (Conductivity Temperature Depth) profiles in a Θ-S diagram, zoomed on the nWMDW hook.

A focus on the Ligurian Sea water currents (Figure 2) is in the following reported, given its key role in the development of the present study. The LS circulation pattern is constituted by a marked frontal structure associated with the Liguro-Provençal Current, or Northern Current (Millot, 1999), which is basically cyclonic year-round, but does undergo significant seasonal changes (Astraldi et al., 1994). The LPC variability seems to be strongly influenced by the Tyrrhenian outflow, i.e. Eastern Corsica Current, in fact both currents present higher transport in winter and lower in summer (Astraldi et al., 1994). It is unclear how deep is the LPC, some authors refer to it as a surface current involving the first hundred meters of the water column (Astraldi and Gasparini, 1992, Robinson et al., 2001, Picco et al., 2010, Alvarez et al., 2013), others mention the possibility of the LPC carrying WMDW (Conan and Millot, 1995). The ECC involves the surface and intermediate layers of the water column transporting Atlantic Water and Levantine Intermediate Water. The ECC shows a marked seasonal and interannual variability. The winter flow across the CC can be 80% more intense than the summer flow (Astraldi et al., 1990). In summer the CC can be inactive or can even present reversals, especially in the Capraia Channel, between the Italian Coast and the Capraia Island (Manzella, 1985). The LPC is fed also by the Western Corsica Current (WCC). The WCC is the most unknown of the three currents characterising the LS. Astraldi et al. (1994) describe the WCC as a feature with a weak seasonal cycle if compared with the ECC. The WCC flow increases in autumn and reaches its maximum in early summer. This oscillation can be observed in the entire water column, but it is more evident in the surface layers. The WCC is also subjected to the Ligurian front, i.e. LPC, displacement influence, that compresses the WCC during winter to early summer (Astraldi et al., 1994).

The present study aims to define the functioning of the Ligurian Sea, in the light of present technologies, different platforms and available datasets. As already mentioned it is unclear how deep is the Liguro-Provençal Current and what speed characterises its deep layers. In Chapter 3 this question is answered using a dataset deriving from lagrangian seismic instruments, from which the velocities of the deep LPC have been calculated. In the past several authors tried to link the Eastern Corsica Channel temporal evolution to various factors. For instance Astraldi et al. (1990) ascribe the ECC activity to the steric difference between the Ligurian Sea and the Tyrrhenian Sea, that leads generally to a northward flux through the channel. Astraldi et al. (1994) attribute the ECC variability to the winter volume loss occurring in the LS and in the GoL through air-sea interactions, which needs to be replenished. This would explain the winter increase of the northwards transport across the CC. Vignudelli et al. (1999) studied the North Atlantic Oscillation (NAO) connection with the CC water flux and demonstrated that during winters with negative NAO index, the ECC was stronger, especially for NAO index values lower than -1. In the light of all these factors taking part to the ECC behaviour, the CC is considered to be a choke point (Aracri et al., 2016) for observing the exchanges between the TYS and LS, to monitor the DWF events and to study the influences of the incoming water masses from the eastern to the western Mediterranean basin, as a preconditioning factor. It is important also in terms of air-sea interaction since it would be possible to link the variability of the volume transport through the CC to the wintertime volume and heat losses in the Liguro-Provençal basin. Moreover, being sensitive to the NAO oscillation, the CC is important for studying the relationship between the atmospheric oscillations and the circulation in the WMED. In the present study the relationship between the ECC and the steric Liguro-Tyrrhenian variations has been investigated using an altimetry dataset coming from along track (Vignudelli et al., 2000) and gridded satellite data, Chapter 4. In the same chapter the sea surface pressure and the wind stress have been related to the CC water transport to study their influence on the ECC variability. In previous studies, such as Schroeder

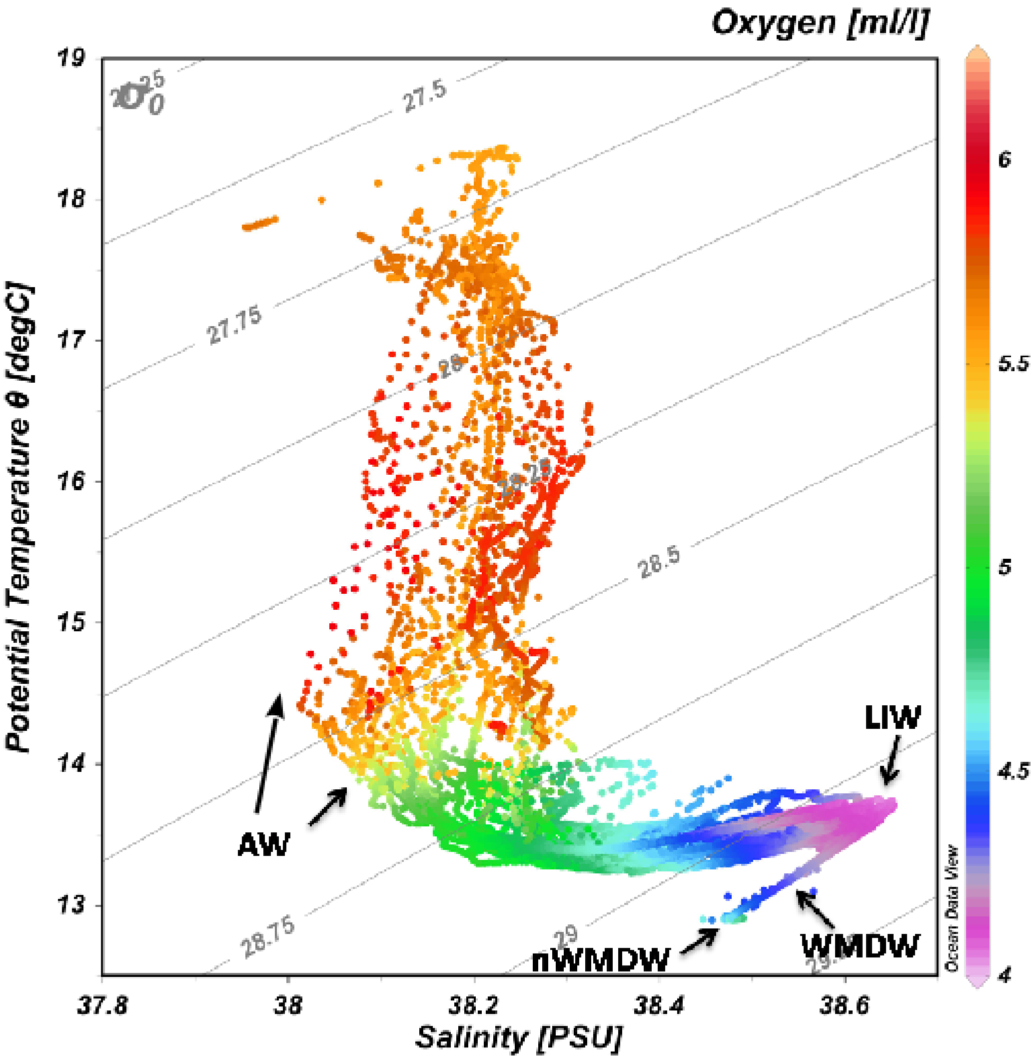

Figure 3: Typical Western Mediterranean $\theta - S$ diagram. The plot represents the distribution of water masses in the potential temperature-salinity space. Colour indicates the oxygen content. Diagonal black lines represent density ($\sigma - 1000\ Kg/m^3$). LIW = Levantine Intermediate Water, AW = Atlantic Water, it is actually Atlantic modified water, WMDW = Western Mediterranean Deep Water, nWMDW = new Western Mediterranean Deep Water. Data represented in the figure were collected during the oceanographic cruise EUROFLEET12, November 2012

et al. (2008a) and Vetrano et al. (2010), the absolute geostrophic circulation in the LS has been estimated through Inverse Box Modelling. In Chapter 6 hydrographic data from 9 oceanographic sampling campaigns have been used to estimate the absolute geostrophic circulation in the LS, resulting in a new transport estimates for the LPC, WCC and ECC. Almost nothing can be found in literature about the flow rate of the Capraia Channel (CL), right eastward of the CC. In Chapter 6 an attempt has been made to describe the CL role in LS circulation. In Chapter 7, the main findings of the studies here presented are summarised and some suggestions for future work are made. The lists of the main abbreviations used in this work can be found in alphabetical order

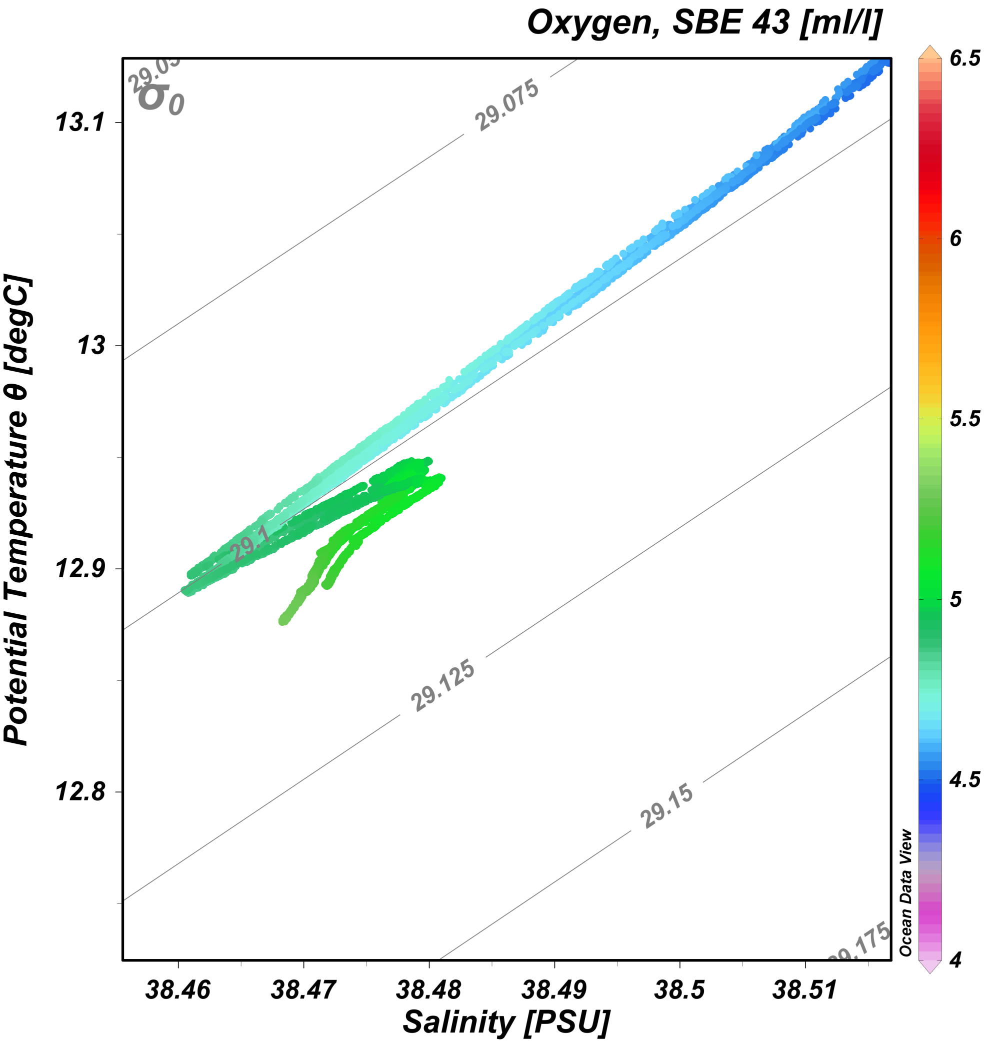

Figure 4: Θ-S diagram from CTD stations off the Corsica coast. Data has been collected during the Sirena06 cruise, in July 2006. Colour represents oxygen. Black diagonal lines indicate density ($\sigma - 1000\ Kg/m^3$)

for each group in the Glossary. Each abbreviations is defined when it first appears in the text.

3 The Deep Liguro-Provençal Current as Observed by Free Floating Lagrangian Devices

3.1 Abstract

The velocity of the deep Liguro-Provençal Current, in the north-western Mediterranean has been estimated using for the first time submarine drifting instruments that record seismic waves called MERMAIDs (Mobile Earthquake Recording in Marine Areas by Independent Divers)(Sukhovich et al., 2015, Hello et al., 2011). In this study the deep western Mediterranean Sea circulation shows an intense activity even in the deep layers of the water column. Through pseudo-eulerian statistics, different components of the observed variability are analysed and described, revealing the turbulent nature of the Liguro-Provençal basin deep circulation.

3.2 Introduction

The collection of deep in situ data is a highly demanding task both in terms of time and financial support and therefore it still constitutes a challenge for modern oceanography. Direct observations of the deep currents in the Mediterranean Sea, Figure 5, are very few and sparse in time, but extremely valuable. In this particular study the evaluation of a reference velocity for the LPC using MERMAID data is important also for the evaluation of the absolute geostrophic circulation in Ligurian Sea with the Inverse Box Model (IBM), see Chapter 6.

Over the course of time dedicated experiments have tried to depict the LPC temporal and spatial variability (Taupier-Letage and Millot (1986); Conan and Millot (1995); Sammari et al. (1995); Alberola et al. (1995)), but only a few refer to it as a current involving the whole water column and therefore carrying deep waters (Millot, 1999). Most authors treat the LPC as a surface or intermediate flow (Astraldi and Gasparini (1992); Robinson et al. (2001); Picco et al. (2010); Alvarez et al. (2013)). Others limit the LPC influence to 1100 m depth (Taupier-Letage and Millot, 1986) and some mention the possibility of the LPC dragging along Western Mediterranean Deep Water (WMDW) (Conan and Millot, 1995).

In the Mediterranean Sea sub-surface lagrangian instruments have mostly been used to investigate intermediate currents (Menna and Poulain (2010); Poulain et al. (2007); Bosse et al. (2015)). During the SOFARGOS project (MAST2-EU, 1996), RAFOS floats drifting depths were set to 350 m, 600 m and 1200 m in order to capture features of the behaviour of the entire water column. Several studies identified Submesoscale Coherent Vortices (SCV), and investigated their spatial distribution in the Algerian Basin (Testor et al., 2005) and in the north-western Mediterranean (Testor and Gascard, 2003), relating the occurrence of SCV with Deep Water Formation (Testor and Gascard, 2006). To the best of our knowledge no other attempts have been made to quantify the LPC vertical influence and strength at depth or to study the deep NWMS circulation using lagrangian instruments.

Some very well known problems arise when dealing with free floating devices. For instance it is notoriously difficult to establish the exact sinking/surfacing position because of the unknown instrument drift at the surface and at depth (Katsumata and Yoshinari, 2010), consequently also the coordinates of the instruments after reaching their parking depth is an unknown piece of information that needs careful study. Lagrangian floats data are also affected by uncertainties associated with clock drift (Katsumata and Yoshinari, 2010). During SOFARGOS experiments, deep floats such as RAFOS were localized at depth by triangulation using an array of moored acoustic sources, (Testor and Gascard (2003); Testor et al. (2005); Testor and Gascard (2006)). Using Argo floats or, as in the present work, MERMAIDs, the positioning is done via satellite communication when the floats are at surface, instead of an acoustic triangulation. Katsumata and Yoshinari (2010) infer that the longer the float drifts at depth the smaller is going to be the error in velocity. In the case of Argo, the floats are programmed to surface approximately every 5 days or 10 days in the Mediterranean depending on the chosen sampling schedule, which renders an accurate estimation of the error and of its position difficult in most cases. MERMAIDs in the present dataset surface more often than Argos, i.e. on average every 4-5 days, so the uncertainty associated with their positioning remains an open question. MERMAIDs are programmed to ascend to the surface every 10 days, but since they are also designed to surface when they detect a seismic event, they can emerge more often, despite their default setting parameters.

The development of the large scale oceanographic Argo project provided a model for the global seismic community to follow (Simons et al., 2006). MERMAIDs floats are therefore akin to Argos when position uncertainties, communication and displacement techniques are considered. Alike Argos network, the MERMAID network main mission is to create a uniform seismic geographical data coverage to allow accurate tomography. Tomography is a technique for imaging the shape of the Earth interior through the propagation of seismic waves. The fact that two thirds of the Earth is covered by the ocean constitutes a challenge to collect sufficient data around the globe to obtain a uniform tomographic reconstruction. MERMAID floats in particular are equipped with a hydrophone able to capture water pressure variations caused by P waves (Simons et al., 2006). P waves are primary, or pressure, seismic waves, generated by earthquakes and travel faster than any other seismic wave. Given their employment, MERMAID floats carry different sensors than Argo floats. The former are equipped with pressure sensor and hydrophones, the latter payload is constituted by CTD probes. The two instruments also differ about the sampling schedule. Argo floats drift at a prefixed parking depth, e.g. 350 m in the framework of MedArgo (Poulain et al., 2007), and once every 5-10 days they sink to a greater depth, i.e. 700 m or 2000 m. During the up-cast they perform a CTD profile (Menna and Poulain (2010); Poulain et al. (2007)), then after surfacing the instruments communicate their position and data to the satellite. MERMAIDS, instead, surface every time that they detect a P wave, therefore they do not transmit their position and data following a fixed schedule. The ideal cruising depth for MERMAIDs is reassessed after each cycle. It depends on the P wave depth detection during the previous dive and on the location of the SOFAR channel (Joubert et al., 2016, Simons et al., 2009).

The MERMAID data presented here are particularly important because they represent a rare deep dataset. This study also highlights the possible extraction of useful data from alternative collecting platforms, not strictly dedicated to oceanographic studies. During the present investigation Argo data and MERMAID data have not being merged, because the abundant Argo data would have buried the MERMAID data, whose contribution to the study of deep currents would have been obscured.

The focus of this work is to study the deep circulation of the northern WMED and in particular to observe the LPC evolution at depth by means of MERMAID (Hello et al., 2011). In section 3.3 instruments, data and methods are presented. The results are described in section 3.4, where also the reference velocities for the LPC are evaluated. Finally the study is summarized in section 3.5.

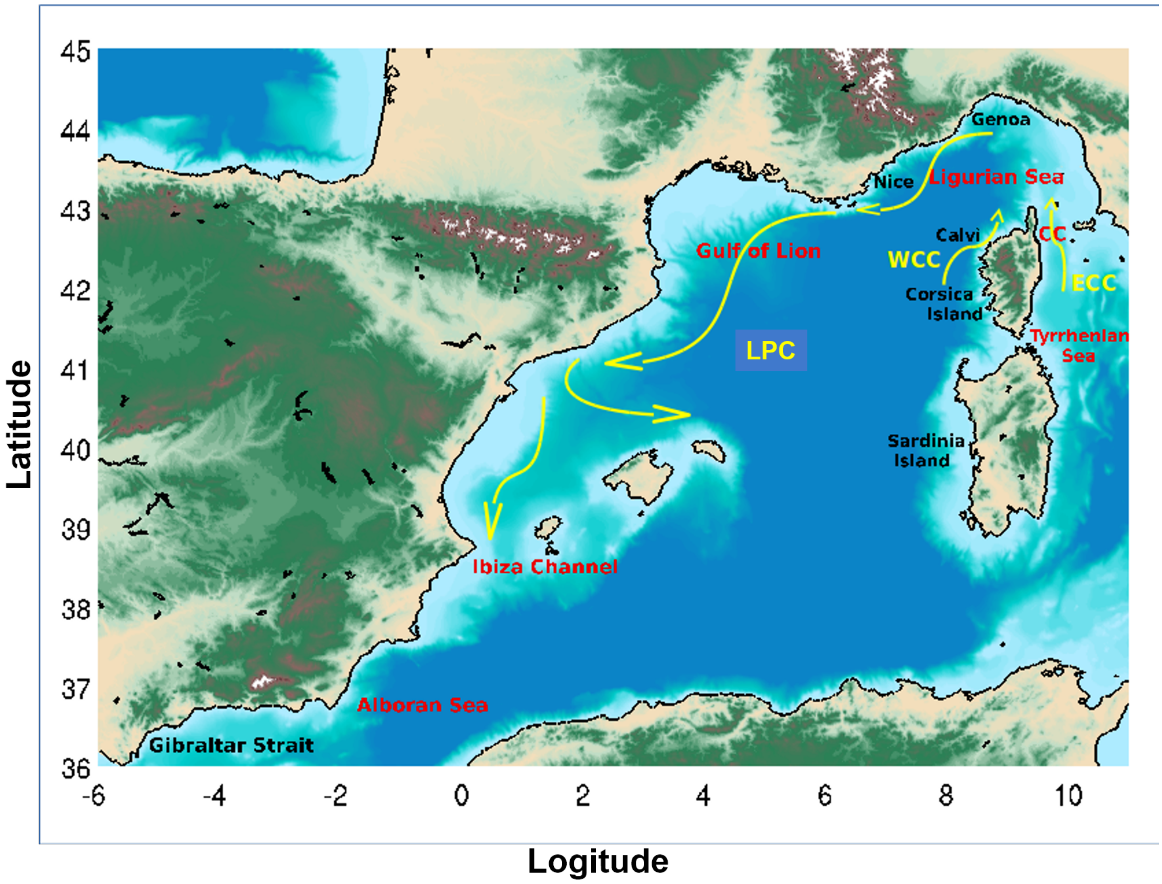

Figure 5: Western Mediterranean Sea map. Yellow arrows indicate the water paths for Liguro-Provençal Current (LPC), Eastern Corsica Current (ECC) and Western Corsica Current (WCC). CC stands for Corsica Current

3.3 Data and Methods

MERMAIDs are freely floating devices, deployed to capture underwater seismic waves (Sukhovich et al., 2015). The MERMAID float, Figure 6, is made of an aluminium tube container, which encapsulates the batteries, electronics and hydraulic system (oil pump, reservoir and valve). There is also an air parallel system (pump and valve). Attached to the float there is a bladder located in the foot. This bladder, divided in two compartments, one for the oil and the other for air, can be filled by oil and air stored in the solid aluminium tube container. The total volume of the float, can then be increased by transferring oil and air in the bladder. To ascend the oil is transferred from the inside of the float (aluminium tube) into the bladder, using the hydraulic pump. Therefore the total volume (float and bladder) increases and its density decreases, forcing the float to ascend. At surface the bladder is full of oil and air is added to inflate it completely. Pumping oil is power consuming, especially at deep depths, and it will consume the battery quickly. To enable the float to navigate in the water column 0.5 litres of oil are needed. Pumping air requires less energy, it happens only at surface in order to provide to the MERMAID a better stability and therefore a better data communication with satellite (GPS and Iridium). Therefore both air and oil are used. To descend the float needs to decrease its whole volume by first transferring the total volume of air from the bladder to the inside of the float and then a certain amount of oil depending on the target depth. This is made by opening a valve. The external bladder is located at approximately one meter below surface, the hydrostatic pressure at this depth is sufficient to push air and oil from the bladder inside the float.

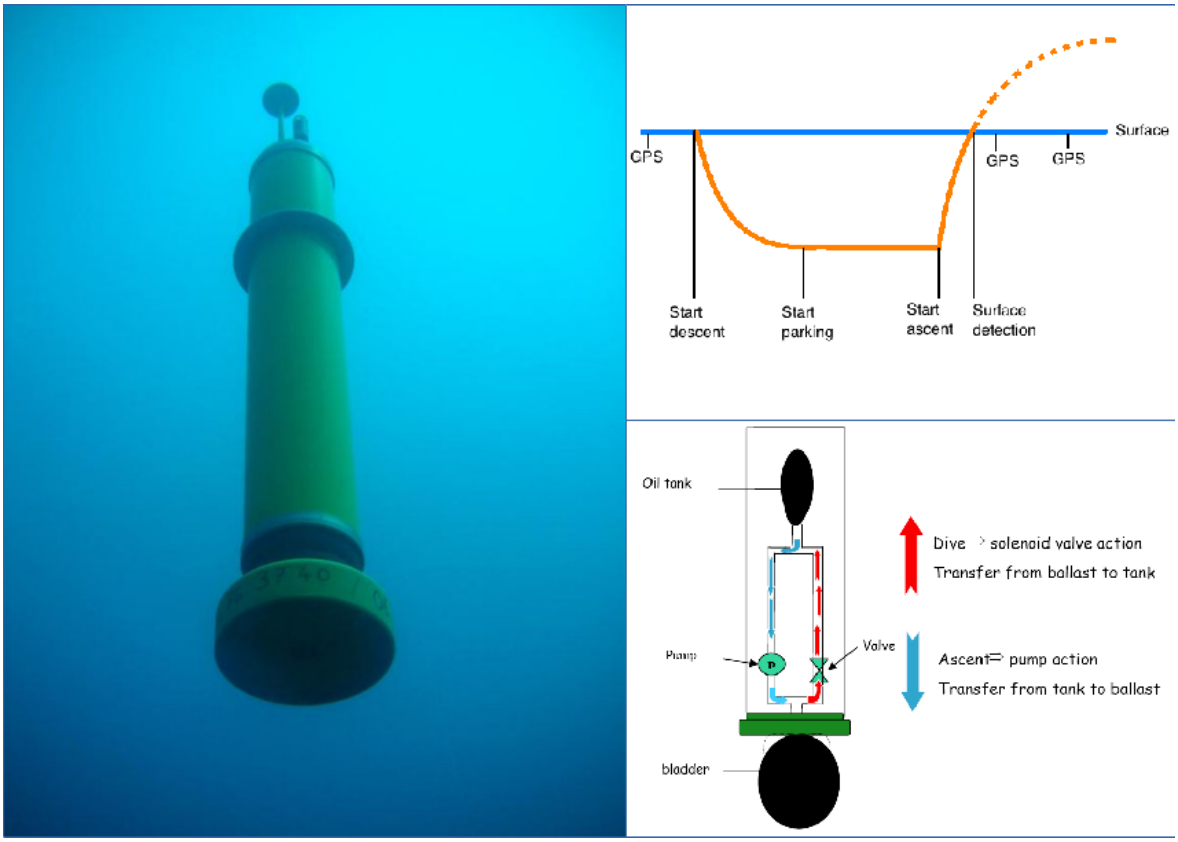

Figure 6: MERMAID functioning and instrument specification. Figure courtesy of Yann Hello (Géoazur - Valbonne, France)

Seven MERMAIDs were deployed in the Ligurian Sea between December 2012 and July 2014: m17, m18, m30, m31, m32, m33, m35 (GLOBALSEIS, 2015). After the deployment the instrument stays at the surface to communicate its position, sends its data and gets new parameters for the following profile via Iridium satellite. Then air and oil are transferred from the external bladder into the float. At 50 m depth the transfer stops temporarily for further control and the profiler sinks until it reaches its parking depth where the data acquisition starts (Table 2 summarizes mean parking depths, deployment and recovery times and coordinates for each MERMAID). The actual pressure at the parking depth is measured by a pressure sensor embedded in the instrument. After about 4-5 days (i.e. each time a seismic signal has been recorded by the instrument) the bladder is gradually filled up and the ascent phase begins.

Depending on the water density the float can descend more slowly and the time it takes to reach the parking depth, with a standard deviation of ±5 dbar (Simons et al., 2009), might vary. The position at 50 m depth is calculated assuming a linear drift evinced by two consecutive GPS communications before the float starts its descent or finishes its ascent. The distance between the parking start and the parking end is divided by the time necessary for the float to move from one GPS point to the next in order to obtain a velocity for each segment of the trajectory. When the detection of a seismic wave forces the float to ascend, the MERMAID speed is set to the maximum in order to ascend as fast as possible to minimize the difference between its position at detection and the one at which it communicates with the GPS just after surfacing. This setting aims to minimize the error derived from the drifting that the float undergoes during its up-cast. When descending the float is set to optimize the electrical consumption by minimizing the pump and valve actions. For these reasons the ascent velocity is higher by a factor of $\sim$5 than the descent velocity. During Simons et al. (2009)'s study, typical rising velocities were under 20 cm/s, in our investigation the rising velocities, for m17, vary between 23 cm/s and 27 cm/s, while the diving velocities range between 5 cm/s and 7 cm/s. The uncertainty associated with MERMAID positioning, caused by surface and deep drifting remains an open question. Joubert et al. (2016) estimated that in the Ligurian Sea the drift of the floats associated with deep currents can be approximated to 1.8 Km/day, which translates in 0.021 m/s error in our estimation of the deep currents through MERMAID positioning data. Trying to estimate the underwater drift using the climatological geostrophic velocity resulted in a mean positioning correction during the descend phase of $\sim$ 270 m between the surface and 200 m depth and between 200 and the parking depth $\sim$ 95 m. During the ascending phase, the mean correction has been estimated to be $\sim$ 20 m between the parking depth and 200 m and $\sim$ 60 m between 200 m depth and the surface. The division of the water column in two sectors, 0-200 m and 200 m - parking depth, has been chosen to resemble Bethoux's approach (Bethoux and Prieur, 1978). The geostrophic current correction has been reported here for completeness and for general interest, as such a suggested adjustment might help the seismic community to elaborate more precise P waves positioning. The impact on this study of such a small positioning correction, resulted in a change at the third decimal place when calculating the velocities in m/s, therefore the correction has been considered negligible and has not been applied to the following calculations.

3.4 Results

All seven MERMAIDs missions deployed in the Liguro-Provençal basin are shown in Figures 7, 8, 9, 10, 11, 12, 13. The operational depths can be found in the blue graph inserted over each map, together with the along track bathymetry. It is important

name	start	end	mean pd	start/end Lon E° Lat N°
m17	20-12-2012 11:27:31	20-07-2014 07:21:21	916.4m	8,06 43,20 /-0,77 37,39
m18	20-12-2012 11:29:41	21-10-2013 04:57:01	871.3m	8,06 43,20 / 3,67 42,21
m30	14-03-2014 12:04:51	25-06-2014 07:00:11	1606.4m	8,52 43,80 / 6,08 42,62
m31	14-03-2014 11:05:11	04-07-2015 06:36:01	1476.3m	8,40 43,75 / 4,10 42,32
m32	14-03-2014 13:22:01	02-07-2014 05:58:31	1461.5m	8,59 43,87 / 7,16 43,28
m33	17-07-2014 11:32:21	09-07-2015 21:27:11	1513.2m	8,40 43,23 / 8,27 43,56
m35	17-07-2014 13:43:31	23-01-2015 06:56:21	1498.1m	8,26 43,45 / 6,97 43,07

Table 2: Deployment and recovery times and mean parking depth for each MERMAID

to notice that the bathymetry is the result of an interpolation, so its values are not as precise as a direct measure. Moreover the represented along track sea bed depth corresponds to the closest bathymetry point to the position of the MERMAID. This position is subject to uncertainty due to the unknown horizontal displacement of the float during the ascending phase. Once at the surface the device might drift before communicating its position to the satellite, adding a further error. Because of the mentioned uncertainties even data, which appear close to the sea bed, have not been removed. If an instrument got trapped against the sea floor the calculated speed would appear as an outlier in Figure 15. During this study it is assumed that the instrument descends vertically. The floats, e.g. m33 and m35, that were deployed away from the coast, between Nice and Calví remained trapped, at least at the beginning of their mission, in the middle of the cyclonic circulation, that characterizes the north-western Mediterranean Sea. MERMAIDs that were deployed near the boundary of the LPC immediately went westwards, following the main current (Figures 7, 8, 9, 10, 11, 12, 13). The initial displacement direction for each MERMAID is represented in Figure 14, based on the first 15 dives of each float. To identify outliers two thresholds were set: speed exceeding 30 cm/s has been considered unrealistic and removed; data points shallower than 700 m have not been retained deep enough to be included in the study of the deep LPC, see Figure 15. Based on the mean velocities of m17, m30, m31, m32, that drifted along the NC, the estimated time to travel from the deployment location to the Ibiza Channel ranges from 437 to 841 days. The velocity variations with time of each float are represented in Figure 16. Pseudo-eulerian statistics were computed from the MERMAID dataset. For this a bin size equal to 0.5 degrees was defined. Poulain (2001) suggests to use a minimum number of independent observations in order to discard bins with few observations, choosing 5 data per bin, as a practical trade-off between accuracy and geographical coverage. As the MERMAID dataset is new and limited, setting 5 independent data per bin results in a very poor geographical coverage. With such settings, the area between the GoL and the Ligurian Sea is scarcely represented and the portion of sea between the GoL and the Ibiza Channel is almost empty. Therefore, to accomplish this trade-off in the MERMAID dataset the threshold number was set to 3 data per bin. Increasing the size of the bins, on the other hand, impinged on the spatial resolution of the results, as the bigger the bin the more uniformed is the spatial observation. Figure 17 shows the entire dataset, with all the data available per bin before setting the threshold.

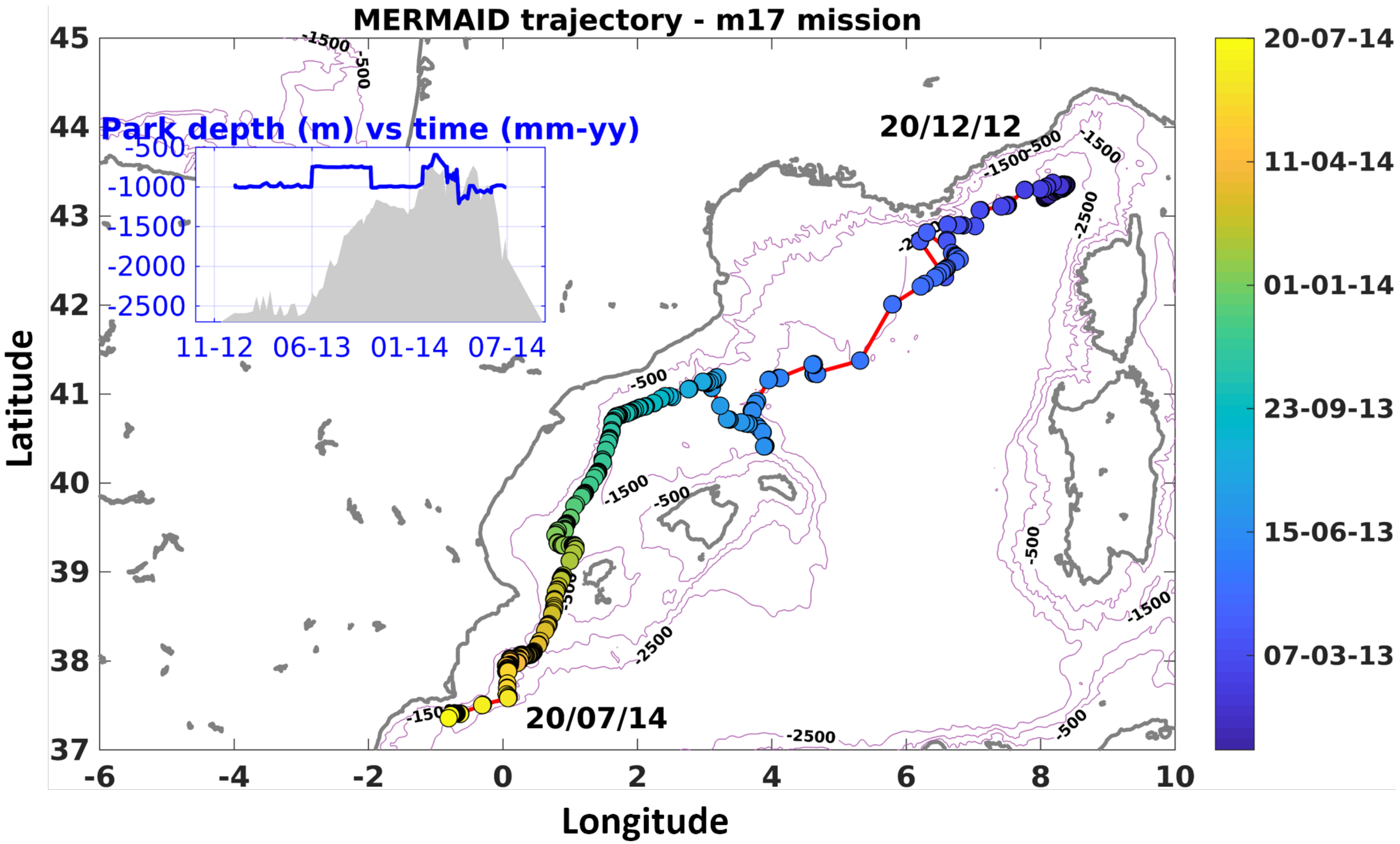

Figure 7: MERMAID m17 trajectory. The colour represents time. On the plot starting and ending deployment days are displayed. The top left graph represents the parking depth against time for the MERMAID whose trajectory is displayed on the same plot, in the same graph the grey area indicates the bathymetry at the closest position that the float communicated to the satellite at the surface

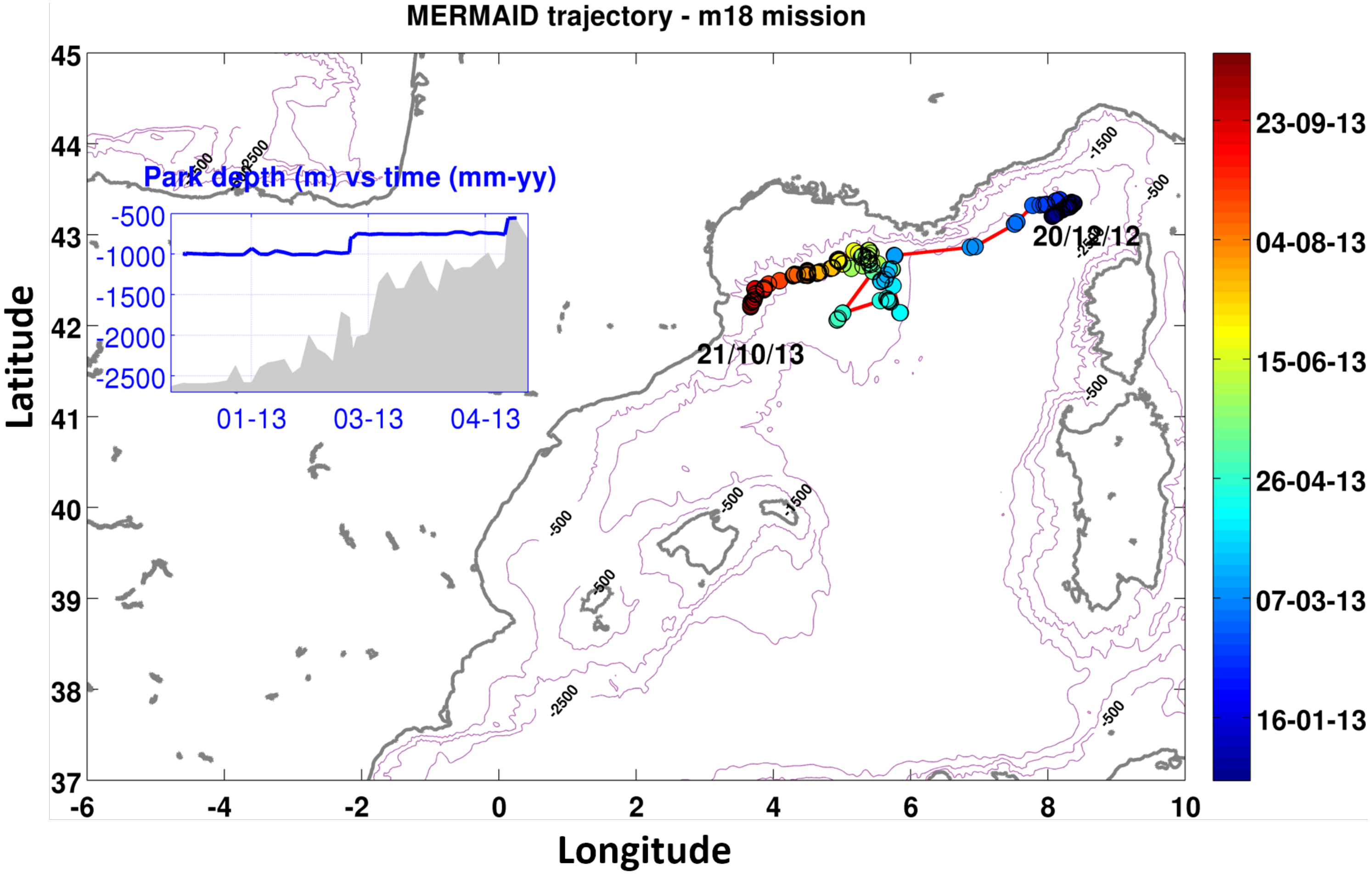

Figure 8: MERMAID m18 trajectory. The colour represents time. On the plot starting and ending deployment days are displayed. The top left graph represents the parking depth against time for the MERMAID whose trajectory is displayed on the same plot, in the same graph the grey area indicates the bathymetry at the closest point where the float communicates with the satellite at the surface

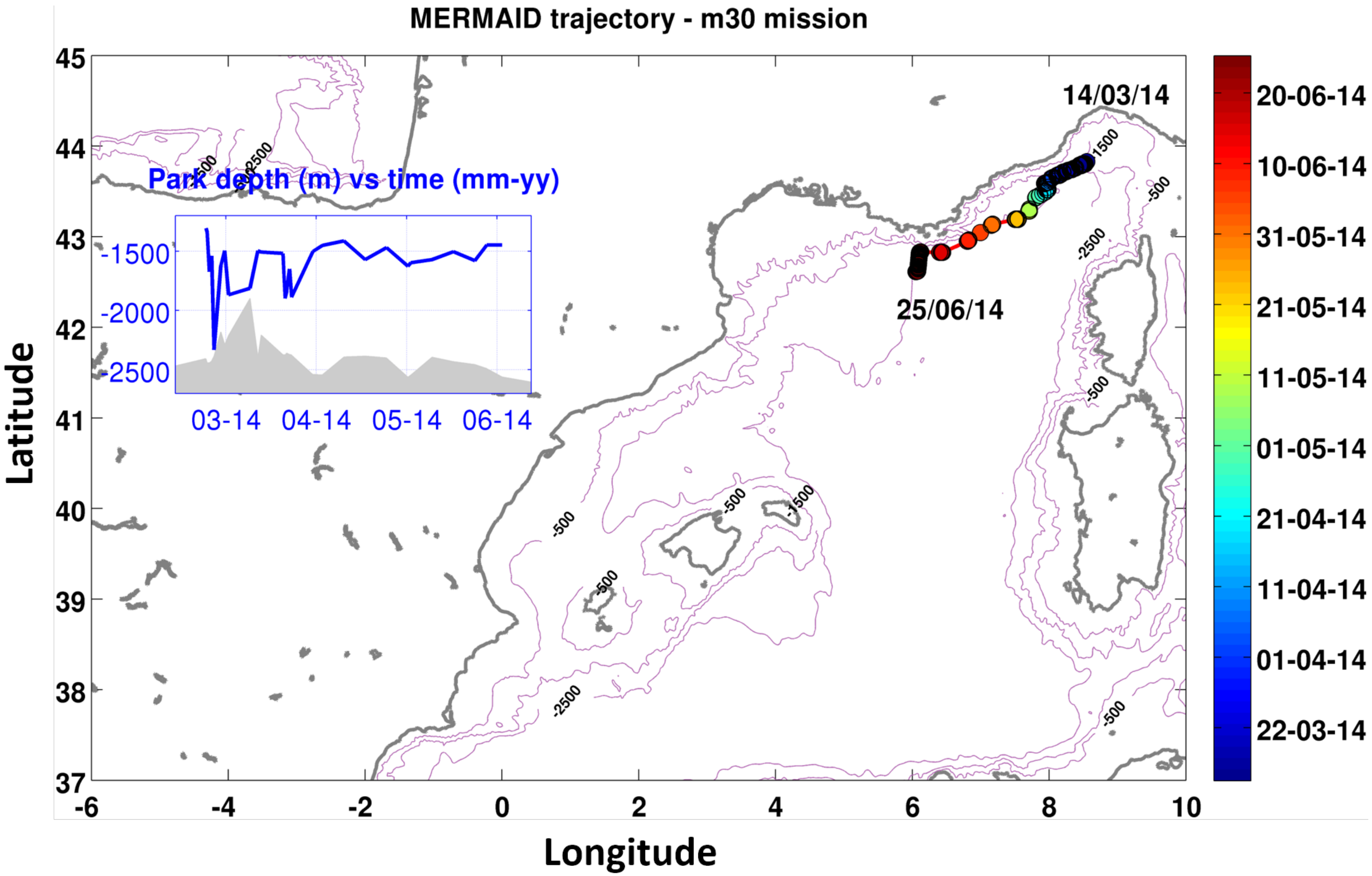

Figure 9: MERMAID m30 trajectory. The colour represents time. On the plot starting and ending deployment days are displayed. The top left graph represents the parking depth against time for the MERMAID whose trajectory is displayed on the same plot, in the same graph the grey area indicates the bathymetry at the closest point where the float communicates with the satellite at the surface

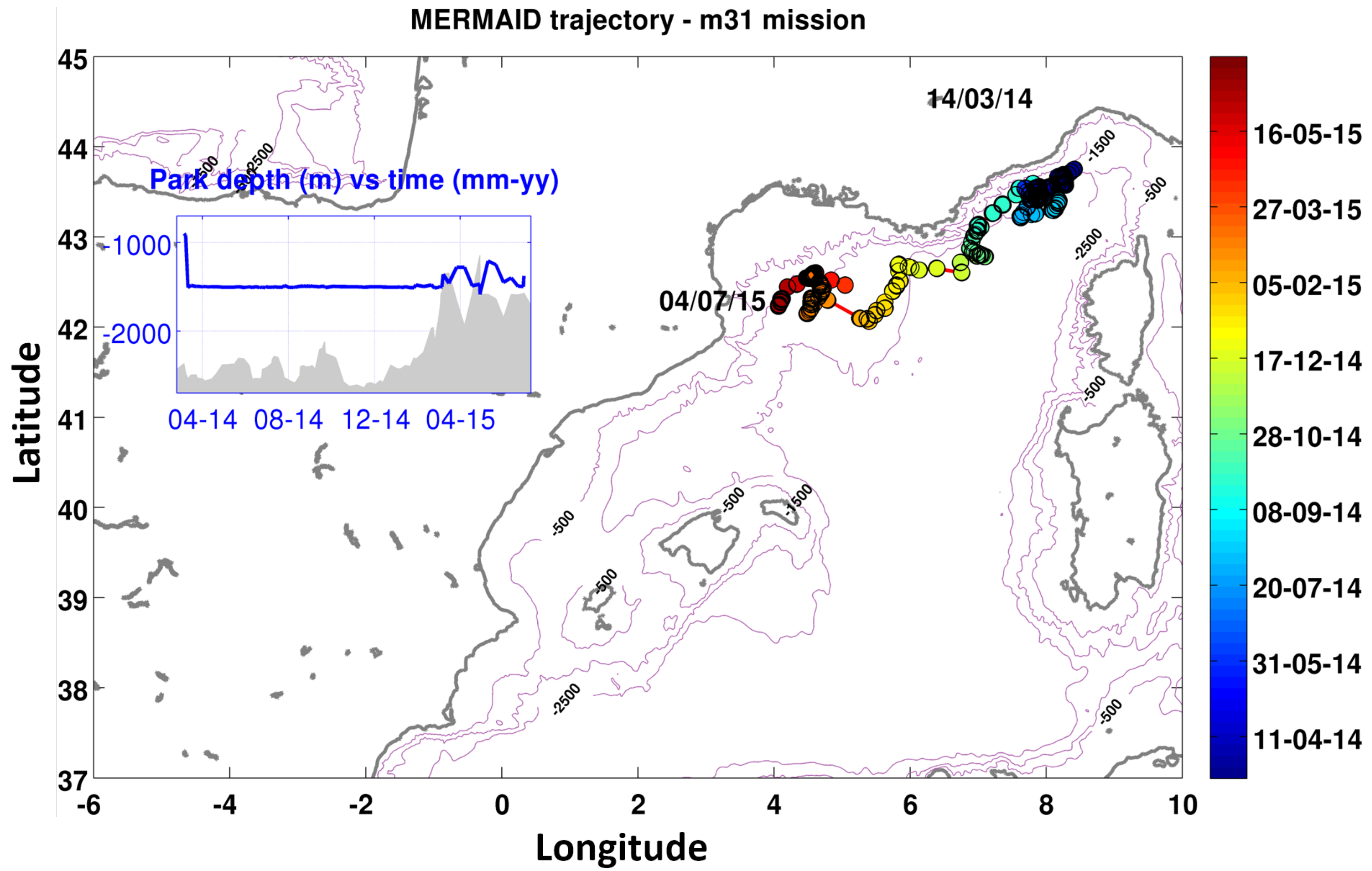

Figure 10: MERMAID m31 trajectory. The colour represents time. On the plot starting and ending deployment days are displayed. The top left graph represents the parking depth against time for the MERMAID whose trajectory is displayed on the same plot, in the same graph the grey area indicates the bathymetry at the closest point where the float communicates with the satellite at the surface

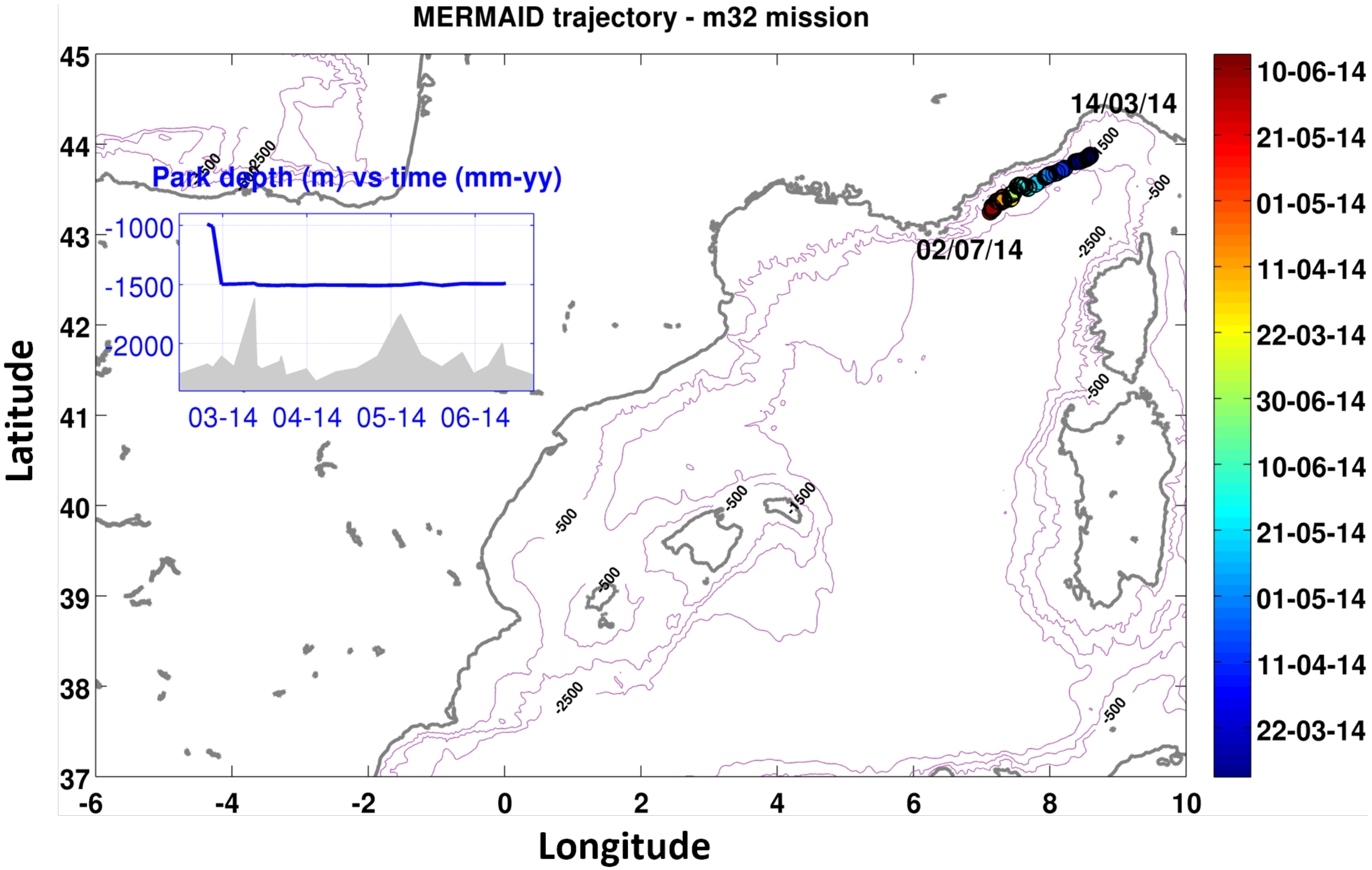

Figure 11: MERMAID m32 trajectory. The colour represents time. On the plot starting and ending deployment days are displayed. The top left graph represents the parking depth against time for the MERMAID whose trajectory is displayed on the same plot, in the same graph the grey area indicates the bathymetry at the closest point where the float communicates with the satellite at the surface

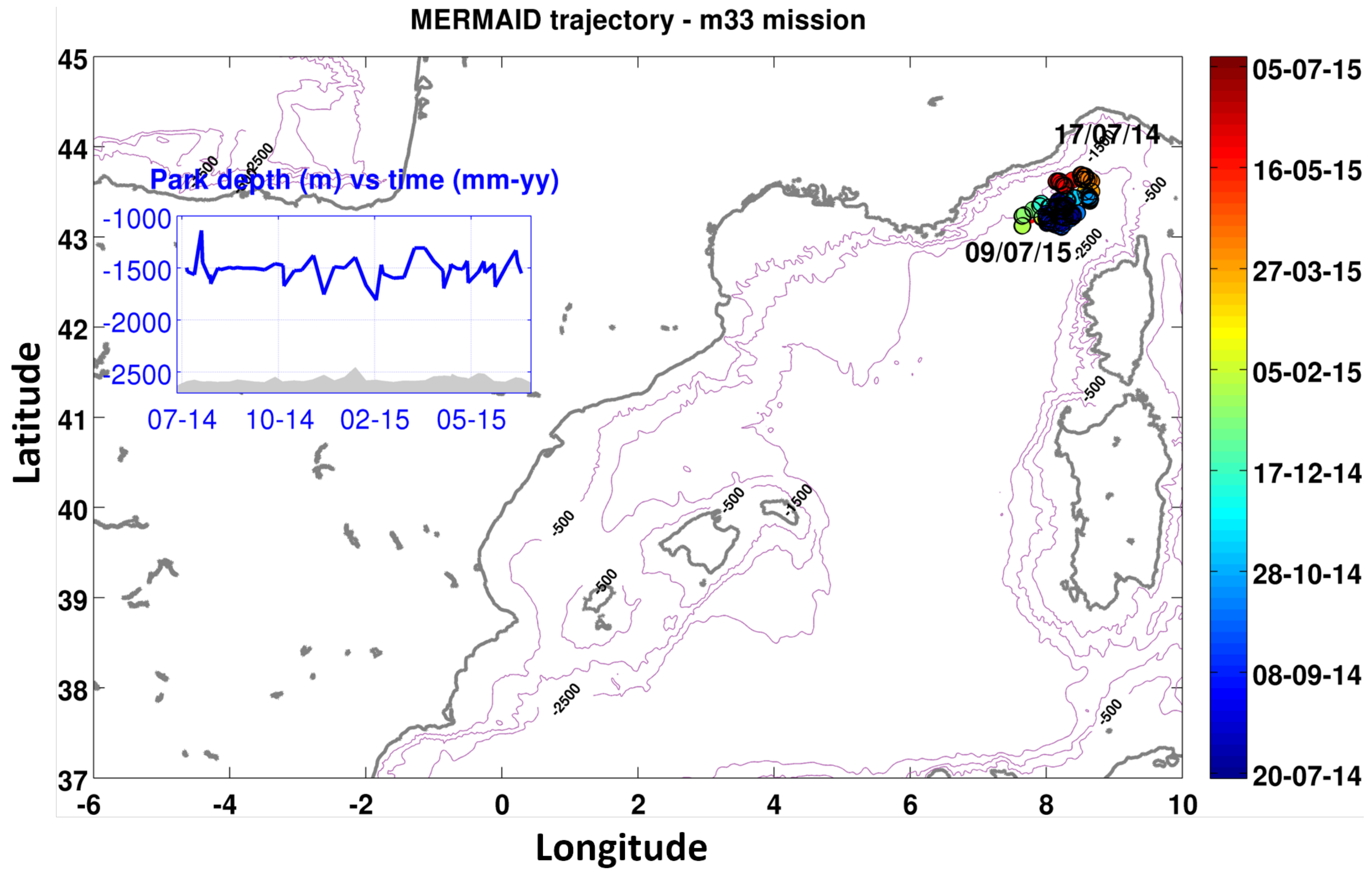

Figure 12: MERMAID m33 trajectory. The colour represents time. On the plot starting and ending deployment days are displayed. The top left graph represents the parking depth against time for the MERMAID whose trajectory is displayed on the same plot, in the same graph the grey area indicates the bathymetry at the closest point where the float communicates with the satellite at the surface

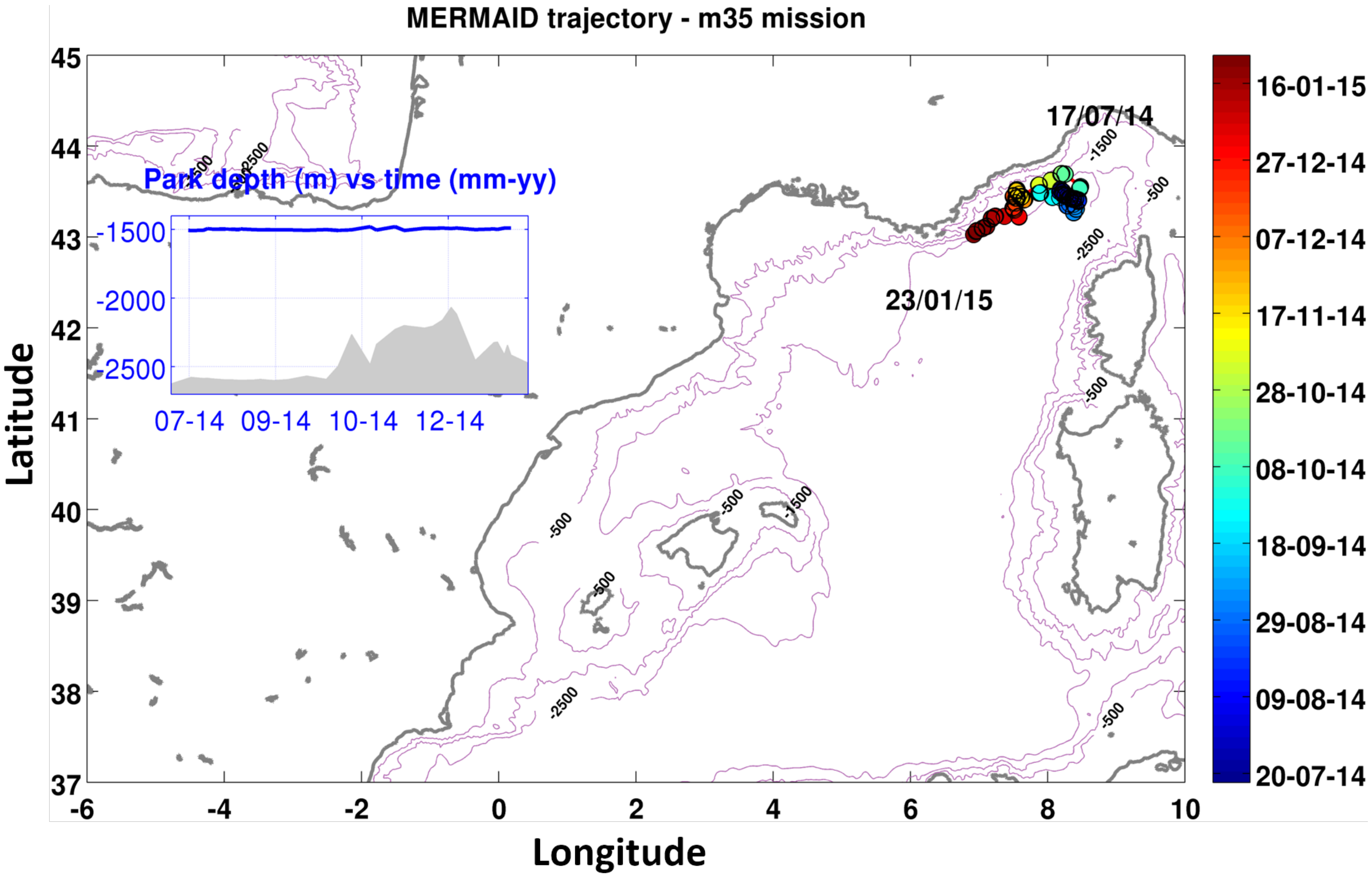

Figure 13: MERMAID m35 trajectory. The colour represents time. On the plot starting and ending deployment days are displayed. The top left graph represents the parking depth against time for the MERMAID whose trajectory is displayed on the same plot, in the same graph the grey area indicates the bathymetry at the closest point where the float communicates with the satellite at the surface

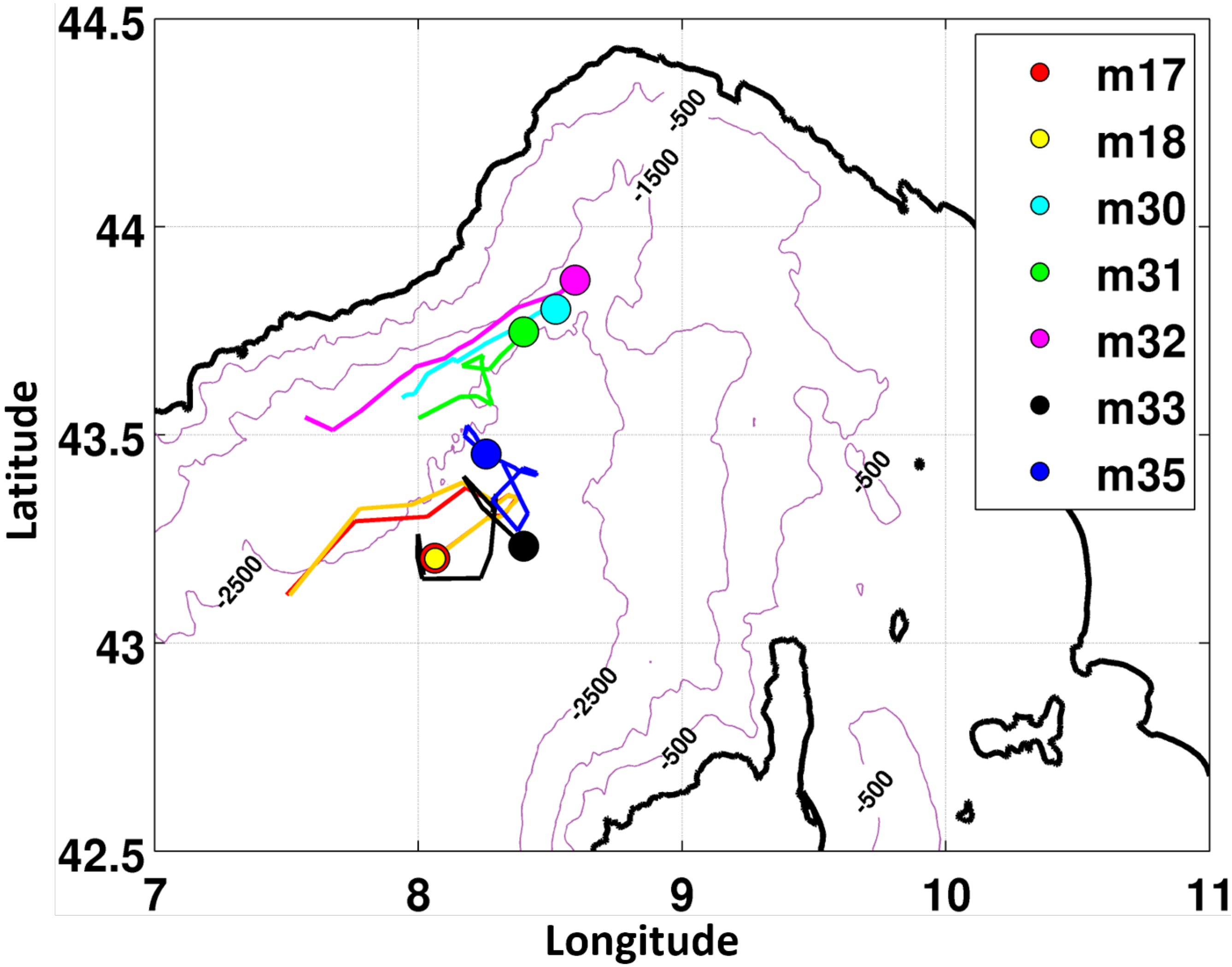

Figure 14: Deployment positions and first 15 dives for each MERMAID

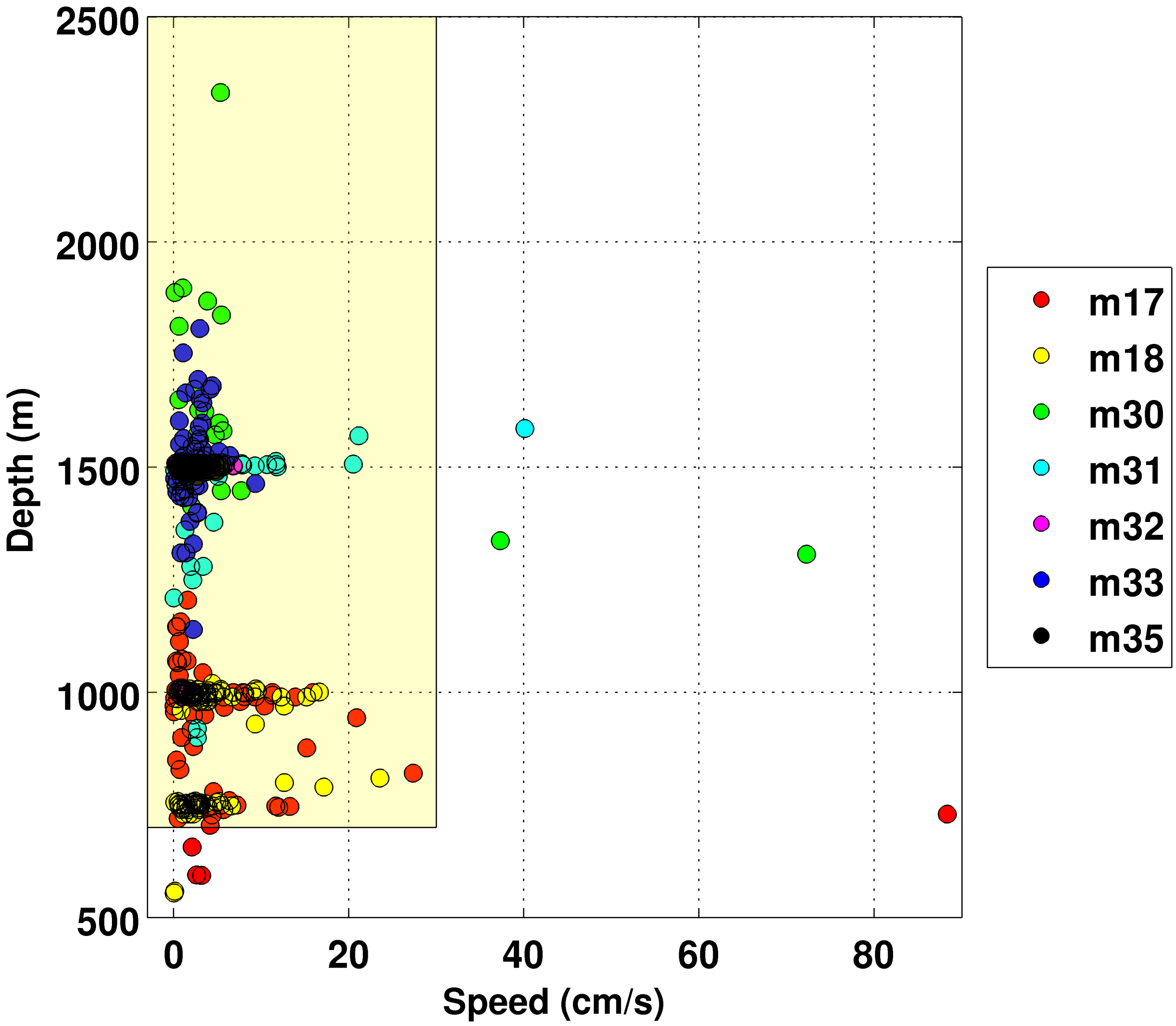

Figure 15: MERMAID data points. The horizontal axis represents speed (cm/s). The y axis shows depth (m). Each float data are represented with a different color. The shaded yellow area encloses all the data considered from now on, after the outliers are removed, which lay outside of the shaded area. Speed exceeding 30 cm/s has been considered unrealistic and data points shallower than 700 m have not been retained as they are not deep enough to be included in the study of the deep LPC

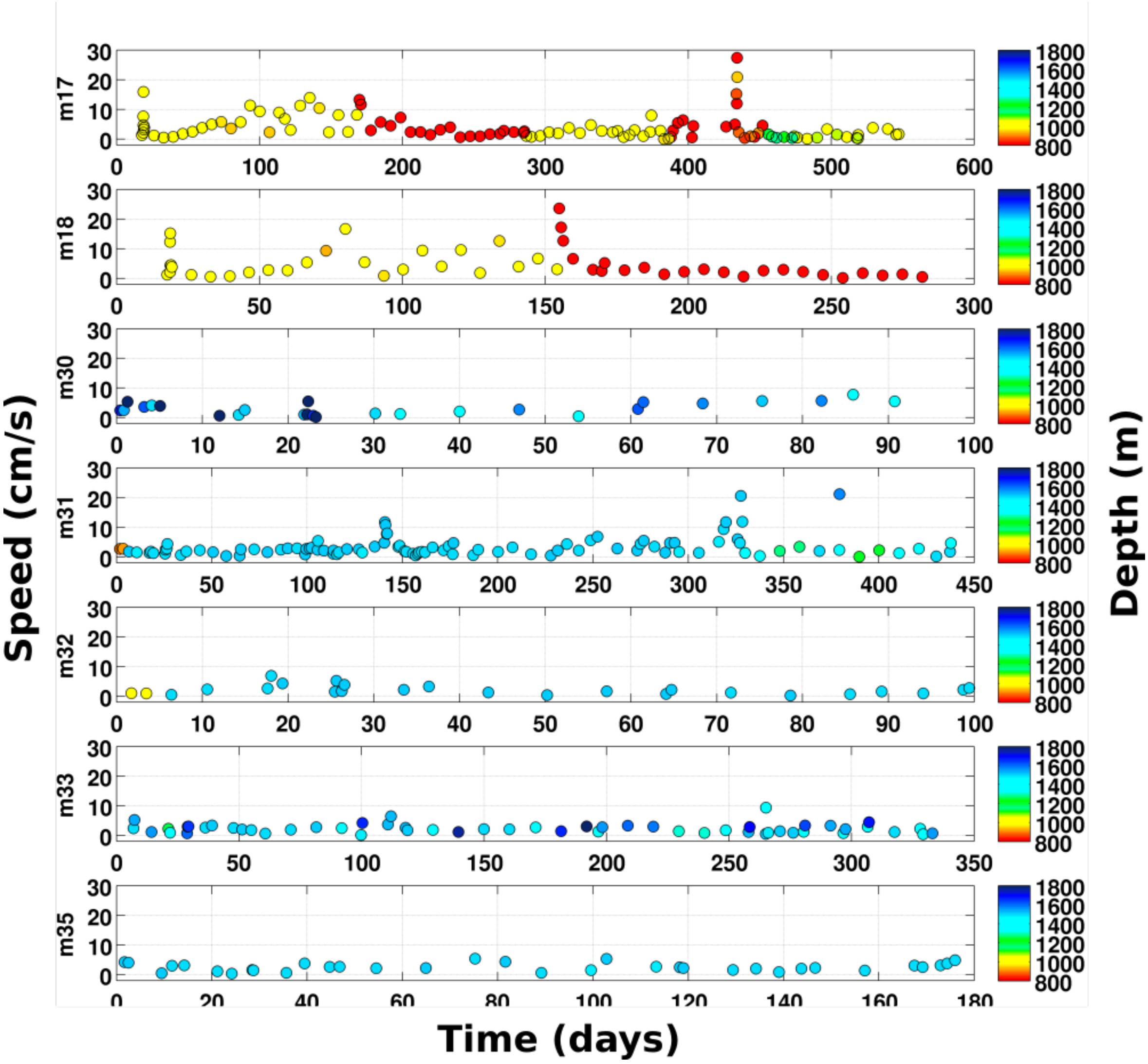

Figure 16: MERMAID speed. The horizontal axis represents days at sea, from deployment to recovery. The y axis shows speed (cm/s) in the direction of the displacement, which is mostly south-westward. The colour changes with depth, whose range is represented in meters by the color-bar on the right of each plot

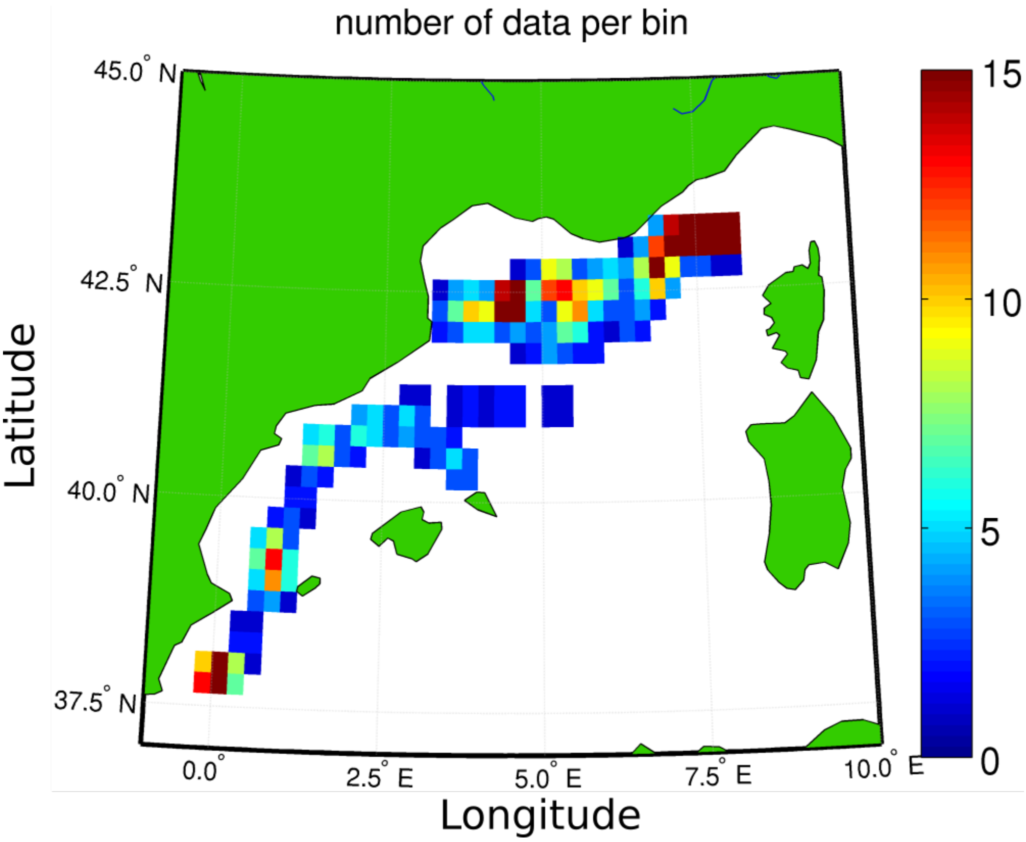

Figure 17: Number of data for bin before the bins containing less than 3 data points were removed

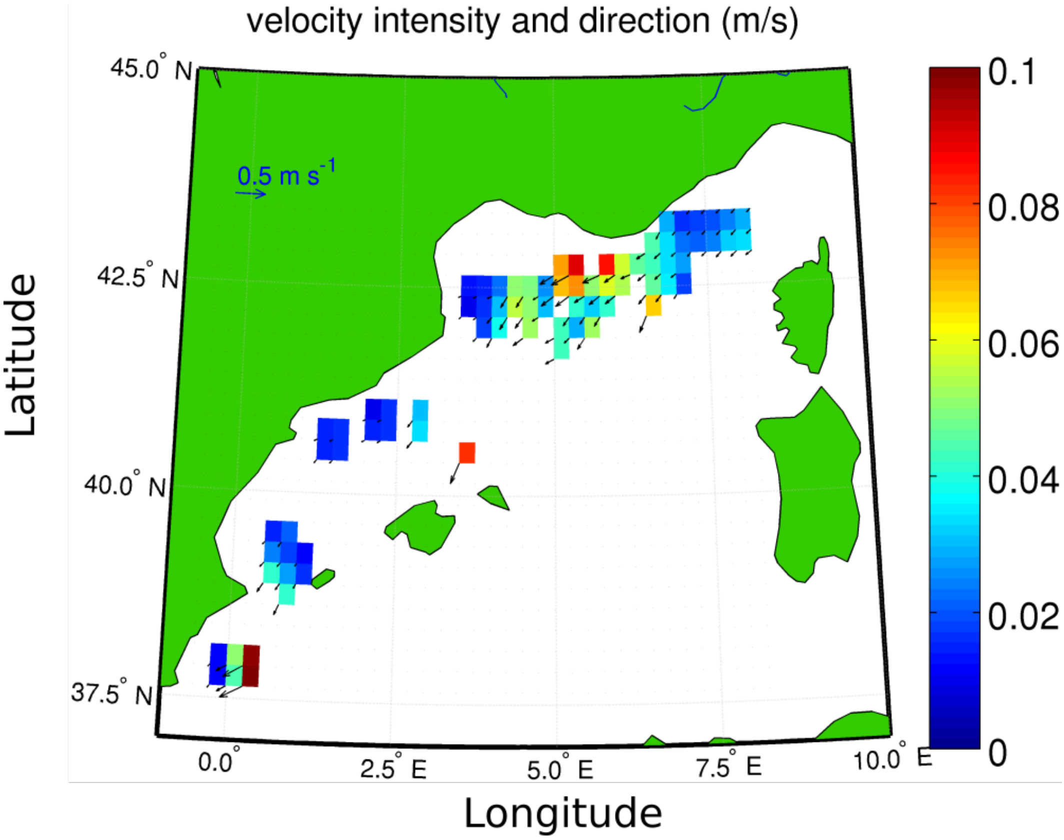

Figure 18: Deep speed and velocity directions. The figure shows data from 20th December 2012 to 23rd January 2015, i.e. the entire dataset considered in the study. Bins with less than 3 data points are not represented

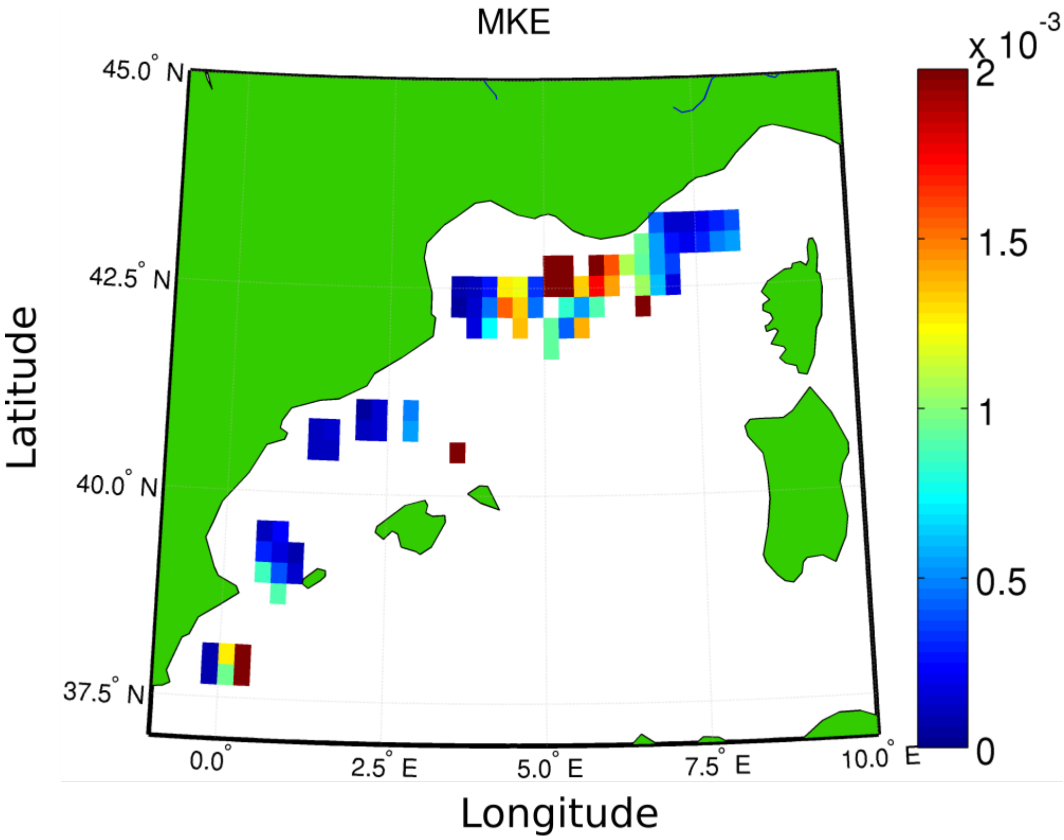

Figure 19: Mean Kinetic Energy (MKE) map. The figure shows data from 20th December 2012 to 23rd January 2015, i.e. the entire dataset considered in the study. Bins with less than 3 data points are not represented

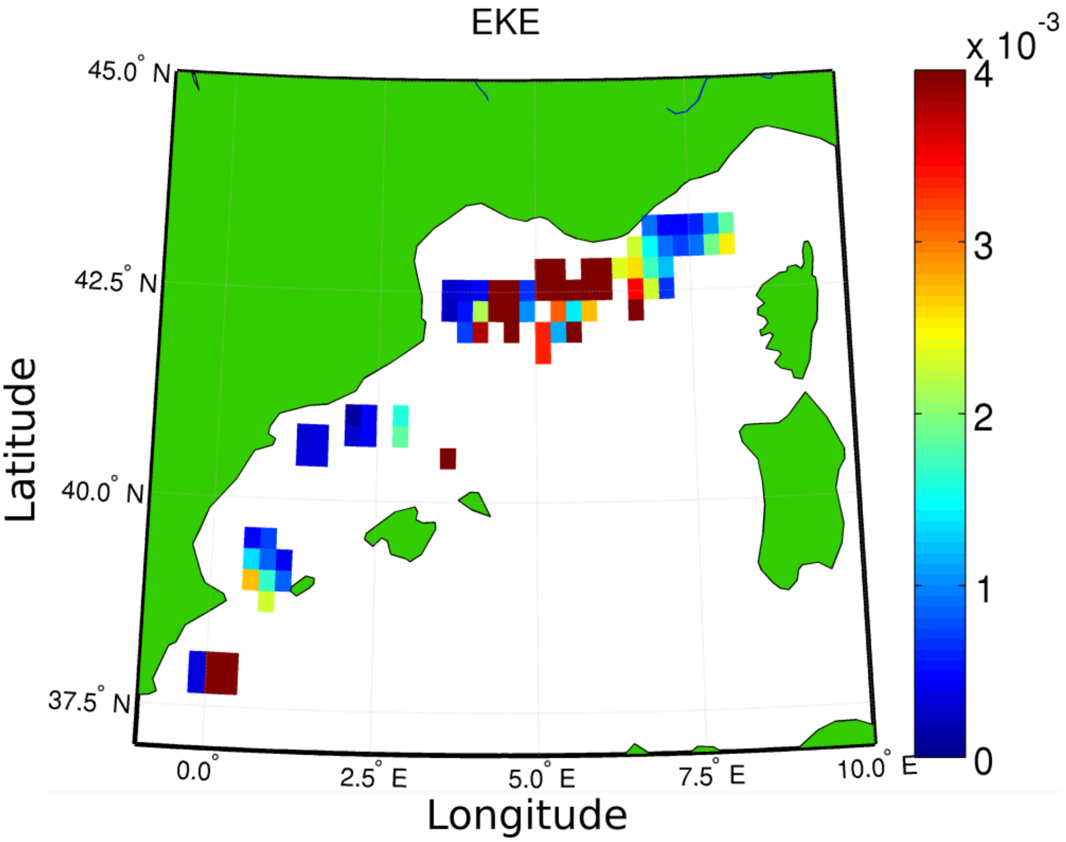

Figure 20: Eddy Kinetic Energy (EKE) map. The figure shows data from 20th December 2012 to 23rd January 2015, i.e. the entire dataset considered in the study. Bins with less than 3 data points are not represented

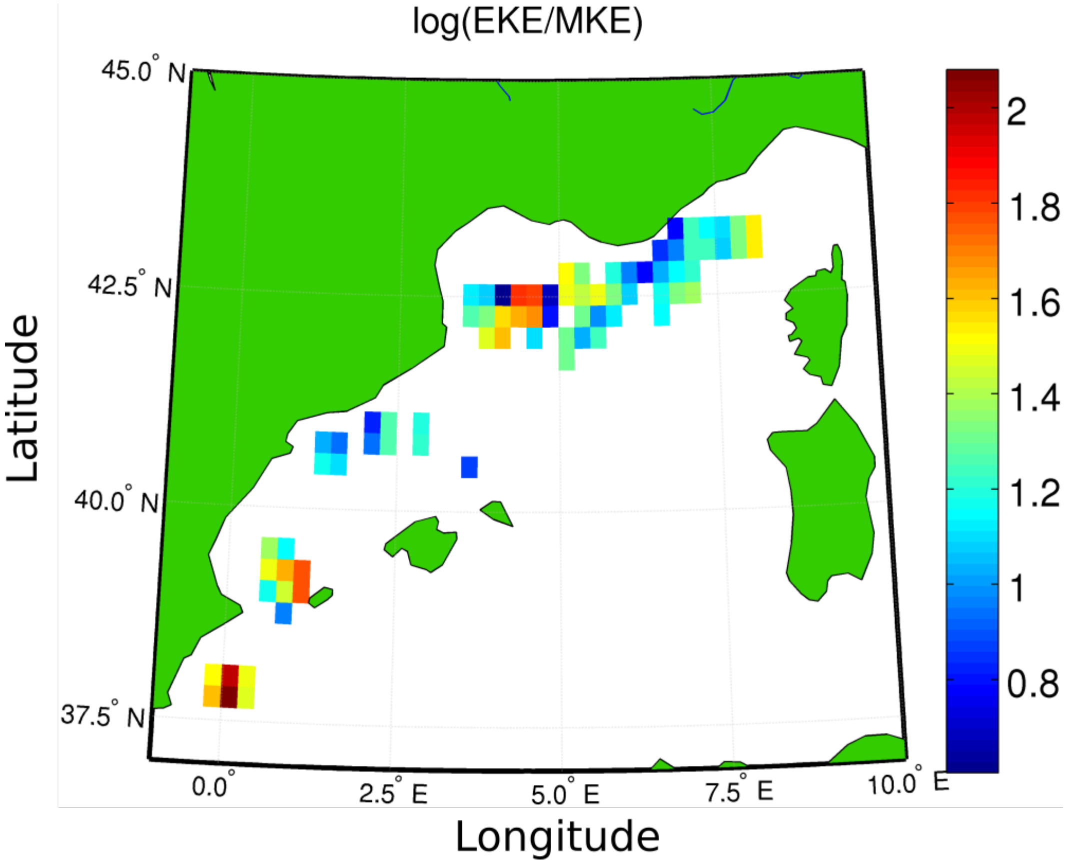

Figure 21: Logarithmic EKE/MKE map. The figure shows data from 20th December 2012 to 23rd January 2015, i.e. the entire dataset considered in the study. Bins with less than 3 data points are not represented

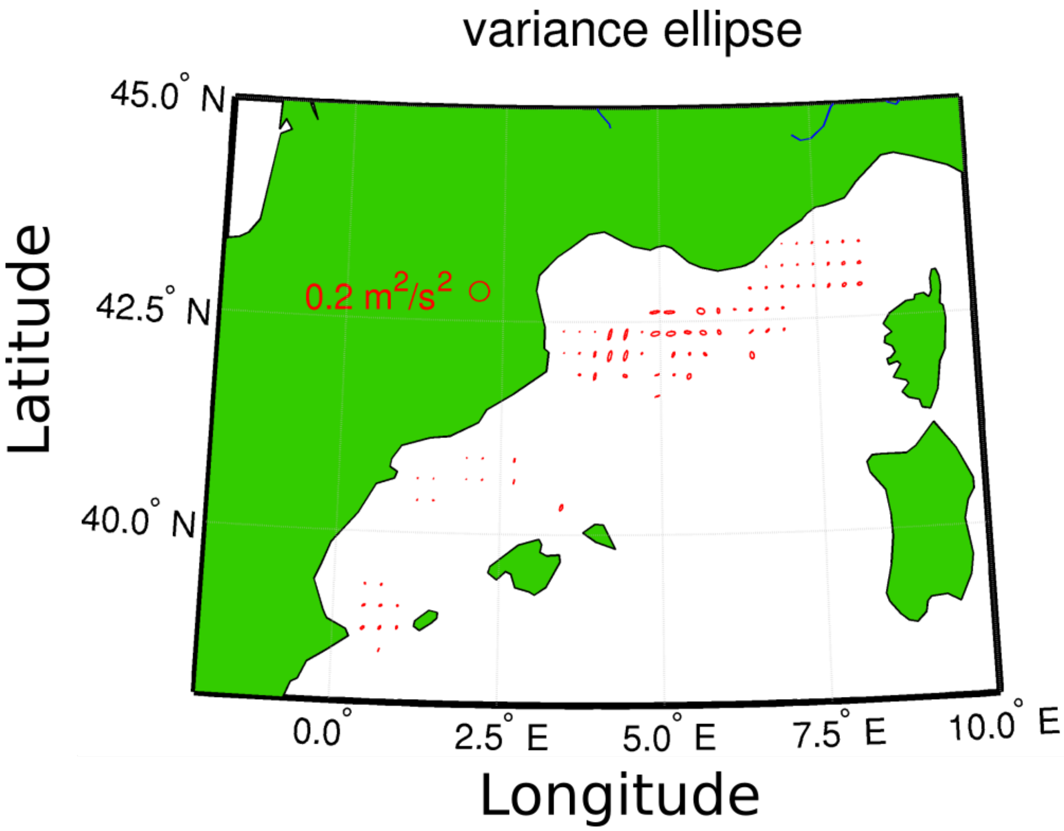

Figure 22: Variance ellipses map. The figure shows data from 20th December 2012 to 23rd January 2015, i.e. the entire dataset considered in the study. Bins with less than 3 data points are not represented

More than 90% of the calculated velocities are below 5 cm/s. Generally the current tends to follow the main stream westwards, as can be evinced from Figure 18, but it is interesting to notice how sometimes MERMAIDs get trapped in eddy features, especially in the Gulf of Lion (GoL) and in the western Ligurian Sea, e.g. m17, m31, m33, m35 (figures 7, 10, 12, 13). Moreover the deep currents look enhanced to the south of the Ibiza Channel (800 m depth) and in the GoL with respect to the Ligurian Sea. The Ibiza Channel is known to be a monitoring 'choke point' in the western Mediterranean Sea. Its importance is due to the high variability in water transports (Heslop et al., 2012). In the GoL the intense activity at depth might be linked to the spreading of deep water formed in late winter, although not every year. As already observed for the surface by Poulain et al. (2012), the LPC starts to spread and to flow more off shore after leaving the Ligurian coast. One could notice, in fact, that just before the GoL, the offshore component of velocity increases, distancing the LPC from the coast. The deep velocity observations suggest that the entire water column is involved in the cyclonic circulation of the Liguro-Provençal basin, differently from what was inferred by (Bethoux et al., 1982) and (Astraldi et al., 1994), who refer to the LPC as a feature involving the surface and intermediate layer of the circulation. Following the formulation suggested in Poulain (2001) the Mean Kinetic Energy (MKE) per unit mass of the mean flow has been calculated for each bin (Figure 19).

$$MKE = 0.5 * (\overline{U}^2 + \overline{V}^2) \tag{1}$$

Where $\overline{U}$ and $\overline{V}$ are the mean zonal and meridional velocities averaged on each bin. In Figure 19 the most active parts of the deep Liguro-Provençal basin as seen from the MERMAIDs are actually the GoL and the Ibiza Channel. Again the results are coherent with those obtained by Poulain et al. (2012) for the surface circulation. In fact the Ligurian Sea presents low MKE values, which increases closer to the GoL and off the French coast, then it remains quite low moving northwards of the Balearic Islands until it reaches again high values through the Ibiza Channel.

Eddy Kinetic Energy (EKE) (shown in Figure 20) represents the mean eddy kinetic energy, per unit mass of the flow fluctuations (Poulain, 2001) and it has been computed as:

$$EKE = 0.5 * (\overline{U'U'} + \overline{V'V'}) \tag{2}$$

Where $U' = U - \overline{U}$ is the residual zonal velocity component and $V' = V - \overline{V}$ is the residual meridional velocity. Observations suggest that EKE dominates in the global ocean, because the ocean circulation is dynamic and turbulent (Delworth et al., 2012). In several points (Figure 21) the EKE is higher than the MKE. EKE fluctuations can reach 0.024 $\mathrm{m^2s^{-2}}$ south of the Ibiza Channel, while the MKE maximum is 0.0056 $\mathrm{m^2s^{-2}}$. The pattern of the EKE follows that of the MKE and the surface trend described in Poulain et al. (2012). In fact the EKE is largest in areas of strong currents (Delworth et al., 2012), i.e. the GoL and the Ibiza Channel in the area covered by MERMAIDs.

The variance ellipse has been computed (Figure 22) following the formulation in (Emery and Thomson, 2001). The variance ellipse axes and rotation are functions of the variance and the covariance of the two velocity components. The covariance ellipses are therefore orientated in the direction of the main current (Figure 22). Apart from the above mentioned intense westward flow off the Ligurian coast, close to the GoL and in the Ibiza Channel, in the central GoL the ellipses are more rounded, this can be linked in the GoL to the spreading nWMDW towards the interior of the basin. South of the Ibiza Channel the circulation might be influenced by the presence of a cyclonic eddy (Heslop et al., 2012) that deviates the recently entered Atlantic Water, forcing it to skew towards the center of the western Mediterranean basin.

The logarithm of the ratio between EKE and MKE (Figure 21) gives information about the distribution of the energy in the observed currents (Poulain, 2001). In areas where the log(EKE/MKE) is higher, the current fluctuation kinetic energy is higher than that of the mean flow, from Figure 21, these areas are the western Ligurian Sea, the GoL, the Ibiza Channel and the area just to north of the Alboran Sea. The logarithm

component	speed (cm/s)	std
u	-1.77	1.55
v	-1.40	1.46
$\sqrt{u^2+v^2}$	-2.47	1.88

Table 3: Mean LPC speed from MERMAID's dives between 1400 m and 1600 m depth and standard deviation. Zonal velocity component (u), meridional velocity component (v), speed in the direction of displacement ($\sqrt{u^2+v^2}$)

is close to zero when the two kinetic components are close to each other, this happens mostly towards the interior of the basin and in the LPC branch between the Balearic Islands and the main land.

Isolating a set of data close to the Nice-Calví section (shaded blue area in figures 23, 24 and 25) gives insights about the LPC speed at 1500 m depth. By averaging data highlighted by the yellow shaded area in the mentioned figures was possible to obtain mean speed values (table 3) for dives between 1400 m and 1600 m depth. The mean velocity values here calculated will constitute a basis for comparison when evaluating the Inverse Box Model reference levels velocities for the LPC in Chapter 6.

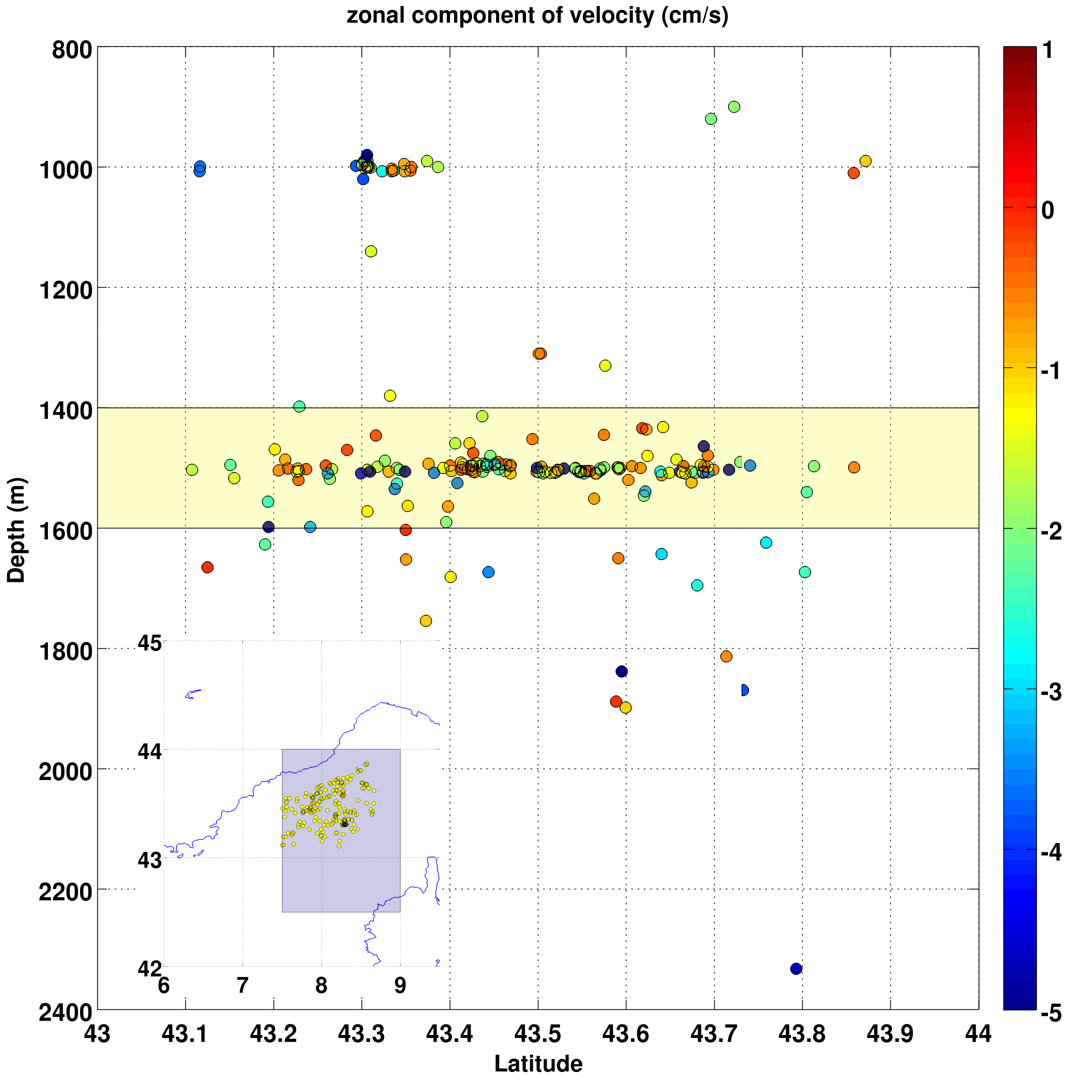

Figure 23: In the small bottom left panel the blue shaded patch encloses the MERMAID dive positions, where zonal velocity component has been calculated and represented in the main plot. The plot shows the selected data points' zonal velocity values. The yellow shaded patch highlights the zonal velocities between 1400 m and 1600 m depth, that have been used to calculate the mean zonal velocity. Negative numbers represent southward velocities

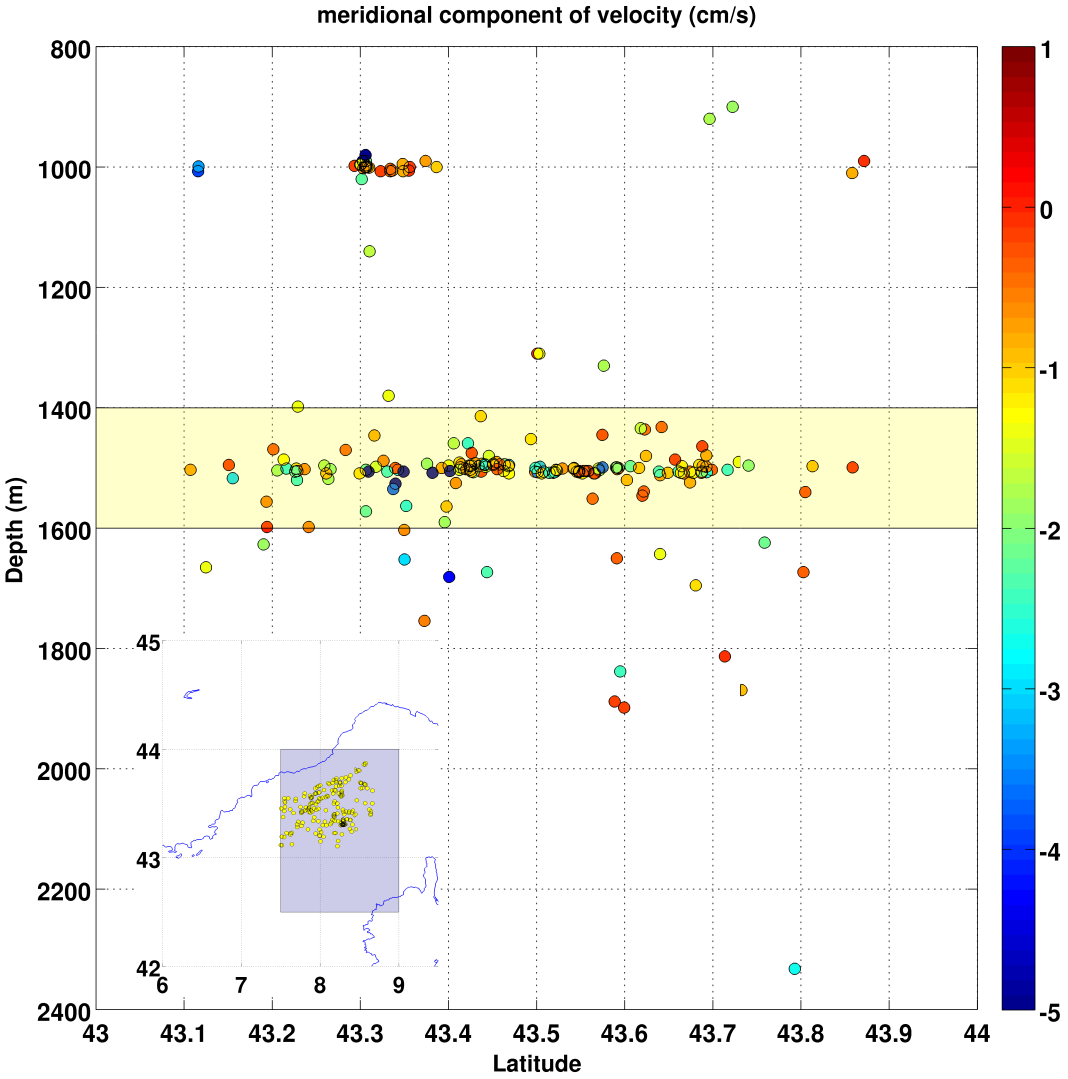

Figure 24: In the small bottom left panel the blue shaded patch encloses the MERMAID dive positions, where meridional velocity component has been calculated and represented in the main plot. The plot shows the selected data points' meridional velocity values. The yellow shaded patch highlights the meridional velocities between 1400 m and 1600 m depth, that has been used to calculate the mean meridional velocity. Negative numbers represent westward velocities

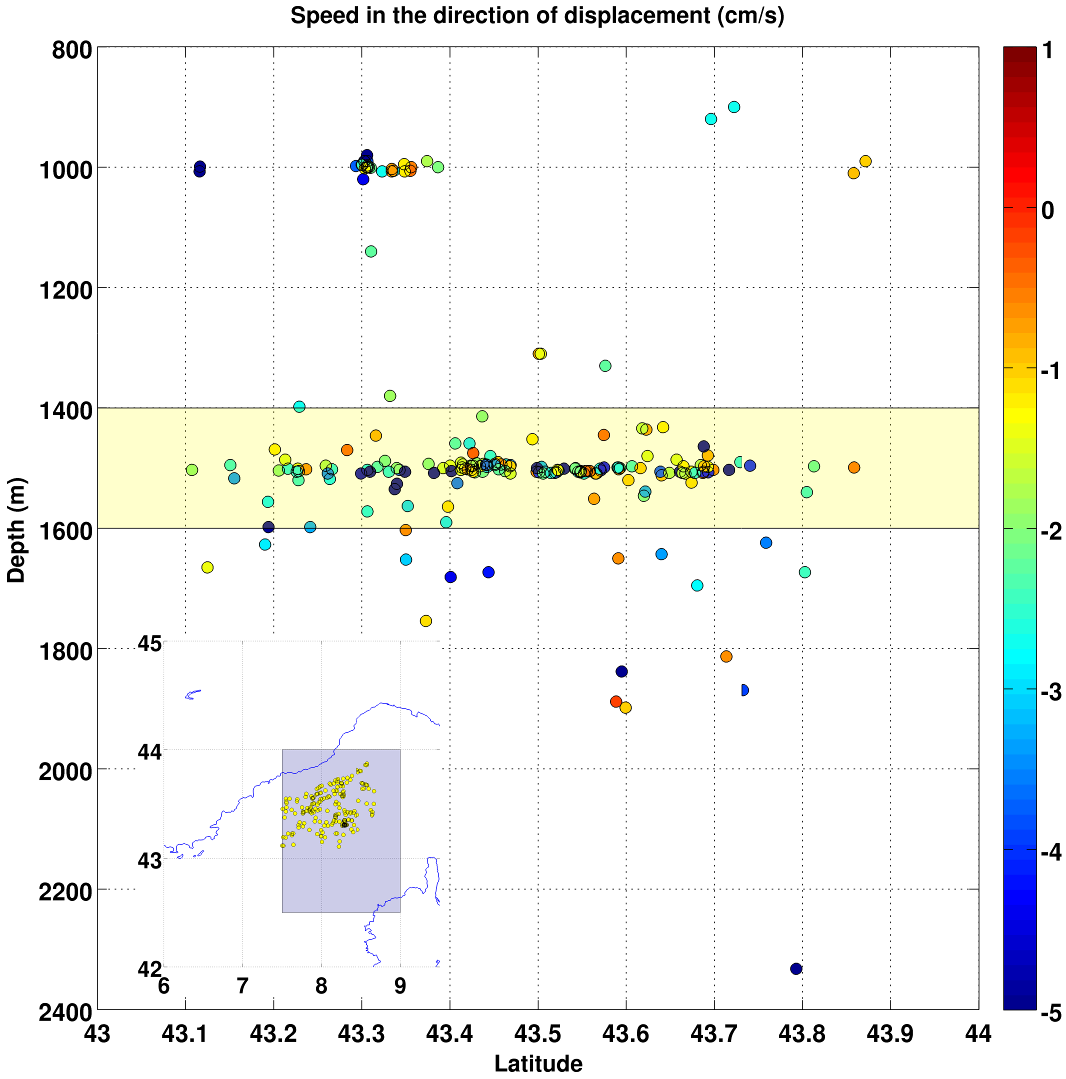

Figure 25: In the small bottom left panel the blue shaded patch encloses the MERMAID dive positions, where velocity component in the direction of displacement has been calculated and represented in the main plot. The plot shows the selected data points' speed values. The yellow shaded patch highlights the speed between 1400 m and 1600 m depth, that has been used to calculate the mean speed. Negative numbers represent south-westward velocities

3.5 Discussion and Conclusion

MERMAIDs mostly dived deeper than 800 m, following LIW's lower part and WMDW (Schroeder et al., 2010). The instruments tended to follow the deep LPC, suggesting that the LPC involves the whole water column, despite what was inferred by (Bethoux et al., 1982) and (Astraldi et al., 1994). MERMAID data and analysis presented in this work support Taupier-Letage and Millot (1986)'s observations: the LPC can reach 1500 m of depth. The data also endorse Conan and Millot (1995)'s hypothesis about the LPC transporting LIW, WIW and WMDW. It was interesting to notice some eddy features even at MERMAID parking depths. From Figure 18 south-westward LPC speed deeper than 800 m is enhanced in the GoL and in the Ibiza Channel. Figures 10 and 13 shows how MERMAID m31 and m35 got trapped, at least at the beginning of the deployment, in the central cyclone. In particular MERMAID m33 remained in the central cyclone, at approximately 1500 m, for at least one year. During SOFARGOS experiment, RAFOS remained at sea for five to seven months and they floated in a depth range from 350 m to 1450 m detecting several cyclones and anti-cyclones in the north-western Mediterranean (Testor and Gascard, 2006). The m33 path provides new information about the persistence and the depth of deep LPC meanders. The LPC presents less eddies the closer it gets to the Balearic Islands. Given the average velocities of m17, m30, m31, m32, the time necessary to flow from the Ligurian Gulf to the Ibiza Channel at 900-1600 m depth ranges from 385 to 875 days; it took 575 days for m17 to reach the Ibiza Channel. An intense activity is evident even at depth, from the pseudo-eulerian study. The GoL and the adjacent Ligurian Sea, together with the Ibiza Channel have a key role in the circulation of the basin. Most of the kinetic energy observed in these areas is EKE, being, then, due to turbulent and dynamic circulation. Bearing in mind that the dataset is quite small and the statistics must then to be interpreted with care, here it is important to stress that deep sea data are rare and extremely valuable, hence the MERMAID dataset, although small, well agrees with previous studies at the surface, and indicates the presence of a persistent eddy at 1500 m between July 2014 and July 2015. It can then add important information to the present knowledge of the deep western Mediterranean Sea.

4 Regulating Agents of the Mass Transport between the Ligurian and the Tyrrhenian Seas across the Corsica Channel

4.1 Abstract

The aim of this chapter is to describe the seasonal and interannual variability of the system composed of the Ligurian and the Tyrrhenian Seas, connected by the Corsica Channel, that has been monitored for more than 30 years through moored instruments. An attempt to ascribe the analysed variability to the main forcing acting on the north-western Mediterranean Sea is made. In this study sea level anomaly (from satellite gridded products and along track products), sea surface stress, sea surface pressure and wind fields are investigated in relationship with the water mass transport through the Corsica Channel, deduced from moored current meters.

4.2 Introduction

The Tyrrhenian Sea, Figure 26, is the deepest basin of the western Mediterranean Sea and the most isolated (Vetrano et al., 2010). It is connected in the south-west with the Algerian basin and in the north with the Ligurian Sea through the Corsica Channel. The CC bathymetry is shown in Figure 27, it is approximately 400 m deep and it is bordered on the west by the Corsica Island and on the east by the Capraia Island.

The Liguro-Tyrrhenian system is exposed to long term atmospheric pressure patterns that contribute to its functioning. From previous studies it is known that the Ligurian Sea is covered by an atmospheric depression (Bethoux et al., 1982), due to the particular orographic configuration of the surrounding lands. Therefore the Ligurian Sea Surface atmospheric Pressure (SSP) is generally lower than the Tyrrhenian SSP and this configuration forces the water to flow through the CC mostly towards the Ligurian.

The same cyclonic wind distribution, with almost 50% of the variance of the entire Liguro-Tyrrhenian system, acts over both basins; the incoming cold wind, coming form the Rhône valley blows over the sea and then channels between Corsica and Sardinia, to enter in the TYS (Astraldi and Gasparini, 1986). The Strait of Bonifacio is 100 m deep, its activity is mainly related to the action of the wind. As described in Marullo et al. (1994), the strait presents a strong seasonality. During summer, an intrusion of cold water from the eastern side of the Strait of Bonifacio into the Tyrrhenian Sea can be observed from satellite images. In winter, the cold filament evolves into an organised eddy, surrounded by warmer water flowing towards the Ligurian Sea through the Corsica Channel. The eddy can reach 100 Km of extension towards the Italian coast. Marullo et al. (1994) state that the transition of cold water intrusion from a filament into an

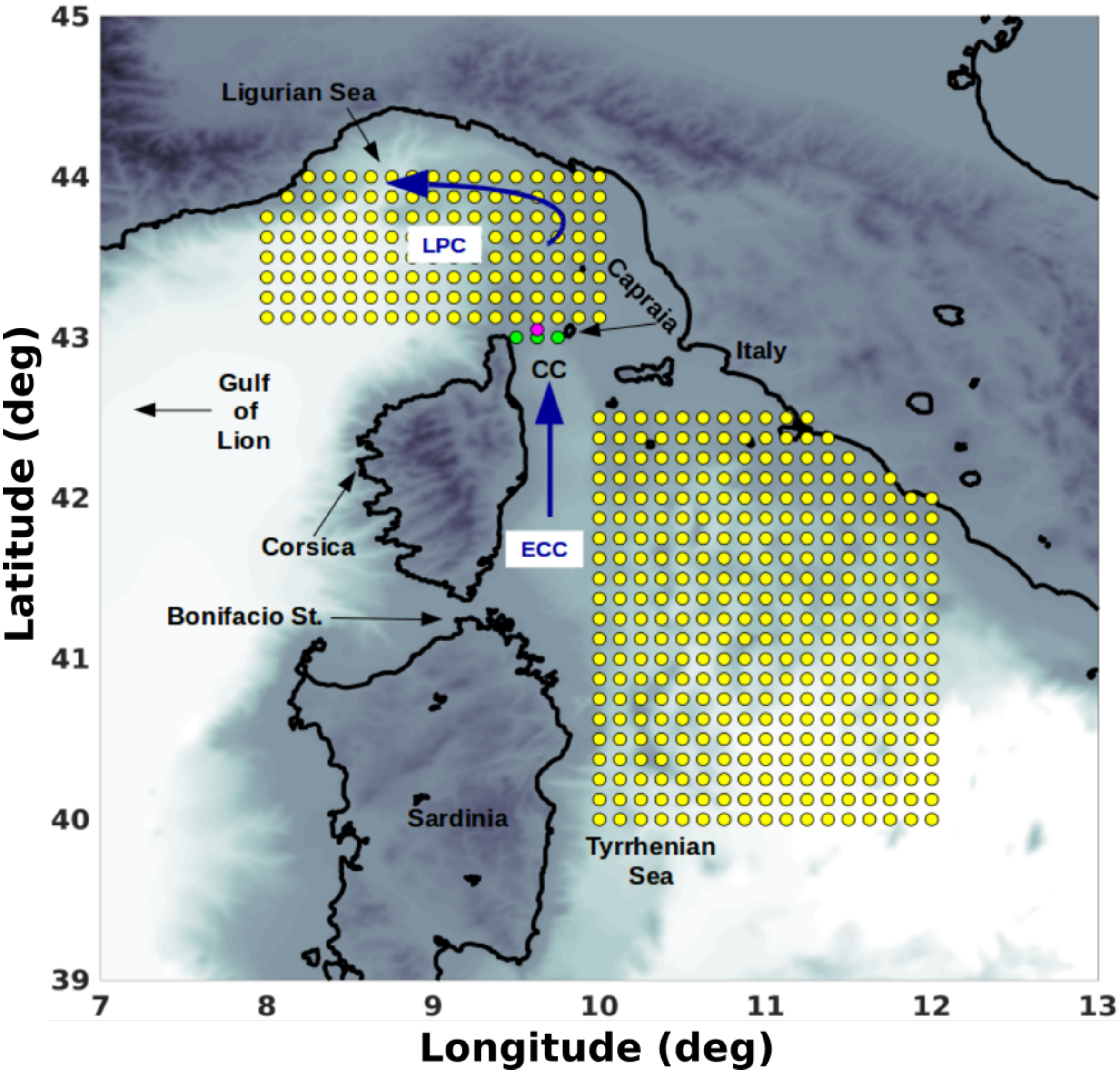

Figure 26: Map of data used. Ligurian and Tyrrhenian yellow dots in boxes are locations where SSP, SLA_{grid} are used. In the CC three points for Sea Surface Stress due to instantaneous turbulent wind are represented by green points. In the CC the magenta circle marks the mooring position, where the current meters that recorded water velocities were deployed. A schematic of the circulation with the ECC and LPC is also presented

eddy might be related with the Ligurian Sea and Gulf of Lion demand of replenishing water, especially consequent to strong evaporation and deep water formation. Thus, the Strait of Bonifacio appears to be a good monitoring point to assess the state of the Liguro-Provençal Basin and its water exchange with the Tyrrhenian Sea. The dynamics of the Bonifacio Strait influences the surface waters and it is mainly driven by the action of the wind. This study considers the strait too shallow for the water flowing into the Tyrrhenian through it to play a major role into the water budget of the basin. Astraldi and Gasparini (1986) described a clear cyclonic structure, appearing mostly in winter, with more than 30% of the variance, located in the Ligurian Sea. The main

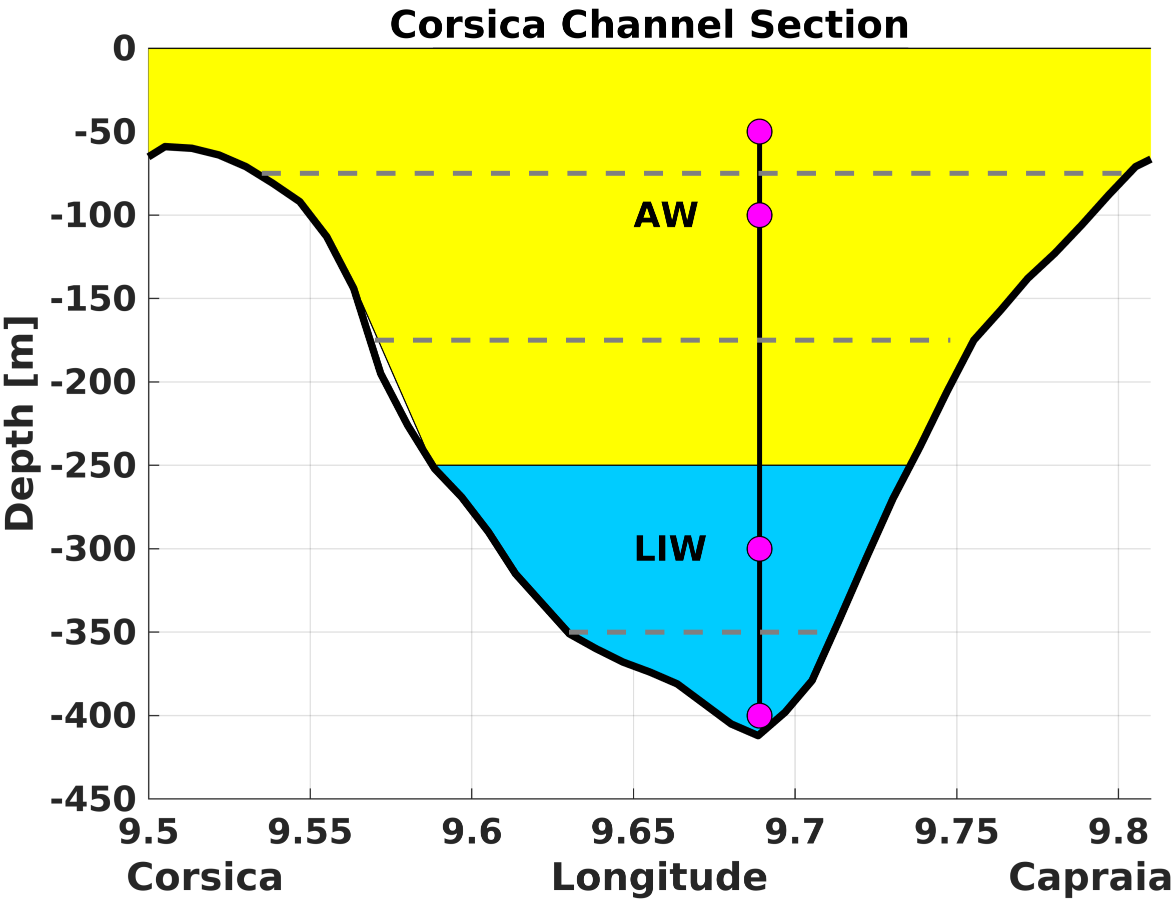

Figure 27: Bathymetry of the CC, the principal water masses flowing across the channel are Atlantic Water (AW) and the Levantine Intermediate Water (LIW). Purple dots represent the position of the moored current meters, gray horizontal dashed lines mark the areas for which the measured velocity in the defined area, has been multiplied to calculate transport

wind blowing in winter from the Rhône Valley is the Mistral, which is particularly dry and cold. Its flow creates intense air-sea interactions (Astraldi et al., 1994, Astraldi and Gasparini, 1992), that cool down the Liguro-Provençal basin and enhance evaporation, rendering the surface Ligurian water denser than the Tyrrhenian water, which is situated out of the direct trajectory of the Mistral. The wintry wind action contributes to lower the steric level of the Liguro-Provençal basin (Astraldi and Gasparini, 1992); in fact historically the Ligurian has been observed to be colder and denser than the Tyrrhenian (Manzella, 1985). The south-to-north steric gradient enhances the northward water transport through the CC. The Ligurian waters get warmer and less dense in summer nearly balancing the steric difference that makes the Tyrrhenian waters flow northwards in winter and lowering or almost stopping the exchanges between the two basins. When winter returns the steric gradient is re-established and the northward water transport through the Corsica Channel is enhanced, reaching a peak in late winter early spring.

The sea level is representative of the sea steric height. In the Mediterranean Sea the

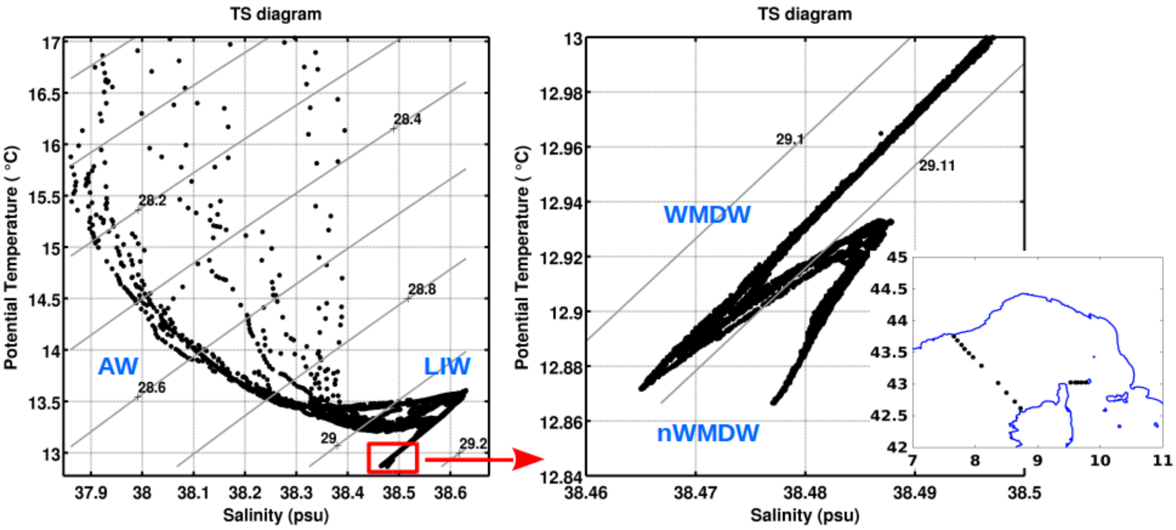

Figure 28: The $\theta - S$ diagram represents potential temperature against salinity. On the graph are also reported isopycnal lines calculated from potential density and principal water masses are labelled: Atlantic Water (AW), Levantine Intermediate Water (LIW), Western Mediterranean Deep Water (WMDW), new Western Mediterranean Deep Water (nWMDW). The plot has been created with hydrological data subset from MEDOCC07 cruise (right bottom map) that took place in October 2007 in the Western Mediterranean Sea

mean sea level is composed by two parts: the mass component and the steric component; the communication with the world ocean through the Strait of Gibraltar balances the surface water flux inside the basin, leaving room to the steric component to largely influence the sea level (Bonaduce et al., 2016). Larnicol et al. (1995) infer that half of the variability observed in a two years Mediterranean altimetry dataset is ascribable to the steric component. Vignudelli et al. (2000) investigated the relationship between water transport across the CC and sea level derived from along track satellite data, that at the time covered the time period from 1993 to 1998. They found that the correlation coefficient between the two time series was 0.72, with 0.58-0.85 confidence interval at 95% significance level. Vignudelli et al. (2000) demonstrated that the high quality along track satellite data can accurately represent sea level variation and can be applied to investigate water fluxes driven by steric oscillations.

A static response of the sea level to a variation in atmospheric pressure indicates a inverse barometer (IB) effect, this means that for 1 mbar increase in SSP the sea level decreases by approximately 1 cm. Ponte and Gaspar (1999) and Fu and Pihos (1994) investigated the IB effect using altimeter data to estimate the sea level, finding that at time periods longer than 20 days the response of the ocean is close to the IB response. Although their studies focused on the global ocean the same approach can be applied in the western Mediterranean Sea. Over the Mediterranean the correlation coefficient between the sea level and the atmospheric pressure is approximately 0.7 (Fu and Pihos, 1994).

For all the reasons listed above the activity of the CC can be indicative of the mutual behaviour of the two basins. Monitoring the water transport through the channel provides information about the atmospheric oscillations over the Liguro-Tyrrhenian system and their link with the marine environment and sea level.

The datasets used are presented in section 4.3. In section 4.4 computation of Ekman transport and altimetry data treatment are described. In section 4.5 the results are illustrated taking into consideration seasonal, correlation, time-lag, and spectral analyses. In the same section the interannual variability is investigated comparing the winter values of the time series considered. Further, basin atmospheric patterns for extreme transport events are described. Finally, in section 4.6, the main conclusions are drawn.

4.3 Data

In the present work the principal time series is represented by 25 years of water transport data, through the CC, from 22nd November 1985 to 12th March 2010. In situ measurements are derived from moored Rotor Current Meters (RCM) that are positioned at 4 levels (50 m, 100 m, 300 m, 400 m) in the deepest point of the Channel, Figure 27.

The CC water transport time series has been compared with local Ekman transport calculated from sea surface zonal wind stress (τ_x). The τ_x data points are represented by green dots in Figure 26, a detailed discussion of Ekman transport computation can be found in section 4.4.2.

SSP and wind fields over the Ligurian and Tyrrhenian are provided by the ERA-INTERIM (Dee et al., 2011) reanalysis at 1/8°, represented by yellow dots, Figure 26. E.U. Copernicus Marine Service Information (http://marine.copernicus.eu/) made available gridded Sea Level Anomaly (SLA_{grid}) data, which come from multimission altimeter (HY2, Saral/AltiKa, Cryosat-2, Jason-2, Jason-1, T/P, Envisat, GFO, ERS1/2) data processing system. Sea Level Anomaly (SLA) represents the difference between the instantaneous sea surface height and the mean sea surface. As explained in the SLA data sheet: "After a repeat-track analysis, a mean profile, which is peculiar to each mission, or a Mean Sea Surface (when the orbit is non repetitive) is substracted to compute sea level anomaly". Monthly meridional and zonal wind components and monthly SSP have been used to investigate the wind and surface pressure patterns during extreme water transports and Ekman transport events.

Details of the considered time series can be found in Table 4 and locations of the data points are shown in Figure 26. Figure 29 represents all the time series analysed. Data represented in Figure 29, have been filtered with a 20-day moving average window. Altimetry data have been interpolated onto a regular time step with a 35/10 days time step for Envisat/Jason-2.

The main abbreviations used have been explained in the Glossary. It is useful to remember here that subscript 'a' indicates the anomaly of a time series, i.e. series minus long term average of the same series; 'Δ' indicates the difference: Tyrrhenian basin average minus Ligurian basin average.

Data	start	end	download	resolution	time step	units
SLA_{grid}	01-01-1993	11-09-2015	Copernicus: AVISO satellite	1/8°	daily	m
SSP	02-01-1985	01-07-2010	ERA-INTERIM	1/8°	daily	Pa
transport	22-11-1985	12-03-2010	Moored RCM	–	daily	Sv
τ_x,τ_y	01-01-1985	31-12-2010	ERA-INTERIM	1/8°	daily	N/m^2
Wind	01-01-1979	01-02-2016	ERA-INTERIM	1/8°	monthly	m/s
SSP	01-01-1979	01-01-2016	ERA-INTERIM	1/8°	monthly	Pa

Table 4: Data information for SLA_{grid}, SSP, transport, τ_x - Sea Surface instantaneous turbulent zonal wind Stress, τ_y - Sea Surface instantaneous turbulent meridional wind Stress, Wind - 10 m u and v wind components. Wind and SSP monthly values have been used to represent the patterns influencing the extreme events

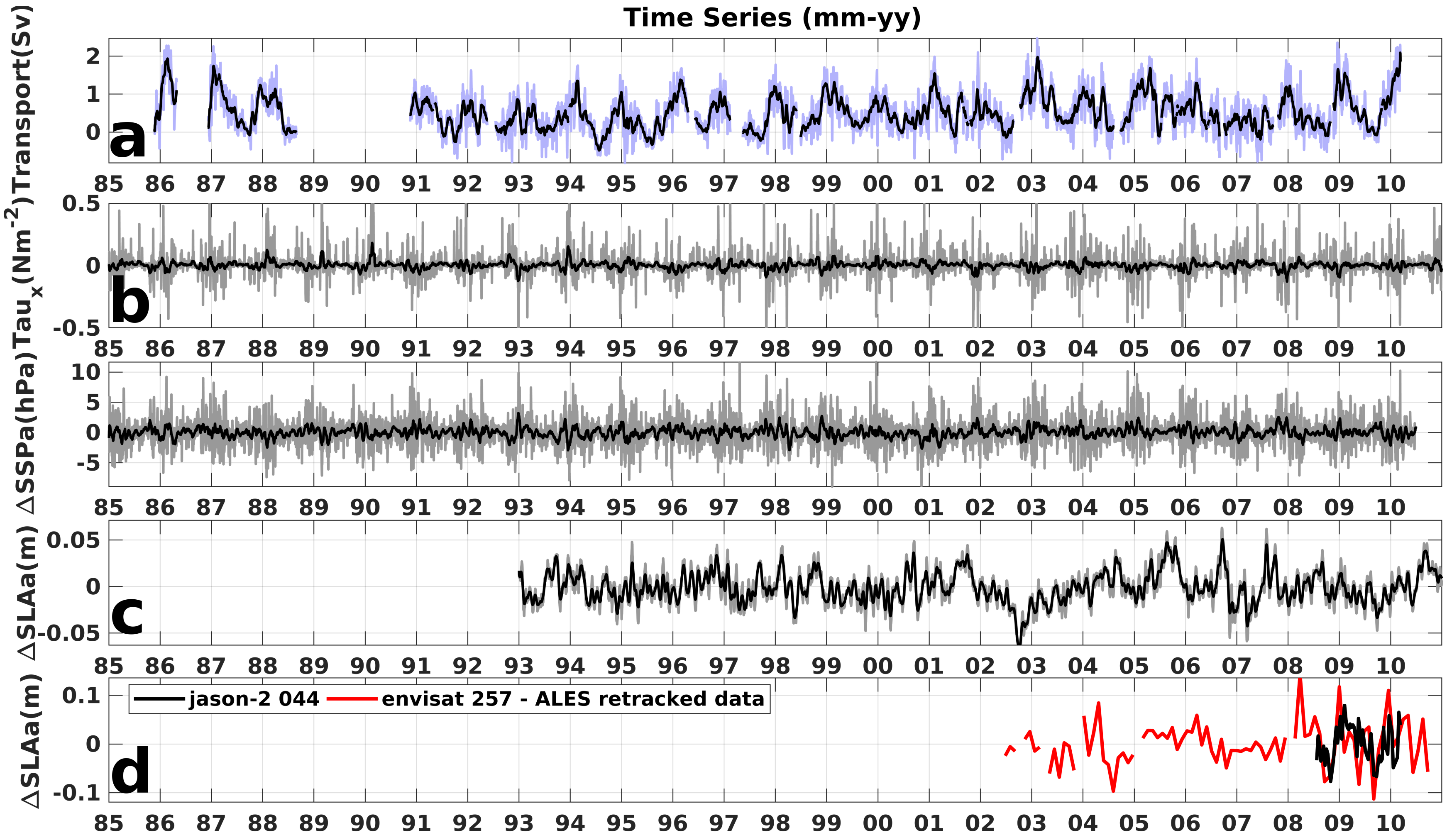

Figure 29: a) Transport, b) τ_x, c) $\Delta SSPa$, d) $\Delta SLAa_{grid}$, e) $\Delta SLAa_{sat}$ from tracks Jason2 044 and Envisat 257. In all plots, with the exception of e), the lighter line represents original data while the filled black line shows the filtered data with a 20 days window moving average

Along track altimetry data derived from two satellite missions are used: Jason-2 (J2) and Envisat (Env). Both missions have been re-tracked using Adaptive Leading Edge Subwaveform retracker (ALES) algorithm (Passaro et al., 2014) in a 50 km along coast strip. The ALES algorithm allows a better waveform interpretation, especially in case of bright targets, calm water patches, unbroken wave crests and vicinity to the coast, maintaining the quality of open ocean measurements but with higher resolution (20hz for Jason-2 and 18hz for Envisat, instead of 1hz). Moreover ALES retracking reduces the root mean square difference calculated against sea level from tide cages measurements by a factor of 1.5 for Jason-2 and by a factor of 4 for Envisat, when compared with old standard Sensor Geophysical Data Record. The root mean square values for ALES data range between 0.4 m and 1.4 m (Cipollini et al., 2015). Selected ground tracks, Table 5 and Figure 30, were downloaded from the NASA repository: $ftp://podaac.jpl.nasa.gov/allData/coastal\_alt/L2/ALES/$, where they are organized in the J2 and Env folders, each of which contains a folder for every cycle (94 cycles for Env and 252 cycles for J2). Inside every cycle folder there is a netCDF datafile for every pass. File name conventions and satellite terminology definition can be found in ALES User Hand Book (Cipollini et al., 2015), Jason-2 Product Hand Book (Dumont et al., 2015) and Envisat Altimetry Level 2 User Manual (Soussi et al., 2011). Figure 31 explains some of the basic satellite parameters. During every pass, satellites revisit the same ground-track within a margin of ±1 Km, this happens approximately every 9.9 days for J2 and every 35 days for Env.

Track	Location	Start time	End time
j085	LS	15-Jul-2008	12-Mar-2010
j044	LS+TYS	23-Jul-2008	5-Mar-2010
e044	TYS	15-May-2002	20-Oct-2010
e502	TYS	5-Jul-2002	1-Oct-2010
e588	LS	5-Jul-2002	10-Oct-2010
e715	TYS	12-Jul-2002	08-Oct-2010
e130	LS	22-Jun-2002	18-Sep5-2010
e257	LS+TYS	26-Jun-2002	22-Sep-2010
e801	LS+TYS	15-Jul-2002	11-Oct-2010

Table 5: Tracks details. The location column indicates whether a satellite track crosses the Ligurian Sea (LS), the Tyrrhenian Sea (TYS) or both (LS+TYS)

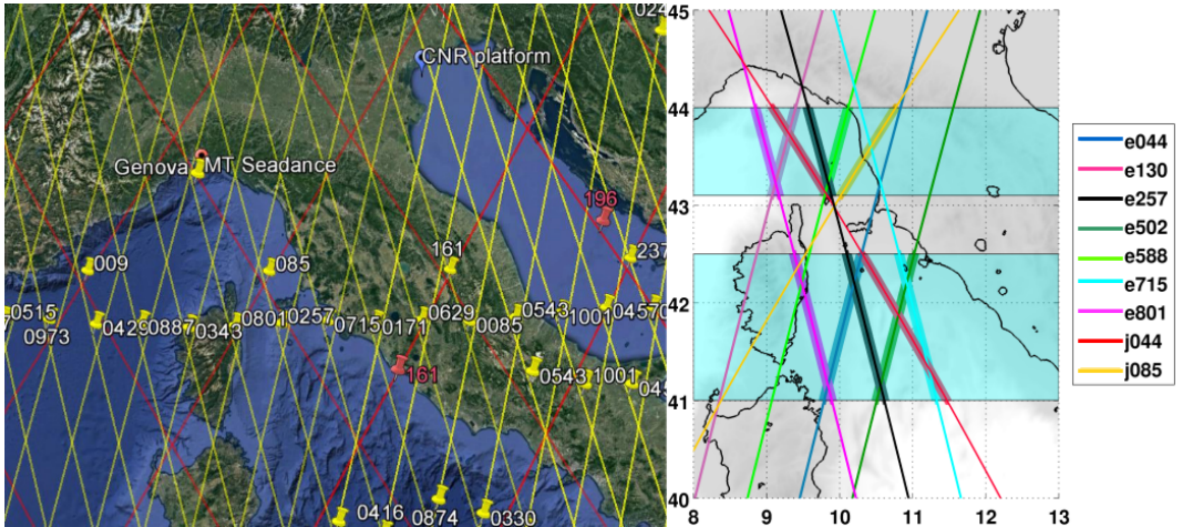

Figure 30: Left panel: Jason-2 (red) and Envisat (yellow) ground track coverage in the CC surroundings. Right panel: selected tracks. The cyan shaded areas represent the stripes containing the select data to represent the Ligurian and the Tyrrhenian along track SLA

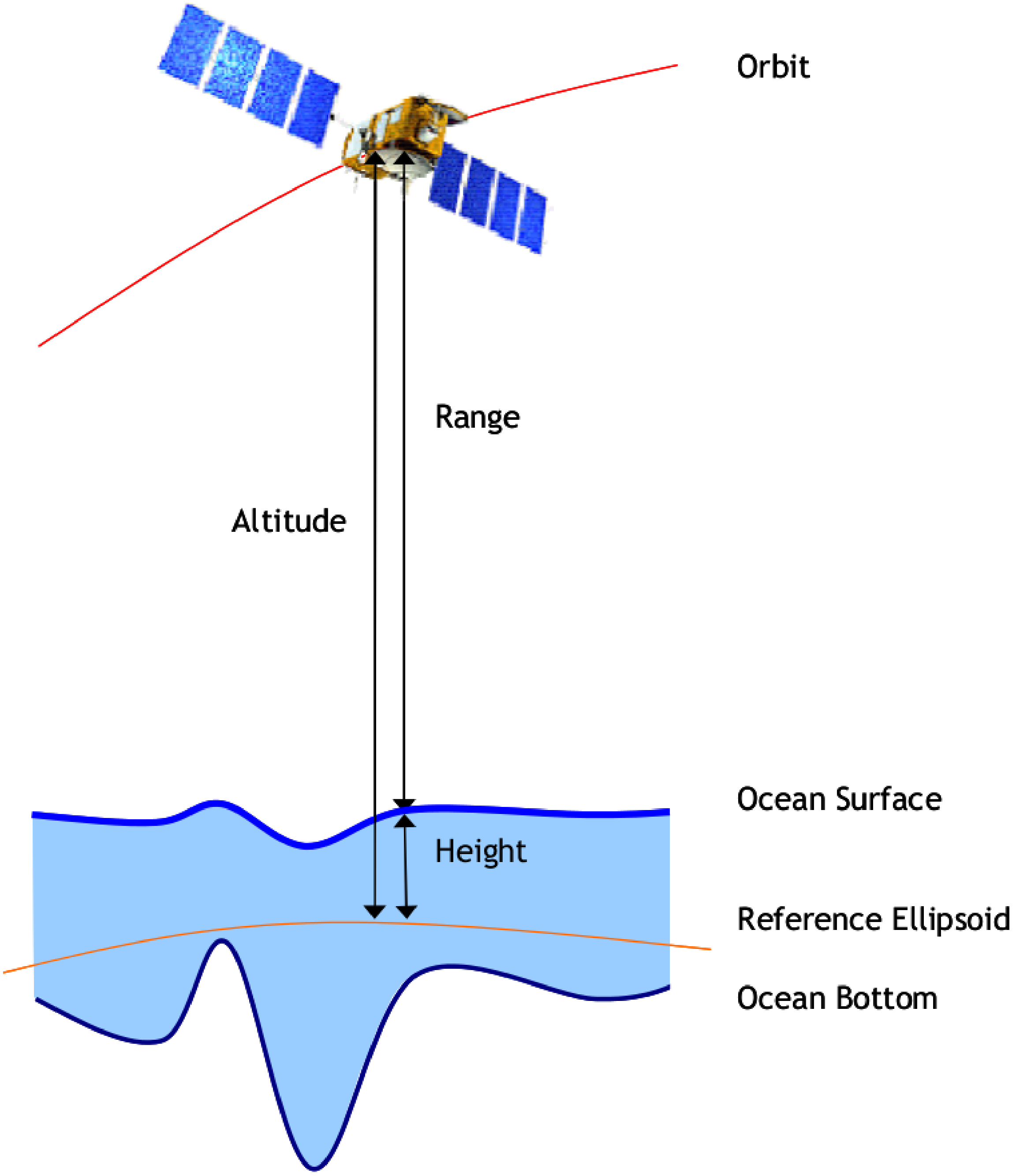

Figure 31: Graphic definition of some of the basic satellite parameters. Image from (Dumont et al., 2015)

4.4 Methods

4.4.1 Total Mass Transport Computation

Data from moored RCM are interpolated onto a regular time grid (original data are every 3 hours to which has been applied a moving average over 48 hours, and then re-sampled every 24 hours). Speed has been multiplied for the CC sectional area of the layer where the RCM belongs, the layers are shown in Figure 27.

4.4.2 Ekman Transport Computation

To calculate the Ekman transport per unit length $[kg/(m*s)]$ the following equations have been applied (Pond and Pickard, 1983) :

$$M_y = -\tau_x/f \tag{3}$$

$$M_x = \tau_y/f \tag{4}$$

The mass transport, $[kg/s]$ equation is:

$$Q_y = M_y * L \tag{5}$$

$$Q_x = M_x * L \tag{6}$$

and the volume transport $[m^3/s]$ equation is:

$$Q_{vy} = Q_y/rho \tag{7}$$

$$Q_{vx} = Q_x/rho \tag{8}$$

where:

- τ_x = instantaneous east-west wind stress $[N/m^2]$
- τ_y = instantaneous south-north wind stress $[N/m^2]$
- $f = 2 * omega * sin(theta)$ Coriolis parameter
- theta = latitude
- $omega = 7.292e - 5$ [rad/sec]
- L = length subsection [m] given by half distances between two consecutive points, including Corsica (longitude 9.439 deg) and Capraia (longitude 9.827 deg).

- rho = 1029 Kg/m^3

After calculating the mass transport per unit length three values are obtained, one for each point, see Figure 32. It is necessary to calculate the sum of the three values to obtain the total Ekman transport in the CC.

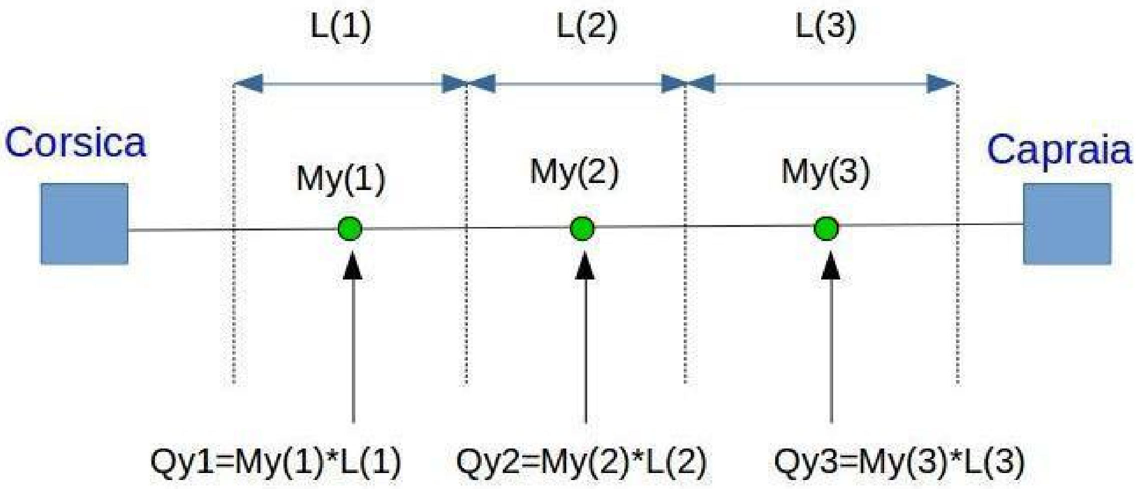

Figure 32: Graphic calculation of Ekman mass transport

4.4.3 SLA Computation from Along-Track Data

Following the approach described by Vignudelli et al. (2000), the computation of SLA is explained in detail in Table 6 and can be condensed in the following equations:

$$SLA = \underbrace{ALT - CR - SETH - GOTH - PTH - IBHC - HFF}_{CSSH} - MSS \tag{9}$$

CSSH is the corrected sea surface height, MSS is the mean sea surface; ALT is altitude, CR is corrected range, SETH is solid earth tide height, GOTH is geocentric ocean tide height, PTH is pole tide height, IBHC is inverted baromenter height correction, HFF is high frequency fluctuations.

The corrected range has been calculated as:

$$CR = range + WTC + DTC + IOC + SSBC \tag{10}$$

In the equation above WTC is wet troposphere correction, DTC is dry troposphere correction, IOC is ionosphere correction and SSBC sea state bias correction.

Several parameters need to be selected from the multitude available in the NetCDFs. Ligurian data are situated between $43.1°N$ and $44°N$, while Tyrrhenian data extend from $41°N$ to $42.5°N$. Not all parameters needed to calculate the SLA_{sat} are available at 20hz or 18hz, i.e. ALES frequency, therefore parameters available only at 1hz are interpolated over a 20hz (Jason2) or 18hz (Envisat) frequency vector. For the considered missions ALES data are available in a 50 km coastal strip. Preliminary analyses demonstrate that trying to fill the gaps (see Figure 33) wherever the 20hz altimetry data are not available with the 1hz does not lead to higher correlation coefficients with the CC water transport time series and introduces discontinuity in the SLA_{sat} values, therefore only ALES retracked data have been used. The Ligurian and Tyrrhenian boxes have been chosen in order to minimize the gaps (see Figure 30). Calculating SLA_{sat} including tracks that do not cross both basins leads to very low correlation coefficients ($r = 0.06$) with the water mass transport across the CC. Track e801 shows highly fluctuating values depending on the type of filter or method used, moreover the unusual position of its Tyrrhenian segment, might result in misrepresentation of the basin sea level. For all the reasons listed above and for their particularly appropriate positions, the ALES retracked e257 and j044 have been selected to be the most suitable to the present study. Therefore from now on where referring to along track data only ALES retracked data from j044 and e257 are intended.

Magnitude	Abbreviations	Name J2 (Hz)	Name Env (Hz)
Corrected Range =	CR		
range		*range_20hz_ku_ALES* (20)	*hz18_ku_ALES* (18)
+wet troposphere correction	WTC	*rad_wet_tropo_corr* (1)	*mod_wet_tropo_corr* (1)
+dry troposphere correction	DTC	*model_dry_tropo_corr* (1)	*mod_dry_tropo_corr* (1)
+ionosphere corrections	IOC	*iono_corr_alt_ku* (1)	*ra2_ion_corr_ku* (1)
+sea state bias correction	SSBC	*sea_state_bias_ku* (1)	*sea_bias_ku* (1)
Corrected Sea Surface Height =	CSSH		
altitude	ALT	*alt_20hz*(20)	*hz18_alt_cog_ellip* (18)
- corrected range			
- solid earth tide height	SETH	*solid_earth_tide* (1)	*solid_earth_tide_ht* (1)
- geocentric ocean tide height	GOTH	*ocean_tide_sol1* (1)	*tot_geocen_ocn_tide_ht_sol1* (18)
- pole tide height	PTH	*pole_tide* (1)	*geocen_pole_tide_ht* (1)
- inverted barometer height correction	IBHC	*inv_bar_corr* (1)	*inv_barom_corr* (1)
- high frequency fluctuations	HFF	*hf_fluctuations_corr* (1)	*dib_hf* (1)
SLA =			
Corrected Sea Surface Height			
- mean sea surface	MSS	*mean_sea_surface* (1)	*m_sea_surf_ht* (1)
longitude		*lon_20hz* (20)	*hz18_lon* (18)
latitude		*lat_20hz* (20)	*hz18_lat* (18)
time		*time_20hz* (20)	*hz18_time* (18)

Table 6: SLA_{sat} Calculation and variable names in Jason-2 (J2) and Envisat (Env) NetCDFs

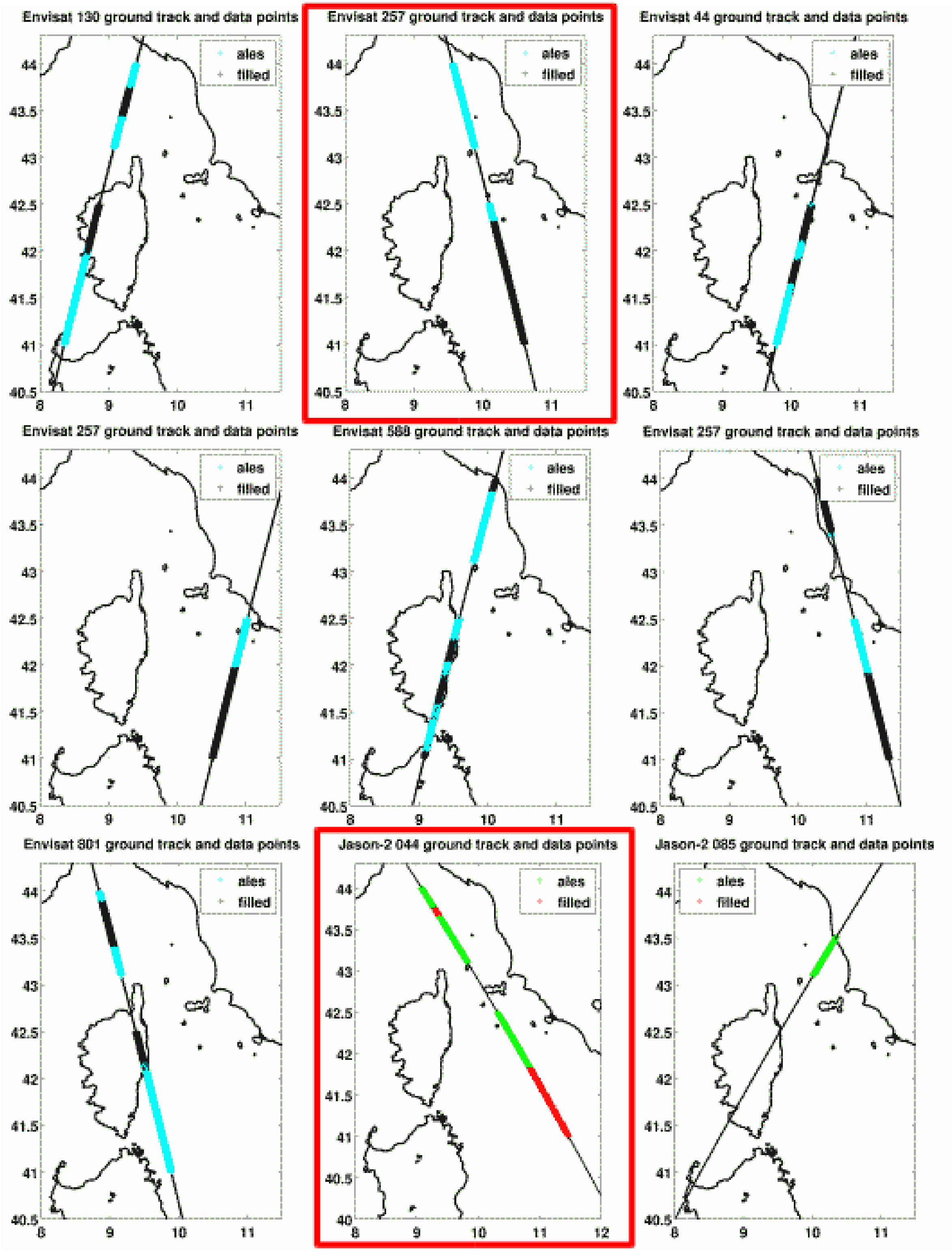

Figure 33: ALES re-tracked data gaps filled with 1hz data. The black (Envisat) and red (Jason) segments indicate the part of the track filled with 1hz data due to lack of 20hz data. ALES data are represented in cyan for Envisat and in green for Jason. Analyses concentrate on ALES retracked Envisat 257 and Jason-2 044 tracks, highlighted by red frames

Data have been checked for distortions in case of crossing a coast point, more precisely the noise along track (difference between SLAs in consecutive points) has been calculated, and, when necessary, degraded data have been removed. In any case neither j044 nor e257 showed unusual behaviours when close to coast. Data that exceed the 98th percentile or lower than the 2nd percentile are removed to avoid outliers. An example of final filtered SLA_{sat} data can be observed in Figure 34. Lastly to smooth further the data a moving average with a 1 second moving average has been applied.

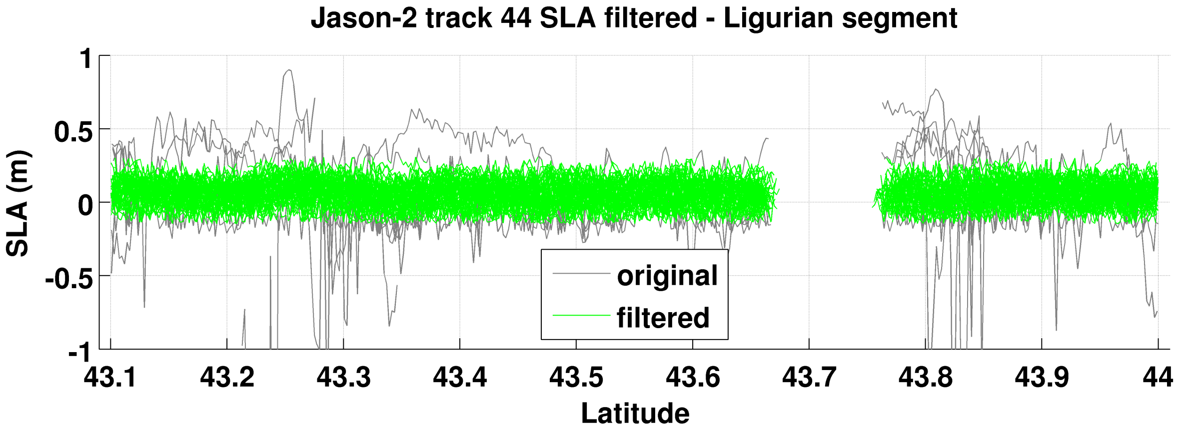

Figure 34: Filtered J044 track. Outliers, i.e. data that lie outside the range between the 2nd and the 98th percentile, were removed from the original data represented in gray. The filtered data are shown in green. No relevant interaction with the coast was detected in this particular case, although the track was very close to the northern shore of Capraia Island

4.5 Results and Discussion

4.5.1 Seasonality

The annual cycle has been computed for SSP, SLA_{sat}, SLA_{grid} for both the mean values over the Ligurian Sea and the mean values over the Tyrrhenian Sea. Basin average has been computed over the yellow dots in Figure 26. Figures 35 and 36 represent the annual cycle for each component. Each point is the mean of the same day of the year throughout the whole time series. In the case of the along track data there were few data to cover all days of the year, therefore here is represented the seasonal cycle along the months of the year. For each component listed above the residual time series has been calculated by subtracting the seasonal cycle from the original data .

In Figure 36a and 36b the Ligurian and Tyrrhenian seasonal cycle mean values are very close, their difference, represented in figures 36d and 36c oscillates around zero, ranging from -2 cm to 4 cm. Both basins reach their minimum, i.e lowest point between February and April, then their levels increase until late autumn, reaching a peak in October, consistent with Larnicol et al. (1995) observations. The trend for the difference, calculated between the Ligurian mean value and the Tyrrhenian mean

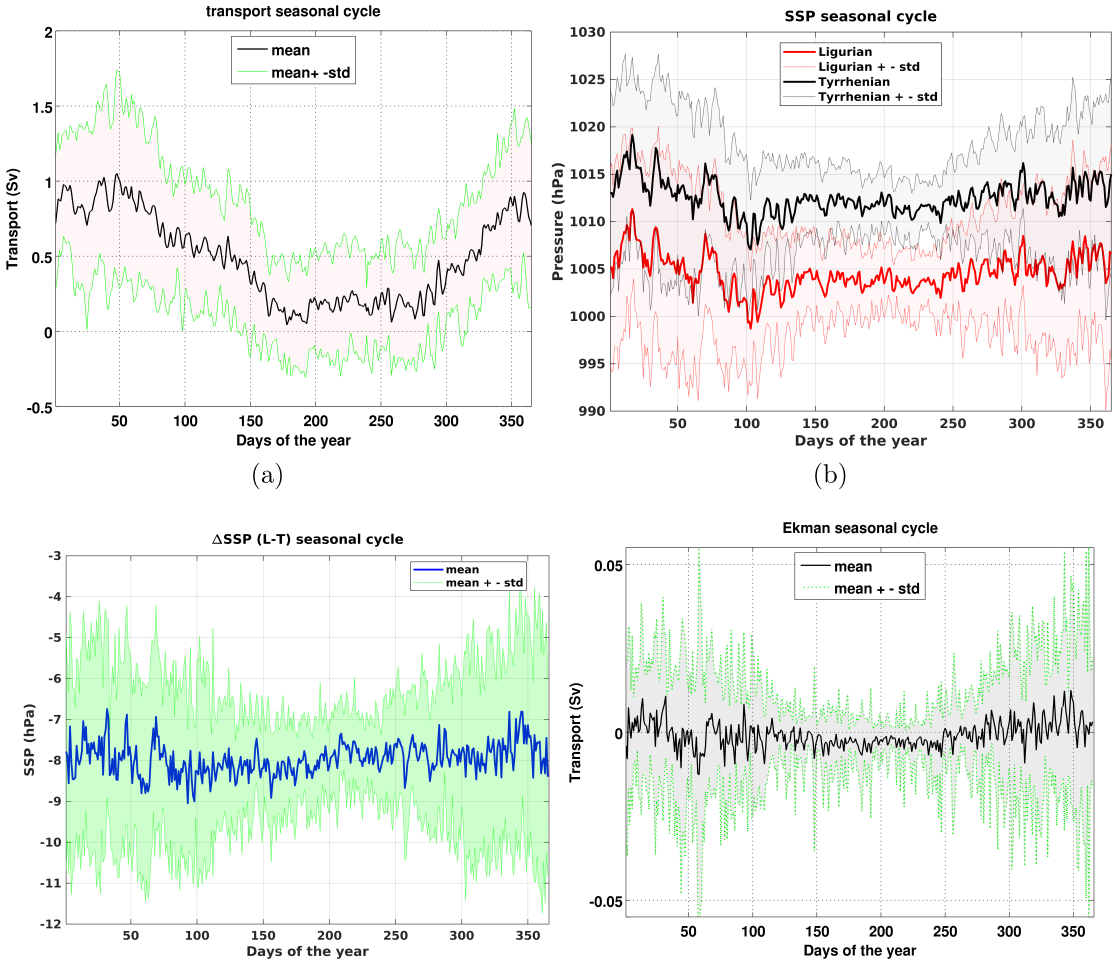

(a) (b)

(c) (d)

Figure 35: (a) Daily seasonal cycle from transport time series. (b) Daily seasonal cycle from Ligurian and Tyrrhenian SSP. (c) Daily seasonal cycle from SSP difference (Tyrrhenian minus Ligurian). (d) Daily seasonal cycle from Ekman transport. Plots (b) and (c) have been produced considering the Ligurian and Tyrrhenian means calculated over the yellow dots (Figure 26). Dotted lines indicate the standard deviation of the series. Each point of continuous lines is the mean of the same day of the year throughout the whole time series

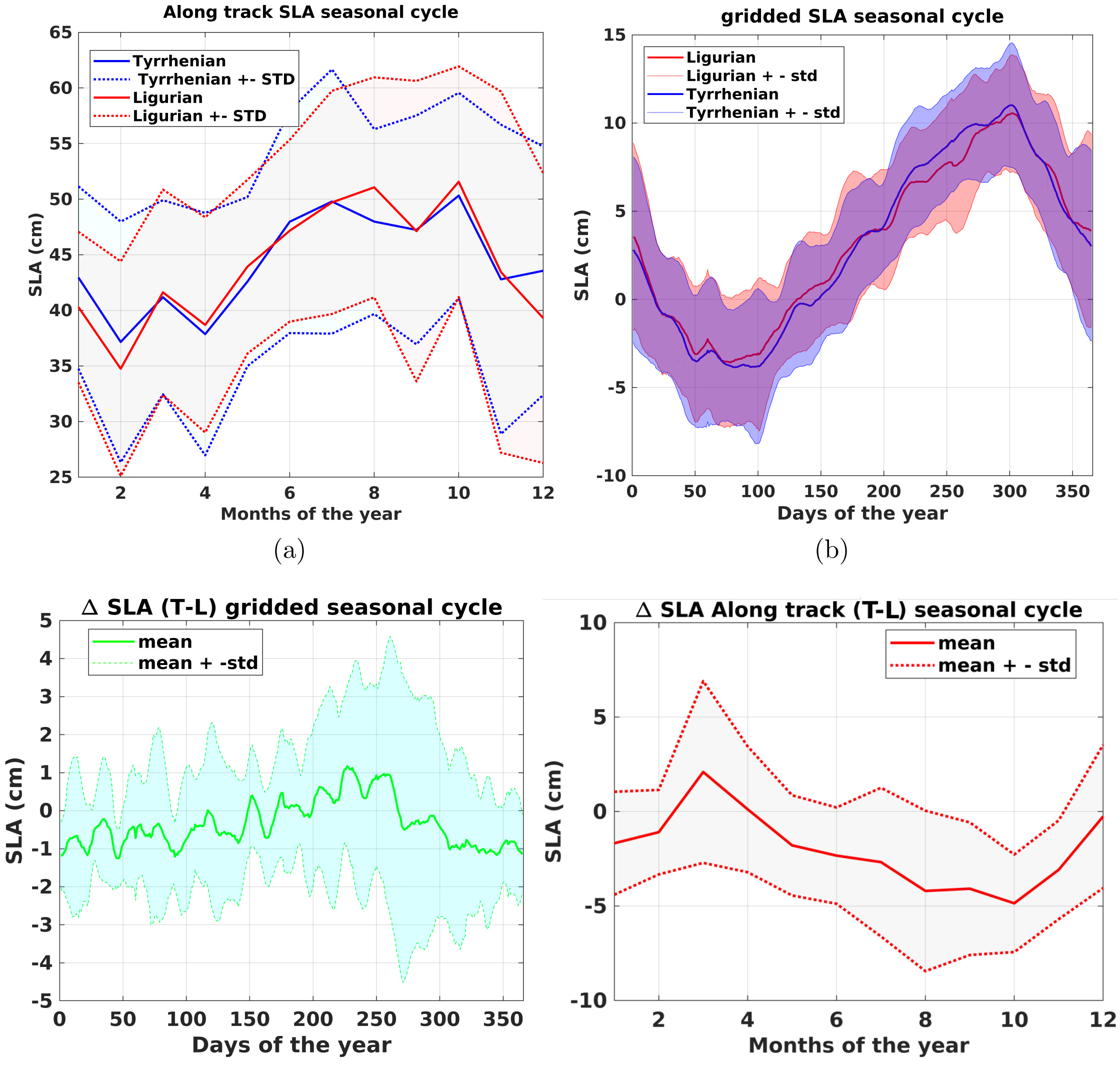

(a) (b)

(c) (d)

Figure 36: (a) Monthly seasonal cycle from along track altimetry data, considering tracks e257 and j044. (b) Monthly seasonal cycle SLA_{sat} difference (Tyrrhenian minus Ligurian) (c) Daily seasonal cycle from Ligurian and Tyrrhenian ΔSLA_{grid}. (d) Daily seasonal cycle from ΔSLA_{grid} (Tyrrhenian minus Ligurian). Panels (b) and (d) refer to the same time period from 22nd July 2002 to 31st March 2010. Plot (c) and (d) have been produced considering the Ligurian and Tyrrhenian means calculated over the yellow dots (Figure 26). Dotted lines indicate the standard deviation of the series. Each point of continuous lines is the mean of the same month/day of the year throughout the whole time series

value, for SLA_{grid} and SLA_{sat}. SLA_{sat} shows a local minimum in March while SLA_{grid} has a local minimum in late summer. in fact in March in plot 36b the Ligurian has a slightly higher value than the Tyrrhenian, in Figure 36a the opposite happens. Bearing in mind that in late winter the steric difference of the two basins should be positive and maximum in absolute value for driving the water flux across the CC, then the local minimum in March in Figure 36d matches better with this theory. The different behaviour observed in Figure 36d and 36c might be due to the diversity of the two series. Given the fact that this study focuses on a small portion of a marginal sea the gridded altimetry product has a poor quality and is not precise enough to faithfully represent such a specific area.

From the seasonal cycle of the SSP, Figure 35b it is clear that the mean SSP over the Tyrrhenian is higher than the SSP over the Ligurian. April is the month with low SSP and wider standard deviations for both basins, indicating possible unstable weather conditions. Figure 35c, that represents the difference between the Ligurian and the Tyrrhenian mean values, shows a minimum in late winter suggesting a role also of SSP during the maximum activity of the CC.

Both the total water transport and the meridional Ekman transport present seasonal cycles (Figure 35), although the order of magnitude is different, the Ekman seasonal cycle mostly agrees with the total transport seasonal cycle. For both datasets, the water transport through the CC increases during the last months of the year. Only the end of winter/beginning of spring, Figure 35a and 35d, the meridional Ekman transport disagrees with transport calculated from moored instrument. March is the month traditionally associated with DWF and deep convection in the Liguro-Provençal basin, which, as discussed by (Astraldi et al., 1994), might influence the exchanges between Tyrrhenian and Ligurian seas, but the winds that affect the DWF area blow from the north and the CC is out of their trajectory, while Ekman transport calculated here is related with τ_x, i.e. with zonal winds that blow from east to west. The Ekman annual cycle has a marked variability in winter, in Figure 35d the standard deviation clearly increases in cold months.

4.5.2 Correlation Analysis

Correlations between the different time series, have been investigated (Table 7). The correlation coefficients have been computed comparing the time series difference (Tyrrhenian minus Ligurian) anomaly over the same period. The anomalies are obtained by subtracting the long term average of a time series from the same time series. In order to detect any IB response the basin mean Ligurian/Tyrrhenian SLAs (along track and gridded) have been compared with the basin mean SSP Ligurian/Tyrrhenian. An example of the mean SSP and SLA_{sat} is shown in Figure 37, the SSP shows higher frequency variations especially in winter (Le Traon and Gauzelin, 1997). SLA_{sat} value used to investigate the IB response, neglects the IB correction, listed in Table 6.

	r	95% CI	r residuals	95% CI residuals
ΔSLA_{a-grid} vs $transport_a$	0.03	0.004 / 0.05	-0.05	-0.08 / -0.03
ΔSSP_a vs $transport_a$	0.16	0.14 / 0.18	0.17	0.15 / 0.19
τ_{x-a} vs $transport_a$	0.16	0.14 / 0.18	0.15	0.13 / 0.17
τ_{y-a} vs $transport_a$	-0.10	-0.12/-0.08	-0.05	-0.07/-0.03
SLA_{grid} vs SSP Ligurian	-0.09	-0.11 /-0.06	-0.18	-0.20 / -0.15
SLA_{grid} vs SSP Tyrrhenian	-0.09	-0.11 /-0.06	-0.17	-0.19 / -0.15

Table 7: r stands for correlation coefficient. CI stands for Confidence Interval. ΔSLA_a and $\Delta SSPa$ here indicate the difference anomaly, i.e. Tyrrhenian minus Ligurian mean values, calculated over the defined boxes, that are represented in Figure 26 by yellow dots. The anomaly is obtained by subtracting the long term mean of the series from the same series. Subscripts 'a' indicates that the anomaly has been considered

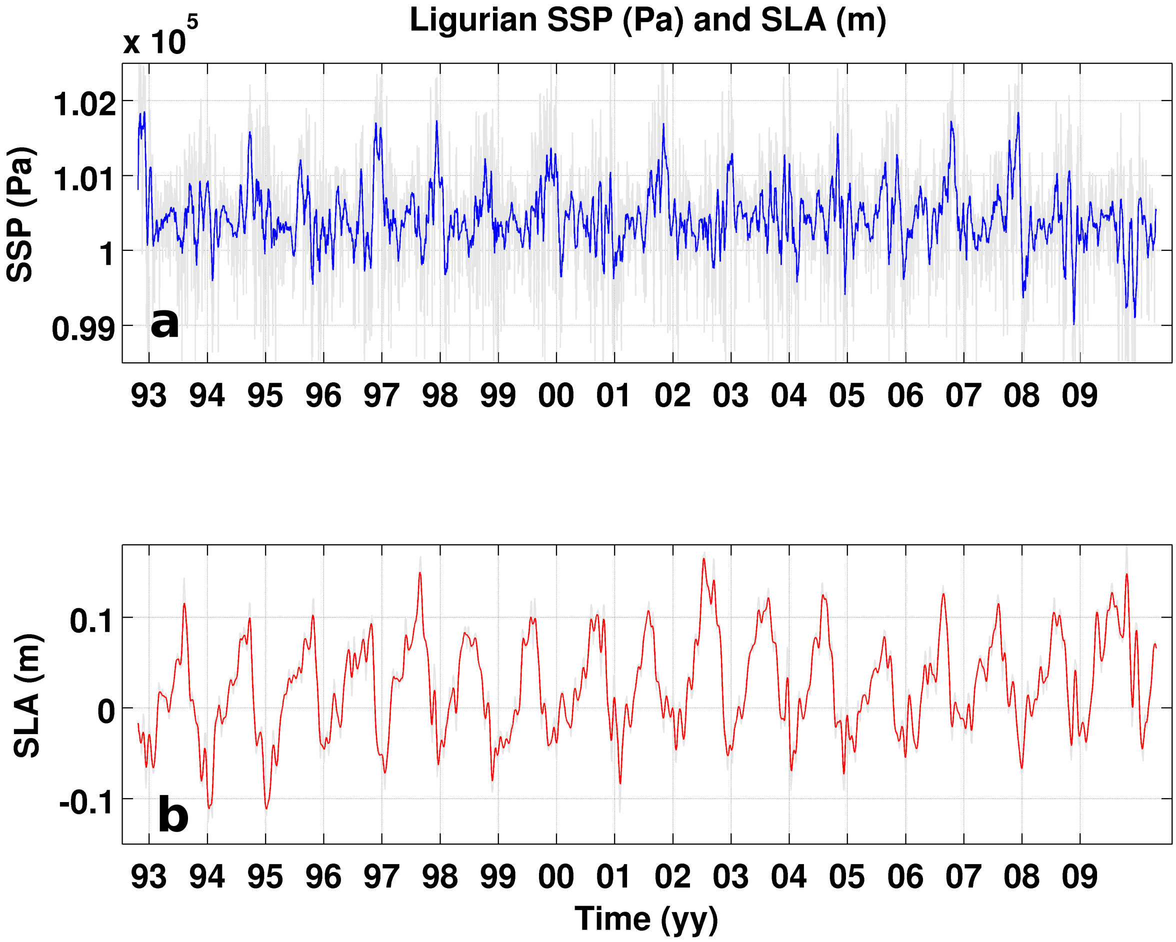

Figure 37: a) Mean over all grid points in the Ligurian Sea for SLA_{gri} and b) Mean over all grid points in the Ligurian Sea for SSP. To both series a moving average with 20 days window has been applied (light grey line, more evident in plot (a) than in plot (b))

There is a weak positive correlation between τ_x and total transport (Table 7) although it is the one of the highest correlation coefficient among those calculated between the total transport and all the other time series considered in this study. The residual, i.e. without considering the seasonal cycle, r is slightly lower indicating that part of the correlation is due to a common seasonal cycle as already noticed during the seasonal analysis.

Each point of SLA_{sat} Ligurian/Tyrrhenian time series represents the mean of the altimetric values measured in the Ligurian/Tyrrhenian Sea that belong to the same pass. From this values the ΔSLA_{sat} between the 2 basins has been evinced. From 26th June 2002 to 4th June 2008 the only considered satellite track is e257; from 9th July 2008 to 31st March 2010, j044 data have been interpolated over the same e257 time grid, j044 and e257 data have been averaged over the overlapping period, that goes from 9th July 2008 to 31st March 2010. Therefore the common time over which the correlation with the CC transport has been calculated goes from 26th June 2002 to 31st March 2010. The transport has been filtered with a moving average window of 20 days and then resampled at the corresponding data points with the SLA_{sat} time series constructed as explained above, see Figure 38. In Figure 39 only the ΔSLA_{sat-a} from j044 is compared with $transport_a$ to better resemble Vignudelli et al. (2000)'s study. The 20 days window has been chosen because it is a good trade-off between the original satellite data temporal resolution and the 'noise' that can be introduced in the correlation by a finer time scale resolution, e.g. daily. The correlation between the total water transport and the SLA_{sat} time series can be found in Table 8. In the same table a possible IB effect is investigated. The encouraging correlation coefficients, which can reach a value of -0.69, found while investigating a possible IB response, i.e. SLA_{sat} vs SSP Ligurian and SLA_{sat} vs SSP Tyrrhenian, lead us to investigate also the ratio:

$$C = (\delta SLA_{sat})/(\delta SSP) \tag{11}$$

Where δ indicates the difference between consecutive data points in the time series built calculating the average over all the gridded point belonging to the same basin, LS or TYS. Bearing in mind that for the IB effect 1 cm change in the sea level is induced by 1 mbar variation in the surface atmospheric pressure, for an IB response C values need to be as close as possible to 1, which is the case for almost the 25% of the data points within a margin of few thousandth.

In order to investigate any IB effect over the behaviour of the two basins the SSP and the SLA_{sat} and SLA_{grid} have been compared over the Ligurian and the Tyrrhenian separately. On the basis of the IB effect, high pressure on the water surface would produce a lower sea level. In fact the correlation coefficients between SSP and SLA_{sat} over the Tyrrhenian and over the Ligurian are negative. Correlation coefficients for SSP

Track	r	95% confidence interval
$\Delta e257$ vs $transport_a$	+0.34	+0.53 and +0.12
$\Delta j044$ vs $transport_a$	+0.49	+0.67 and +0.27
$\Delta(j044+e257)_a$ vs $transport_a$	+0.35	+0.53 and +0.12
$SLA_{sat}j044$ vs SSP Ligurian	-0.45	-0.61 and -0.26
$SLA_{sat}j044$ vs SSP Tyrrhenian	-0.69	-0.80 and -0.45
$SLA_{sat}e257$ vs SSP Ligurian	-0.45	-0.61 and -0.26
$SLA_{sat}e257$ vs SSP Tyrrhenian	-0.49	-0.64 and -0.30
$SLA_{sat}(j044+e257)$ vs SSP Ligurian	-0.29	-0.48 and -0.07
$SLA_{sat}(j044+e257)$ vs SSP Tyrrhenian	-0.30	-0.49 and -0.09

Table 8: Correlation coefficients for selected tracks: j044 and e257 with transport. To investigate possible inverted barometer effects, basin average SLA_{sat} values from e257 and j044 has been compared with basin average SSP. Δ indicates the difference between the Tyrrhenian and the Ligurian values

and SLA_{grid} are not reported in Table 8 because they are almost zero, i.e. $r = -0.09$ for both basins. Residual time series, i.e. time series obtained by subtracting the seasonal cycle from the time series, have a slightly stronger negative correlation coefficient (~ -0.18) than the correlation coefficient of the total time series. Again SLA_{sat} gives better correlation coefficients (from -0.29 to -0.69), in particular track j044 has strongly negative r over both basin. After some attempts with different interpolation time steps, this analysis does not seem to be sensitive to the dt choice, which influences the final correlation coefficient value only to the third decimal place. A brief comparison over the same time period as SLA_{sat} with SLA_{grid} resulted in a null correlation 0.0158 (-0.0211 / 0.0527 for 95% confidence interval). The correlation coefficient between the basin mean SSP and the basin mean SLA_{grid} can be found in Table 7. A very low correlation ties the SLA_{grid} to transport and similarly low correlation coefficient links the residual series. SLA_{sat} shows instead a positive correlation: +0.35 to +0.49. When the Ligurian sea level is lower than the Tyrrhenian the ΔSLA_{sat} assumes a positive

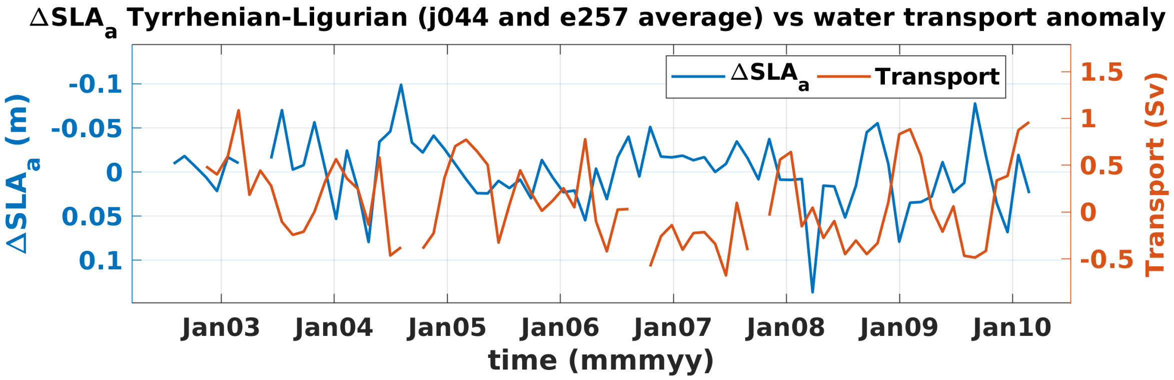

Figure 38: SLA_{sat} difference (Tyrrhenian minus Ligurian) anomaly calculated with ALES from tracks e257 and j044 and transport anomaly across the Corsica Channel

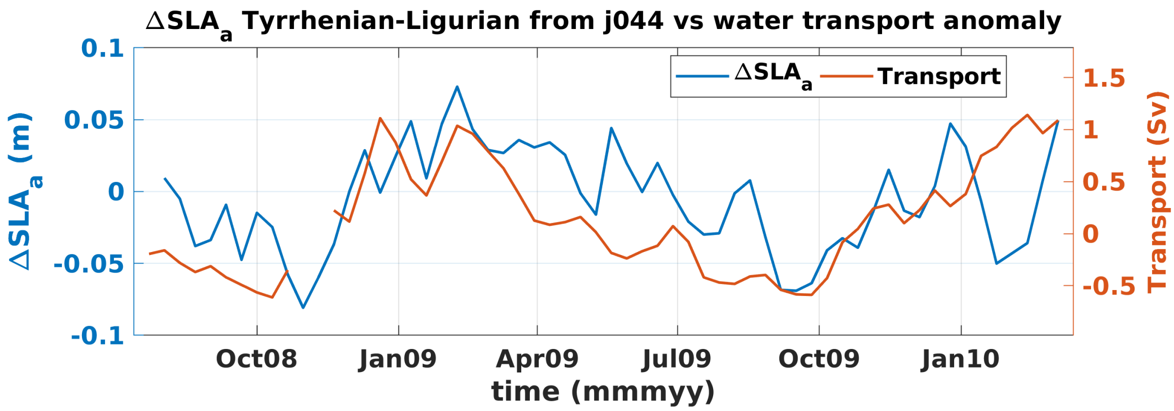

Figure 39: SLA_{sat} difference (Tyrrhenian minus Ligurian) anomaly calculated with ALES from tracks j044 and transport anomaly across the Corsica Channel

value because it is calculated as the mean Tyrrhenian SLA_{sat} minus the mean Ligurian SLA_{sat}, when this happens the sea level difference acts over the CC to enhance the northward transport. The contradiction between gridded and along track data results highlights the important difference between the two products, suggesting to the final user a careful investigation prior the definitive data choice.

The SSP correlation analysis, relative to the CC transport, shows weak correlation with the CC total water flux, a similar r has been found for the residual series (Table 7).

4.5.3 Time-lag Analysis

Cross correlation analysis allows to find the time-lag between two time series, or better said, the amount of time that one of the two series needs to be moved to maximise the correlation with the second series. This kind of analysis allows to estimate the time that the CC transport needs to respond to the influence of a certain agent. Table 9 reports the time-lag results. Negative values mean that the considered time series needs to be moved forward in time to resemble at its best the CC transport time series. A negative value means that the CC responds with a calculated delay to a certain agent. A positive value, when SSP and SLA series are compared, means that the SSP influences the SLA. No significant time lag between SLA_{grid} and transport emerged during this investigation. For SLA_{sat} no time lag analysis was performed, due to the filters and interpolations needed during the along track data processing and considering that the time step of the data varied from 10 days for Jason missions to 35 for Envisat missions. The time lag that is expected to be found can be masked by the applied filters or can happen at finer time scales.

Total	Time-lag (days)	time-lagged r	bounds 95% CI
ΔSLA_{a-grid} vs transport	~ -284 not significant	0.14	-
ΔSSP_a vs transport	~ -1	0.17	±0.021
SLA_{grid} vs SSP Ligurian	~ 8	-0.14	±0.025
SLA_{grid} vs SSP Tyrrhenian	~ 8	-0.15	±0.025
τ_{x-a} vs transport	~ -1	0.22	±0.021
τ_{y-a} vs transport	~ -3	0.16	±0.021
Residuals			
ΔSLA_{a-grid} vs transport	~ -129 not significant	-0.16	±0.025
ΔSSP_a vs transport	~ -1	0.19	±0.025
SLA_{grid} vs SSP Ligurian	~ 7	-0.24	±0.025
SLA_{grid} vs SSP Tyrrhenian	~ 7	-0.27	±0.025
τ_{x-a} vs transport	~ -1	0.21	±0.021
τ_{y-a} vs transport	~ -2	0.11	±0.021

Table 9: Time-lag analysis. Negative values mean that the considered component is early with respect to the transport. A positive value, when SSP and SLA series are compared, means that the SSP influences the SLA

τ_y is expected to mirror the ΔSSP, some resemblance emerges during the time-lag analysis: τ_y anticipates the CC transports by 3 days ($r = 0.16$), ΔSSP is 1 day early with respect to the transports ($r = 0.17$). If τ_y is a consequence of a pressure shift, when it is directed northward, from high pressure to lower pressure, it agrees with the direction of the flux, from the Tyrrhenian to the Ligurian. The τ_y component in the CC promotes an Ekman transport perpendicular to the coast. Colder, deeper water migrates to the surface to replenish the water moved under the action of the along shore wind. The upwelling tilts the isopycnals and slopes the sea surface upwards offshore. This phenomena introduces a pressure gradient perpendicular to the coast. The pressure gradient, in a rotating system as the Earth, is balanced by the Coriolis force. This scenario by definition induces a northward geostrophic flow. From the time-lag analysis we can evince that the total transport time series has a correlation coefficient peak with 1 day delay, almost immediate, with respect to the τ_x action and to the ΔSSP. The time-lag analysis comparing the total transport with τ_y, reveals a longer delay, i.e. 3 days. As mentioned before the τ_y action provokes upwelling, consequent isopycnal tilting and creation of pressure gradient, which induces a northward geostrophic flow. For this scenario to built up and participate to the ECC takes 3 days. Therefore the x-component adjusts faster than the y-component. This might explain why the RCM recorded an enhanced northward water velocity three days after the wind started to blow.

4.5.4 Spectral Analysis

The spectral analysis presented in this work has been carried out following Aslak Grinsted's method (Grinsted et al., 2004). Spectra were obtained from the Morlet wavelet, whose scale is almost equal to the Fourier period (Torrence and Compo, 1998), i.e. the fundamental period of the analysed time series. Through the Morlet wavelet the spectral analysis result can be extracted into a more simple spectral representation, see Figure 42. This approach allows to consider the results already compared with red noise, against which only significant results are retained and represented, giving to the plots a smoother look than a classic spectral analysis. Interannual oscillations have been investigated by comparing residual time series.

The spectral analysis results are synthesised in Tables 40 and 41. SSP, SLA_{grid}, Ekman transport and τ_y have been filtered with a moving average with a window amplitude of 10 days, in order to remove white noise. Along track data have been treated slightly differently, given their different nature, see section 4.3. Data have been interpolated on a regular time vector with a 35 day time step, so transport data to be related with SLA_{sat} have been filtered with a moving average window of 20 days and re-sampled at the same time of the satellite passes, i.e. every 35 days. All series have been standardized in order to have zero mean and unit standard deviation. Since the series failed the statistical test for normality their probability density functions has been forced to be rectangular, using a box function (Grinsted et al., 2004). The frequency peaks reported in Tables 40 and 41 are all those that met the 5% significance level against red noise criteria and that were phase locked, see (Grinsted et al., 2004).

Investigating the residual time series the significant power at yearly frequencies disappears as expected, to highlight different oscillations that go from $\sim$ 15 days to 3-4 months. Interannual oscillations common for most of the agents are at $\sim$ 2 and $\sim$ 6 years, they appear in both the total time series analysis and in the timeseries without the seasonal cycle. These long term common variations can be related to large scale dynamics, such as the North Atlantic Oscillation, which influences the CC water transport as demonstrated in Vignudelli et al. (1999). Shorter scale variations are instead linked to the dynamics of the entire air-sea system, as already observed in the correlation analysis. SSP variations over the Ligurian and the Tyrrhenian basins act both on the IB effect distribution and on the wind patterns. SSP variations have an immediate effect on the CC transports. SSP, τ_x, τ_y are linked and directly related to the large scale dynamics of the air masses distribution over the Mediterranean and the surrounding regions.

Spectral analysis of the total time series reveals common yearly significant powers for τ_x, SLA_{grid}, SLA_{sat}, SSP and τ_y in relationship with the CC transport. This means that the spectra analysis confirms a common seasonal variability in the CC water

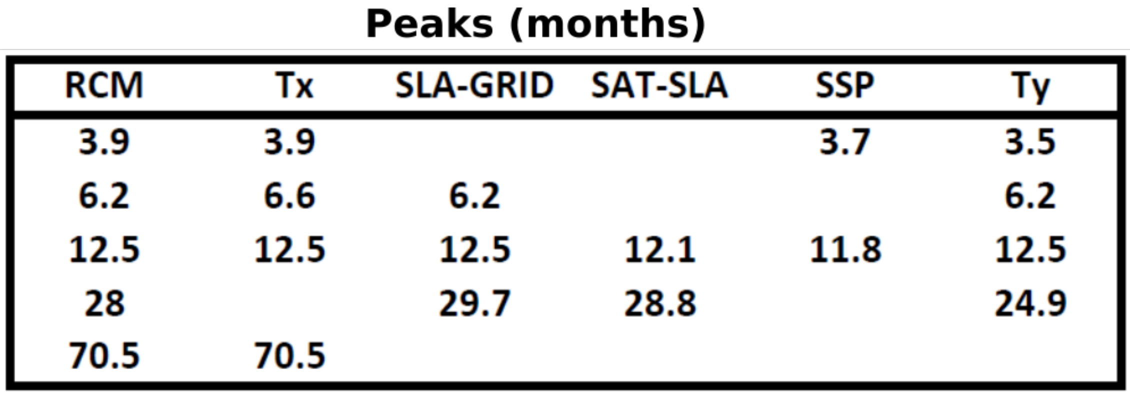

Peaks (months)

RCM	Tx	SLA-GRID	SAT-SLA	SSP	Ty
3.9	3.9			3.7	3.5
6.2	6.6	6.2			6.2
12.5	12.5	12.5	12.1	11.8	12.5
28		29.7	28.8		24.9
70.5	70.5				

Figure 40: Common peaks resulting from the spectral analysis of the total time series. Numbers represent months

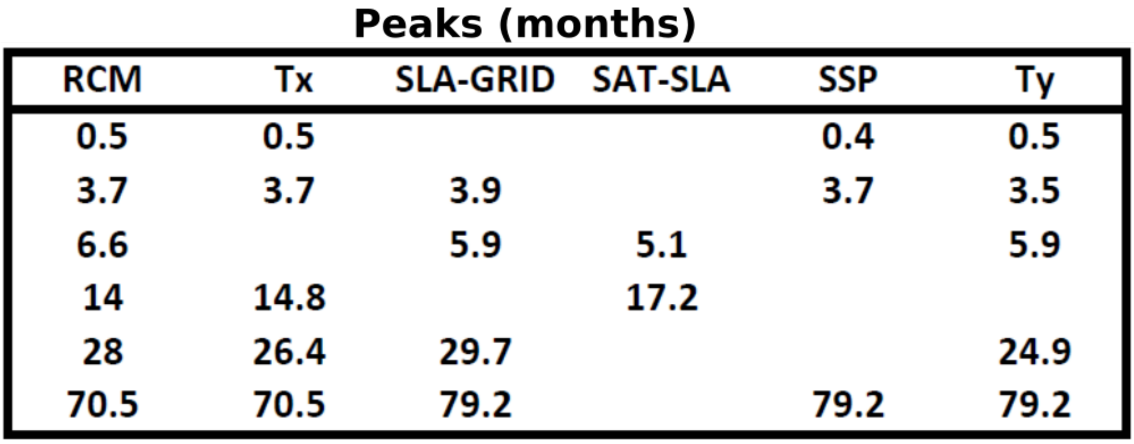

Peaks (months)

RCM	Tx	SLA-GRID	SAT-SLA	SSP	Ty
0.5	0.5			0.4	0.5
3.7	3.7	3.9		3.7	3.5
6.6		5.9	5.1		5.9
14	14.8		17.2		
28	26.4	29.7			24.9
70.5	70.5	79.2		79.2	79.2

Figure 41: Common peaks resulting from the spectral analysis of the time series without the seasonal cycle. Numbers represent months

transport time series and in the considered driving agents. The graphical results of the spectral analysis are reported in Figure 42 showing the spectra obtained from the CC total transport, τ_x, SLA_{grid}, SLA_{sat}, SSP and τ_y time series.

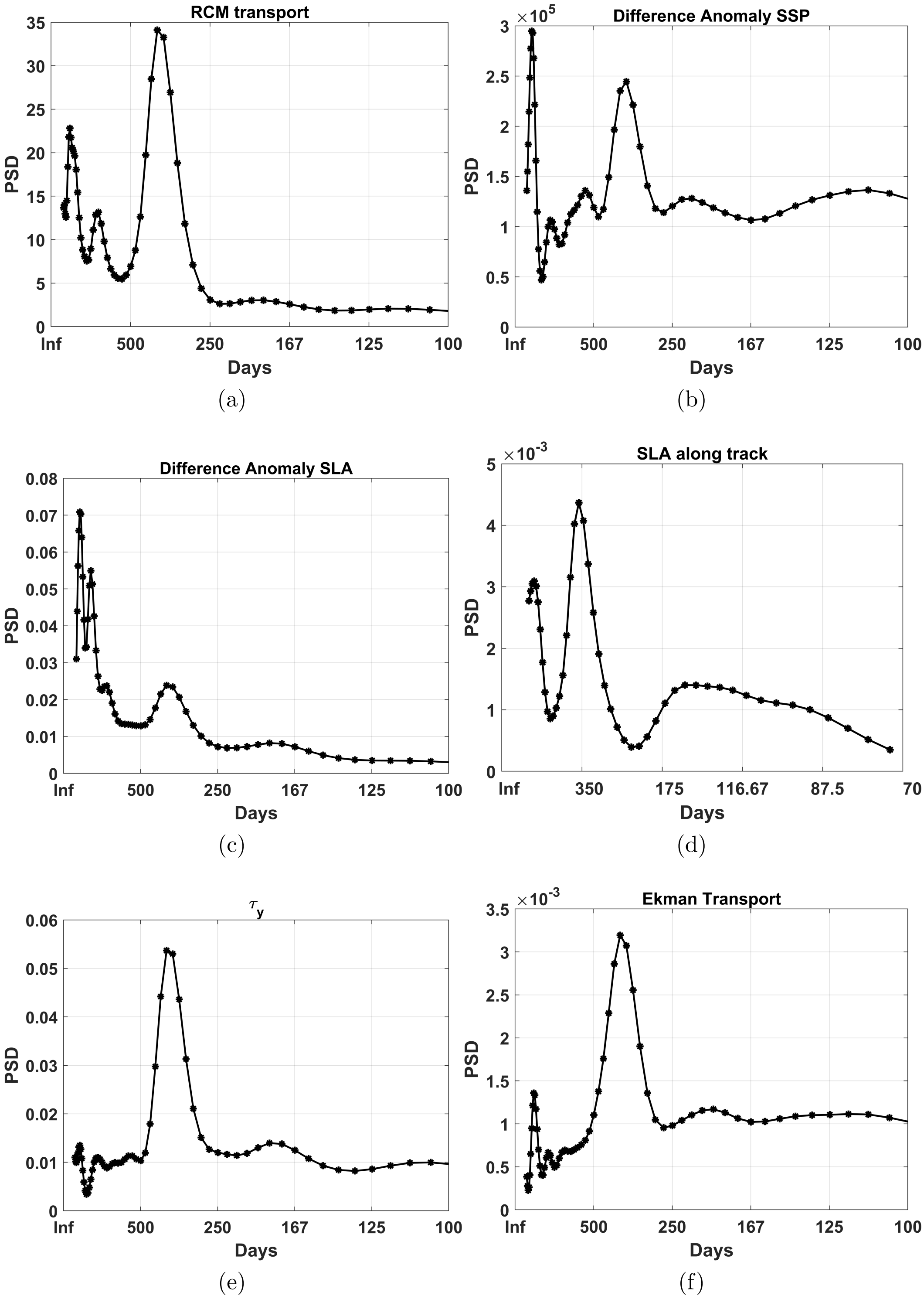

(a) (b) (c) (d) (e) (f)

Figure 42: Spectral analysis results. 42a and 42b show the power density spectra of the CC transport and the SSP series respectively. 42c and 42d represent the density spectra of the SLA obtained from gridded adata and from along track satellite data.42e and 42f show the power density spectra of the τ_y the τ_x series in the same order

4.5.5 Ekman Transport Percentage

Meridional Ekman transport ranges between -0.2 to 0.32 Sv and is almost 1 order of magnitude smaller than total transport which ranges between -0.8 to 2.5 Sv (Figure 43). Nevertheless considering just the northward Ekman transport smaller than the total water transport and narrowing down the analysis to only total water transport exceeding 0.5 Sv, the Ekman transport represents on average the 1.5% (maximum 27% on the 29th October 1997 and minimum 0.0004% on the 26th January 2002) of the total transport, as viewed by the moored RCM, Figure 44. It has been retained appropriate to set a minimum total water transport, i.e. 0.5 Sv, in order to avoid considering days during which the water flux across the CC was very weak, so that even if the Ekman transport were to represent an important percentage of the water transport in such days, its contribution would still be very small.

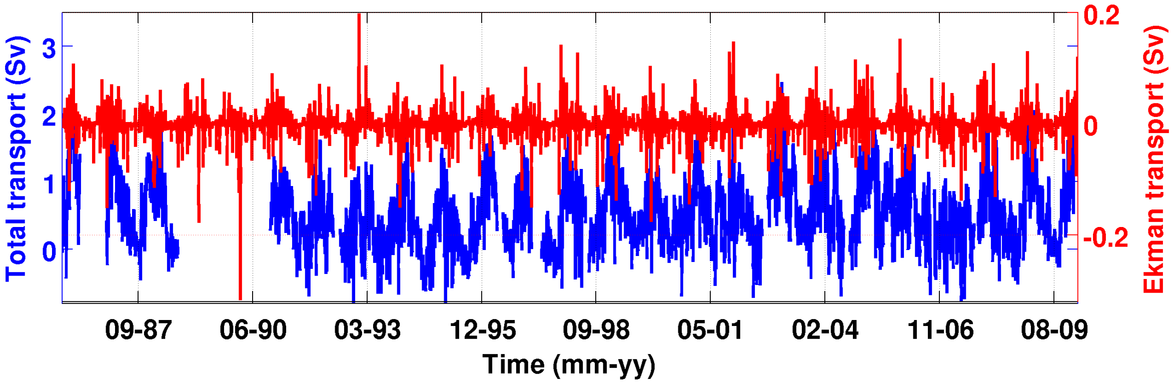

Figure 43: Meridional Ekman transport compared with total water transport

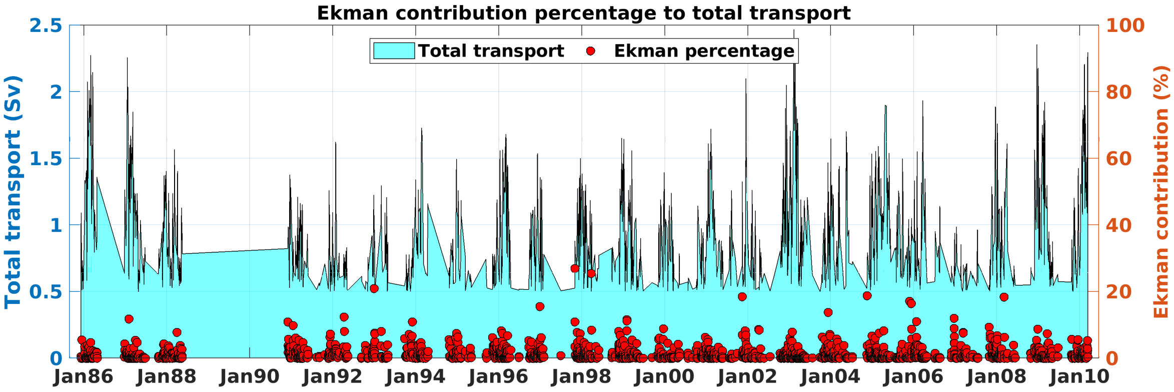

Figure 44: Total transport percentage ascribed to meridional Ekman transport. Red circles represent the percentage of total transport ascribable to Ekman transport calculated considering only total transport values exceeding > 0.5 Sv. Only northward total water transport exceeding the value of the calculated Ekman transport for a particular day have been considered. Cyan area represents the total water transport

4.5.6 Interannual Investigation

The main purpose of interannual analysis is to detect a long term variability, a trend or a cycle that lie outside the seasonality of a considered series. The long term variability might be for instance ascribed to climate change. As can be seen in Figure 45 winter transport decreases from more than 1 Sv average transport in 1987 up to 1993, then it oscillates between 0.4 Sv to 0.7 Sv until 2002. In 2003 the highest transport of the whole series occurs. After 2003 there is a decrease until 2007, the weakest winter mean transport of the series. In the 2009 and 2010 the CC transport is very active again. Higher transports, more than 1 Sv, happened in years 1986, 1987, 2003, 2009 and 2010, in winter. Very little can be said about 1986-87 transport because only SSP and wind stress data were available for those years. In any case Ekman transport is positive, directed northward, and ΔSSP are slightly below the average during both years. In 2003 the main forcings were ΔSSP and Ekman effect, ΔSLA_{grid} configuration instead does not favour the northward transport. For the ΔSLA to facilitate the northward flux across the CC, the computed ΔSLA value needs to be positive. In 2003 ΔSLA_{grid} shows a positive peak, the opposite of what one would expect. This might be due to the fact that the SLA_{grid} data did not result to constitute a good dataset for this investigations, as shown in section 4.5.2. The unexpected ΔSLA_{grid} value in winter 2003 might also indicate the independent behaviour of the steric component with respect to the other considered agents. In 2009-10 ΔSSP and ΔSLA_{grid} drove the CC northward flux, Ekman transport was very weak and directed southwards. ΔSLA_{grid} and ΔSLA_{sat} have opposite signs during the last two years of the series, this might be due to the different nature of the two series: ΔSLA_{sat} is constituted by along track satellite observation from missions Jason2 and Envisat, retracked with ALES; ΔSLA_{grid} on the other hand is constituted by data from Copernicus Marine Service gridded Sea Level Anomaly that includes data from multimission altimeter data processing system.

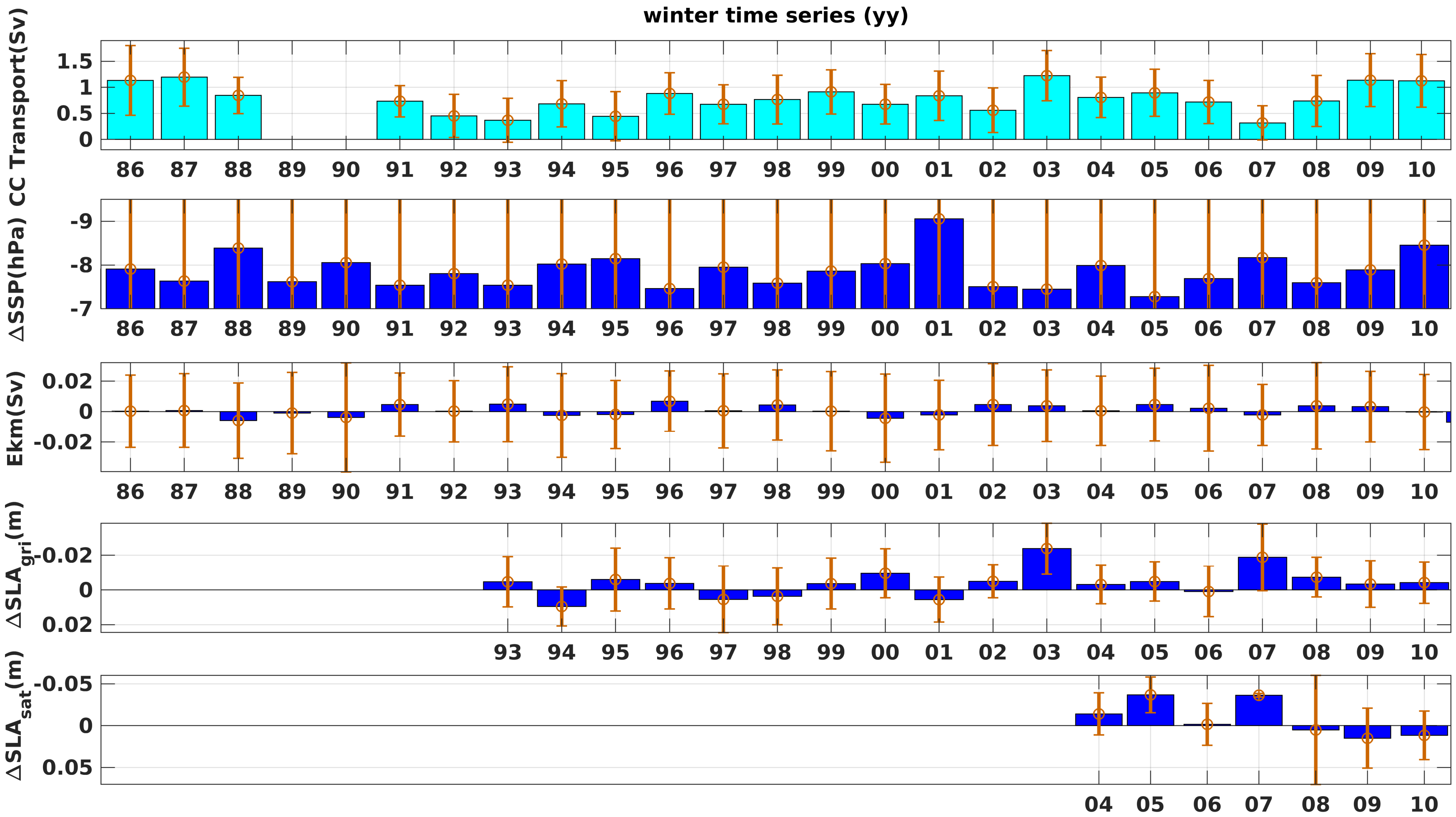

Figure 45: Winter mean values computed for every time series considered. Each bar represents the average value computed over cold months: from November to March included. Orange bars are errorbars, i.e. they indicate the standard deviations of the mean of the data associated to each winter. Remember that Δ is Tyrrhenian mean minus Ligurian mean

4.5.7 Wind and Pressure During Extreme Transport Events

In order to investigate the influence of the pressure and wind pattern over the total water transport and the Ekman transport across the CC, a set of extreme events have been selected. Daily series during this analysis introduce high frequency variability that are not necessarily representative for the time scales that are investigated here. To avoid selecting poorly representative events the monthly mean calculated both for the CC total water transport and the Ekman transport has been considered, see Figure 46 and then the annual cycle has been subtracted from each series. See Figure 47.

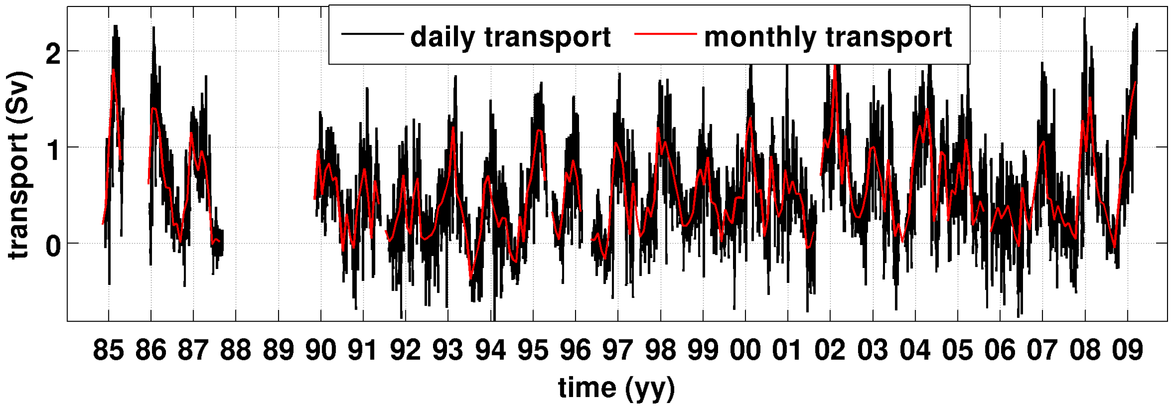

(a)

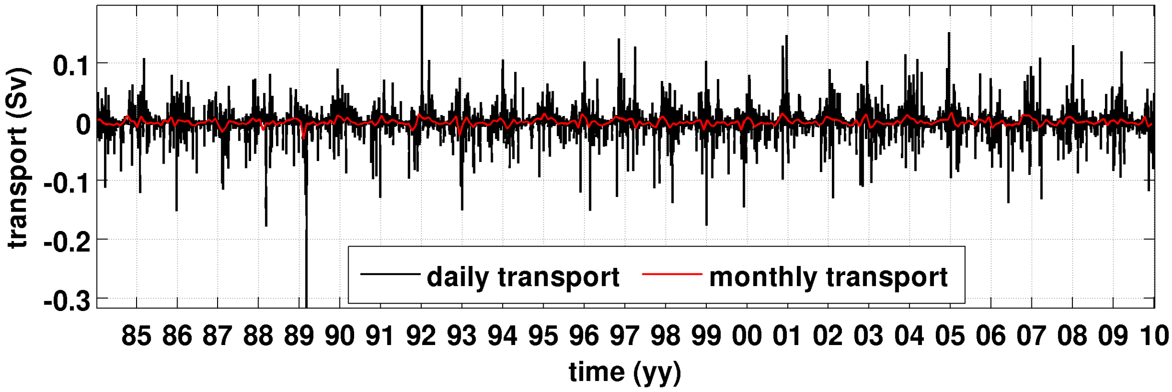

(b)

Figure 46: Comparison between daily total transport time series and the monthly series, plot 46a, calculated by averaging monthly mean from daily values, similar plot for Ekman transport in plot 46b. The x axes ticks are positioned at 24th December of every year

The extreme events selected from the time series obtained after averaging the monthly values from daily data and after subtracting the seasonal cycle are represented in Figure 48. The Ekman transport is very small in comparison with the total transport, hence subtracting it from the total transport time series did not make a big difference, as can be seen in Figure 49. Looking for positive and negative transport peaks in the series shown in Figure 49 would give a very similar, if not exactly the same, result as

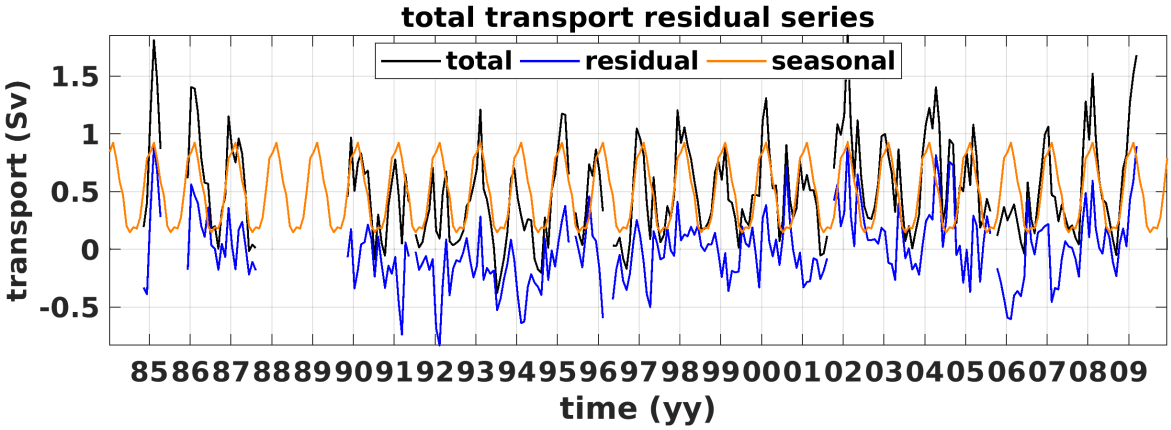

(a)

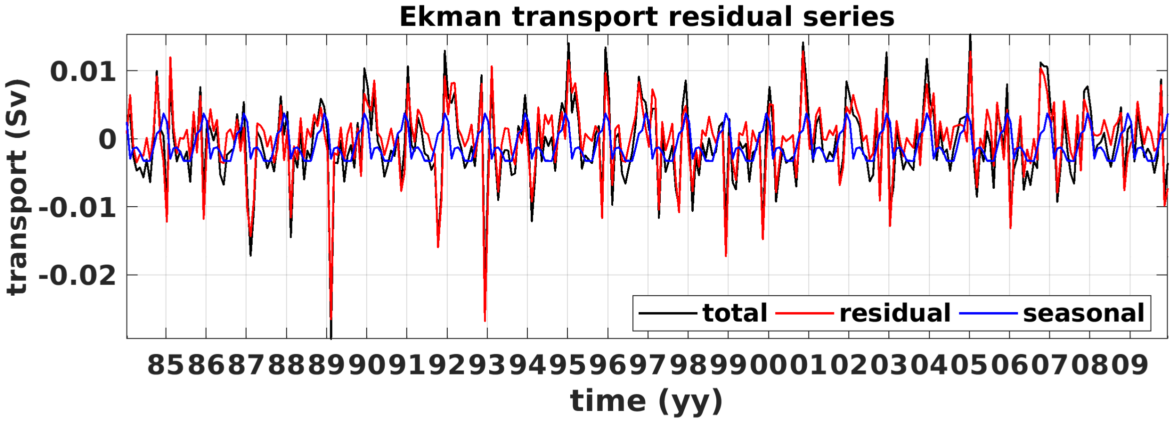

(b)

Figure 47: Total CC transport (47a) and Ekman transport (47b) from which the seasonal cycle has been subtracted to obtain the residual time series. The plot aims to explain better the changes applied to the analysed time series

looking for extremes in the total transport time series. Therefore in this section the times series given by total water transport minus Ekman transport have been considered. From Figure 48b emerges an increasing transport trend from 2000 to 2010, in fact the mean transport before 2000 is 0.45 Sv (0.0285 Sv standard error) and from 2001 to 2010 the mean transport results to be 0.59 Sv (0.0382 Sv standard error). The mean transport from 2005 to 2010 is 0.58 Sv (0.0511 Sv standard error). The standard error has been calculated as the ratio between the standard deviation of the transport that belong to a certain period of time and the number of data for which that standard deviation has been calculated. The observed increasing transport might be due to the major deep water formation event that happened in 2005, which created the nWMDW, a new deep water saltier and warmer than the WMDW. During 2005 the water column in the LS and GoL was 'preconditioned' (Grignon et al., 2010), which means that during prior years the LIW displayed an increasing salinity. which might have resulted in a lower steric height for the Liguro-Provençal basin. This scenario enhances the water transport across the CC. In addition to the steric factor, the water transport across the

CC increased in order to replenish the volume of water involved in the massive DWF event that took place during the WMT, in 2005.

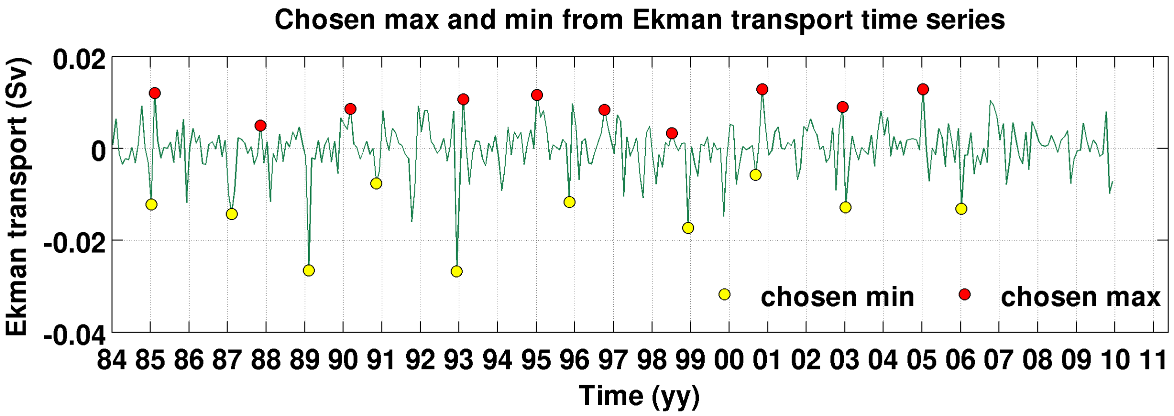

(a)

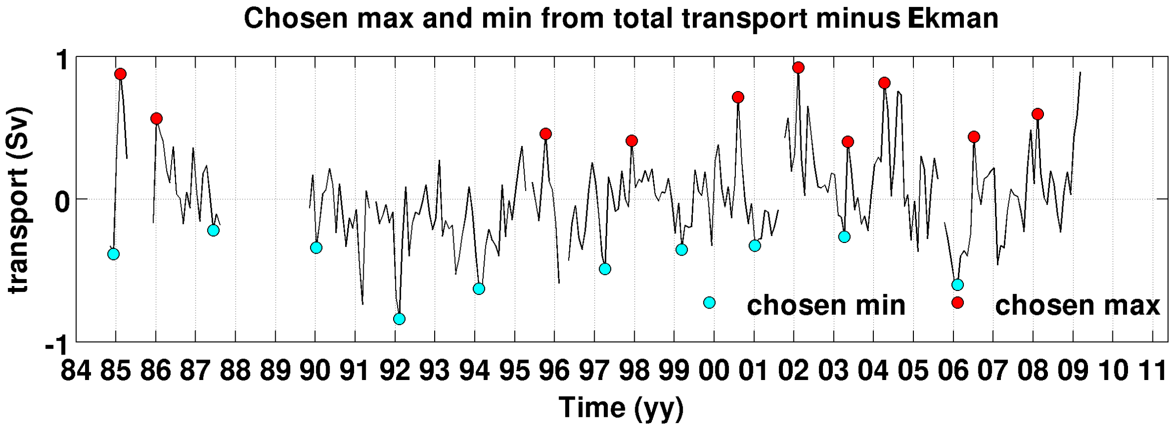

(b)

Figure 48: Chosen extreme events (positive and negative) for Ekman and total transports minus Ekman transport, from both time series the seasonal cycle has been subtracted. The peaks have been chosen in order to be distributed almost equally along all the time series, therefore a minimal spacing has been set for the extreme (positive and negative) events

From SSP and wind values the climatological monthly mean has been subtracted in order to take out any seasonal temporal and spatial variability. Figures 50 represent the mean scenario of pressure and wind pattern that characterise the 10 extreme northward events selected for Ekman transport, similarly 51), 52, 53 show the same information for extreme southward Ekman transport events, extreme northward total water transport events, extreme southward total water transport events. Mean wind direction and SSP observed in the singular maps used to create the mean plots introduced above, for each basin are reported in tables 10 and 11.

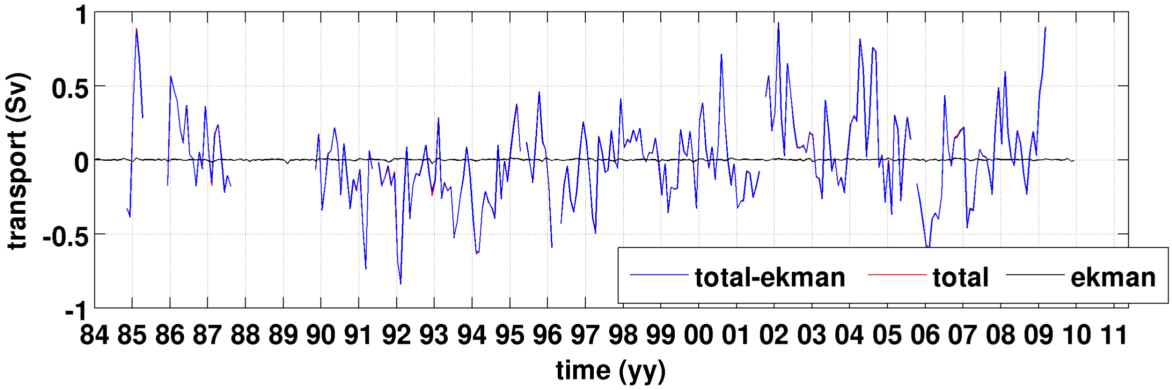

Figure 49: Total transport (red line) minus Ekman transport (black line) time series, the seasonal cycle has been subtracted from both series. The Ekman transport is so small that the blue and red line are superimposed

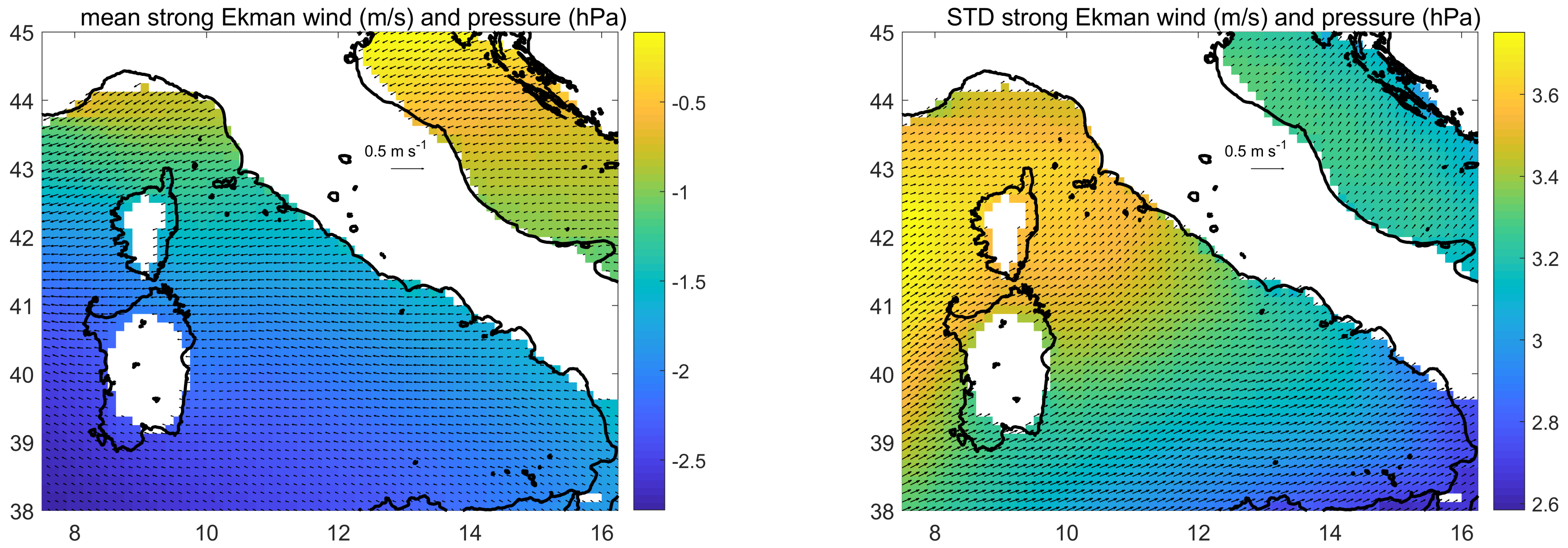

(a)

(b)

Figure 50: 50a Mean map and standard deviation 50b of wind and pressure derived by the 10 selected strongest events for Ekman transport. Pressure is in hPa and wind is in m/s^{-1}. The maps aim to reveal a pattern in wind and pressure that characterise the strong Ekman transport events

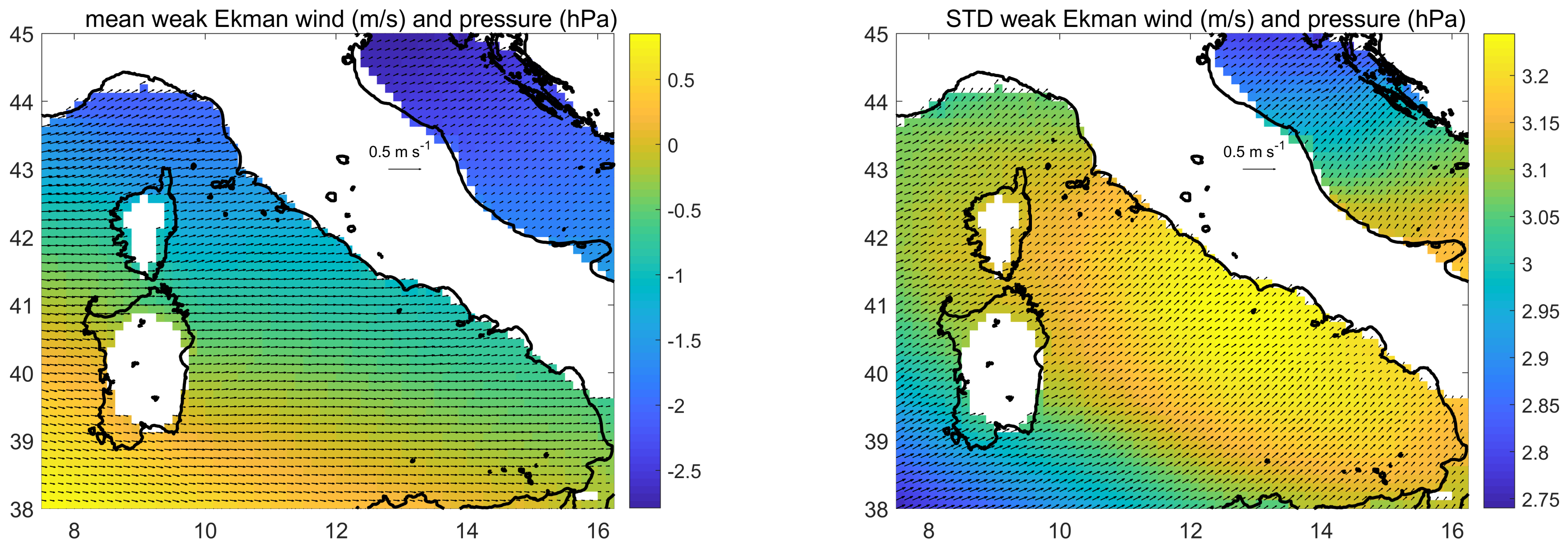

(a)

(b)

Figure 51: 51a Mean map and standard deviation 51b of wind and pressure derived by the 10 selected weakest events for Ekman transport. Pressure is in hPa and wind is in m/s^{-1}. The maps aim to reveal a pattern in wind and pressure that characterise the weakest Ekman transport events

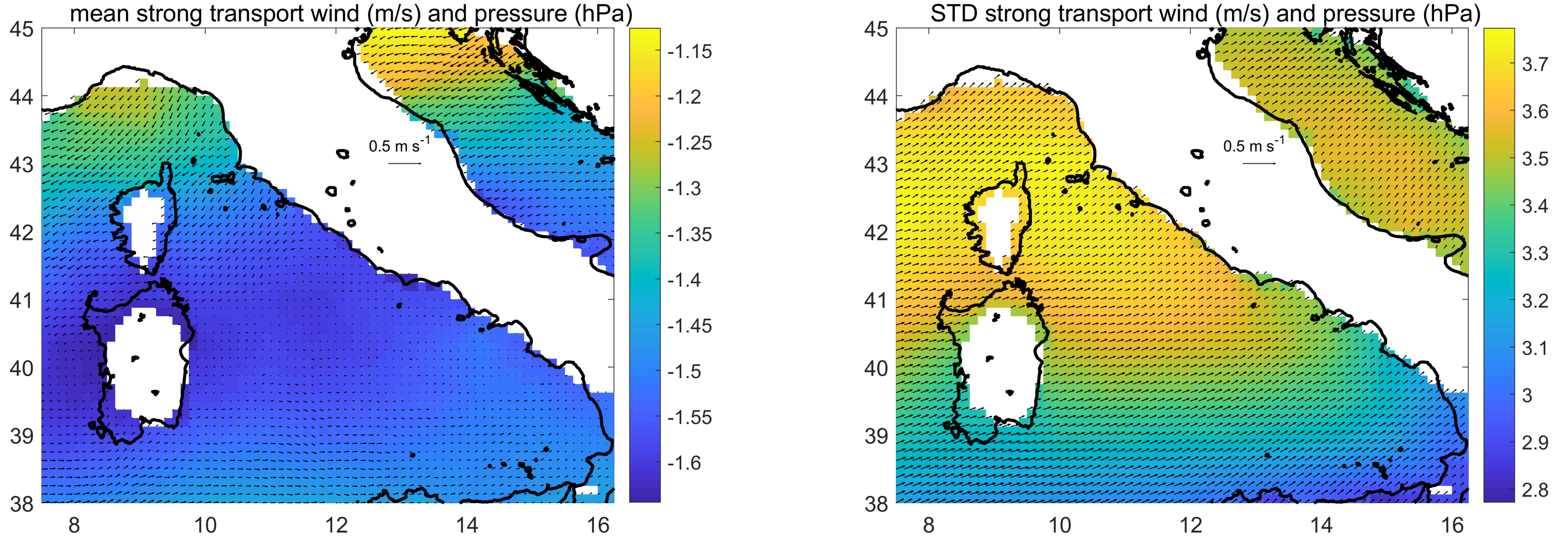

(a)

(b)

Figure 52: 52a Mean map and standard deviation 52b of wind and pressure derived by the 10 selected strongest events for total water transport. Pressure is in hPa and wind is in m/s^{-1}. The maps aim to reveal a pattern in wind and pressure that characterise the strong total transport events

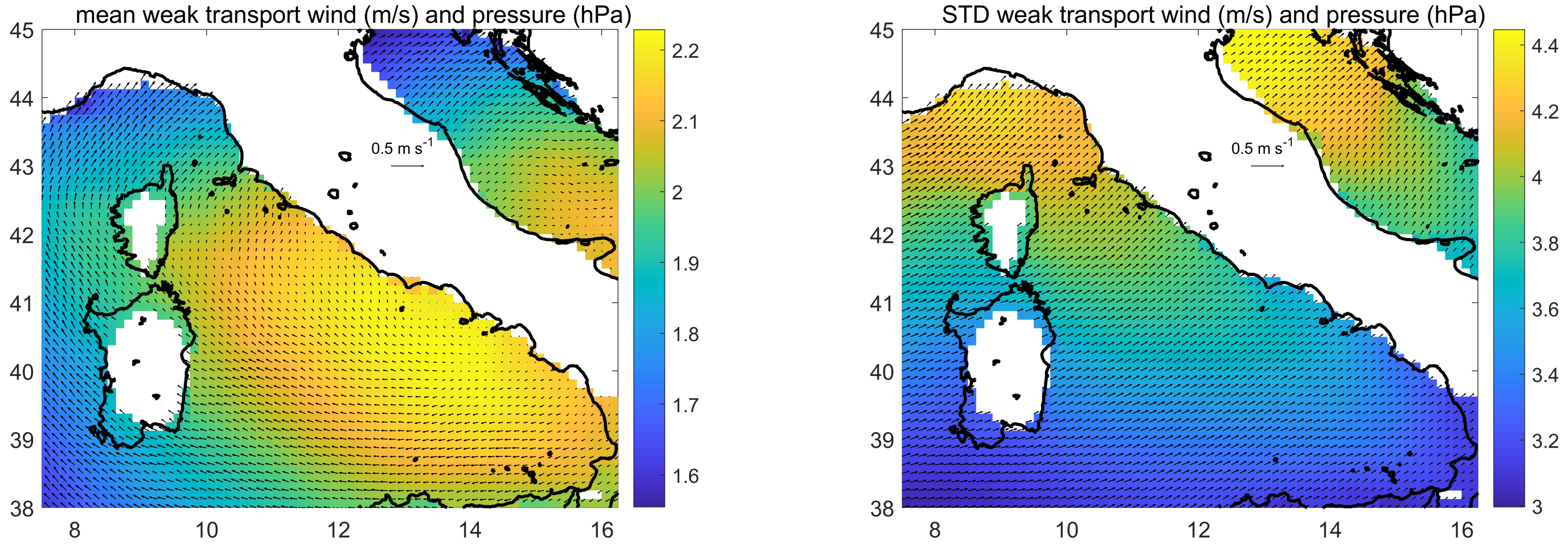

(a)

(b)

Figure 53: 53a Mean map and standard deviation 53b of wind and pressure derived by the 10 selected weakest events for total water transport. Pressure is in hPa and wind is in m/s^{-1}. The maps aim to reveal a pattern in wind and pressure that characterise the weakest total transport events

Water Total transport minus Ekman transport Weak Events				
	Ligurian		Tyrrhenian	
Date (mm - yyyy)	Dominant Wind Direction	SSP (hPa)	Dominant Wind Direction	SSP (hPa)
12 - 1985	S	1.9	S	2.4
06 - 1988	np	-2.1	np	-2.0
01 - 1991	NE	5.9	E	5.4
02 - 1993	NE	7.6	E	7.0
02 -1995	SW	1.0	SW	2.0
04 - 1998	SW	-4.0	SW	-2.2
03 - 2000	SW	3.2	SE	4.0
01 - 2002	S	8.6	NE	8.6
04 - 2004	W-NW	-1.0	N	-1.4
02 - 2007	SW	-2.8	W	-2.5
Water Total transport minus Ekman transport Strong Events				
	Ligurian		Tyrrhenian	
Date (mm - yyyy)	Dominant Wind Direction	SSP (hPa)	Dominant Wind Direction	SSP (hPa)
02 - 1986	NE	-9.1	E	-9.7
01 - 1987	N	-4.9	W	-5.1
01 - 1996	NE	-0.3	np	-0.6
12 - 1998	NE	3.6	NE	3.0
08 - 2001	SW	0.8	NW	7.8
02 - 2003	NE	2.3	NE	1.4
05 - 2004	NW-SW	-1.2	np	-1.3
04 - 2005	NE	1.0	NW	-1.0
07 - 2007	SE	-0.5	SE	-0.3
02 - 2009	W-SW	-0.5	np	-0.48

Table 10: Transport extreme events. The first column represents the date of the event the following columns indicate the predominant wind direction in the given date (np stands for 'none prevalent' wind direction) and the mean SSP minus the seasonal climatological values both for the Ligurian and Tyrrhenian seas

The TYS appears to be dominated by different wind cells. North of the Bonifacio Strait the same wind pattern acts over the LS and the TYS. South of the Bonifacio Strait a different wind cell can be noticed. The boundary between the two wind systems changes depending on the intensity of the winds in each cell. Sometimes the TYS presented patches with different wind directions, then the area closer to the CC has been retained to be the most influential in the CC Ekman transport. Figures 50, 51, 52, 53 represent the syntheses of all the 40 extreme events selected. Moreover figure 54 shows the difference between the mean maxima total minus Ekman transport minus the mean minima total minus Ekman transport. A similar plot for Ekman transport is

Ekman Transport Weak Events

	Ligurian		Tyrrhenian	
Date (mm - yyyy)	Dominant Wind Direction	SSP (hPa)	Dominant Wind Direction	SSP (hPa)
01 - 1986	W	-6.0	W	-5.3
02 - 1988	W	-2.1	W	-1.3
02 - 1990	SW	3.4	SW	4.1
11 - 1991	W	-0.2	NW	0
12 - 1993	W	-2.4	W	-1.1
11 - 1996	SW	-2.3	SW	-1.2
12 - 1999	W-SW	-1.7	W	-1.3
09 - 2001	W	-2.8	SW	-2.2
01 - 2004	W-SW	-6.3	W-NW	-6.0
01 - 2007	SW	3.3	SW	4.5

Ekman Transport Strong Events

	Ligurian		Tyrrhenian	
Date (mm - yyyy)	Dominant Wind Direction	SSP (hPa)	Dominant Wind Direction	SSP (hPa)
02 - 1986	NE	-9.1	np	-9.7
11 - 1988	NE	4.2	NE	3.5
03 - 1991	E	-2.0	S-SE	-2.3
02 - 1994	E-NE	-1.5	E	-2.0
01 - 1996	NE	-4.2	SE	-4.5
10 - 1997	NE	-1.6	NE	-2.6
07 - 1999	NE	-1.1	NE	-1.6
11 - 2001	NE	1.3	NE	0.6
12 - 2003	NE	0.3	NE	-0.7
01 - 2006	E	3.0	E	2.0

Table 11: Ekman extreme events. The first column represents the date of the event the following columns indicate the predominant wind direction in the given date and the mean SSP both for the Ligurian and Tyrrhenian seas

represented in Figure 55.

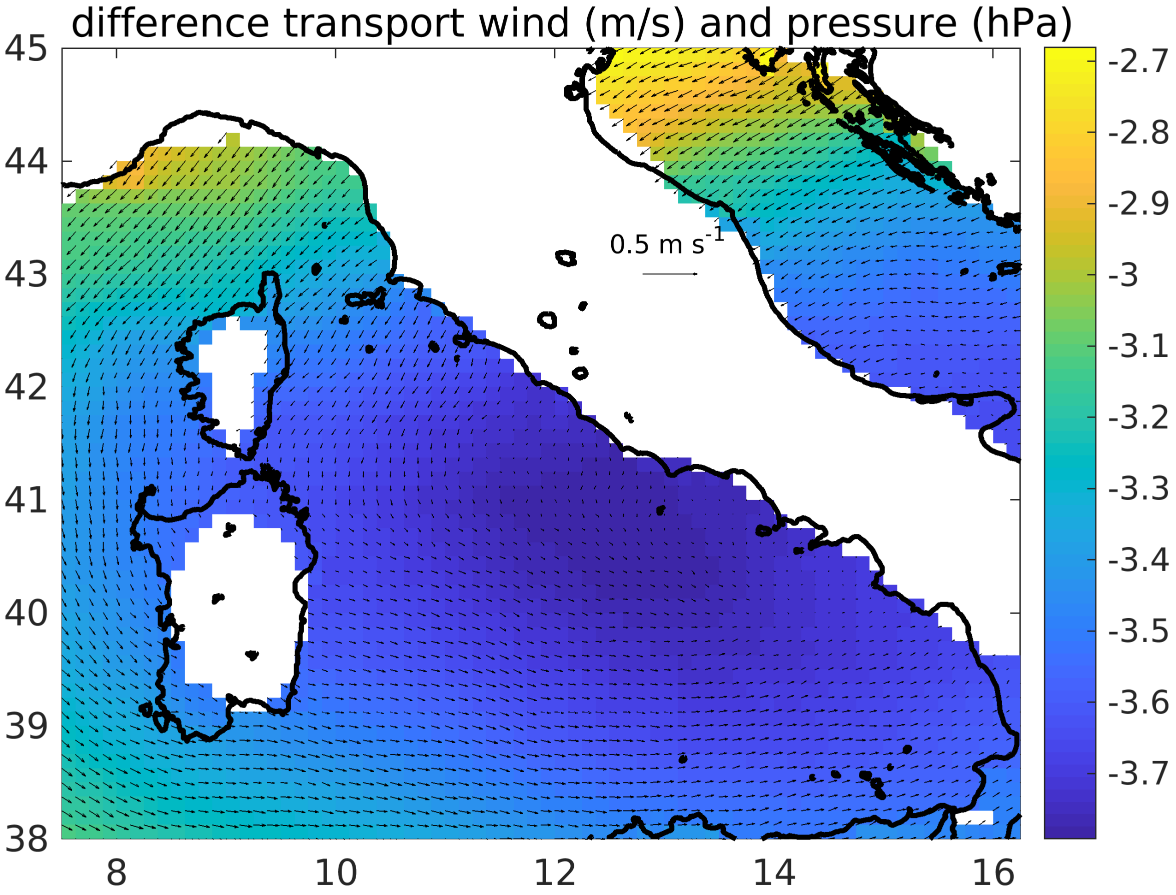

Figure 54: Difference mean total minus Ekman transports. Pressure in bar and speed in m/s. The plot represents the difference between the mean calculated form the 10 strongest northward total minus Ekman transport events and the mean calculated from the 10 strongest southward total minus Ekman transport events. The map obtained is a clear picture of the wind and SSP distribution during strong northward total transport across the CC

Weak Transport Events (WTE) take place mostly in late winter and spring, June 1988 is an exception, during which no dominant wind direction could be established. Here the pressure anomaly refers to the value of SSP in a considered month minus the climatological value for the same month of SSP. During WTE the mean anomaly SSP values over the Ligurian and the Tyrrhenian are approximately 1.8 hPa and 2.1 hPa respectively. Wind over the Ligurian is sometimes stronger than over the Tyrrhenian, but most of the time the wind intensity is the same over the two basins. The predominant direction is SW-W. Pressure is higher on the Tyrrhenian than the Ligurian during 6 events out of 10, for the remaining 4 events the situation is reversed and the surface pressure anomaly has higher values on the Ligurian, especially this is true for 1993 the lower value of the series. During the WTE, on average in Figure 53 the surface pressure over the Tyrrhenian basin undergoes an increase with respect to the average and the wind principal direction is SW on the Ligurian and on the Tyrrhenian,

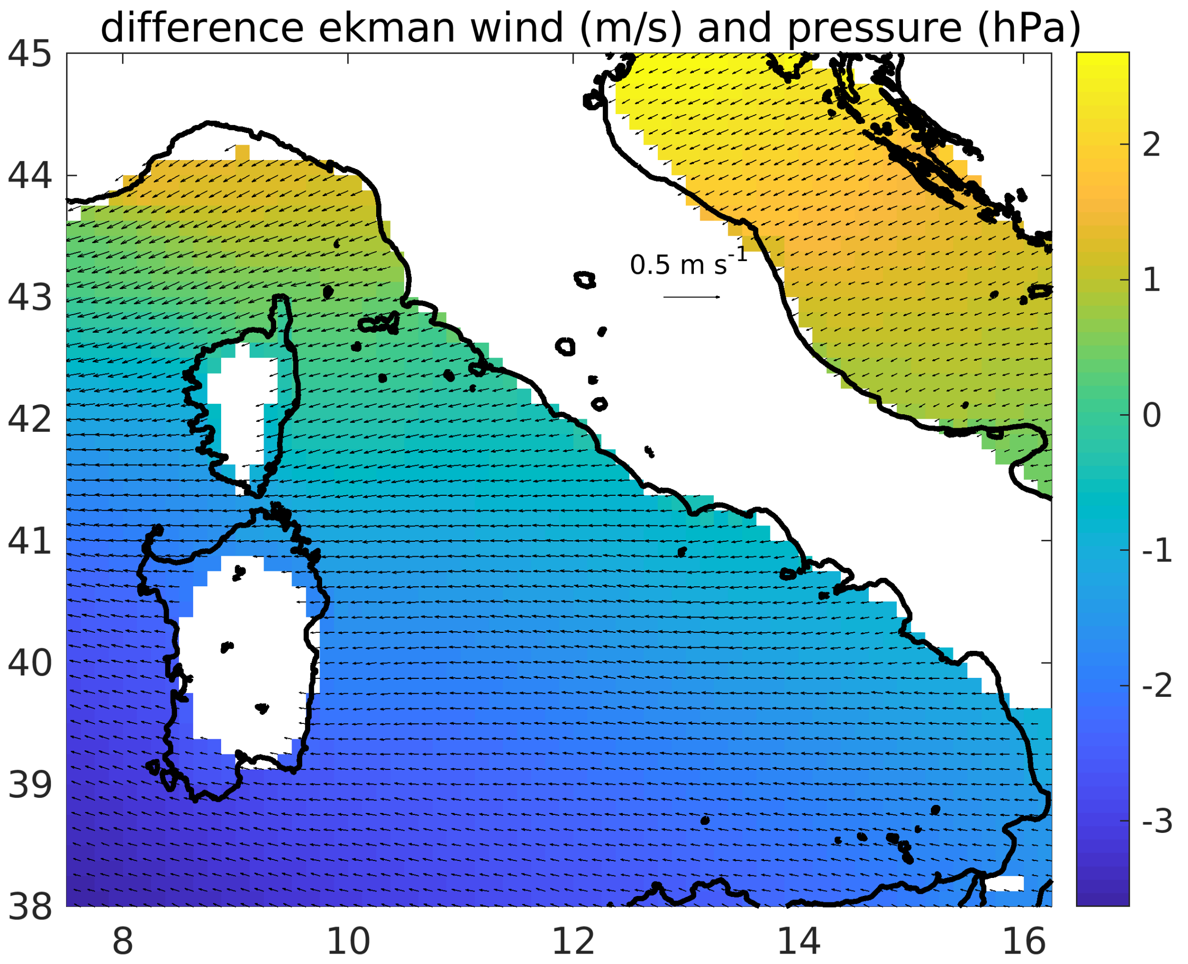

Figure 55: Difference mean Ekman transports. Pressure in bar and speed in m/s. The plot represents the difference between the mean calculated form the 10 strongest northward Ekman transport events and the mean calculated from the 10 strongest southward Ekman transport events. The map obtained is a clear picture of the wind and SSP distribution during strong northward Ekman transport across the CC

close to the CC. During WTE the wind is on average directed north-eastward and most of the SSP variability happens in the Ligurian Sea.

Mostly Strong Transport Events (STE) happen distributed in winter months, one in spring and the other two events happened is summer 2001 and 2007. Differently from WTE, STE are characterised generally by NE-N wind direction, same as Tramontane and Mistral, considered responsible for strong evaporation and heat loss in the Liguro-Provençal basin. The wind pattern looks quite patchy during summer and spring events, in the remaining ones the Ligurian presents stronger wind values. The Tyrrhenian pressure anomaly is on average -1.6 hPa, while on the Ligurian sea rests an average pressure of -1.3 hPa. The pressure values are lower than those found during WTE and the Tyrrhenian in this examples might be subject to unstable weather conditions. Figure 52 shows how on average the variation from the climatological mean that induce a strong northward flow across the CC happens over the Ligurian. The wind direction indicates that a wind coming from north-east is mainly blowing over the two basins during STE, with a considerably lower intensity in the Tyrrhenian away from the CC.

Weak Ekman Events (WEkE) occur in winter or late autumn. Winds blow principally from the west over both basins. Anomaly average pressure values are 1.7 hPa over the Ligurian and -0.97 hPa over the Tyrrhenian Sea. The SSP here is generally higher on the Tyrrhenian than on the Ligurian, indicating that the Ekman transports probably are not closely related to the SSP pattern that in this case would favour the water to flow northward across the CC. A summary figure for these events is Figure 51. WekE are characterised by a eastward blowing wind, lower SSP on the Ligurian and variability focused in the Tyrrhenian basin.

The selected Strong Ekman Events (SEE) happen in late fall and winter. Here the pressure is generally higher on the Ligurian than on the Tyrrhenian, again indicating that the surface pressure probably does not play a major role on the Ekman induced circulation across the CC. But the fact that the pressure pattern is actually inverted from what we would expect for the extreme Ekman events might indicate that a particular surface pressure pattern, e.g. higher in the Ligurian and lower on the Tyrrhenian, coincide with winds coming from the east. Figure 50 synthesises the SEE. During strong Ekman transports directed northwards the wind blows westwards and most of the SSP variability takes place in the Ligurian.

In Figure 54 and 55 all the above characteristics are visibly more enhanced.

4.6 Conclusions

The Corsica Channel flows have an essential role in the north-western Mediterranean Sea circulation and variability. Through its monitoring a large variety of factors can be linked to the atmospheric and sea dynamics of the Tyrrhenian and Liguro-Provençal basins. Within the present study the transport through the CC has been related to the Ekman transport, SSP, SLA_{grid}, SLA_{sat}, τ_y, monthly wind and pressure fields. SSP and τ_y, resulted to be dynamically linked. The sea surface atmospheric pressure difference between the Ligurian and the Tyrrhenian seas, creates a meridional wind component. The wind action, or more precisely the τ_y activity, creates an Ekman transport perpendicular to the shore, this induces colder waters to upwell along the Corsican shelf in the Channel. The upwelling of denser waters results in the tilting of the isopycnals and of the sea surface. A pressure gradient arises from this structure, which is balanced by the Coriolis force, and gives place to a geostrophic current along the Corsican shore, across the channel. In particular time-lag analysis revealed the dynamic response of the Corsica Channel transport to the τ_y action.

The seasonal behaviour of the analysed factors are all coherently participating in making the exchanges between the Tyrrhenian and the Ligurian more intense in winter, in particular in March. SLA_{grid} is the only investigated agent that does not show a configuration that facilitate the exchanges from the Tyrrhenian Sea to the Ligurian Sea. Summer, on the other hand, pushes all the involved parameters towards steadiness. This common annual oscillation is confirmed by the spectral analysis.

Although the total transport and Ekman transport seasonal cycles mostly agreed (Figure 35a and 35d) at the end of winter/beginning of spring the meridional Ekman transport disagrees with transport calculated from moored instrument: the Ekman seasonal transport presents a local minimum around February/March while the total transport presents a local maximum. March is the month traditionally associated with DWF and deep convection in the LPB, which, as discussed by (Astraldi et al., 1994), might influence the exchanges between Tyrrhenian and Ligurian seas, but the winds that interest the DWF area blow from the north and the CC is out of their trajectory, while Ekman transport calculated here is related with τ_x, i.e. with zonal winds that blow from east to west. Therefore during extreme positive total transport events, happening mostly in winter, the responsible for the enhanced flux is unlikely to be the meridional Ekman transport. Ekman transport is generally 1 order of magnitude weaker than the total transport, contributing on average for the 1.5%, but during some events it might contribute to the flux for more than 27%. During winters characterized by transport that exceed 1 Sv the Ekman component of the transport is directed northwards. Extreme positive Ekman transport is associated with winds coming from the east and high SSP on the Tyrrhenian, the exact opposite situation occurs during weak Ekman events. Extreme positive CC transport events are mainly characterised by winds blowing from north-east. Extreme negative total transport minus Ekman transport events are characterised by winds coming from the south-west.

δSSP anticipates the transport by 1 day, suggesting an almost immediate response of the CC to ΔSSP variations. The mean Tyrrhenian SSP value is almost constantly higher than the mean Ligurian value. This configuration favours the water to move from high to low SSP, i.e. northward, crossing the Corsica Channel. The meridional wind stress, τ_y, favours a zonal Ekman flow, which drives the water away from the coast. Denser, deep water migrates to the surface along the shelf to replenish the flow moved by the action of the wind. The isopycnals tilt and the sea surface slopes upwards offshore introducing a pressure gradient perpendicular to the coast. The pressure gradient is balanced by the Coriolis force. This layout results in a geostrophic current along the shore, i.e. across the Corsica Channel. It takes three days for the described phenomena to be structured, hence the three days delay observed in the time-lag analysis between the Corsica Channel transport and τ_y.

δSLA_{sat-a} has been defined as the difference between the Tyrrhenian and the Ligurian SLAs, calculated from along track altimetry data, minus the long term average of the time series constituted by the described difference between the two basins. The correlation coefficient (r) between δSLA_{sat-a} and transport ranges from 0.34 to 0.49. j044's r shows a higher correlation, where j044 indicates Jason2's mission and track number 044. Vignudelli et al. (2000)'s result for the same computation was 0.72. Some differences in the present study and Vignudelli's need clarification: Vignudelli et al. (2000) used a SLA_{sat} time period that went from 1993 to 1998, the time series used here goes from 2002 to 2010 and in this chapter ALES retracked data were used. This dataset only covers a 50 km coastal data strip. ALES data were not available for Vignudelli's investigation. Track j044, the same track used by Vignudelli et al. (2000), has a better agreement with the CC water flux (r=0.49) than track e257 (r=0.34). ALES retracking, the different spatial and temporal cover are all elements that are very likely to introduce differences between Vignudelli's investigation and the present study. Through SLA_{sat} emerged an IB response in both the Ligurian and the Tyrrhenian. For 25% of the considered data points, the basins had a pure static response. Fu and Pihos (1994) found a correlation coefficient between SSP and $SLA_{sat} \sim 0.7$ for the Mediterranean Sea, the same correlation with j044 gives 0.4 for the Ligurian and 0.69 for the Tyrrhenian. The SLA_{grid} dataset, differently from SLA_{sat} data, did not show any IB effect neither in the Ligurian Sea, nor in the Tyrrhenian Sea. It did not show any strong correlation with the total water transport across the CC either. Jason 044 track is the best source of data to study the SLA influence in the Corsica Channel behaviour, maybe thanks to its particularly suitable position and high quality data.

From 2004 to 2007 in winter on average the SLA of the Ligurian was higher than the

SLA of the Tyrrhenian, not promoting the northward flux across the CC. From 2008 to 2010 instead the difference between the Ligurian SLA and the Tyrrhenian SLA was positive, favouring the northward flux across the CC. This change from 2004 to 2010 can be noticed also in Figure 38, where the winter peaks reach higher values with respect to previous years. SLA_{grid} resulted unsuitable to the present investigation due to the spatial resolution of the gridded data and multi-mission data treatment. ALES retracked data are more reliable close to land and the tracks used have been specifically selected for their optimal position with respect to the Corsica Channel. Alike the gridded data, ALES data are not subject to averaging or interpolation, which can mask important features for the Corsica Channel. Also the presence of noise in the gridded data might obscure the steric difference between the Ligurian and the Tyrrhenian Seas as happens in Figure 36c, where the SLA configuration in the two basins appears to drive a northward flux across the Corsica Channel in late summer. Figure 36c contradicts the physical argument sustained by the rest of the dataset, that a water flux from the Tyrrhenian to the Ligurian is favoured in late winter and it happens when the Tyrrhenian SLA_{grid} is higher with respect to the Ligurian, this is instead well represented by the SLA_{sat}.

In the light of the present analyses the pressure patterns over the Ligurian and Tyrrhenian seas result to have a direct and permanent influence on the exchanges between the two basins with a clear and defined seasonal cycle. High surface pressure over the Tyrrhenian favours the northward CC flow. In any case when the seasonal cycle is not considered, as in the extreme positive total transport minus Ekman events analysis, the lower sea surface pressure over the Tyrrhenian relative to the Ligurian, favours a strong transport towards an enhanced inverse barometer effect. In the case of low sea surface atmospheric pressure on the Tyrrhenian the sea level tends to rise, 1 cm per 1 mbar, if contemporary the sea surface atmospheric pressure is higher over the Ligurian Sea, the sea level in the Ligurian basin decreases. The described situation favours the water flux across the CC towards an enhanced inverse barometer effect (Figure 52 and 54). This result translates in the SLA having a key role in the activity of the Corsica Channel. A lower SLA in the Ligurian drives the flux from the Tyrrhenian to the north, even when the SSP configuration is not directly triggering a northward flux across the Corsica Channel.

Interannualy the CC flow is influenced by factors other than SSP, for instance it was enhanced by the steric difference in winters 2008, 2009 and 2010 during which both SSP and SLA_{sat} contributed to three years of winter transport above the average. Focusing especially on the sea level anomaly, it is evident from figures 38 and 39, that the steric gradient, studied through along track data, well resembles the CC total water transport, that it is really the SLA that regulates the behaviour of the Corsica Channel water flux. The Sea Level Anomaly might, therefore, be a good predictor for the Corsica

Channel transport both on a seasonal and on an interannual basis, as demonstrated by the high correlation coefficient between SLA evinced by j044 track. This conclusion is also supported by the interannual investigation that sees three winters with exceptional transport linked to the steric difference between the Tyrrhenian and the Ligurian seas. The spectral analysis revealed interesting long term common oscillations, $\sim$ 2 and $\sim$ 6 years that might be linked to large scale dynamics such as the North Atlantic Oscillation, as discussed in Vignudelli et al. (1999).

To know what influences the SLA in the vicinity of the Corsica Channel future investigation is needed. A successive study might look for an answer in the Levantine Intermediate Water flux across the channel and the evolution of the water mass properties from their original site to the Corsica Channel.

5 The Vertical Structure of the Corsica Channel Water Velocities

This section gives a more detailed analysis of the vertical structure of the flux in the CC. The data shown in figures from 56a to 57d were obtained only after completing the analysis in Chapter 4. Observing the speeds at four different levels (50 m, 100 m, 300 m, 400 m) will provide a solid basis for comparison with the results obtained in the next chapter. In addition, from the data reported here it will be possible to asses the reference velocities in the CC mooring position, useful to perform geostrophic calculations. Geostrophic currents determination lays at the basis of the IBM.

u/v level (m)	mean (cm/s) ± std	negative % and mean	positive mean
u 50	-0.11 ± 9.32	51% -6.77	6.86
u 100	-0.21 ± 6.27	51% -4.74	4.57
u 300	0.41 ± 2.97	46% -1.76	2.21
u 400	2.12 ± 2.68	20% -1.06	2.82
v 50	12.45 ± 14.25	17% -6.85	16.35
v 100	8.61 ± 12.56	26% -6.01	13.61
v 300	7.83 ± 12.74	28% -6.33	13.03
v 400	6.04 ± 11.95	37% -5.36	12.08

Table 12: Main characteristics of the vertical structure of the flux in the CC. For every component the overall mean and standard deviation for each of the four depths of the measurements has been calculated. To investigate the direction of the flux, the tables contains the percentage of the negative (westward/southward) velocities for both components (zonal -u-, meridional -v-). The data have been collected via Rotor Current Meters, positioned at four different depths in the Corsica Channel (50m, 100m, 300m, 400m). The data explored here were collected between 22nd November 1985 and 12th March 2010. Original data have a sampling frequency of 3 hours

In Table 12 the main characteristics of the vertical structure of the flux in the CC are reported. The zonal component of velocity, i.e. u, tends to be directed westwards in the top 100 m layer in 51% of the cases. The u component mean increases towards the bottom layer, at 400 m, but its standard deviation diminishes, indicating a less variable flux closer to the sea bed. The zonal component varies from -0.11 to 2.12 being at least 3 times smaller than the meridional component of velocity. The direction of u, also changes approaching 400 m depth, where only 20% of the u component of velocity is directed westward. The meridional component of velocity, i.e. v, is also the more interesting to the aim of this study, as it is the component that better represents the exchanges between the TYS and the LS. When v is positive the water moves northward across the CC, from the TYS to the LS. The percentage of negative v oscillates between 17% in the top layer to 37% at 400 m depth. If the CC flux were to go south, into the

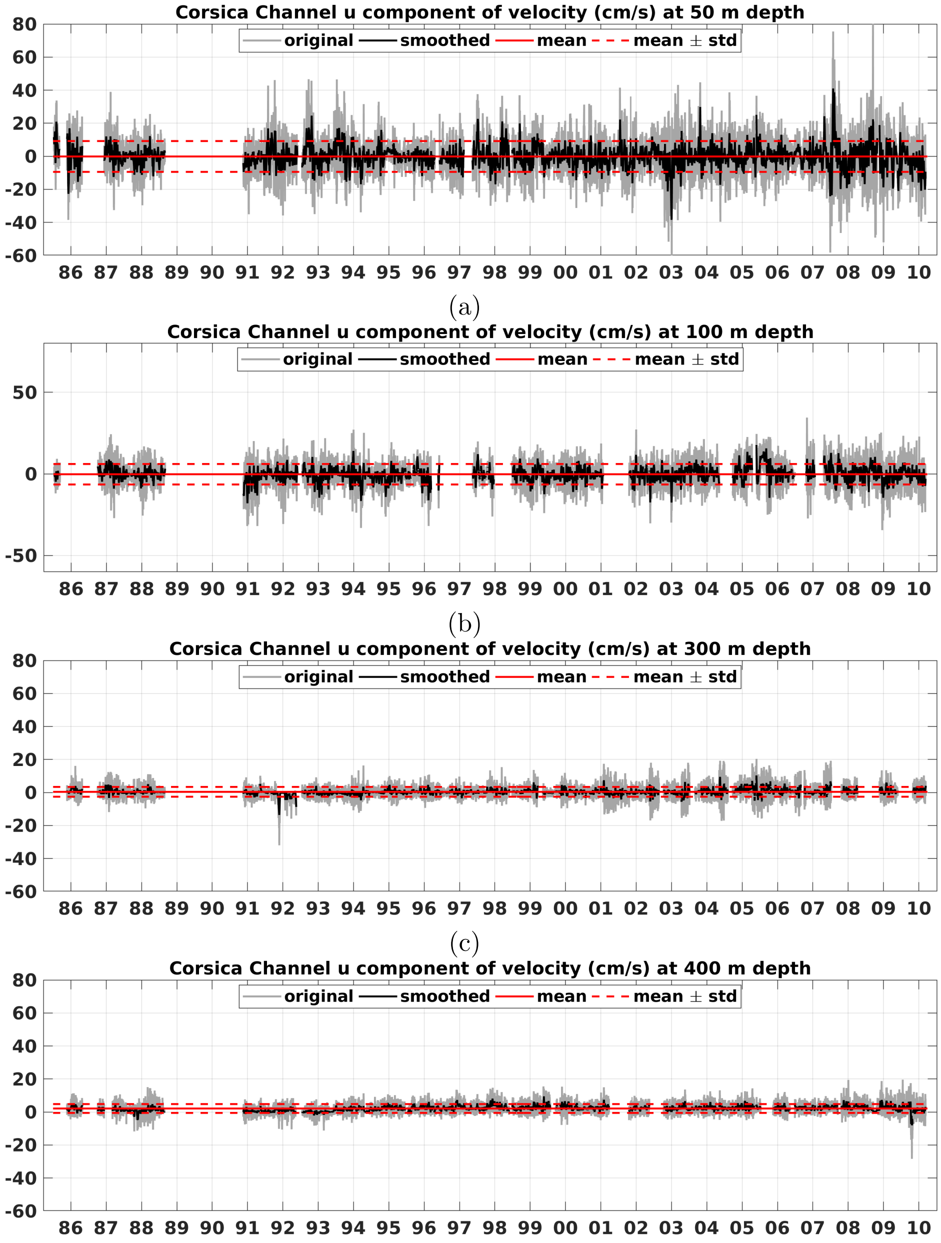

(a)

(b)

(c)

(d)

Figure 56: Component zonal speed (cm/s) of the water in the CC at 50 (a), 100 m (b), 300 m (c), 400 m (d). The original data, in gray, are every 3 hours. The black line represents the data filtered with a moving average with 5 days window. The overall mean (red continuous line) and the standard deviation (red dashed line) are also indicated on the plot. Positive speed is eastward

TYS, this would happen more likely in the bottom two layers, below 300 m depth. The mean value of the meridional velocity is higher at the surface, 12.45 cm/s, and lower at the bottom 6.04 cm/s.

In order to calculate the transport of LIW and AW across the CC, an area of influence has been assigned to each measured velocity, or better it was defined an area to which the v speed measured by a given RCM could be multiplied to calculate the

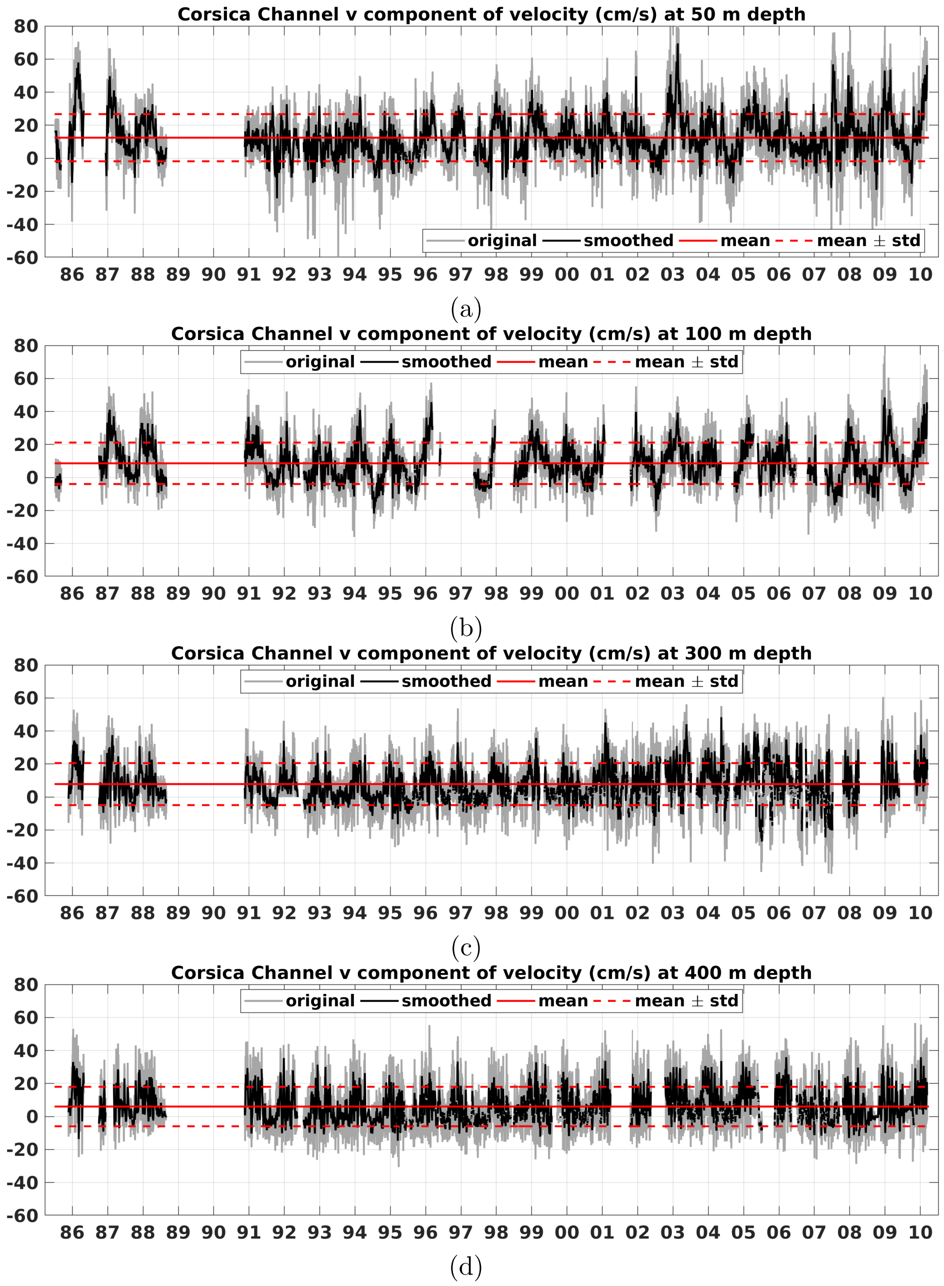

Figure 57: Component meridional speed (cm/s) of the water in the CC at 50 (a), 100 m (b), 300 m (c), 400 m (d). The original data, in gray, are every 3 hours. The black line represents the data filtered with a moving average with 5 days window. The overall mean (red continuous line) and the standard deviation (red dashed line) are also indicated on the plot. Positive speed is northward

water transport across a chosen layer. Knowing that the RCMs are positioned at 50 m, 100 m, 300 m and 400 m, the layer assigned to each RCM goes from half of the distance between the considered RCM position and the shallower RCM plus half of the distance between the considered RCM and the deeper RCM. The width of the layer is constrained by bathymetry. General Bathymetric Chart of the Oceans (GEBCO) has been used. The publishing of the Mediterranean bathymetry within GEBCO is to be attributed to the Head Department of Navigation and Oceanography of the USSR Ministry of Defence, St. Petersburg, under the auspices of the Intergovernmental Oceanographic Commission (IOC) of UNESCO 1981. Figure 58 schematically explains the area definition for the transport calculation.

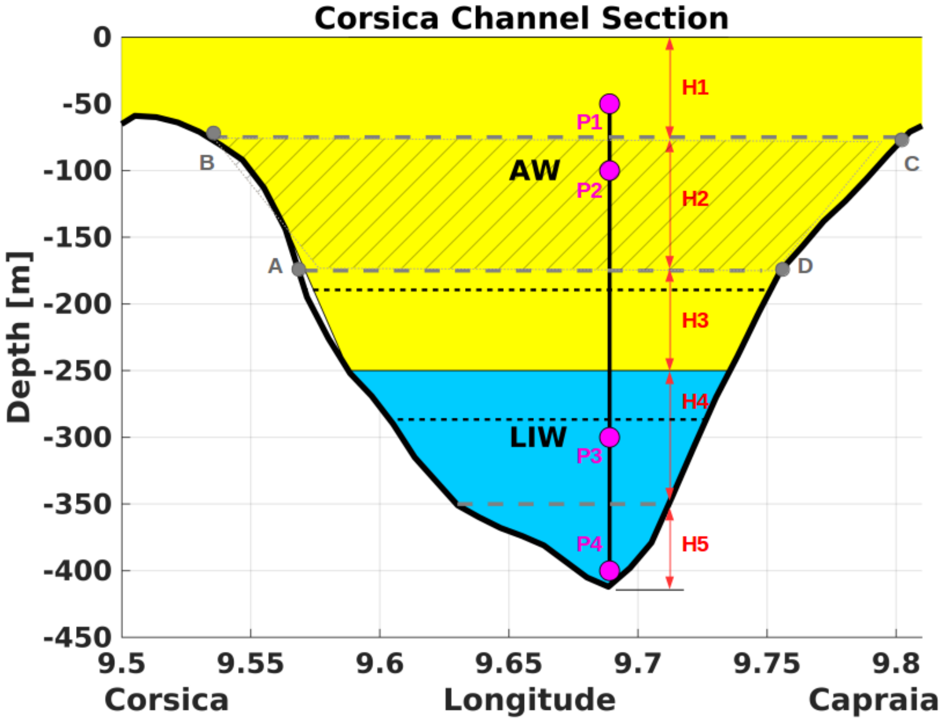

Figure 58: CC section areas for transport. The magenta points represent the position of the RCMs (P1, P2, P3, P4). The red vertical arrowed lines (H1, H2, H3, H4) show the thickness of the layer retained influenced by the velocity measured by the RCM inside the considered layer. H2, for example, has been calculated as (P2-P1)/2, likewise also the other thicknesses have been calculated. Notice that H1 goes from the surface to half of the distance between P1 and P2. H3 and H4 depend from the position of the AW-LIW interface. The AW-LIW interface (yellow-cyan areas border) can be positioned in the mean depth (235 m) calculated from density data collected during 9 cruises from 2002 to 2012. The chosen interface density is $\sigma_{1000} = 29Kg/m^3$. Details are reported in the next chapter. The dashed horizontal black lines represent the mean ± STD positions of the LIW-AW interface (192 m - 279 m). H5 goes form half of the distance between P3 and P4 to the bottom depth (412 m). To each thickness has been associated a trapezoid area, one of which is represented by the gray hatching (ABCD)

The average velocities and water mass transports are presented in figures 59 and 60. Figure 59 shows the water masses velocity and transport averaged over time, the shaded areas are bordered by STD values. Each area step has been determined as explained in Figure 58. In brief Table 13 shows the division of the areas considering the mean position of the AW-LIW interface. Figure 60 represents the total AW/LIW transport calculated along time considering the mean and the mean±STD position of the water masses interface. The mean interface depth is 235 m and has been calculated from density data collected during 9 cruises from 2002 to 2012. The chosen interface density is $\sigma_{1000} = 29Kg/m^3$. Details are reported in the next chapter. The mean ± STD positions of the LIW-AW interface are 192 m and 279 m. From this analysis the AW mean transport results to be 0.50 Sv (0.43 Sv - 0.54 Sv). The LIW mean transport results instead to be 0.10 Sv (0.06 Sv - 0.14 Sv).

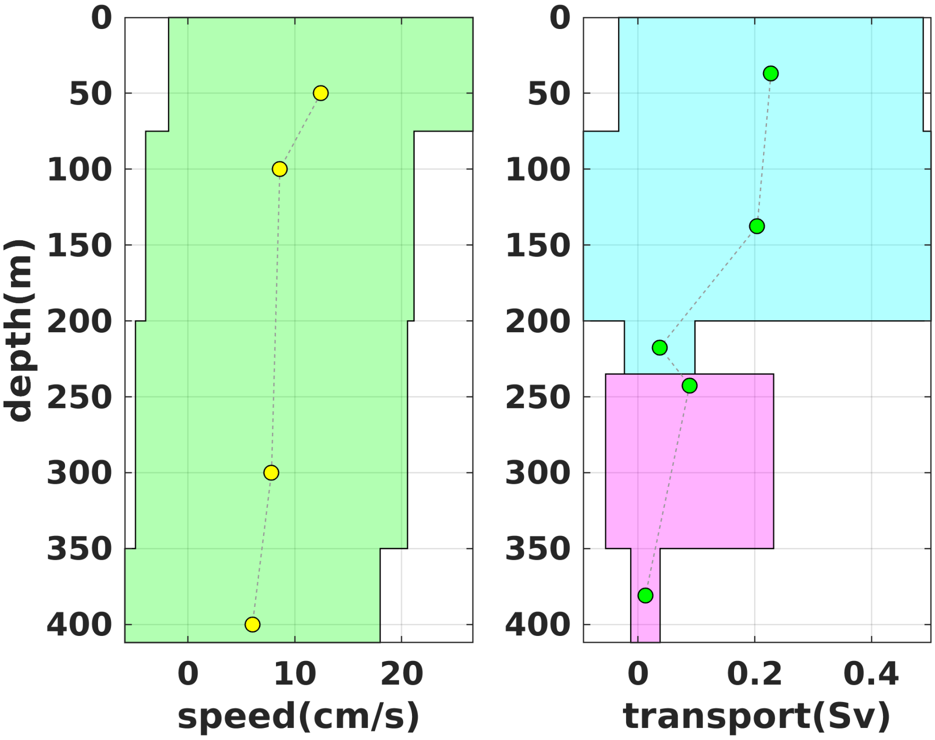

Figure 59: The plot on the left shows the velocities and STD calculated over time per each area interested by the velocity measured by the pertinent RCM. The yellow dots represent the mean velocity at the position of the RCMs. The width of the green shaded area is determined by the STD per each RCM layer. The plot on the right represents the mean and STD of the AW (cyan) and LIW (pink) transports. The green dots are positioned in the middle of each area attributed to a measured velocity and water mass. The AW-LIW interface has been positioned at 235 m

RCM depth (m)	depth area (m)	water mass
50	0-75	AW
100	75-200	AW
300	200-235	AW
300	235-350	LIW
400	350-412 (bottom)	LIW

Table 13: The table represents, column wise, the RCM measured velocity depth in meters, the top and bottom depth of the layer, that define the area to be multiplied for the measured velocity in the same layer, i.e table row, and the water mass to which the velocity has been attributed

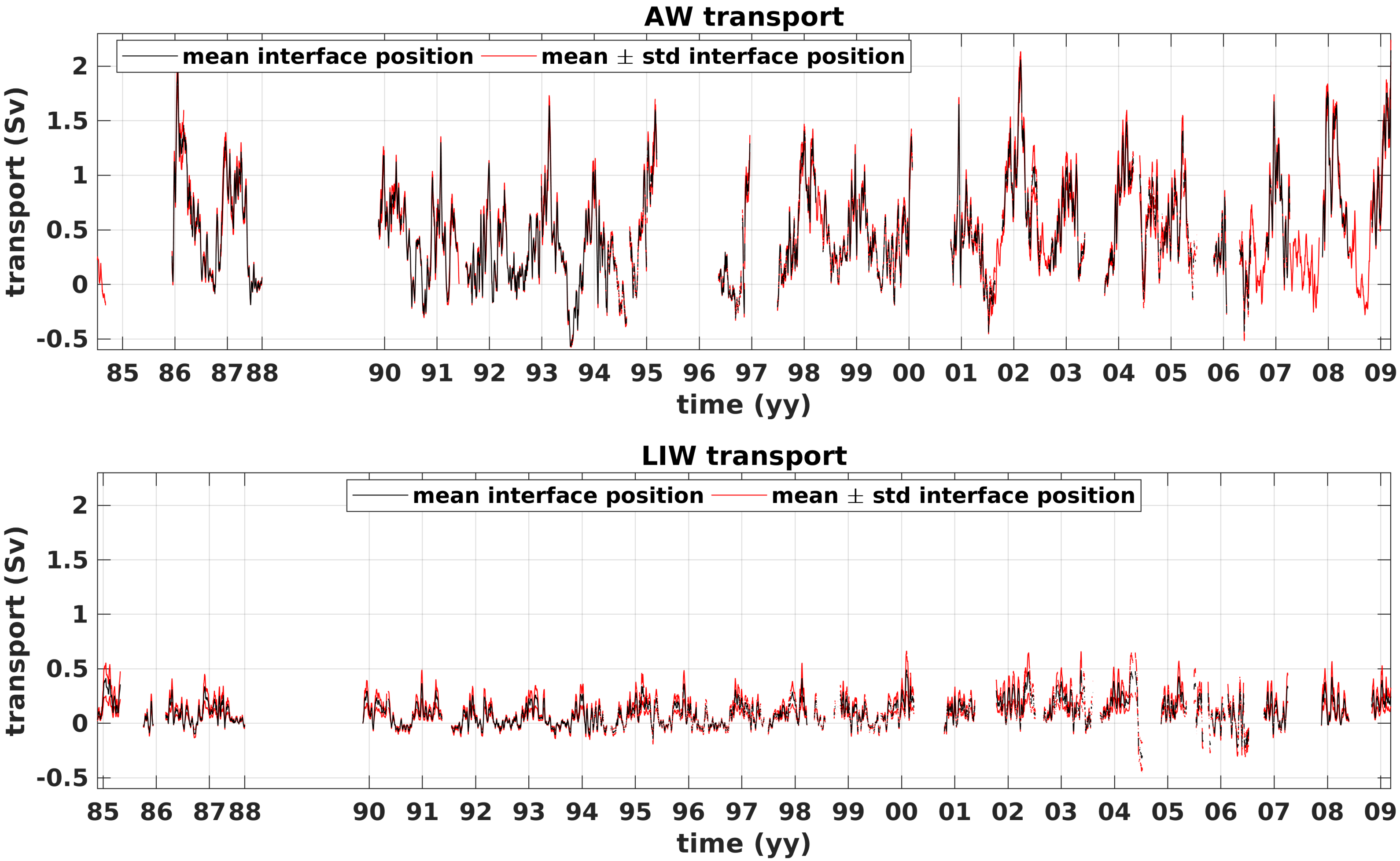

Figure 60: Time series of the AW and LIW transports. The transport belonging to the layers above the mean interface position (235 m) have been integrated to calculate the total AW transport. The same logic has been applied to transports belonging to the layers below the mean position of the interface to calculate the LIW transport. The red lines in both plots represent the time series of the AW/LIW transports obtained by moving the position of the interface up or down by the quantity indicated by STD calculations (192 m and 279 m)

An Empirical Orthogonal Function (EOF), has been applied to investigate the variability modes across the CC section. Data have been filtered with a 48 hours moving average and then re-sampled every 24 hours in order to obtain a daily series. Seasonal cycles and linear trend have been removed. Figure 61 represent the mentioned processing.

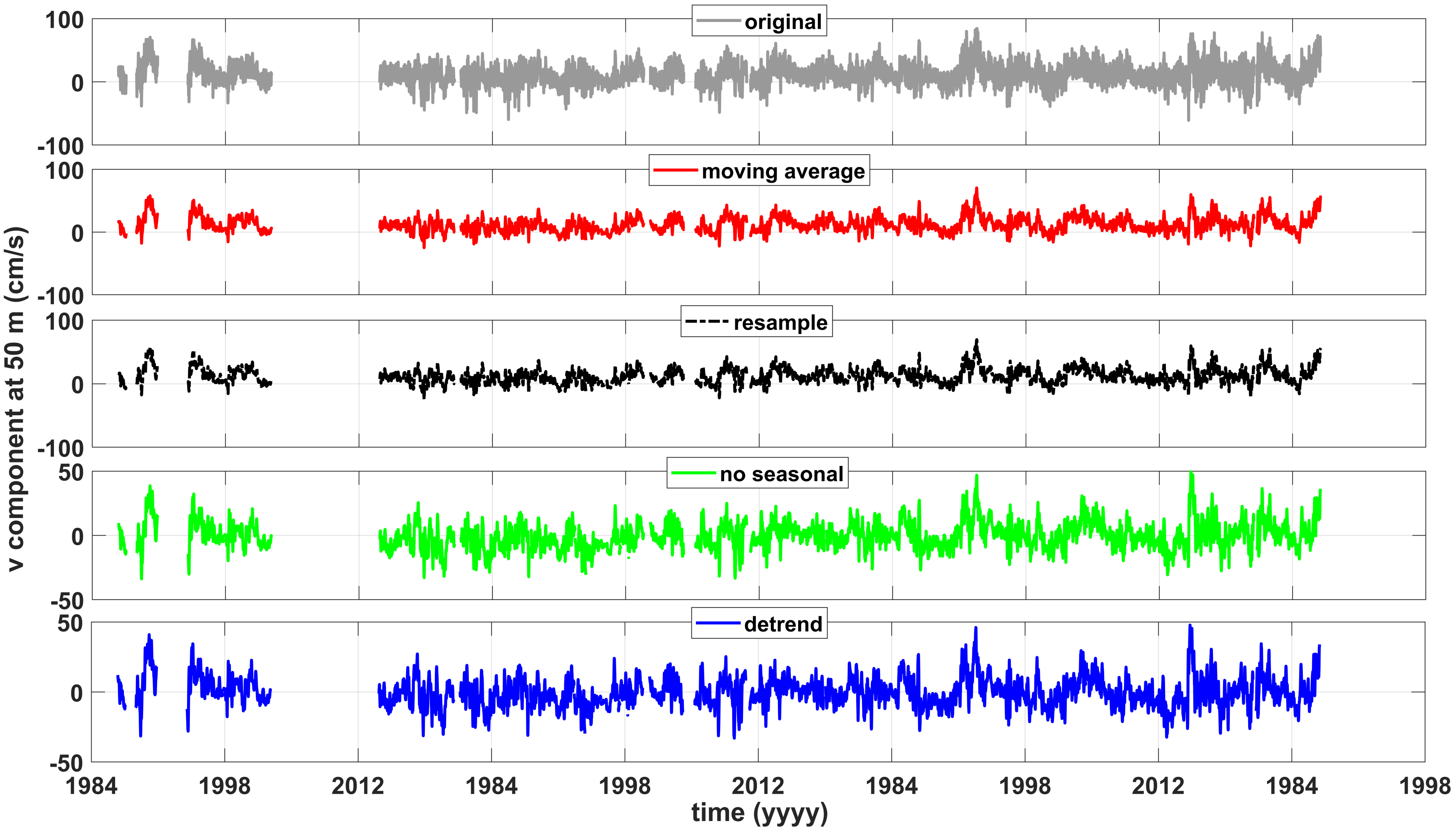

Figure 61: North-south component of velocity, measured by the RCM positioned at 50 m. The figure shows the data manipulation necessary to prepare the time series for the EOF analysis

Figure 62 represents the first 3 EOF (Empirical Orthogonal Function). Figure 63 shows the principal component time series, for each of the three principal components. The first mode explains 65.8% of the variability. The second mode explains the 22.7% of the variability and the third mode explains the 11.3% of the variability. The EOF analysis reveals that the first mode is barotropic, i.e. depth independent, the PC1 time series well resembles the AW transport time series, therefore the first mode is linked to sea surface agents, such as SSP, which constantly resembles the total CC mass transport. The second mode is instead baroclinic, depth dependent, it is linked to the water mass distribution in the water column or better to the AW-LIW interface slope. The second mode therefore well represents seasonal changes, such as an enhanced LIW flow in winter.

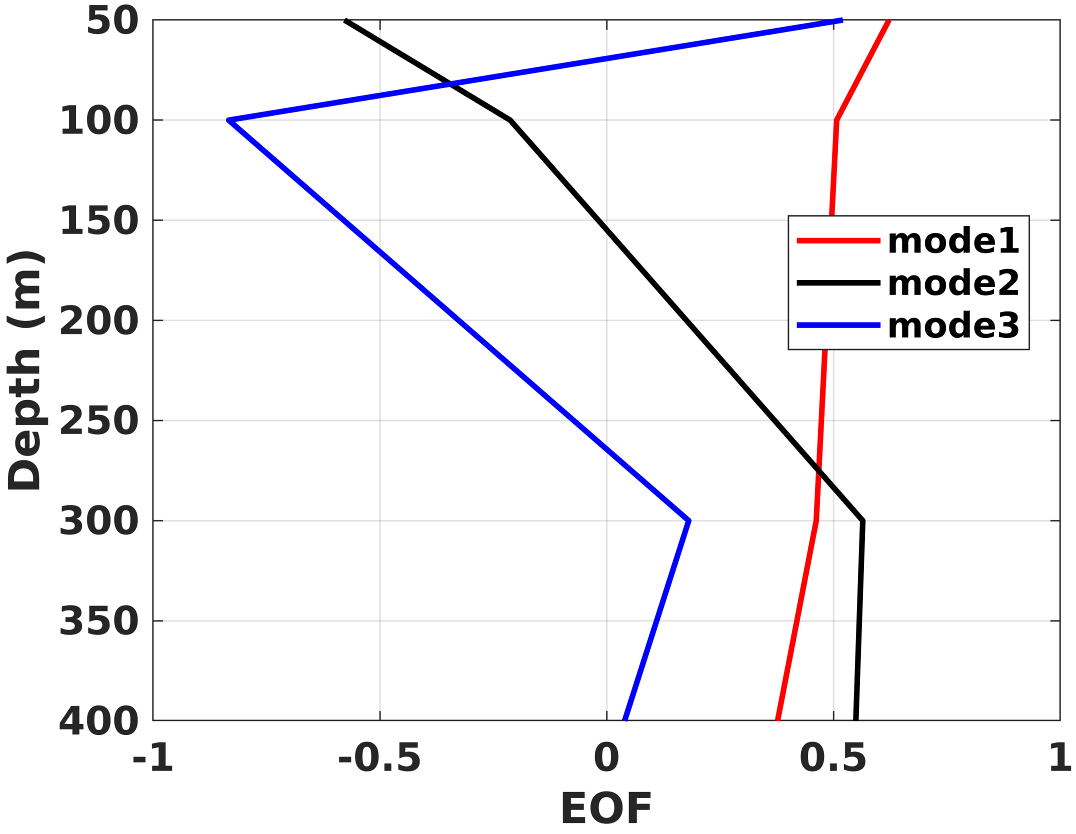

Figure 62: First three Empirical Orthogonal Functions map of the dataset constituted by 4 time series, one per each rotor current meter, moored in the Corsica Channel. There is one moored instrument at 50 m, 100 m, 300 m and 400 m, therefore the spacial variability collapses in only one EOF value per variability mode for each of the mentioned depths

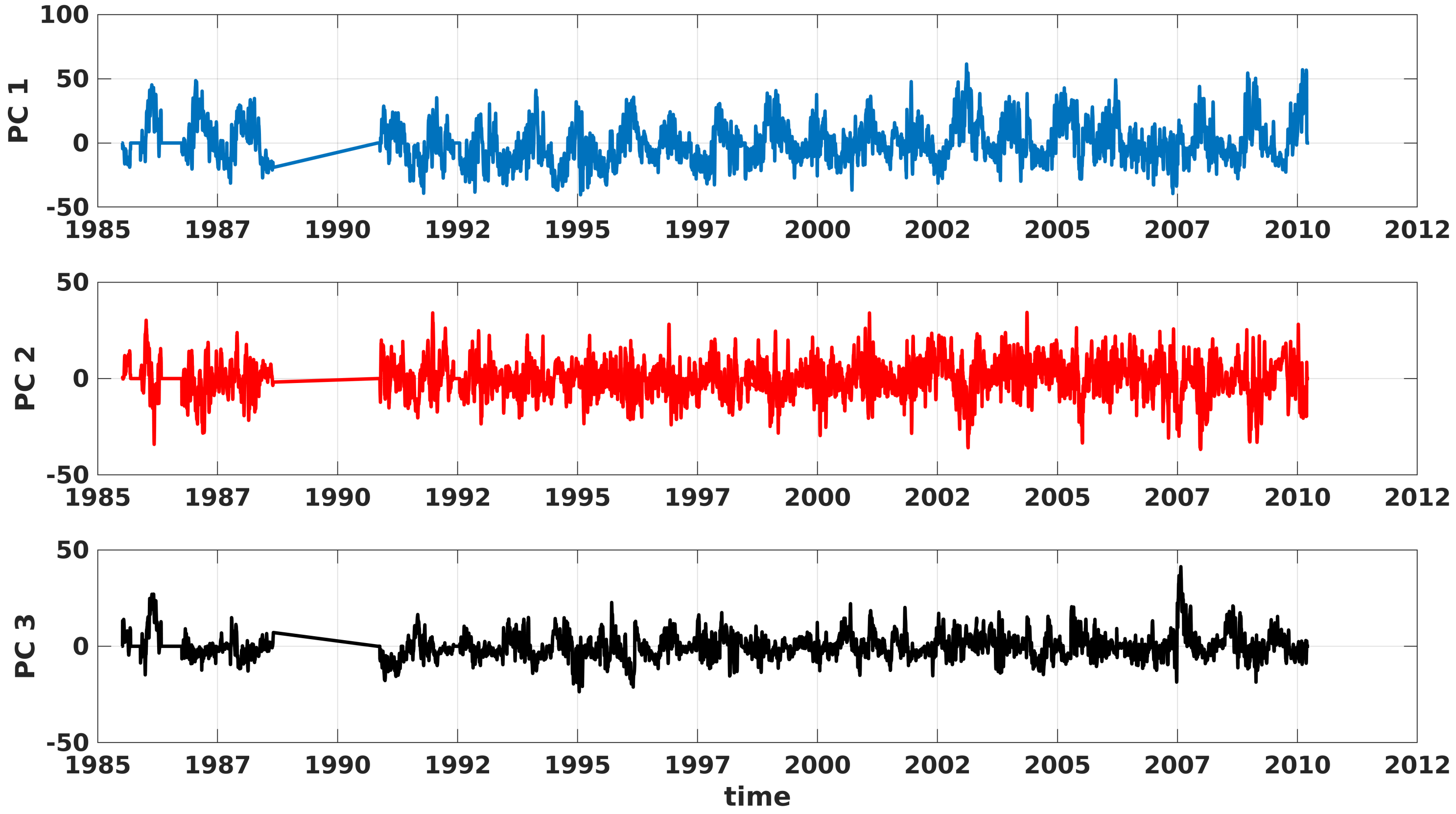

Figure 63: Principal components (PC) time series in the Corsica Channel. Each principal component represents a different mode. PC 1 is the time series of the first (dominant) mode of variability

6 Absolute Geostrophic Velocities in the Ligurian Sea Estimated via Inverse Box Modelling

6.1 Introduction

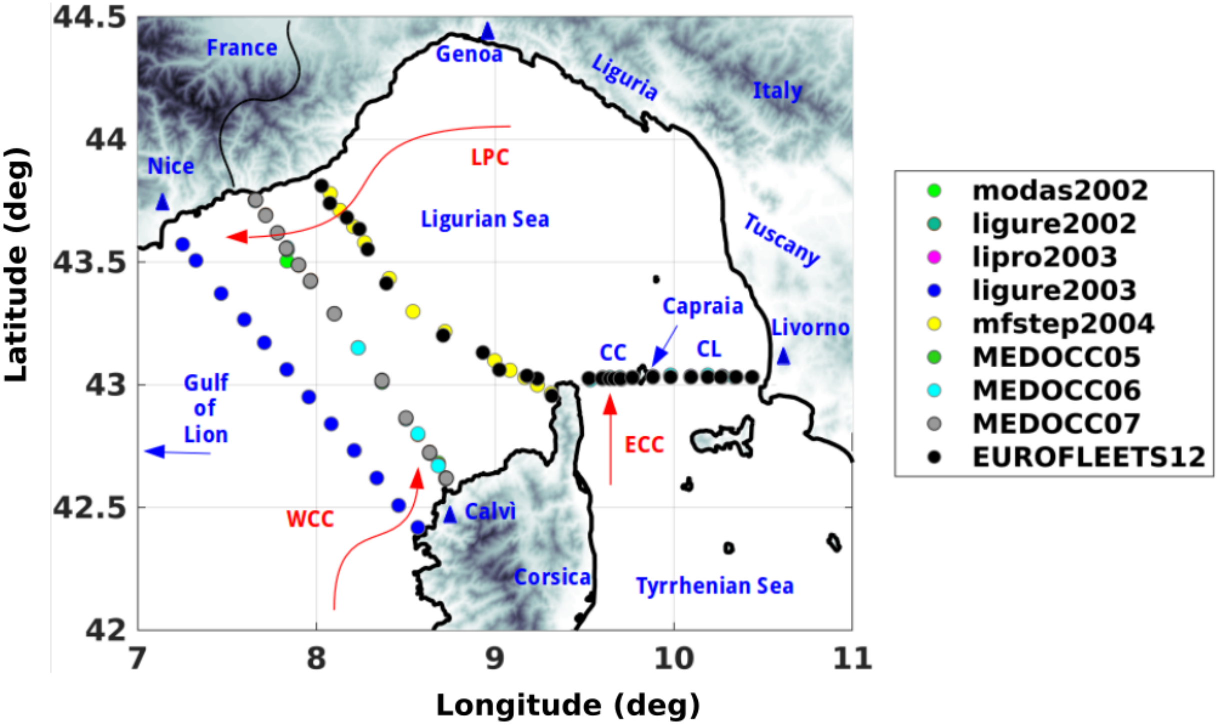

Figure 64: Map of the Ligurian Sea. Geographical places are labelled in blue. Liguria and Tuscany are Italian regions. Blue triangles indicate cities. The currents represented in red are the Eastern Corsica Current (ECC), the Liguro-Provençal Current (LPC) and the Western Corsica Current (WCC). The legend represents the name of all the oceanographic cruises considered in this study

The Ligurian Sea is situated in the north Western Mediterranean Sea. It connects the Tyrrhenian Sea with the Liguro-Provençal basin, which extends west of the LS, beyond the map boundaries in Figure 64. The LS is bordered to the north-west by the French coast, to the north by the Italian coast, in Liguria and to the east by Tuscany's shore. Liguria and Tuscany are Italian regions. The southern limb of the LS is marked by the Capraia Channel, Corsica Channel and the Corsica Island. The west Ligurian Sea boundary can be identified with an imaginary line drawn from Calví in Corsica to Nice.

Three major currents regulate the LS circulation: the Eastern Corsica Current, the Western Corsica Current and Liguro-Provençal Current. The ECC flows across the CC, mainly northwards. Very little is known about the hydrodynamics in the CL, and one of the aim of this study is to investigate its contribution in the LS circulation. The WCC flows northwards along the western Corsican shore. The three currents merge in the oriental LS. The LPC fed by the ECC and WCC flows westwards along the Ligurian and French coast, eventually finding its way to the Balearic Islands (Manzella, 1985).

The Gulf of Lion, together with the LS is one of the world's most active deep water formation places, (Marshall and Schott, 1999), (MEDOC-Group, 1970). These sites play a key role in the ventilation of the deep Mediterranean layers, impacting the abyssal marine life and diversity, The deep waters constitute the principal contribution to the Mediterranean outflow in the Atlantic Ocean, therefore an accurate water budget estimation and comprehension of the circulation are potentially contributing to the understanding of the Mediterranean outflow and its contribution to the world ocean.

This study aims to estimate the transport of the three main water masses of the western Mediterranean Sea: AW, LIW and WMDW, using DIABOX Inverse Box Model (IBM) (Jullion et al., 2014). When present, the nWMDW (Smith et al., 2008) temporal evolution is also quantified.

Cross sections of CC and CL are shown in Figure 65, for salinity and Figure 66, for temperature. Similarly NC cross sections showing salinity and temperature are represented in figures 67 and 68. Data represented in the sections have been collected during MEDOCC06 cruise, which took place in June 2006. In the CC is evident an increase in salinity with increasing depth at 180 m indicating the presence of LIW. In the CL the only water mass present is AW. The NC salinity cross section highlights the doming shape of the distribution of salinity, typical of the cyclonic circulation that characterise the central LS circulation. At approximately 500 m depth a sharp salinity maximum can be noticed, it marks the LIW core position. The temperature distribution in the NC section, apart from resembling the salinity pattern, evidences an increase in temperature below, roughly, 1800 m depth, an indication of the presence of nWMDW (Schroeder et al., 2010).

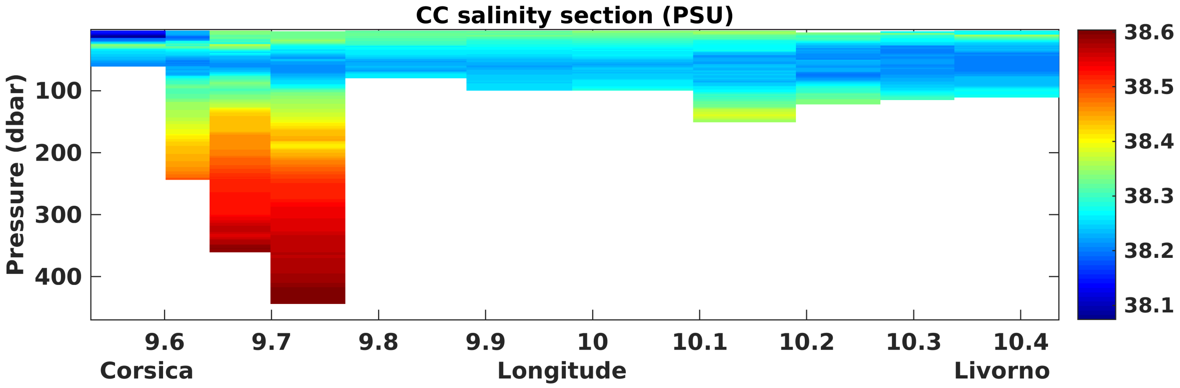

Figure 65: Corsica Channel vertical salinity section. The CTD data used to produce the plot come form MEDOCC06 oceanographic cruise, which took place in June 2016 in the western Mediterranean

Considering the CTD data available for during this study, the temporal window considered goes from 2002 to 2012, it is therefore possible to study the evolution in

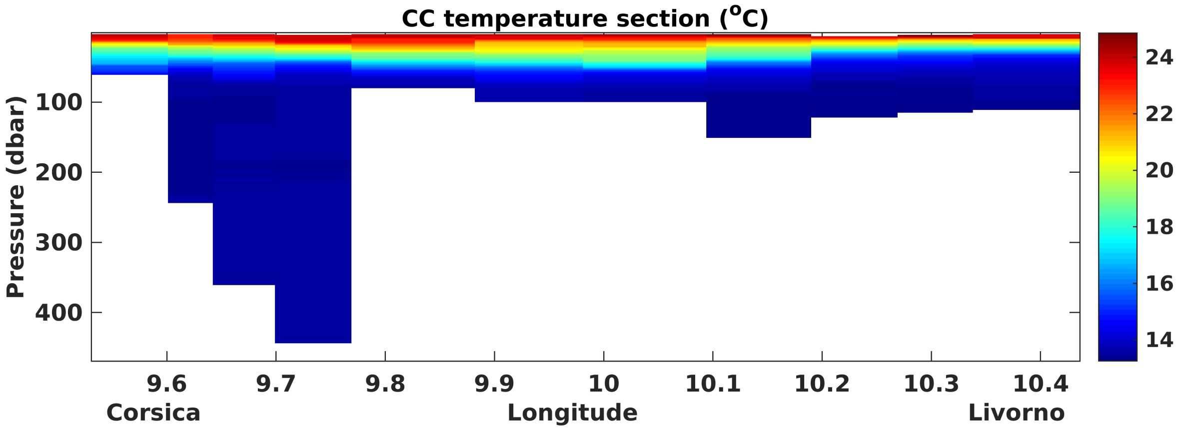

Figure 66: Corsica Channel vertical temperature section. The CTD data used to produce the plot come form MEDOCC06 oceanographic cruise, which took place in June 2016 in the western Mediterranean

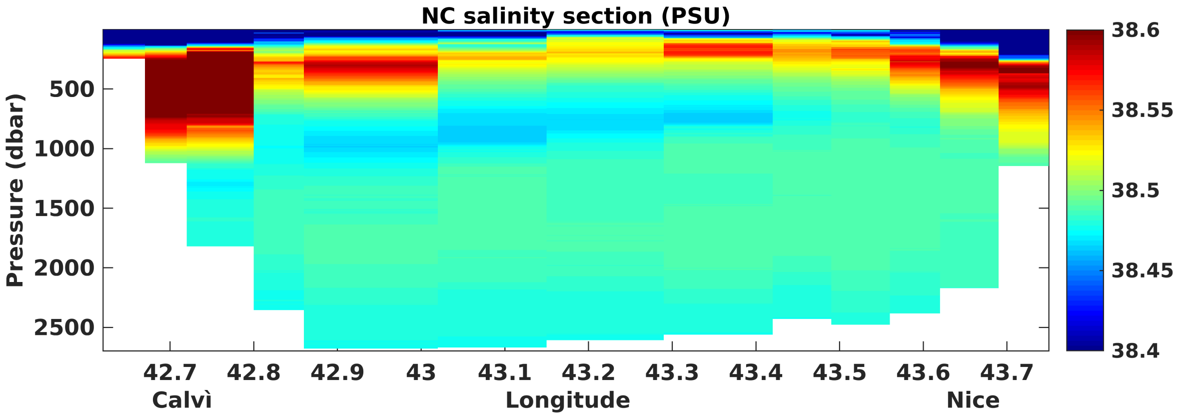

Figure 67: Nice-Calví vertical salinity section. The CTD data used to produce the plot come form MEDOCC06 oceanographic cruise, which took place in June 2016 in the western Mediterranean

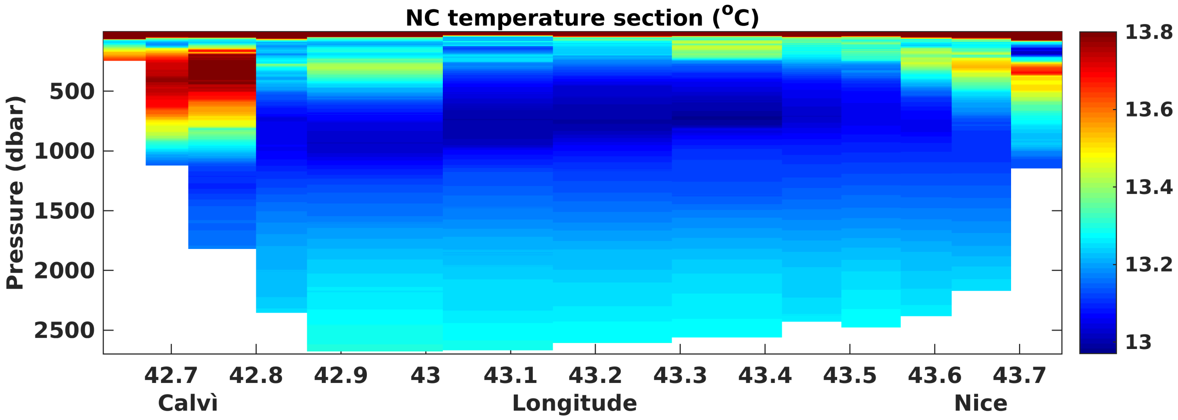

Figure 68: Nice-Calví vertical temperature section. The CTD data used to produce the plot come form MEDOCC06 oceanographic cruise, which took place in June 2016 in the western Mediterranean

time of different water masses budgets. To the best of our knowledge this is the only

IBM study dedicated to the LS and its temporal evolution: none of the previous IBM applications regarded repeated transects for such a long period of time.

Previous studies gave an indication of the water transport in the LS. The main findings are summarized in table 14.

The data collected during 9 oceanographic cruises and the IBM used for this study are thoroughly described in section 6.2 and 6.3. Results and conclusion are discussed in section 6.4 and 6.5 respectively.

layer	ECC (Sv)	WCC (Sv)	LPC (Sv)	author	method
0 - 200 (m)	0.65	0.55	-1.2	(Le Floch, 1963)	geostrophy
200 - 1000 (m)	0.33	0.13	-0.49		
1000(m) - bottom	-	-0.11	+0.06		
0 - 200 (m)	0.7	0.7	-1.4	(Bethoux et al., 1982)	geostrophy
200 - 800 (m)	0.2	0.4	-0.2		
0 - 200 (m)	0.68	-	-	(Manzella, 1985) including CL	direct velocity measurements
> 200 m	0.11	-	-		
AW	0.5-0.43	-	-	(Astraldi and Gasparini, 1992)	direct velocity measurements
LIW	0.15-0.11	-	-		
total	0.71	1.15-1.13	-		
AW	1.05	0.3	-1.29	(Schroeder et al., 2008b)	IBM
LIW	0.35	0.56	-0.86		
WMDW	-	0.2	-0.2		
AW	0.78	-	-	(Vetrano et al., 2010)	IBM
LIW	0.1	-	-		

Table 14: Historical estimates of water transport in the LS. Le Floch observed a flow exiting the LS in the deep layer of the WCC and an entering one in the LPC deep layer (negative sign). The last column indicates the method used for the estimation of the transport. Negative sign means a flow exiting the box, westward in the LPC

6.2 Data and Methods

The Inverse Box Method is a technique to estimate mainly the barotropic component of geostrophic velocity using traditional conservation equations together with hydrographic observations. Embedding real data in the evaluation method was, in the '70s when Wunch formalised the IBM, the innovative aspect. The IBM respects the conservation principle that every inflow in a closed volume of the ocean corresponds to an outflow. This principle applies to mass and to any other property that is conserved together with mass, such as salinity, temperature, silicate, etc... The IBM assumes that the observations embedded within a single inversions are synoptic, i.e. the temporal variability is negligible over the period of the data collection. In the present study feature 9 different inversions, most of which encompasses data collected in summer. Therefore the study results give a picture of the summer months absolute geostrophic circulation in the Ligurian Sea and its interannual variability over, 10 years, period covered by the 9 cruises data gathered here. The Nice-Calví hydrographic transect might differ slightly from one cruise to another. The present investigation assumes that the main circulation differences, especially the mass budget differences, across the NC transect are negligible.

The LS can be closed by two historical hydrographic sections: the CC transect and the NC transect. The CC transect goes from Corsica Island to Capraia Island. During some cruises the section has been extended from Capraia to Livorno. The NC transect links Calví in Corsica Island with Nice in the French south coast (Figure 64). During 9 cruises from 2002 to 2012 both CC and NC transects have been performed. The CL section is present in 7 of the considered sampling campaigns (table 15).

Cruise	Month	Year	NC stations	CC stations	CL stations
MODAS2002	Jun	2002	14	5	7
LIGURE2002	Oct	2002	14	5	7
LIPRO2003	May	2003	11	5	7
LIGURE2003	Sep	2003	12	5	4
MFSTEP2004	Sep	2004	12	5	na
MEDOCC05	Apr	2005	14	3	7
MEDOCC06	Jun	2006	14	5	7
MEDOCC07	Oct	2007	11	5	na
EUROFLEETS12	Nov	2012	12	6	7

Table 15: Data Table. Oceanographic campaigns are listed in chronological order

In this study the hydrographic data, belonging to 204 CTD stations, collected during the mentioned oceanographic campaigns have been used to estimate the absolute geostrophic transport across the LS. The CTD profiles, example in Figure 69, have been processed following British Oceanographic Data Centre (BODC) standards and then they have been quality checked and de-spiked following the guidelines given by UNESCO (2010).

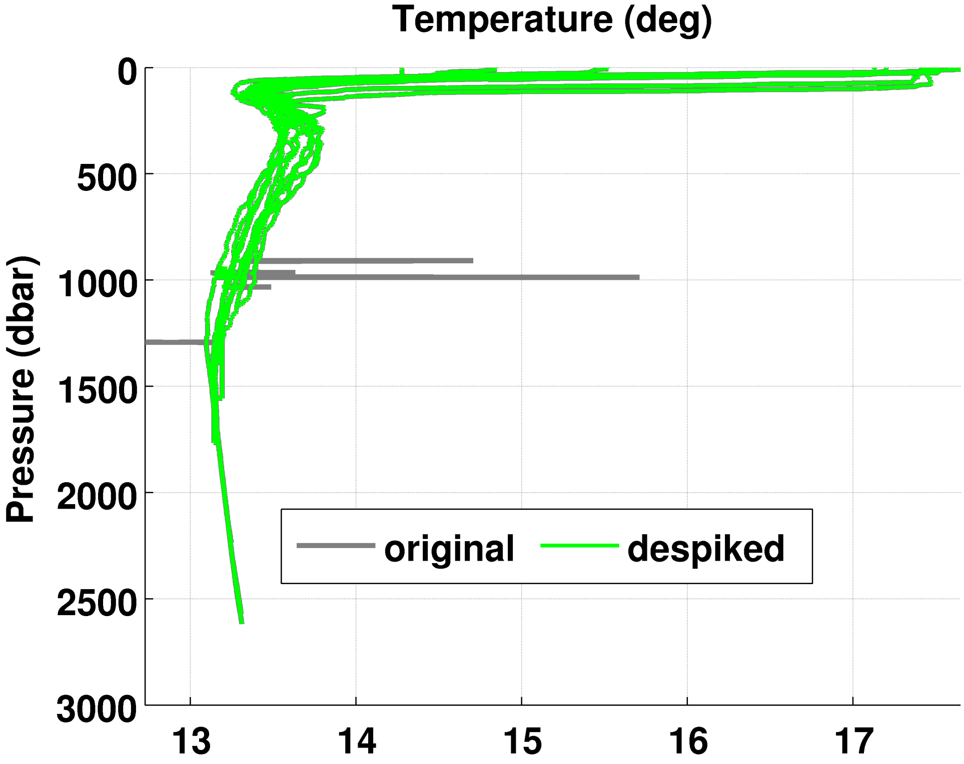

Figure 69: Temperature de-spike example from the EUROFLEET12 NC transect

The more information can be given to the IBM prior the inversion, the better the user knowledge of the circulation can be reflected and reproduced by DIABOX. The considerable amount of data presented and analysed in this work offer to constrain both transects closing the LS. Therefore the IBM application hereby explained includes the current data collected at the CC mooring position by four RCM at 50, 100, 300 and 400 meters, see Chapter 5. In the Nice-Calví section the current speed information has been deduced by free floating devices called MERMAIDs, see chapter 3. One of the limitation of DIABOX, the IBM that has been used, is: ' [...] the inability to specify several reference levels for a given box [...]' (Jullion et al., 2017). The solution that works around this limitation, but keeps into account the available data consists in maintaining the reference level at the Deepest Common Level (DCL) in the entire box, changing the reference velocity in the CC and adding the speed information as an extra constraint in the northern part of the NC section just before the inversion. A graphical explanation of the rationale behind the bottom velocity choice in the CC is represented in Figure 70, where CTD stations are vertical gray lines. Mid-latitude at each station pair is represented by a vertical blue line. At each of the 4 stations pairs (black numbers at the top) has been assigned a DCL speed value indicated by the coloured dots. Each colour corresponds to a specific speed deduced by RCM measurements. The specific speed corresponds to the meridional component of velocity measured by the closest RCM level to the DCL for a station pair. The RCM original data are every 3 hours. The speed specified in the plot legend is the mean of the RCM data belonging to the entire month of the cruise, to take into consideration the temporal variability of the currents measured by RCMs. If the RCM data are missing for a particular cruise then the long term average has been considered. The reference level speed is then padded down along the bottom triangle at each station pair.

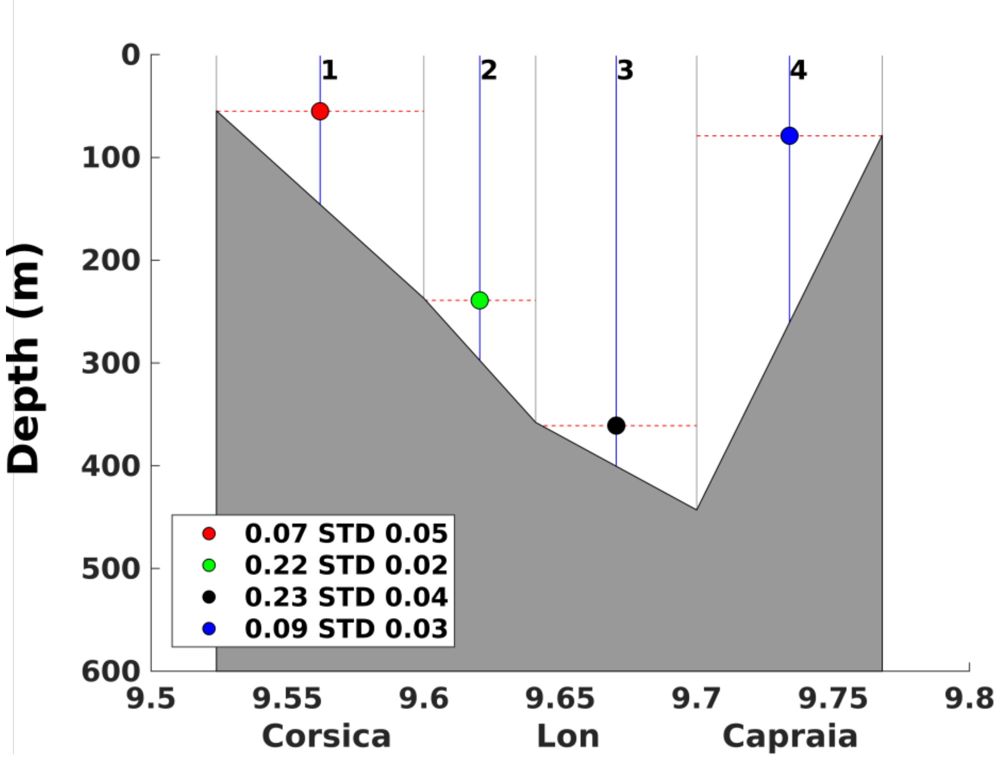

Figure 70: CTD stations are vertical gray lines. Midlatitude at each station pair is represented by a vertical blue line. At each of the 4 stations pairs (black numbers at the top) has been assigned a DCL speed value indicated by the coloured dots. Each colour corresponds to a specific speed deduced by RCM measurements. The specific speed corresponds to the meridional component of velocity measured by the closest RCM level to the DCL for a station pair

An area in the surroundings of the NC sections has been chosen, in order to select the MERMAID data points relevant for the computation of the deep (1500 m) transport across the mentioned transect, see Figure 71. Velocity data between 1400 m and 1600 m depth have been selected. The mean $\sqrt{u^2 + v^2}$ speed, to be used to calculate the transport at each station pair, has been calculated as the mean of the speed values of data points situated between the latitudes delimiting the considered station pair, see Figure 72. To calculate the water transport perpendicular at each NC transect the vector velocity has been rotated. Although for some cruises the position of the CTD stations and the inclination of the transect are very similar, this can not be assumed

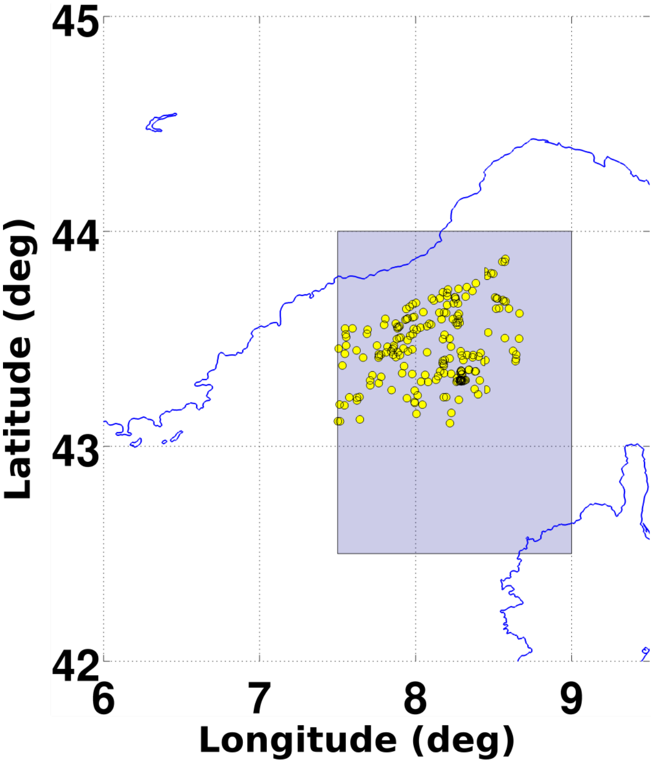

Figure 71: Selected area in the surrounding of the NC section to isolate the relevant MERMAID data points for the computation of the deep (¿1500 m) transport across the NC transect

true for all the cruises. Therefore the singular transports per CTD station pair and the direction of the perpendicular velocity vector has been computed separately for each cruise and station pair.

Another limitation of DIABOX is that the transport to be deduced from additional data, other than CTD, has to be applied to the entire model layer. In this specific case a layer for each water mass has been defined. At 1500 m depth the encountered water mass is the WMDW, layer 3 in the IBM, see Figure 73. The speed, deduced by MERMAID data, multiplied for the thickness of level 3 and for the distance between consecutive stations gives the transport of WMDW at a certain station pair as seen by MERMAID floats. Values of the transport calculated between CTD stations in the area crossed by MERMAID floats, see Figure 74 are presented for each cruise in table 16.

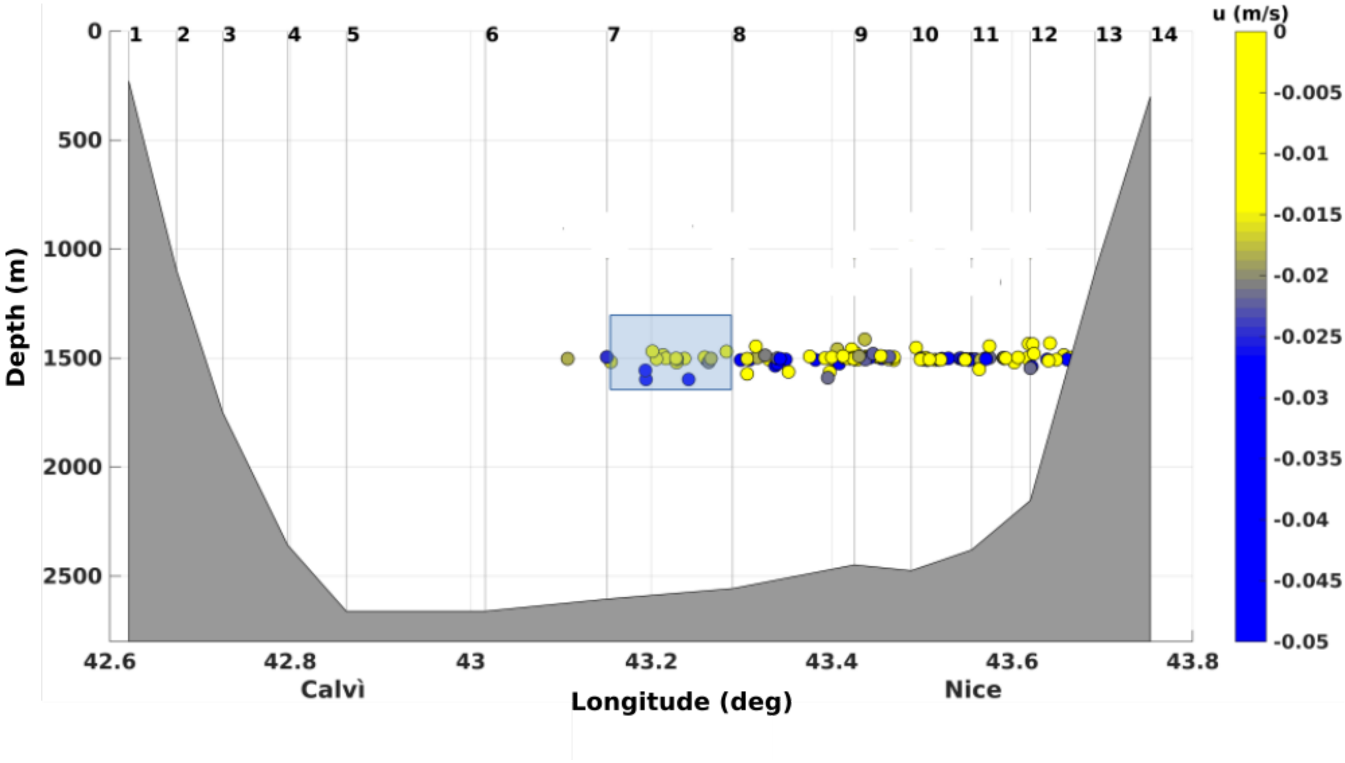

Figure 72: u component of velocity for simplicity, but during the calculation both u and v components have been considered and combined in order to evince the speed component perpendicular to a given NC transect. In this particular plot data are from cruise Ligure2002, that took place in October 2002. The mean speed, to be used to calculate the transport at each station pair, has been calculated as the mean of the speed values of data points situated between the latitudes delimiting the considered station pair

	4-5	**5-6**	**6-7**	**7-8**	**8-9**	**9-10**	**10-11**	**11-12**	**12-13**
modas2002			-0.31	-0.07	0.11	-0.05	-0.11	0.07	-0.07
ligure2002			-0.48	-0.04	0.12	-0.05	-0.05	-0.01	-0.07
lipro2003				-0.19	-0.10	-0.05	0.01		
ligure2003				-0.21	-0.11	-0.06	0.01		
mfstep2004				0.11	-0.13	-0.03	-0.16	-0.07	
MEDOCC05			-0.31	-0.08	0.10	-0.02	-0.07	-0.01	
MEDOCC06			-0.17	-0.04	0.05	-0.01	-0.04	0.00	
MEDOCC07	-0.12	0.08	-0.03	-0.05	0.01				
EUROFLEETS12			-0.05	0.01	0.01	-0.09	-0.23		

Table 16: Transport across the northern part of the NC transect in Sv deduced by MERMAID velocities. The column title indicates the station pair through which the transport has been calculated, row title indicate the cruise name. Stations are counted from south to north

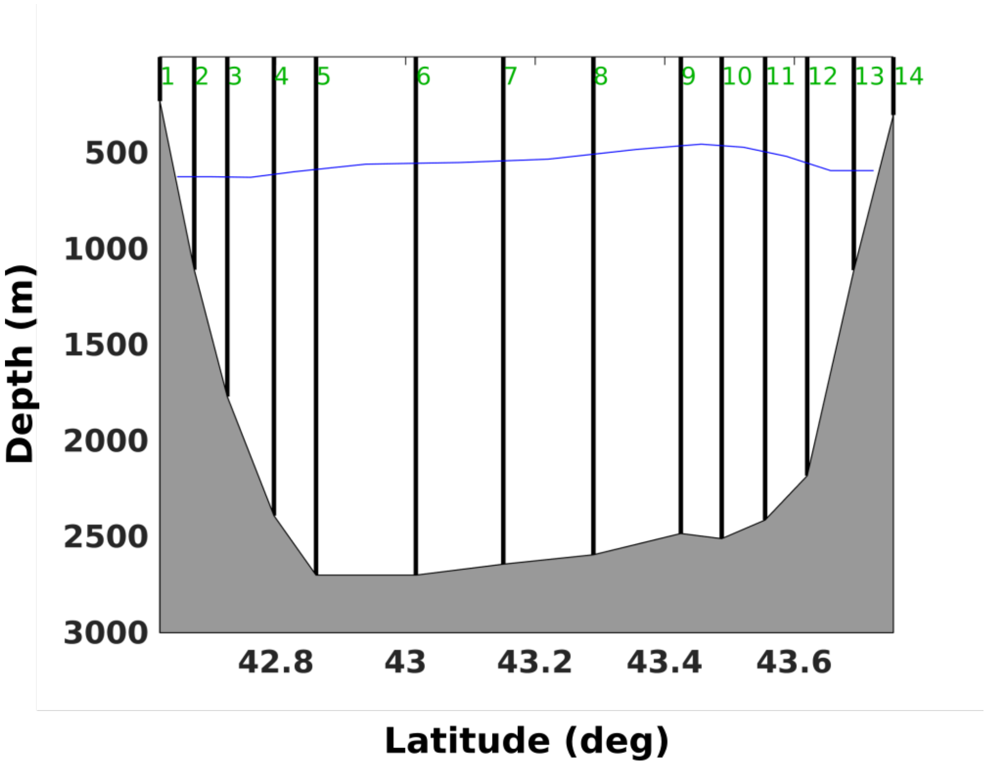

Figure 73: The thin blue line, running across the CTD stations (vertical black lines), is the interface between the LIW (layer 2) and the WMDW (layer 3). The interface is identified through density values

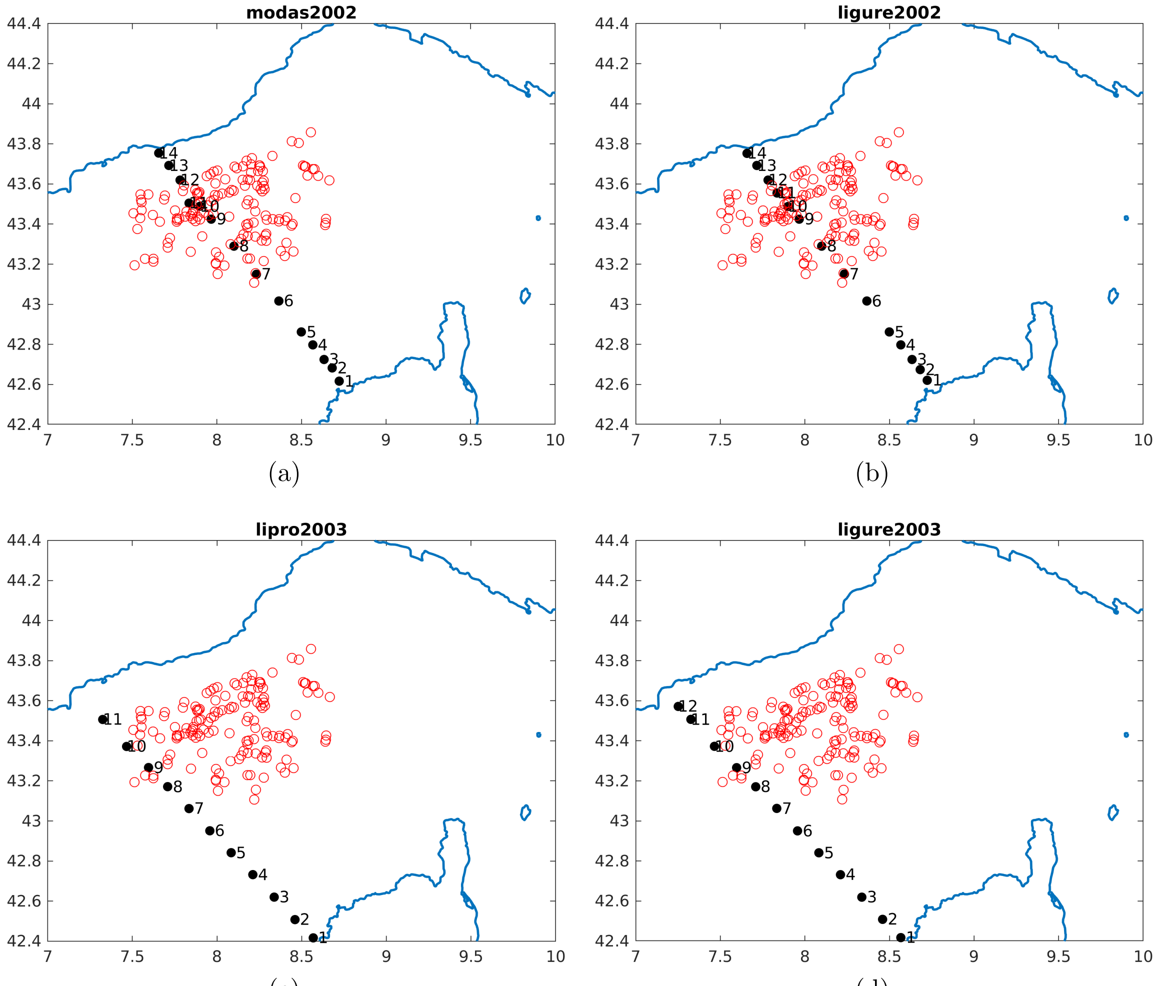

(a) (b)

(c) (d)

Figure 74: Plots represent the NC transect stations numbers and the points where MERMAIDs outcrop

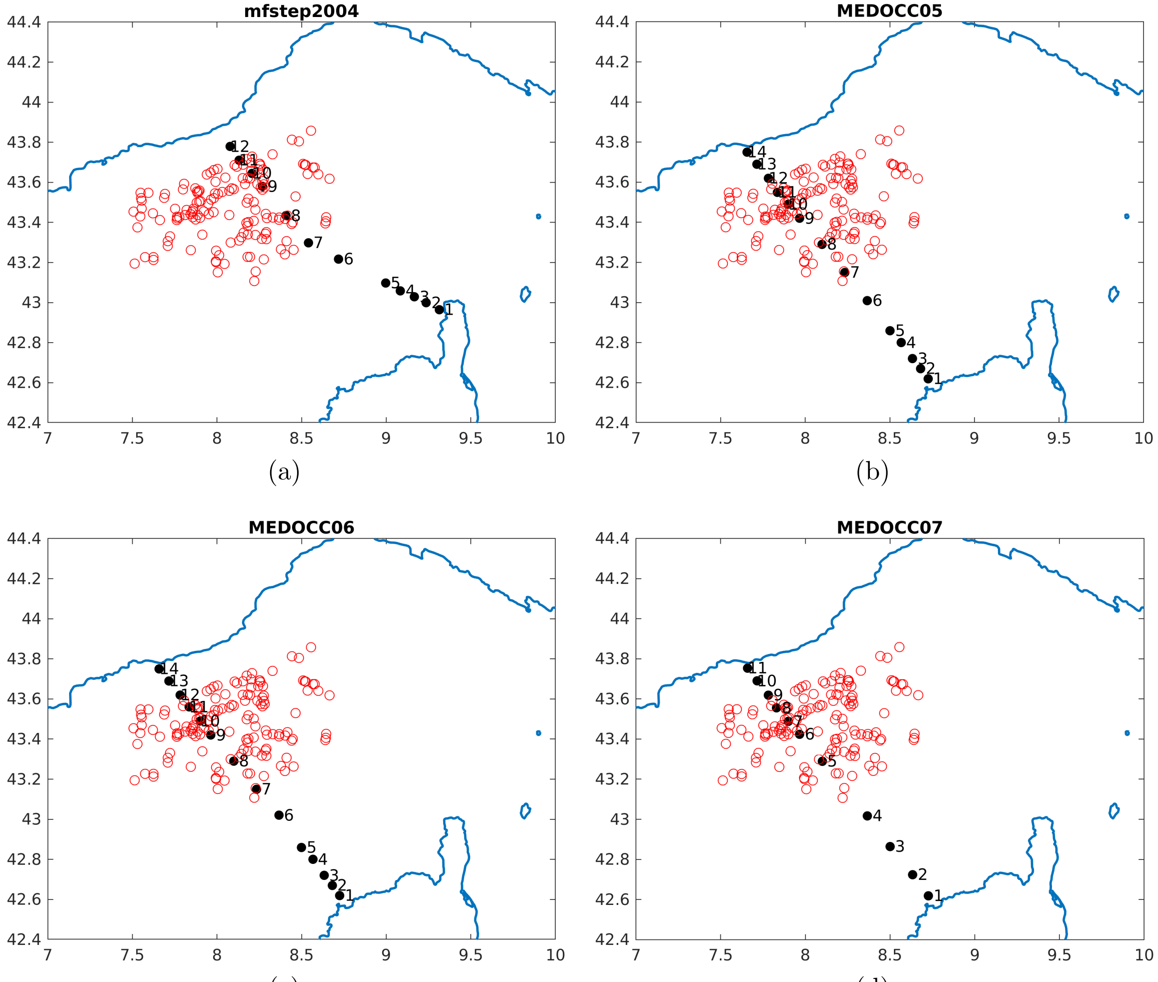

(a) (b) (c) (d)

Figure 75: Plots represent the NC transect stations numbers and the points where MERMAIDs outcrop

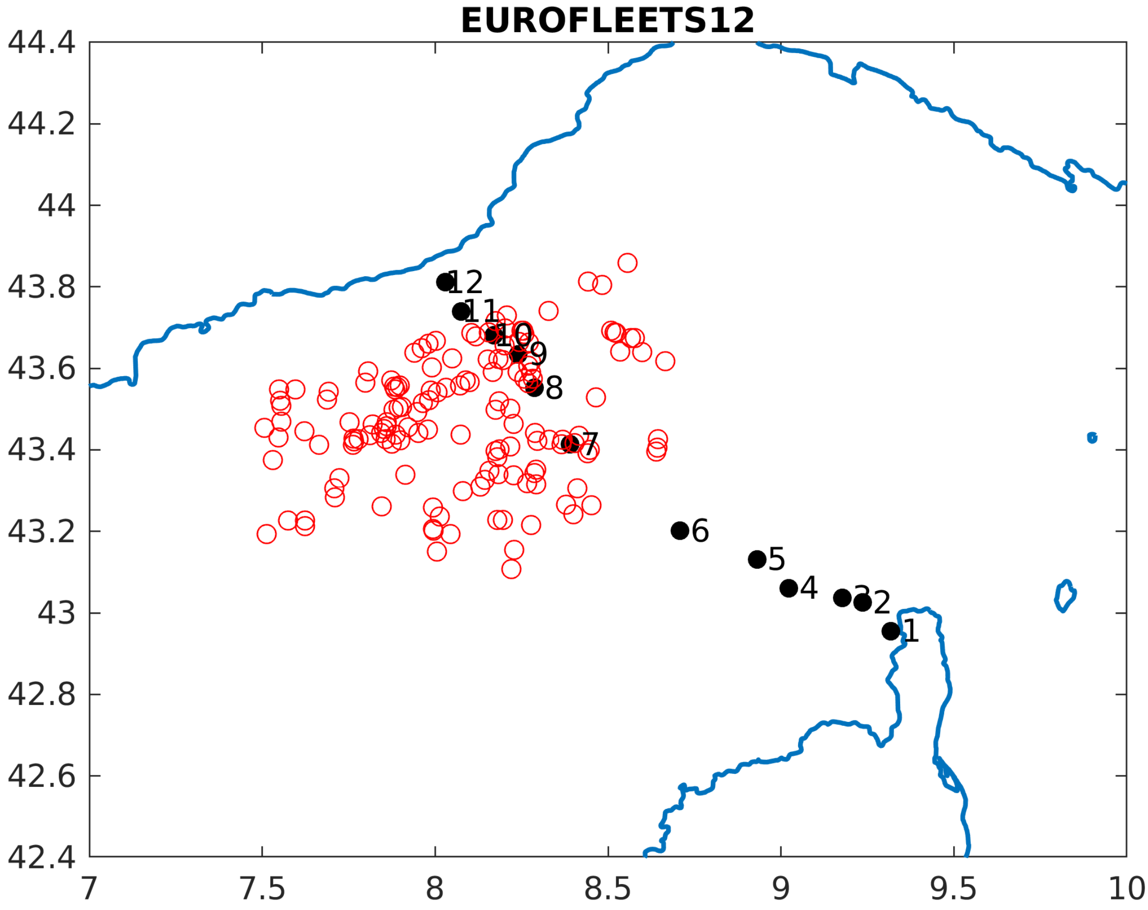

(a)

Figure 76: Plots represent the NC transect stations numbers and the points where MERMAIDs outcrop

6.3 DIABOX IBM

6.3.1 IBM Theory

Inverse box modelling, described by Wunsch (1996), is a technique to estimate the ocean circulation combining conservation equations and in-situ hydrographic observations. Several authors used IBM to estimate oceanic fluxes: Ganachaud (1999) applied it to the global ocean and in Pinot and Ganachaud (1999) the same IBM has been used in the Balearic Sea (WMED), McDonagh and King (2005) applied a DOBOX IBM to the Atlantic Ocean, Schroeder et al. (2008b) estimated with Ganachaud's IBM the circulation in the western Mediterranean Sea, Vetrano et al. (2010) used the same model to estimate the TYS spring circulation. DOBOX is a Matlab software package developed by Morgan (1994) used to perform an IBM calculation. Here a DIABOX IBM, application has been applied, it consists in a DOBOX evolution, whose development started in 2000. DIABOX, differently from DOBOX, automatise several stages, rendering easier and faster to customise the inversion.

In an IBM tracer conservation is constrained in a finite volume of the ocean (box) in order for the mass, heat and salt budgets to be solved. More precisely a system of equations needs to be solved for a set of unknowns: barotropic component of geostrophic velocities, diapycnal velocities and air-sea interaction adjustment. The core equation to bear in mind is:

$$Ax + n = b \tag{12}$$

where A is the conservation matrix containing the coefficients that multiply the unknowns; x is the unknowns vector; n is the model uncertainty vector; here b is the a priori imbalance, it encompasses available observations and the a priori solution of the system, it constitutes the reflection of our circulation knowledge.

The conservation equation for the LS application here discussed is:

$$\sum_{\jmath=1}^{m}\sum_{\imath=1}^{n}[\delta_\imath L_\imath D_{\imath\jmath}(V_{\imath\jmath}+b_\imath)\rho_{\imath\jmath}C_{\imath\jmath}] - [A\overline{\rho C\omega_c^*}^{\gamma}]_{\gamma_\jmath}^{\gamma_\jmath+1} + F_\jmath^{A-S}(C) = 0, \tag{13}$$

where n is the station pairs number; m is layers numbers; $\delta_\imath$ takes the value of +1 or -1 depending on whether the flow is directed into or out of the box; $L_\imath$ is the distance between consecutive stations; $D_{\imath\jmath}$ is the layer thickness at each station pair; $V_{\imath\jmath}$ is the baroclinic component of geostrophic velocity at the station pair i and layer j; $b_\imath$ is the barotropic velocity offset at station pair i; $\rho_{\imath\jmath}$ is *in situ* density; A is the area of the layer interface within the box; ω_C^* is the diapycnal velocity for tracer C; $F^{A-S}(C)$ is the flux of tracer C due to air-sea interactions; $\overline{(\cdot)}^{\gamma}$ indicates the area-mean over a layer interface.

Assuming geostrophy, the horizontal component of water velocity can be calculated from the thermal wind equation:

$$-f\frac{\partial(\rho v)}{\partial z} = g\frac{\partial \rho}{\partial x}, \tag{14}$$

where f is the Coriolis term ($f = \Omega * 2 * sin\varphi$, with $\Omega = 7.292e5$ [rad/sec], rotation rate of the Earth and φ, the latitude), ρ is the sea water density, z is the water depth, g is gravity acceleration, x is the distance between two stations. Equation 14 can be vertically integrated between two layers of the ocean. So, in the case of two full depth CTD stations, belonging to the same transect, the thermal wind equation could be integrated between the surface and the last depth common to both profiles, the following results:

$$\rho v(x,z) = \underbrace{-\frac{g}{f}\int_{z_0}^{z}\frac{\partial \rho}{\partial x}dz}_{baroclinic\ component} + \underbrace{\rho b(x,z_0)}_{barotropic\ component} \equiv (V+b)\rho, \tag{15}$$

where z_0 represents the reference level with respect to which the thermal wind equation has been integrated. The baroclinic component of geostrophic velocities (V) can be calculated from observations, this is the point where in situ observation are implemented in the model. Instead b, the reference level velocity, is unknown, in fact the barotropic velocity offset at each station is the main outputs of the model.

6.3.2 Model Set-up

Salt, mass and heat are constrained to be conserved. One critical and important step when setting up an IBM is the choice of density layers, which divide vertically the sections that close the examined box. The chosen layers represent the interface between water masses, here three density surfaces have been identified, hence 4 layers, one additional layer comprises all water masses and goes from the surface to the bottom of the considered section. The top to bottom layer needs to be considered as well because the IBM allows the user to add section error during the geometry definition phase. In this application the section mass error was set to be 0.3 Sv which corresponds to the mean standard deviation of the sectional transport estimated from historical values. The chosen density layers, expressed as $\sigma_0 = \rho - 1000\ Kg/m^3$, identify the major water masses found in the LS:

1 AW $\longrightarrow$ from surface to $\sigma_0 = 29.00$

2 LIW $\longrightarrow$ from $\sigma_0 = 29.00$ to $\sigma_0 = 29.10$

3 WMDW $\longrightarrow$ from $\sigma_0 = 29.10$ to $\sigma_0 = 29.11$

4 nWMDW $\longrightarrow$ from $\sigma_0 = 29.11$ to bottom

5 total layer ⟶ from surface to bottom

Figure 77 represents the TS diagrams for each cruise, on every plot the chosen density layers are represented.

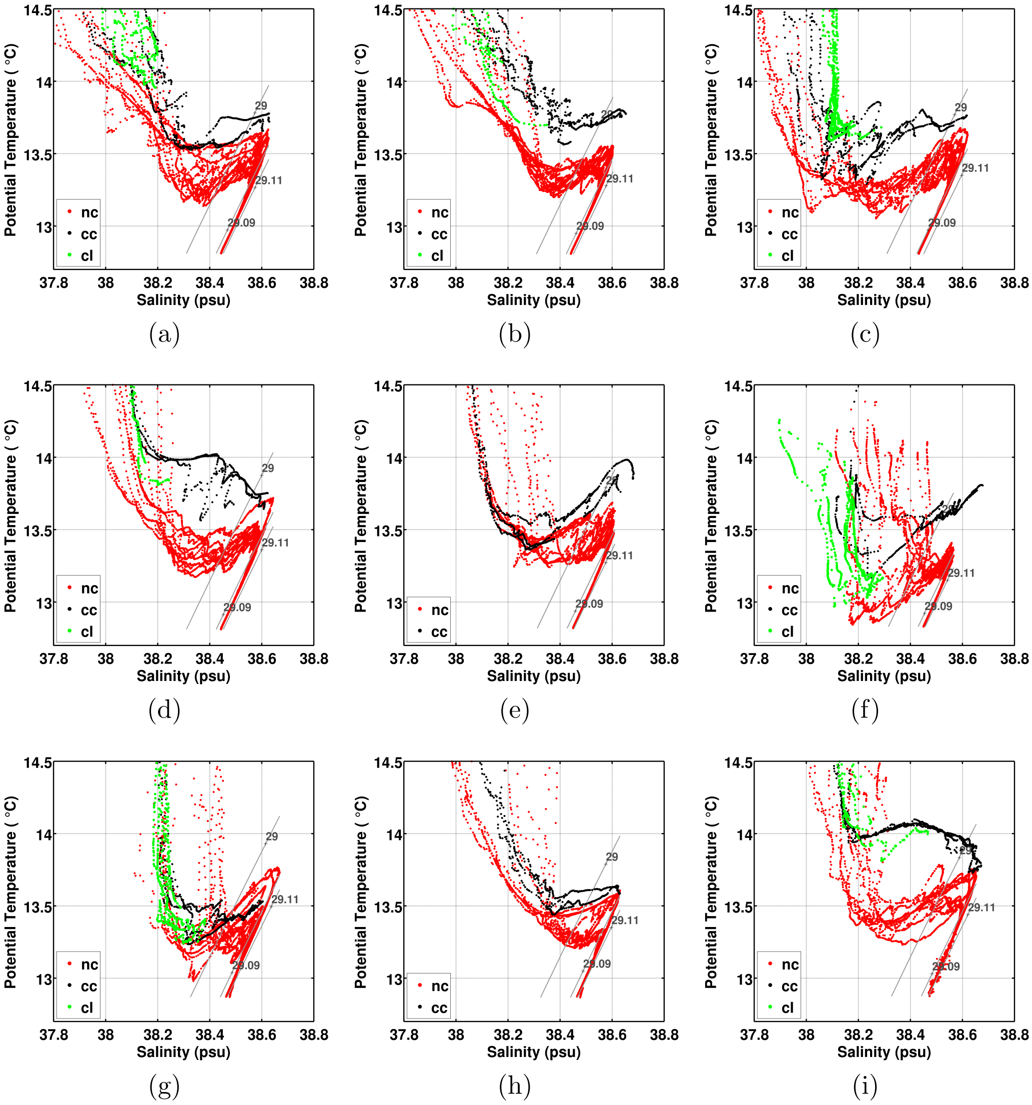

(a) (b) (c)

(d) (e) (f)

(g) (h) (i)

Figure 77: $\theta - S$ diagram. The horizontal axis represents salinity (PSU). The vertical axis represents potential temperature (deg), i.e. θ. Gray lines evidence the isopycnals (potential density) that delimit the chosen density layers. Red dots represent values in the NC section. Black dots show values in the CC section. 77a MODAS2002, 77b LIGURE2002, 77c LIPRO2003, 77d LIGURE2003, 77e MFSTEP2004, 77f MEDOCC05, 77g MEDOCC06, 77h MEDOCC07, 77i EUROFLEETS12

The system of equations, written in matrix form in equation 12, is under-determined, which means that there are more unknowns than equations. The unknowns are given by: number of geostrophic velocities (CTD station pair)+9 diapycnal velocities (3 properties * 3 interfaces)+ 2 Ekman terms (one per section) + 6 air-sea forcing (3 properties * 2 sections). For example if a cruise has in total 14 CTD station pairs, the number of unknown will be 31 but the number of equations will be 5 layers * 3 properties=15. An under-determined system has an infinite number of solutions and can be solved via different methods. Diabox solves the inversion with the Singular Value Decomposition (SVD) technique. The SVD is a tool to choose the solution that minimizes the difference between the expected value (b) and the model solution. Other techniques are thoroughly described in Wunsch (1996). SVD uses a set of row and column weights, for constraints and unknown respectively, to be applied to the solutions, in order to constrain the output to be physically reasonable. For example row weights allow a bigger error in the first row (layer), because the upper layer is subject to air-sea interaction leading to possible evaporation, meteoric water and river outflow, although small in summer, which is the season where most of the analysed cruises took place. The listed factors weaken the capability of the upper layer to conserve mass, salt and heat, for this reason this layer has the smallest weight assigned and the bigger error allowed. The column weighting has been set in a way that renders the method essentially equivalent to the Gauss-Markov statistical estimation. The column weighting is defined as the inverse of the square root of the priori solution covariance diagonal matrix : $W^c = 1/\sqrt{R_{xx}}$. Similarly the row weighting is the inverse of the square root of the diagonal model covariance matrix: $W^r = 1/\sqrt{R_{nn}}$. The a priori solution covariance matrix, R_{xx}, includes the a priori reference velocities uncertainty, that has been estimated through the CC mooring measurements in the CC section and set to default 0.01 m/s for the rest of the station pairs. R_{xx} also encompasses diapycnal mixing, heat flux, fresh water and Ekman, all calculated from the climatologies, whose details are presented later. The model covariance matrix, R_{nn}, is the diagonal matrix constituted by the uncertainties values assigned at each property in each of the four layers plus an additional layer including the top to bottom uncertainties. Heat and salt prior uncertainties are estimated as: $\overline{P} + 2\delta P * \epsilon$, where $\overline{P}$ is the average property value, δP is the property standard deviation and ϵ is the prior uncertainty in the volume conservation.

Ancillary data includes ocean climatology, atmospheric reanalysis and river run off data set, this data it is used to calculate air-sea exchanges, such as Ekman transports, heat and mass loss due to evaporation and to calculate diapycnal fluxes. The original DIABOX used, as ocean climatology, the World Ocean Hydrographic Climatology (WOCE) (Gouretski and Koltermann, 2004), which comprises data collected from 1990 to 1998 during the World Ocean Circulation Experiment (WOCE). In this work the IMEDEA (Institut Mediterrani d'Estudis Avançats) climatology has been used. It is an up to date dataset, that has been created specifically for the Mediterranean Sea. The IMEDEA climatology goes from 1950 to 2013. Atmospheric data have been taken from ERA-INTERIM reanalysis (Dee et al., 2011). River outflow data come from Dai and Trenberth Global River Flow and Continental Discharge Dataset (Dai and Trenberth, 2002). In the area selected for the ancillary data only the Arno river is taken into consideration in the eastern shore of LS.

In this application the bottom triangle velocity has been calculated at each station pair by extrapolating the reference velocity at the deepest common level where baroclinic geostrophic velocity has been calculated Figure 78 shows a graphical explanation of the bottom triangle.

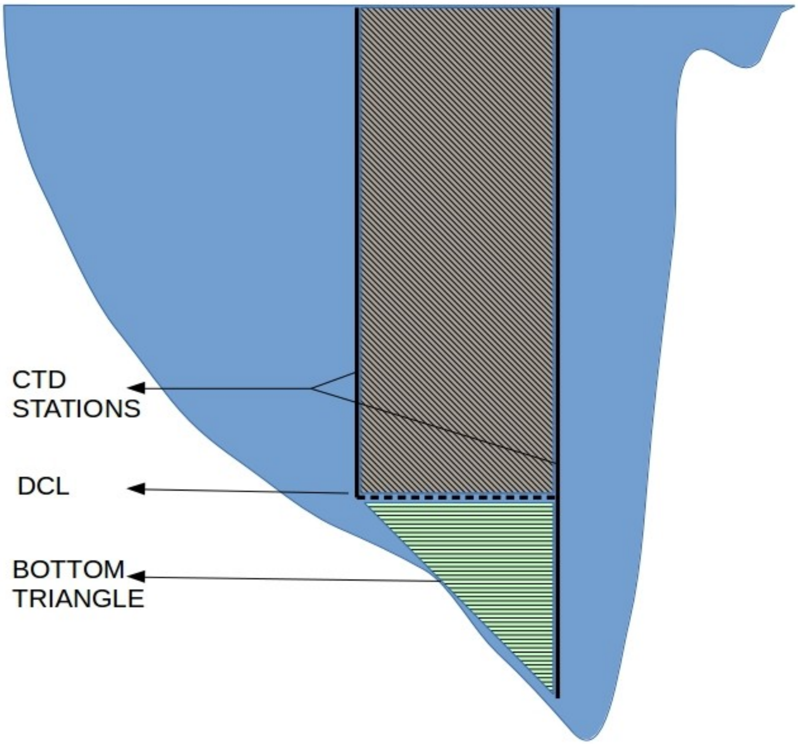

Figure 78: Bottom triangle graphical explanation

6.4 Results

After quality and format checking the data it is possible to calculate the baroclinic geostrophic velocities as previously done in Aracri et al. (2015). In Figure 79 are represented all the three sections NC, CC and CL (when present).

In MODAS2002, Figure 79a, both LPC and WCC are well defined, WCC still involves the entire water column. Both currents strongest cores reach approximately 250 m depth. CC is crossed by a northward current in the middle and southward flow at the channel's borders. In the CC the AW-LIW isopycnal is situated at approximately 300 m. CL's flow points southwards reaching 0.15 m/s speed in its shallow core, i.e. 50 m depth. The AW-LIW and LIW-WMDW interface have both a dome shape. The latter is situated around 500 m depth.

In LIGURE2002, Figure 79b, in the NC transect the doming effect over the isopycnals is attenuated, The WCC extends from 42.6 to 43.45 deg, includes a confined area

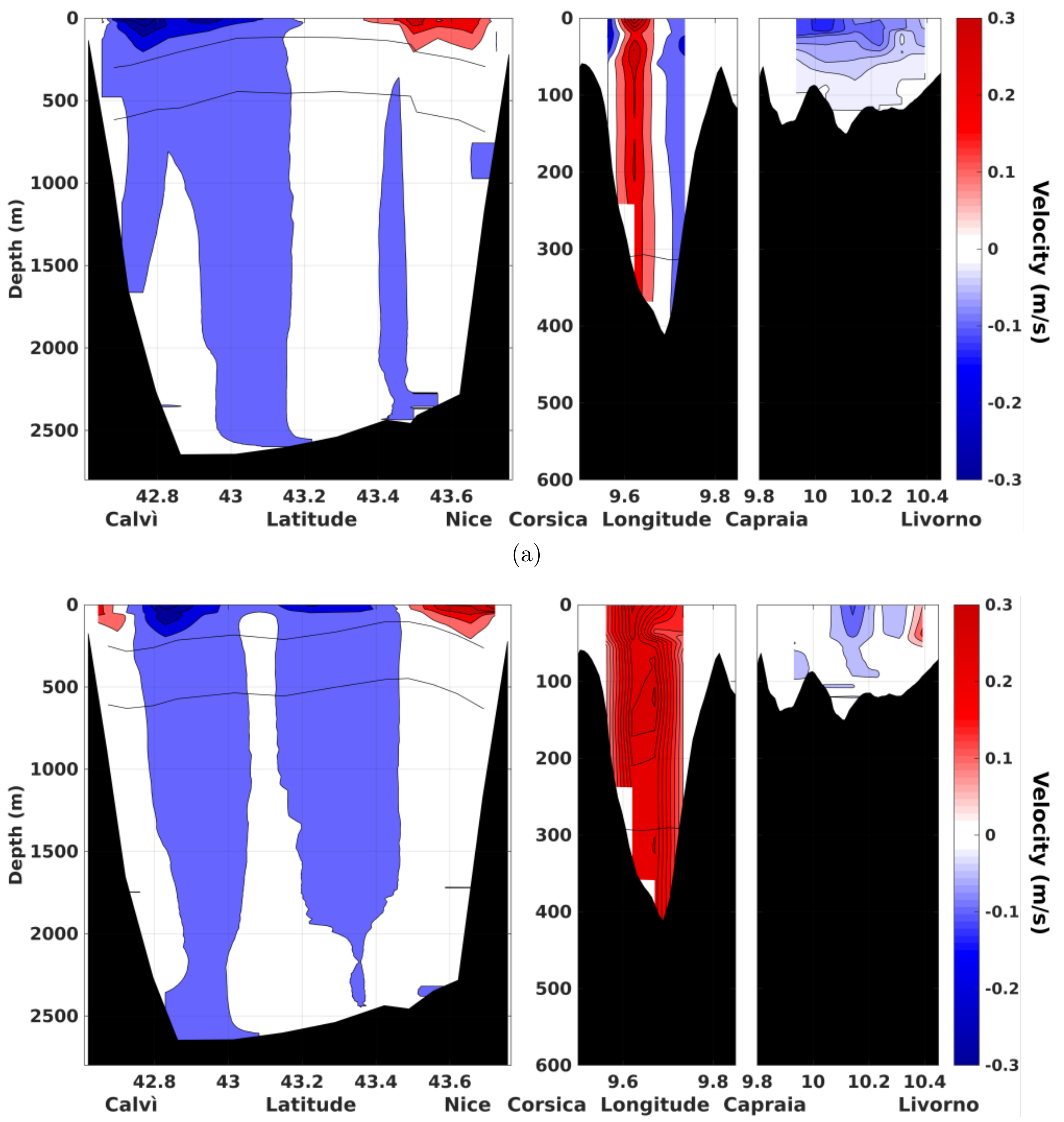

(a)

(b)

Figure 79: Baroclinic geostrophic velocities in m/s. 79a MODAS2002, 79b LIGURE2002. Thin black lines indicate the position of the chosen isopycnals to identify the position of the water masses' interfaces

interested by a westward flow and spreads across most of the transect. the LPC is confined in a narrow latitude band between 43.45 and 43.65 deg. A southward flow crosses most of the CL, exception made for a small northward flow on the oriental edge of the CL. The ECC in the CC is strong and directed northward. The AW-LIW is situated at 300 m.

In LIPRO2003, Figure 80a shows very weak southward currents in the CL and A strong northward flow crossing the CC. Both WCC and LPC reach 350 m.

In LIGURE2003, Figure 80b, almost all CL flow points outside the box, whilst a

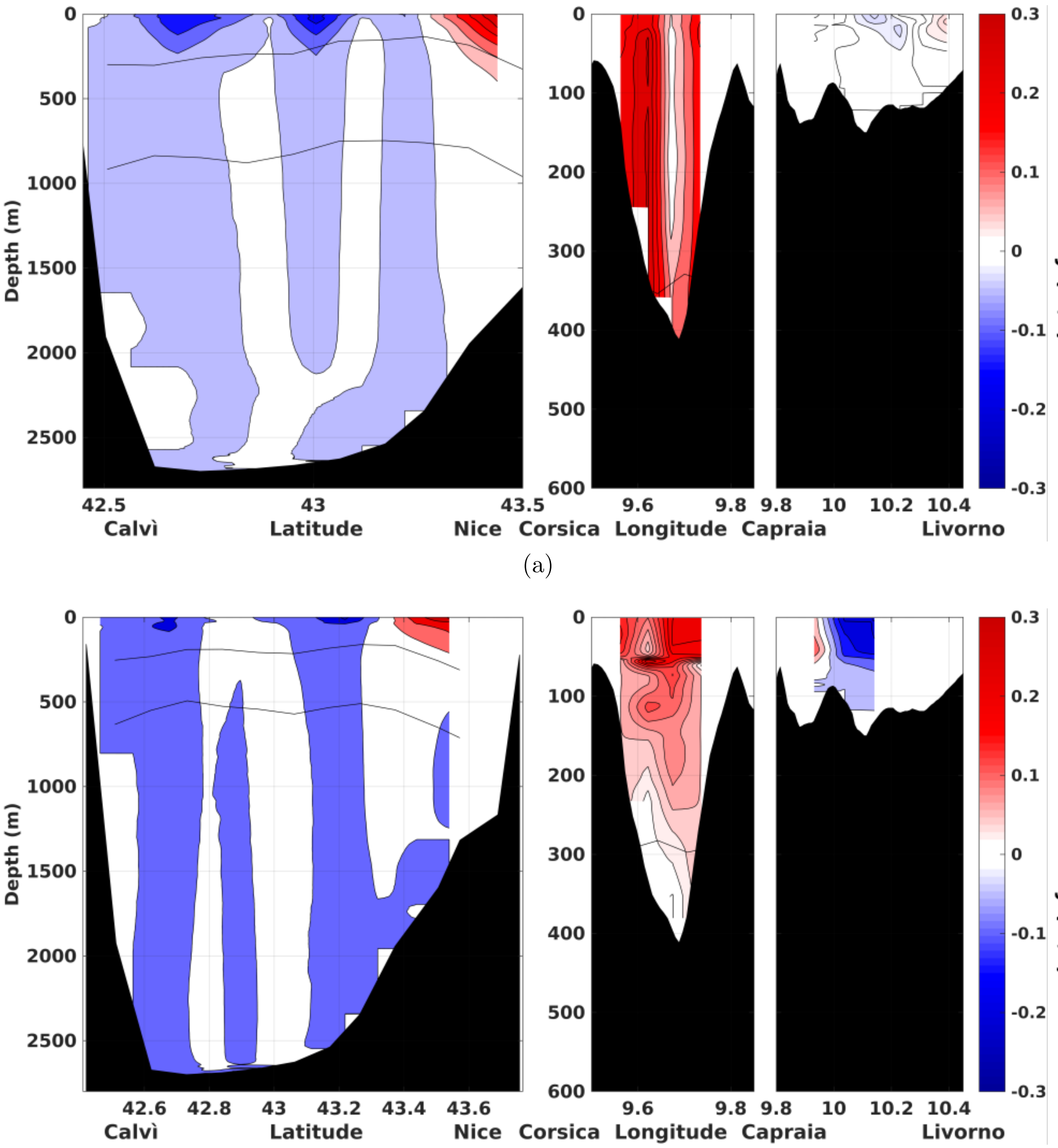

(a)

(b)

Figure 80: Baroclinic geostrophic velocities in m/s. 80a LIPRO2003, 80b LIGURE2003. Thin black lines indicate the position of the chosen isopycnals to identify the position of the water masses' interfaces

much stronger northward flow, up to 2 m/s characterise the ECC in the CC where the AW-LIW interface is detected at 290 m. The WCC looks quite widespread, reaching beyond 43.2 degrees. The LPC involves, as previously seen, mostly AW down to 250 m, where the AW-LIW interface is situated. The WMDW has been measured at 800 m depth.

In MFSTEP2004, Figure 81a, the AW-LIW looks quite shallow (150-200 m) the WCC core is concentrated between 43.05° and 43.2° in the AW layer. The LPC is also carrying mostly AW. The LIW-WMDW interface is situated around 500 m depth. The

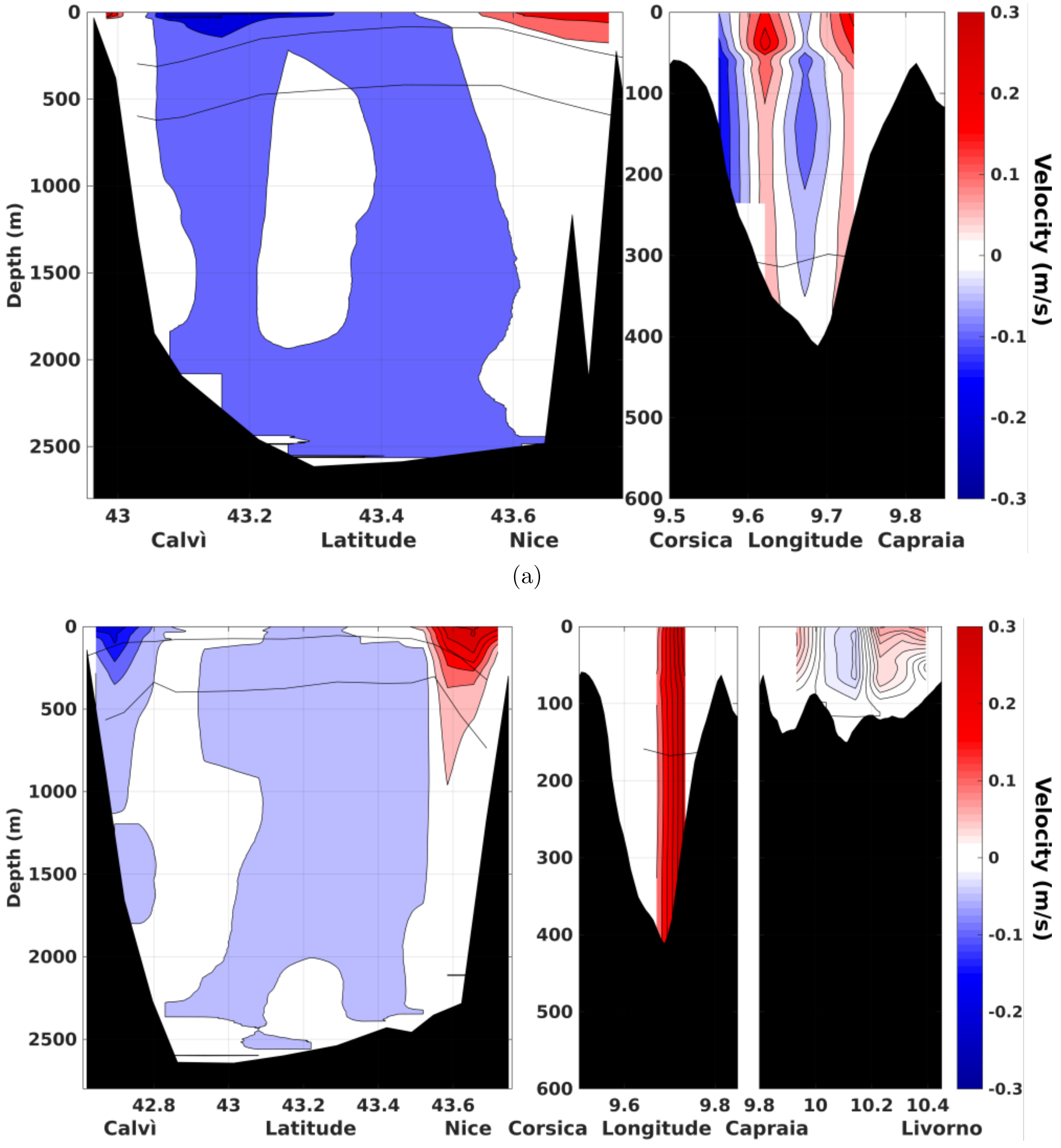

(a)

(b)

Figure 81: Baroclinic geostrophic velocities. 81a MFSTEP2004, 81b MEDOCC05. Thin black lines indicate the position of the chosen isopycnals to identify the position of the water masses' interfaces

CC presents a southward flux at 9.58 deg longitude and at 9.65 deg. It appears that in the upper layer the flow is directed mostly northwards and in the deeper layer, mostly below 50 metres, it is directed southward.

In MEDOCC05, Figure 81b, the NC transect LPC and WCC cores extend in depth to roughly 400 m and are well defined. There is a weak flow, 0.03 m/s directed westwards that extends across most of the transect. The LIW-WMDW is situated close to 400 m depth. In the CC there are only three CTD stations, in the area covered by the 2 geostrophic velocities profiles the northward flow reaches 0.3 m/s. There are weak

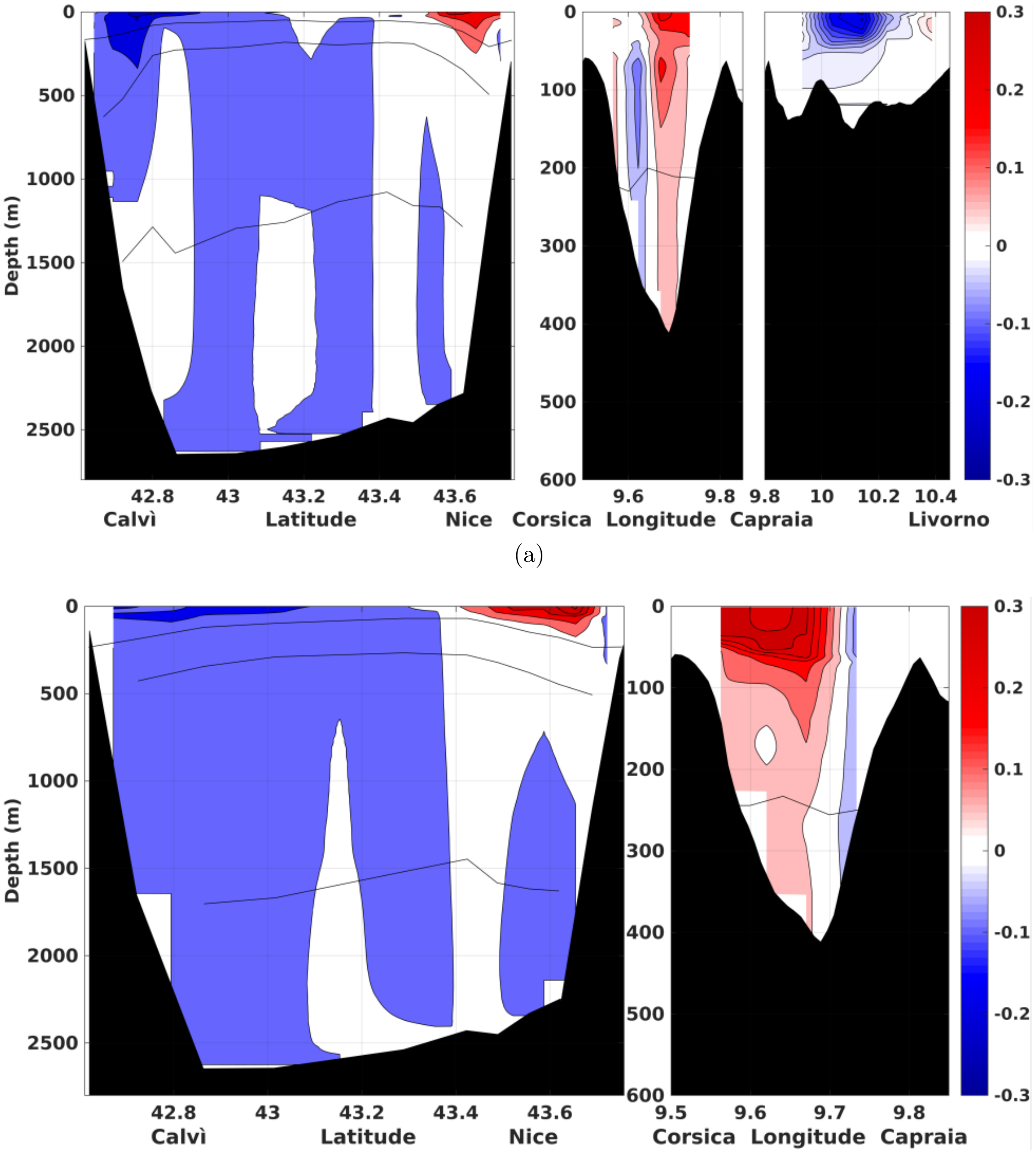

Figure 82: Baroclinic geostrophic velocities. 82a MEDOCC06, 82b MEDOCC07. Thin black lines indicate the position of the chosen isopycnals to identify the position of the water masses' interfaces

currents (in both directions) in the CL.

In MEDOCC06, Figure 82a, in summer 2006 for the first time the interface dividing WMDW from nWMDW appears between 1300-1400 m of depth as a result of the Western Mediterranean Transition (WMT), that was first described in CIESM Monographs (2009). The NC transect presents two well defined cores for WCC and LPC reaching 300 m depth. Below them a weak westward flow covers most of the transect area. There is a southward and strong, 0.2 m/s, flow across the middle of the CL. The CC flow shows a small and sub-superficial reversal close to the Corsica Island. In the CC, below

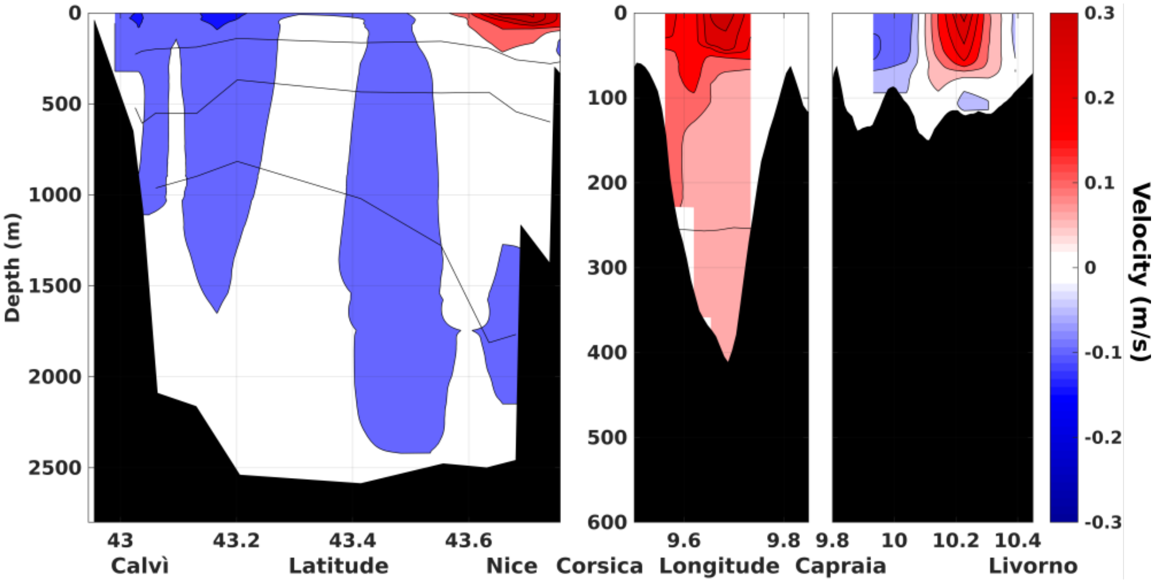

(a)

Figure 83: Baroclinic geostrophic velocities. 83a EUROFLEETS12. Thin black lines indicate the position of the chosen isopycnals to identify the position of the water masses' interfaces

200 m, the interface between AW and LIW has been found.

In MEDOCC07, Figure 82b, the WCC looks more spread out and shallow with a poorly defined core between 42.7 deg and 43.1 latitude, it reaches barely 200 metres. The nWMDW is detected again below 1500 m. The ECC presents reversals mostly at 9.75 and a strong core of northward flow, that extends from the surface down to 150 m. LIW is found in the CC below 250 m depth.

In EUROFLEETS12, Figure 83a, looking at NC section, the WMDW-nWMDW interface is much shallower than before close to Calví (800 m) and deeper close to Nice (1800 m). The WCC does not have a very well defined core whilst the LPC core involves mostly AW. There are reversals (southward currents) in the east part of CL close to Capraia Island. In the rest of the CL and across the CC the flow is directed northwards. In the CC the AW-LIW interface appears at 250 m.

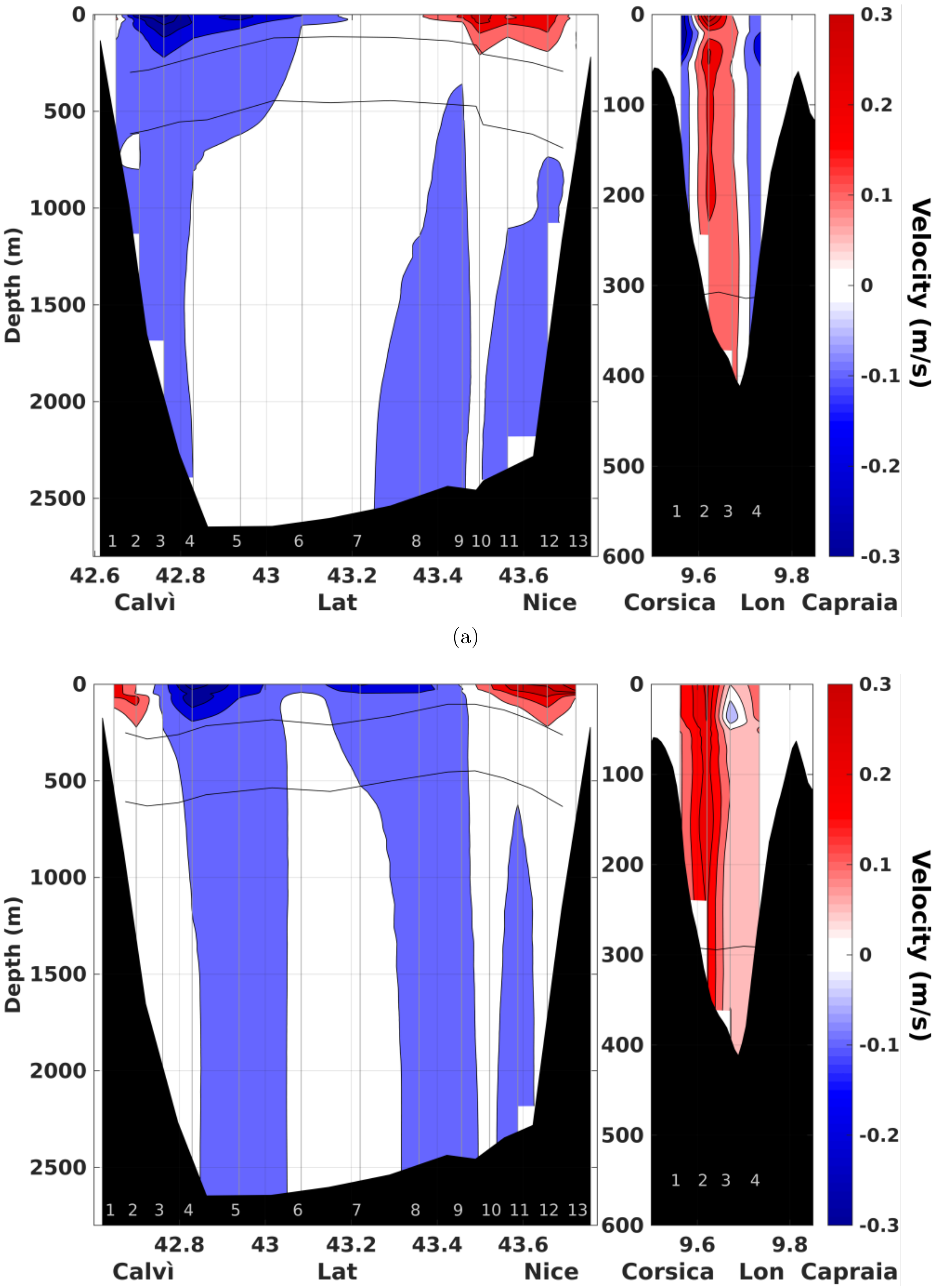

(a)

(b)

Figure 84: Absolute geostrophic velocities, here the inversion has been done without considering the CL transect. The numbers at the bottom of every plot represent the CTD stations 84a MODAS2002, 84b LIGURE2002

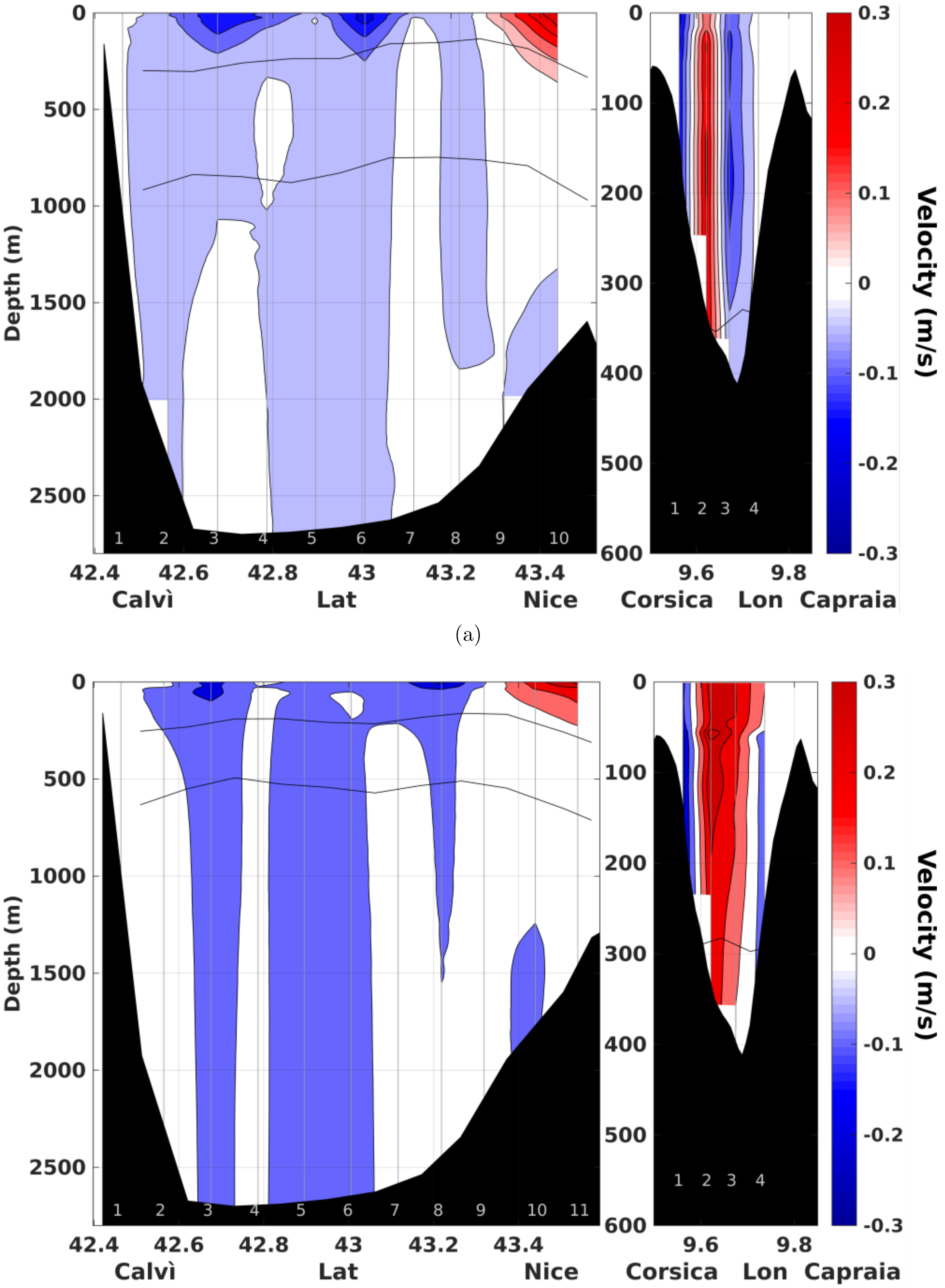

(a)

(b)

Figure 85: Absolute geostrophic velocities, here the inversion has been done without considering the CL transect. The numbers at the bottom of every plot represent the CTD stations 85a LIPRO2003, 85b LIGURE2003

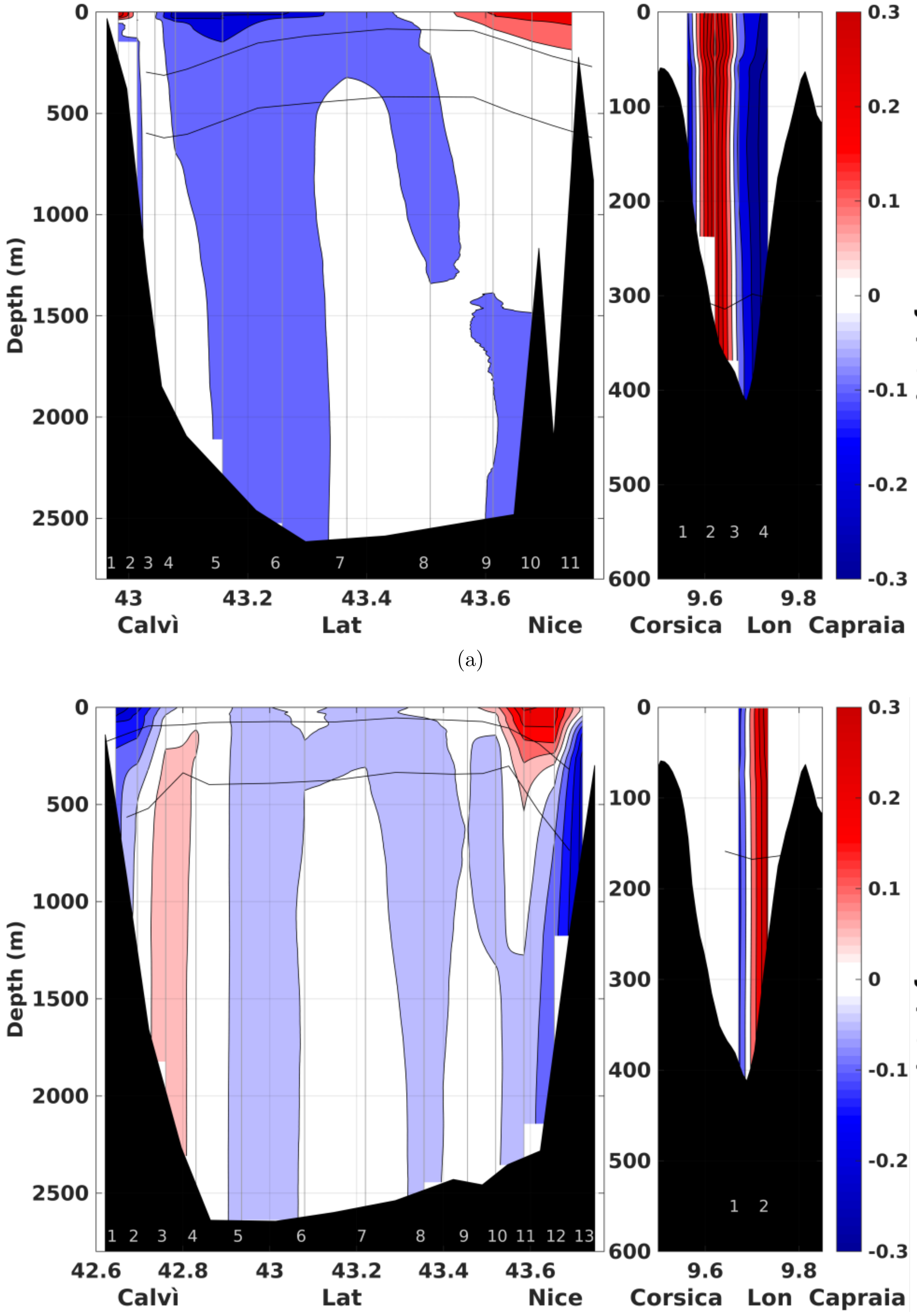

(a)

(b)

Figure 86: Absolute geostrophic velocities, here the inversion has been done without considering the CL transect. The numbers at the bottom of every plot represent the CTD stations 86a MFSTEP2004, 86b MEDOCC05

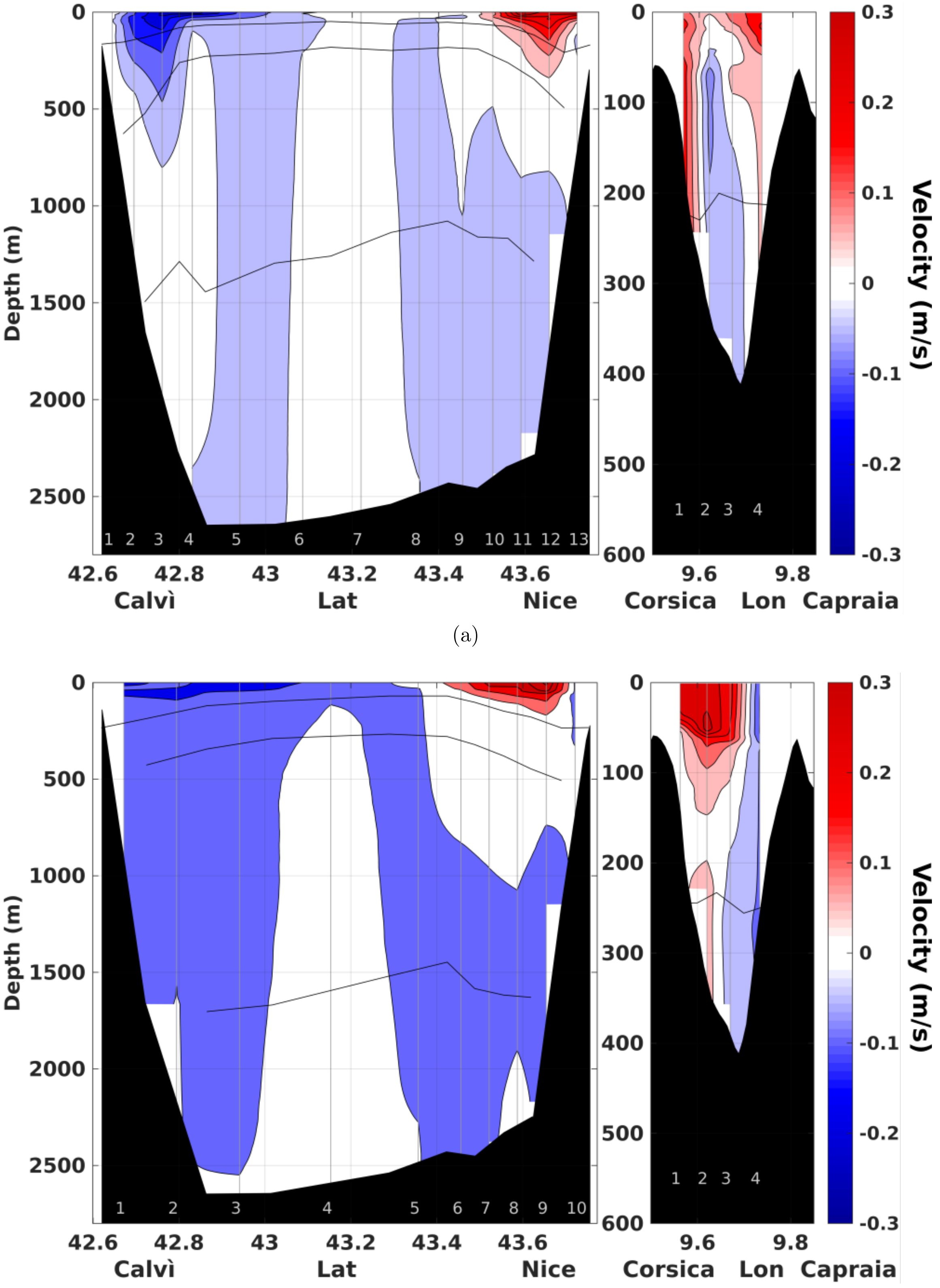

(a)

(b)

Figure 87: Absolute geostrophic velocities, here the inversion has been done without considering the CL transect. The numbers at the bottom of every plot represent the CTD stations 87a MEDOCC06, 87b MEDOCC07

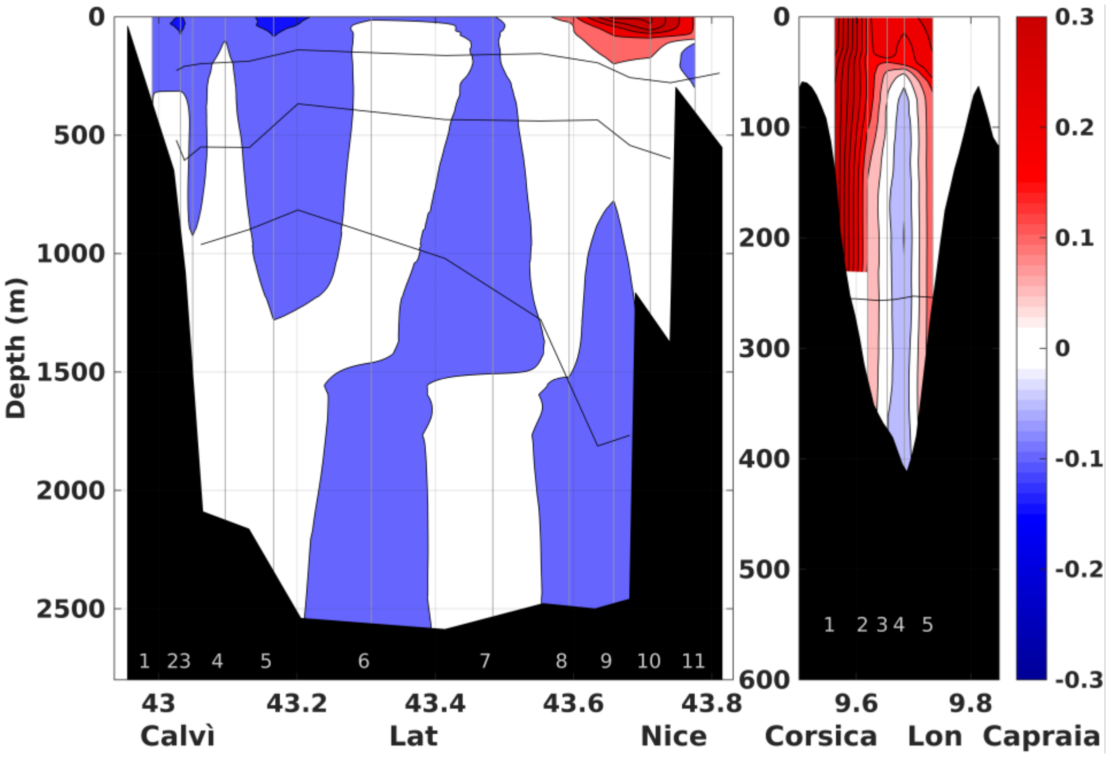

(a)

Figure 88: Absolute geostrophic velocities, here the inversion has been done without considering the CL transect. The numbers at the bottom of every plot represent the CTD stations 88a EUROFLEETS12

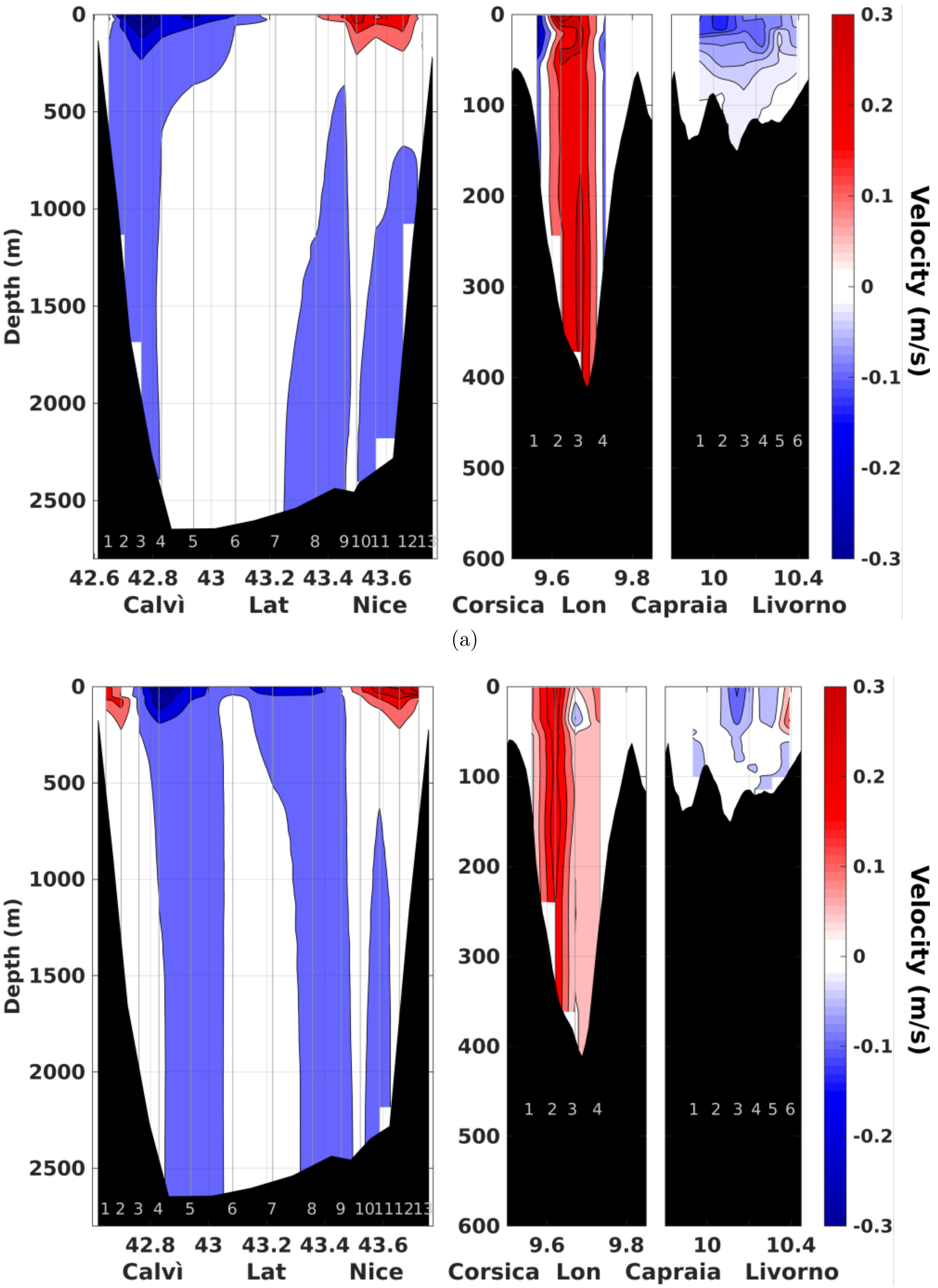

(a)

(b)

Figure 89: Absolute geostrophic velocities, here the inversion has been done considering the CL transect. The numbers at the bottom of every plot represent the CTD stations 89a MODAS2002, 89b LIGURE2002

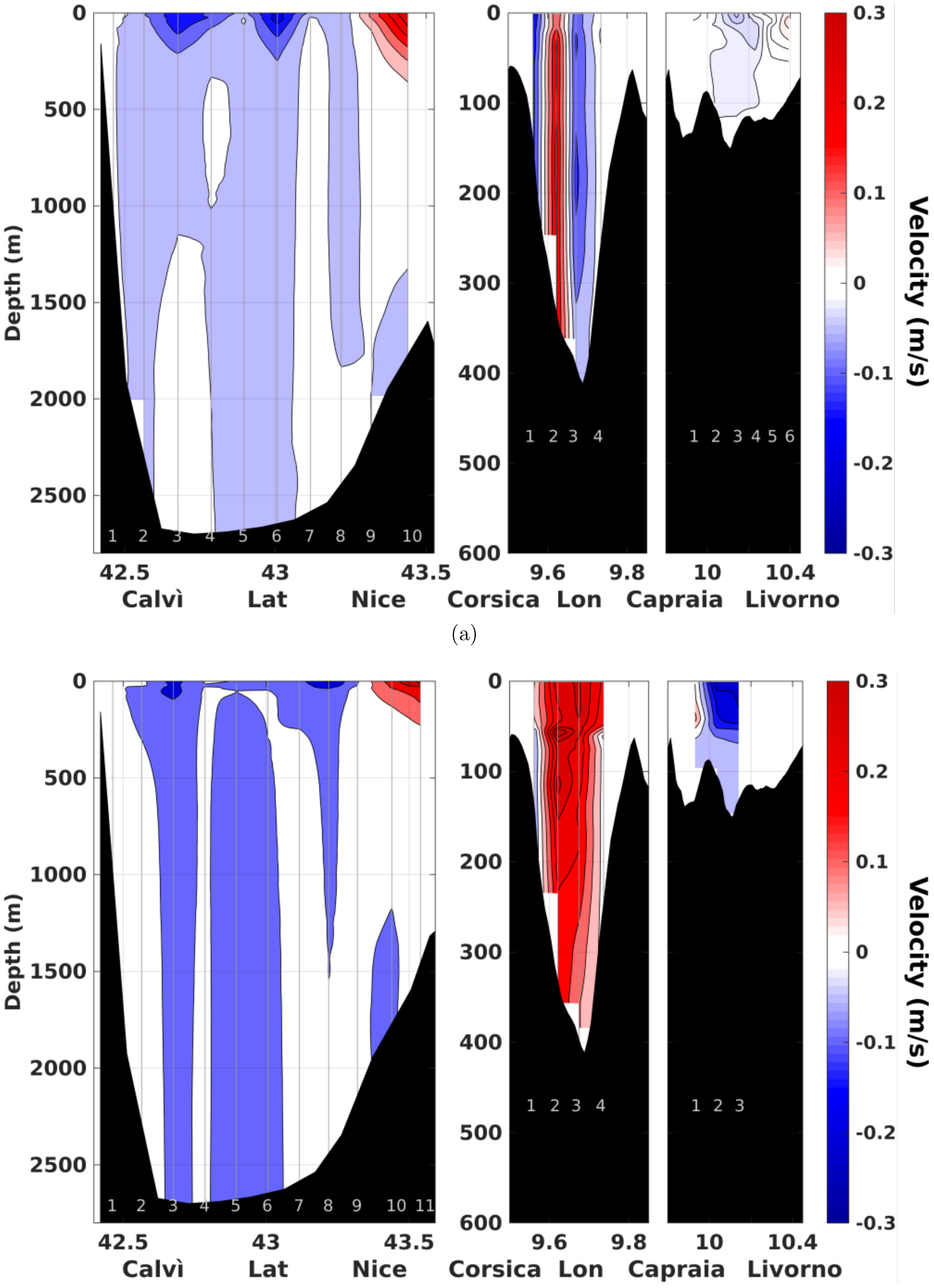

(a)

(b)

Figure 90: Absolute geostrophic velocities, here the inversion has been done considering the CL transect. The numbers at the bottom of every plot represent the CTD stations 90a LIPRO2003, 90b LIGURE2003

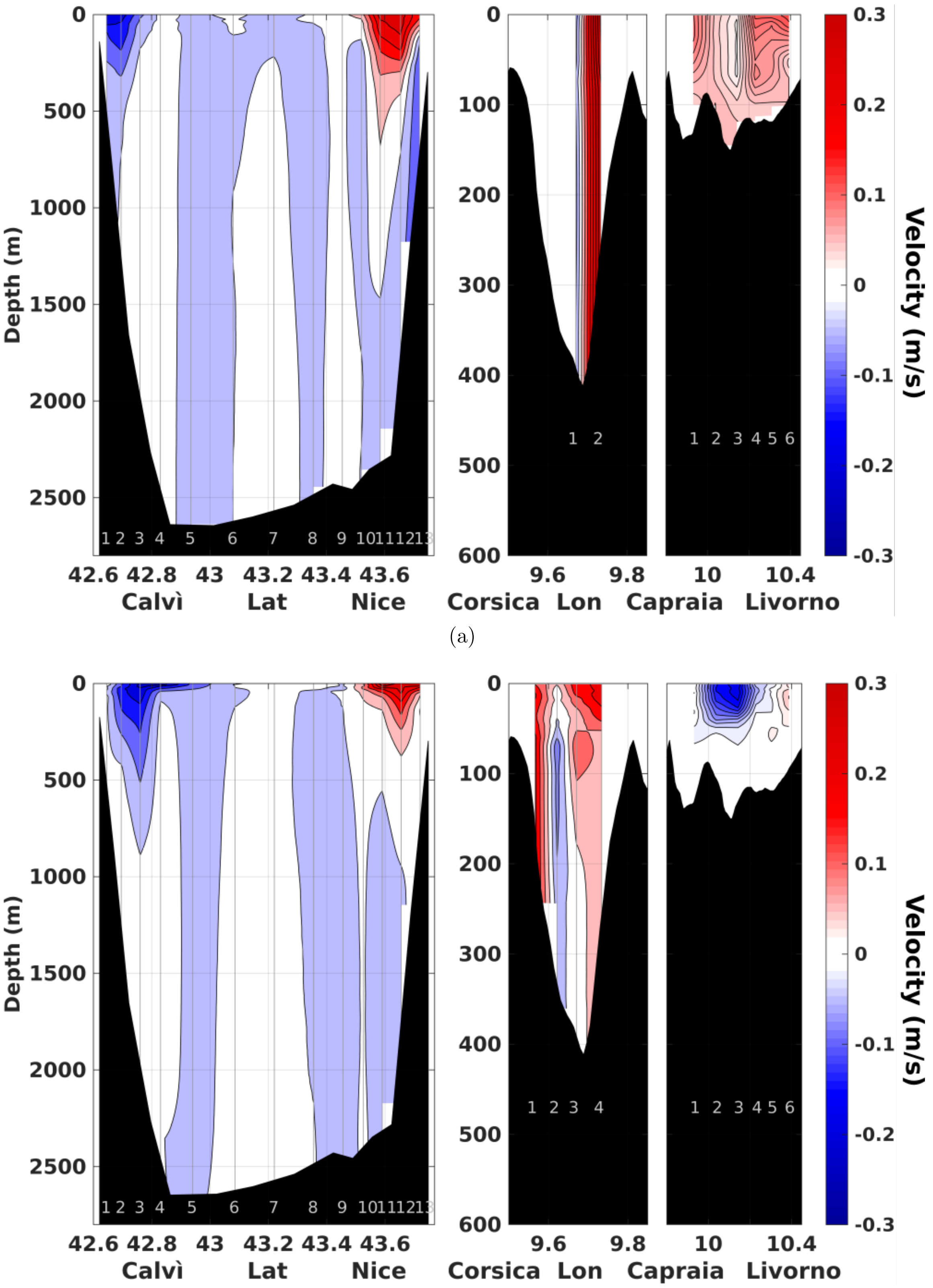

(a)

(b)

Figure 91: Absolute geostrophic velocities, here the inversion has been done considering the CL transect. The numbers at the bottom of every plot represent the CTD stations, 91a MEDOCC05, 91b MEDOCC06

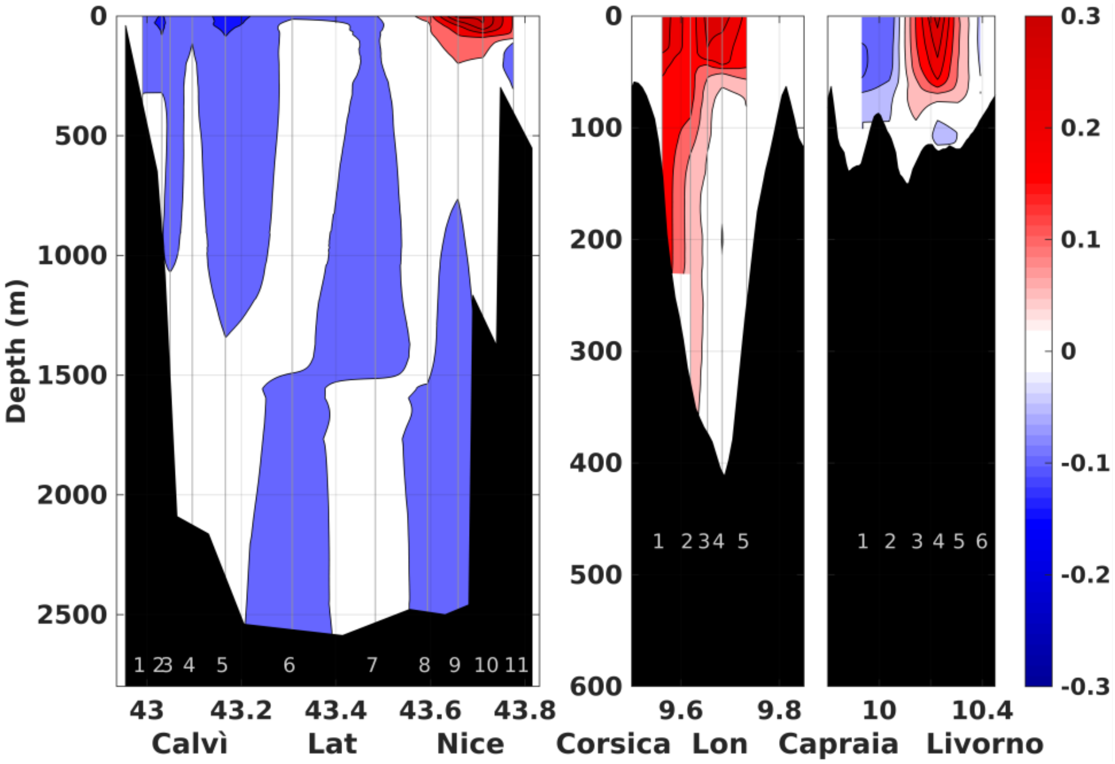

(a)

Figure 92: Absolute geostrophic velocities, here the inversion has been done considering the CL transect. The numbers at the bottom of every plot represent the CTD stations, 92a EUROFLEETS12

In MODAS2002, figures 84a and 89a, without CL, the CC flux is characterised by a central northward flux. Closer to the borders of the CC the water flows into the TYS. Adding the CL's southward flux, the central CC's water vein shows an enhanced northward flux, reaching mostly 0.2 m/s, the areas at the edges of the CC where the fluxes are directed southward appear narrowed. The circulation across the NC is not particularly influenced by the presence of the CL current. The WCC and LPC cores are well defined, respectively centred at 42.7 degrees and at 43,4 degrees. A weaker sparse eastward flux involves most of the NC transect below 400 m.

In LIGURE2002, figures 84b and 89b, there is a eastward flow close to Calví, which is unusual considering what it is known so far about the circulation across this section. There is a weak, small southward flow in the CC. When also the CL's mostly southward flow is considered, the NC and CC circulation distribution remain fairly unchanged. A northward water vein is present in the CL's oriental border.

In LIPRO2003, figures 85a and 90a, the CC shows a central flow from the TYS to the LS, on both sides of this flow there are two southward veins. In the CL the current is very weak, 0.03 m/s, and it does not induce any major change in the circulation. In the NC transect the WCC has two defined cores one centred at 42.7 degrees and another one at 43 deg latitude. Although the last CTD station in the north part of the transect is quite close to the coast to allow the section to be considered closed, the shape of the LPC core induce to think that the LPC extends 1/10 of a degree further towards Nice.

In LIGURE2003, figures 85b and 90b, the CC water current has a marked central flow directed northward and two narrow southward veins on both sides. If the CL flow, into the TYS, is added to the calculation, the two narrow veins almost disappear. The WCC does not have a particularly marked core and it is spread out across the section. The LPC is concentrated in the AW layer and extends horizontally from 43.35 degrees latitude to 43.45 degrees.

In MFSTEP2004, figure 86a, the flow across the CC is essentially divided into two major sectors an occidental northward flux and an oriental southward current. There is also a narrow vein directed into the TYS on the CC western border. The LPC and WCC cores are not as marked as they were in previous cruises, but the general configuration remains, with a fairly weak, < 0.1 m/s, westward flow and a confined LPC.

In MEDOCC05, figures 86b and 91a, the ECC looks divided vertically: the eastern part of the flow enters the LS the western part goes into the TYS. The WCC enters in the box when close to Calví, further towards the centre of the transect the current is directed eastward. The LPC has its core at 43.6 degrees, but below 50 m, closer to Nice, goes eastward. Adding the CL makes the unusual eastward flow, in the WCC, disappear. The CL is crossed by a northward current. This cruise results need to be interpreted with care, though, because only 3 CTD stations have been performed in the CC, which might not be enough to faithfully represent the ECC flow rate and as a consequence to evince also the whole basin circulation, in particular the CL flow.

In MEDOCC06, figures 87a and 91b, the CC presents in the center below 70 m a southward going vein. When also the CL's strong, 0.2 m/s, southward flow is considered, the CC's central vein weakens and the WCC core deepens from approximately 470 m to beyond 500 m. The LPC has still a marked core dragging both AW and LIW.

In MEDOCC07, figure 87b, the WCC is weak and widespread, whilst the LPC appears well marked and concentrated from 43.4 to 43.6 degrees latitude. The CC flow is again divided in two vertical sections: the western flow goes northward and the oriental weaker flow enters in the TYS.

In EUROFLEETS12, figures 88a and 92a, the WCC is very weak and barely recognisable, while the CC flow is directed into the LS, exception made for a weak, 0.03 m/s, vein into the TYS. When considering also the CL, whose circulation is divided vertically into a northward flow (east) and southward current (west), the CC's vein into the TYS disappears. The features of the NC transect observed in previous cruises are here confirmed both with or without the CL flux.

To calculate the final water transport for each current in the NC, it was necessary to identify, looking at the absolute geostrophic velocities the station that divided the LPC from the WCC, that are clearly separated within the first 100-200 m. In table 17 there are the stations up to where the transports have to be accounted as part of the WCC. Once defined what stations belonged to which current the transport was computed as:

$$TF = D + A + E \tag{16}$$

Where TF is the final total transport, D is the initial baroclinic transport, A is the adjustment made by the inversion, i.e. barotropic transport, and E is the Ekman transport calculated through the ERA-INTERIM climatologies. The results are represented in Figure 94 and 96, the two separate sets of plots aim to highlight the importance of the CL during the estimation of the water mass budget using the IBM. The CL has been poorly studied. The only estimate of the flux crossing the CL was provided by Manzella (1985), who estimated the CL water transport to be 0.3 Sv. In other words the CL flux has been considered negligible and almost inactive, or a simple appendix of the ECC. The long CTD dataset that has been blended together in this chapter allowed two separate sets of inversions, with and without the CL flux. This mostly unknown current might give a better insight about the AW circulation in the LS. In defining the boundary between WCC and LPC during this work the transition point has been identified with the position at which the currents intensity is the closest to zero.

Cruise	last station belonging to WCC
MODAS2002	7
LIGURE2002	6
LIPRO2003	8
LIGURE2003	9
MFSTEP2004	8
MEDOCC05	8
MEDOCC06	7
MEDOCC07	5
EUROFLEETS12	7

Table 17: Station in the NC section that indicates the end of the WCC in the final transport calculation, counting the stations from south to north

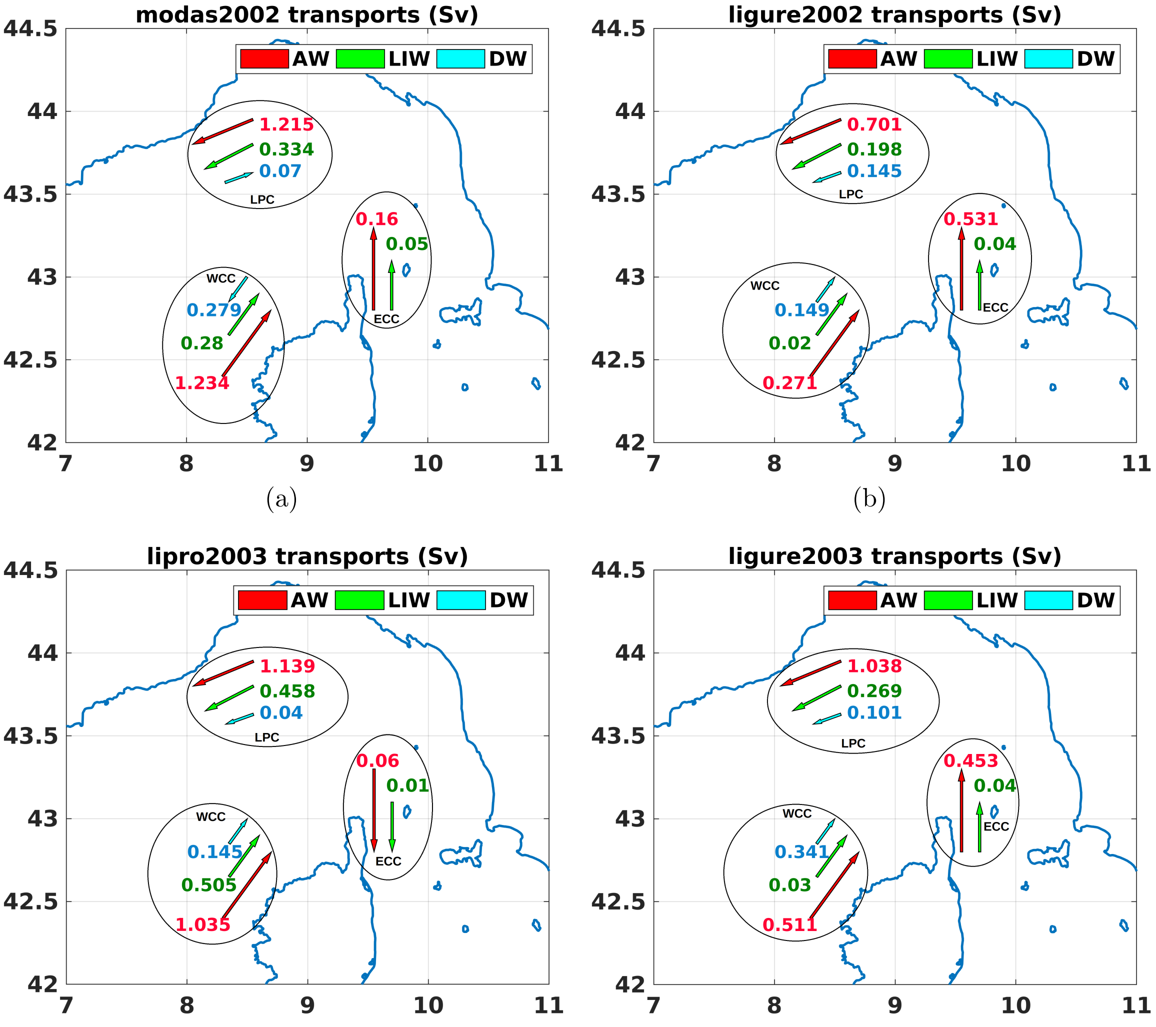

(a) (b) (c) (d)

Figure 93: Mass transport for each cruise considering the CC transect alone, without the CL section. DW stands for WMDW + nWMDW (when present). 93a MODAS2002 in June 2002, 93b LIGURE2002 in October 2002, 93c LIPRO2003 in May 2003, 93d LIGURE2003 in September 2003

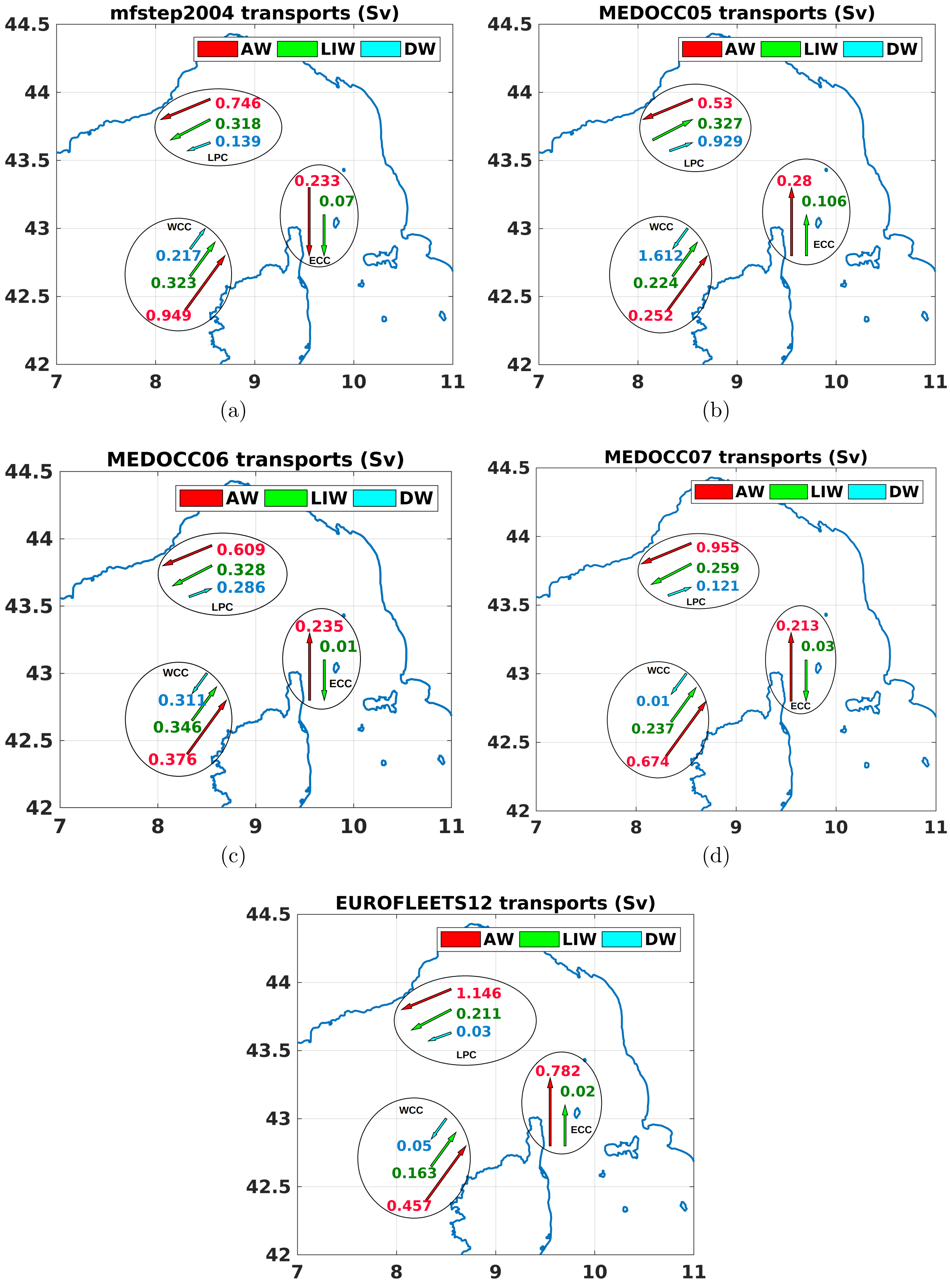

(a) (b) (c) (d) (e)

Figure 94: Mass transport for each cruise considering the CC transect alone, without the CL section. DW stands for WMDW + nWMDW (when present). 94a MFSTEP2004, 94b MEDOCC05, 94c MEDOCC06, 94d MEDOCC07, 94e EUROFLEETS12

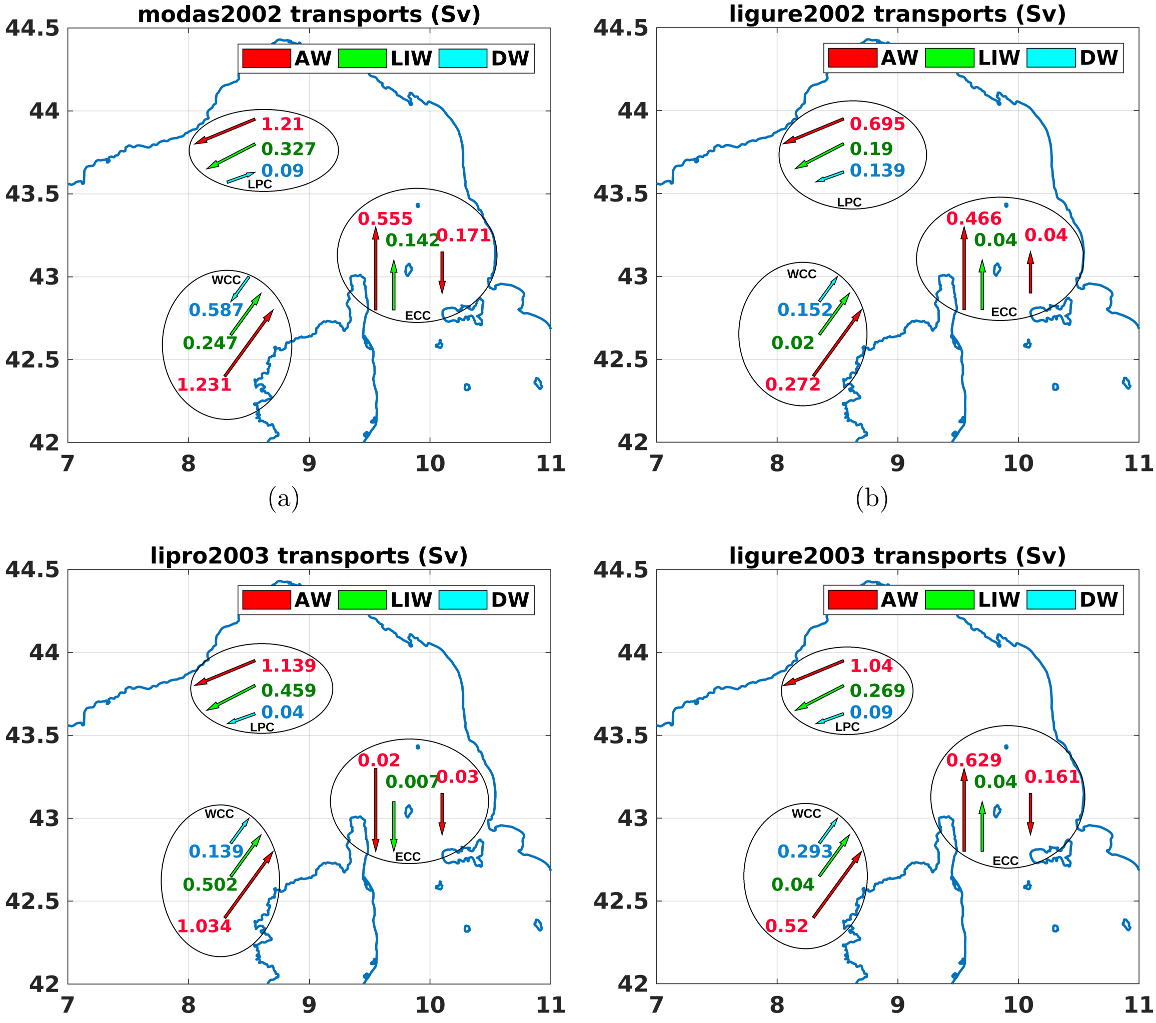

(a) (b) (c) (d)

Figure 95: Mass transport for each cruise considering also the CL section. DW stands for WMDW + nWMDW (when present). 95a MODAS2002 in June 2002, 95b LIGURE2002 in October 2002, 95c LIPRO2003 in May 2003, 95d LIGURE2003 in September 2003

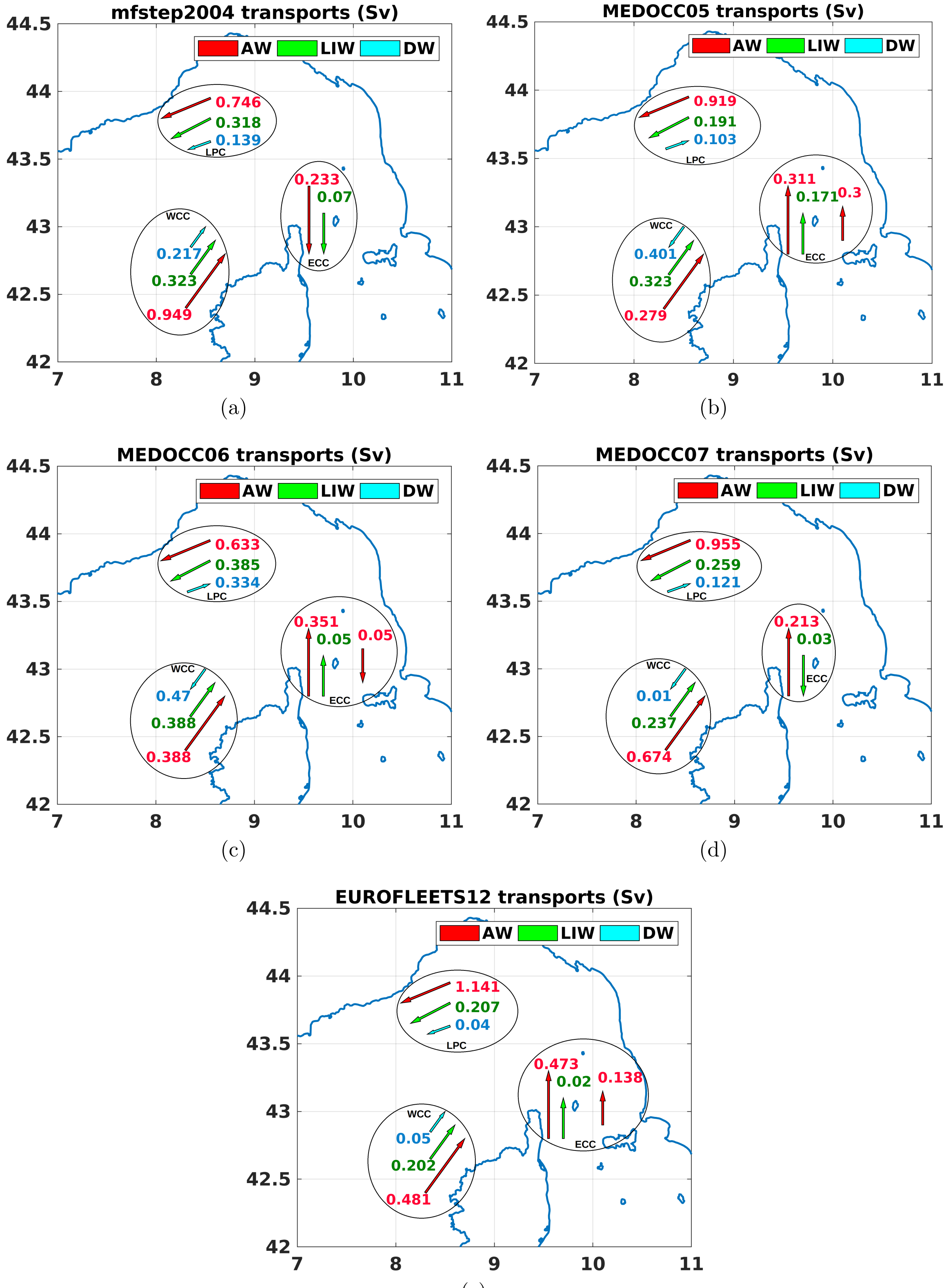

(a) (b)

(c) (d)

(e)

Figure 96: Mass transport for each cruise considering also the CL section. DW stands for WMDW + nWMDW (when present). 96a MFSTEP2004 in September 2004, 96b MEDOCC05 in April 2005, 96c MEDOCC06 in June 2006, 96d MEDOCC07 in October 2007, 96e EUROFLEETS12 in November 2012

MODAS2002, figures 93a and 95a, the final current transport is mostly balanced by WCC and LPC alone, the ECC feeds in minor part only the surface and intermediate layers. The deep water budget is entirely managed by the NC section, but in opposite directions if compared with the current in the above layers. The CL adds an outgoing AW flux, as a consequence the rest of the circulation makes slight adjustments to rebalance the total mass budget, but the peculiarity of the deep water in the NC flowing opposite to the above layers remains.

In LIGURE2002, figures 93b and 95b, the circulation compares well with the one known from literature and described in the introduction. When the CL northward AW transport is added the surface flux readjusted influencing the AW circulation of all the LS.

In LIPRO2003, figures 93c and 95c, the transport across the CC is very weak (0.07 Sv in total) and directed southward, whilst the LPC goes westward, so they are both out-flowing from the box and need to be balanced by the WCC, the NC configuration does not change when the southward flow across the CL channel is added. The CC and the CL share the AW export from the LS to the TYS.

In LIGURE2003, figures 93d and 95d, the circulation resembles the historical current configuration. Adding the CL, across which the AW flows into the TYS, influences the AW flux across the CC that compensates for the AW loss.

In MFSTEP2004, figures 94a and 96a, both the ECC and the LPC are leaving the LS and their outflow needs to be replenished by the WCC.

In MEDOCC05, figures 94b and 96b, the AW and LIW follow the historical circulation pattern in ECC and WCC. Deep layers, though, move in opposite directions with respect to the surface above them. The LPC's AW transport in detected outside of the LS. Intermediate and deep layers are instead flowing inside the LS. If we consider the CL ingoing AW, then the circulation resembles the historically known one, exception made for the deep water across the NC.

In MEDOCC06 and MEDOCC07, figures 94c and 96c, 94d and 96d, the traditionally known circulation is restored, apart from a southward intermediate flow in the CC and reversed WMDW flow with respect to the upper layers. During MEDOCC06 cruise the CL transect has been sampled and the AW directed into the TYS has the effect of reversing the LIW and slightly enhancing general superficial and intermediate flow. Also the deep flow is weaken in the NC.

In EUROFLEETS12, figures 94e and 96e, all the flow across the CC goes from the TYS to the LS. In the WCC, the WMDW current moves in opposite direction with respect to the above currents. When the CL is considered the water transport distribution readjusts, the CC AW transport diminishes and interestingly the WCC and LPC readjust resembling the historical configuration.

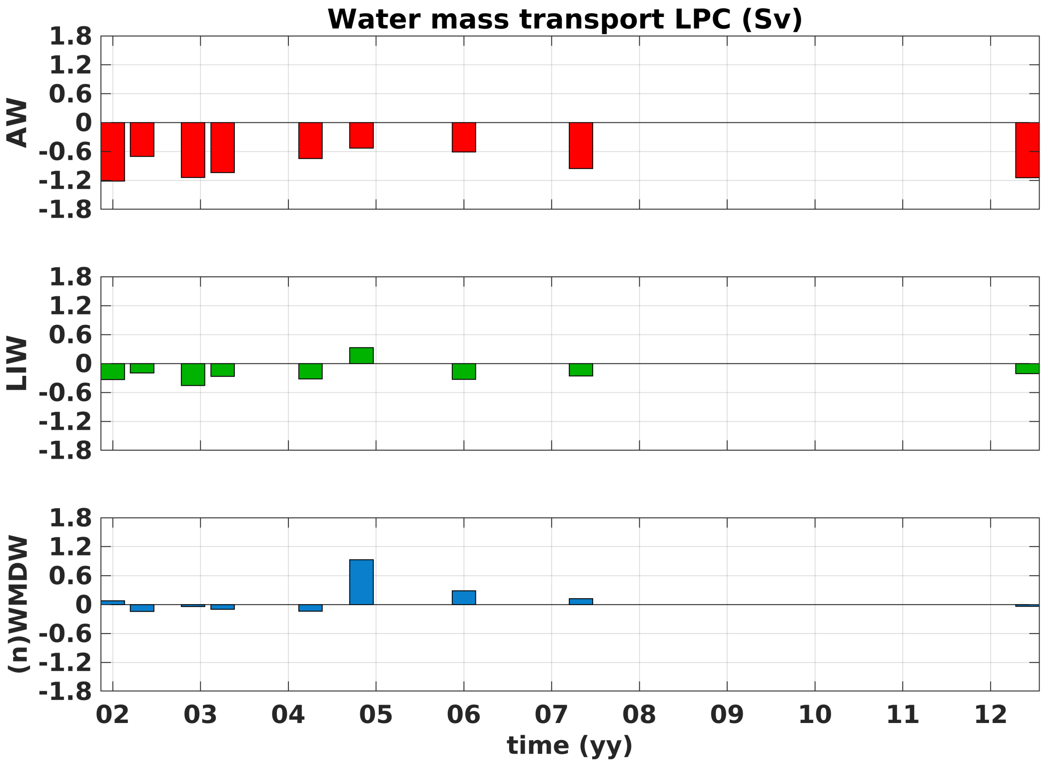

(a)

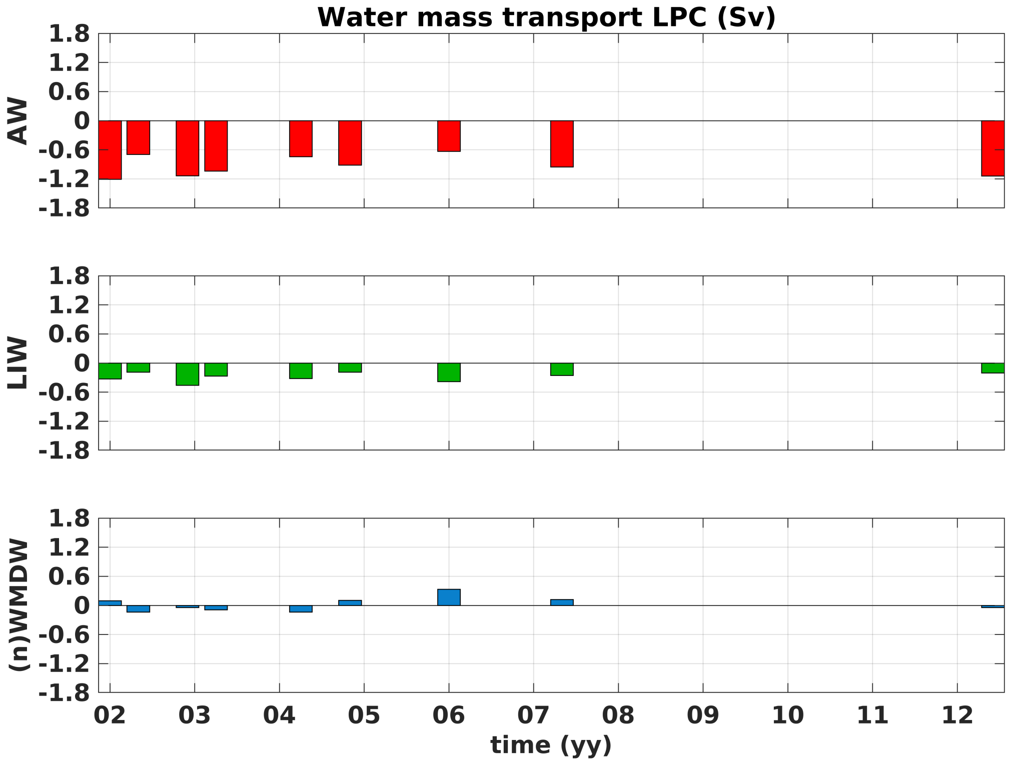

(b)

Figure 97: Liguro-Provençal Current time evolution for each water mass from inversions without the CL (97a) and considering the CL (97b). The total deep water transport includes Western Mediterranean Deep Water and new Western Mediterranean Deep Water. Positive transports are into the LS

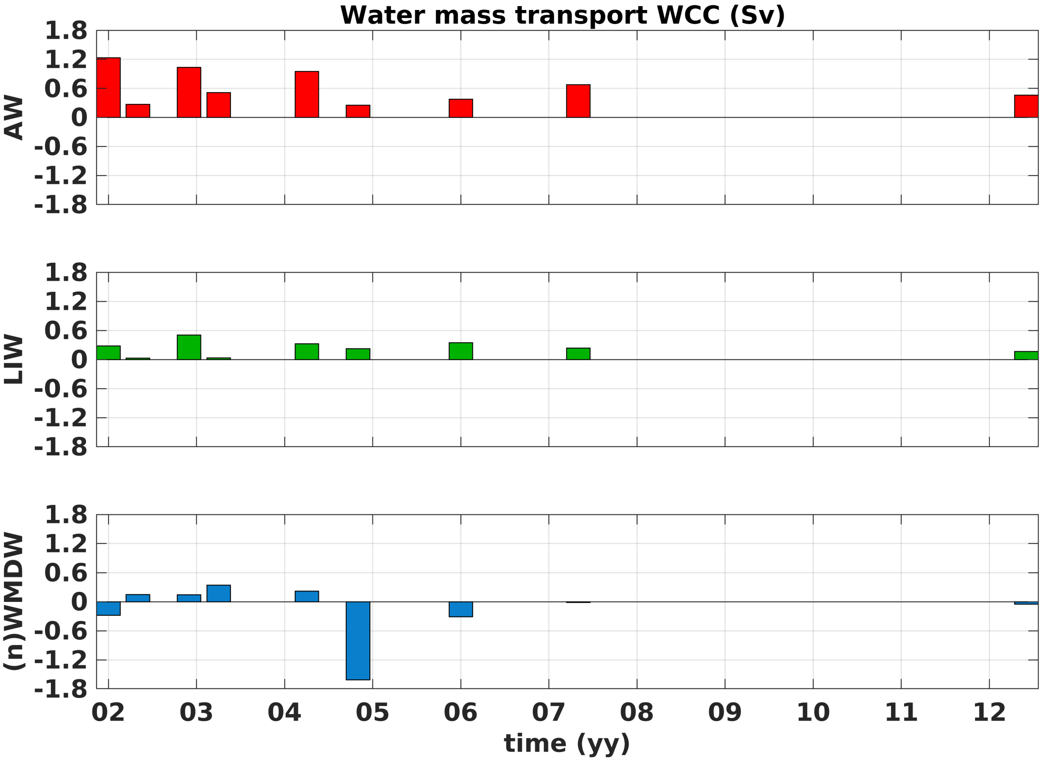

(a)

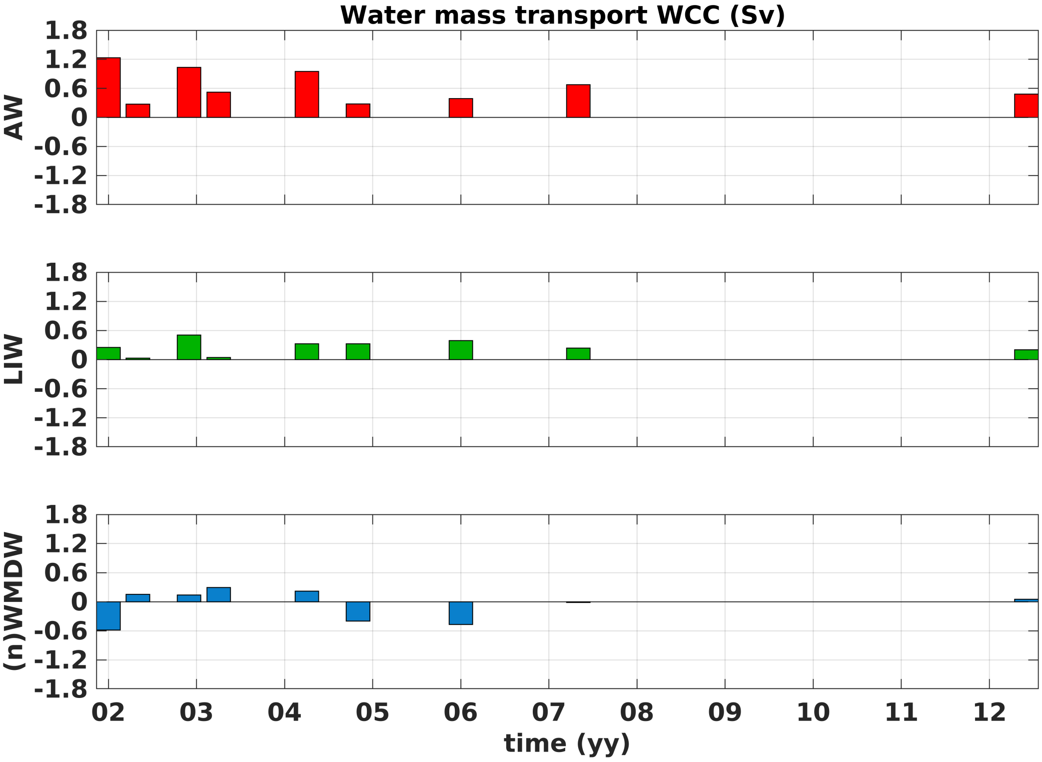

(b)

Figure 98: Western Corsica Current time evolution for each water mass from inversions without the CL (98a) and considering the CL (98b). The total deep water transport includes Western Mediterranean Deep Water and new Western Mediterranean Deep Water. Positive transports are into the LS

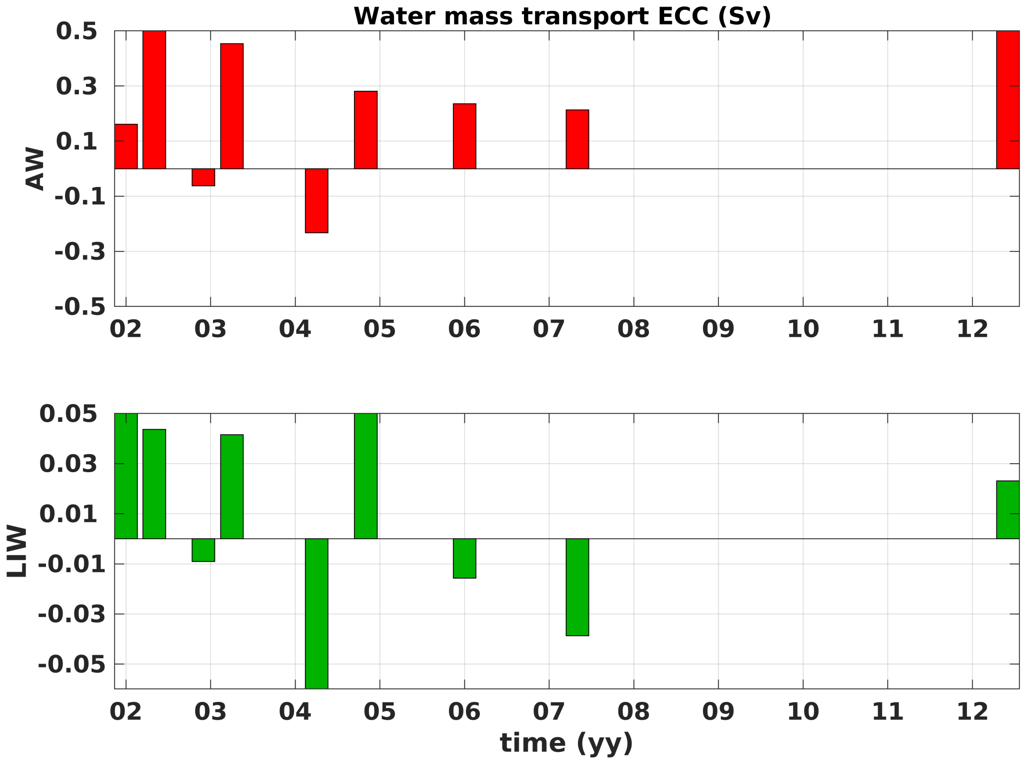

(a)

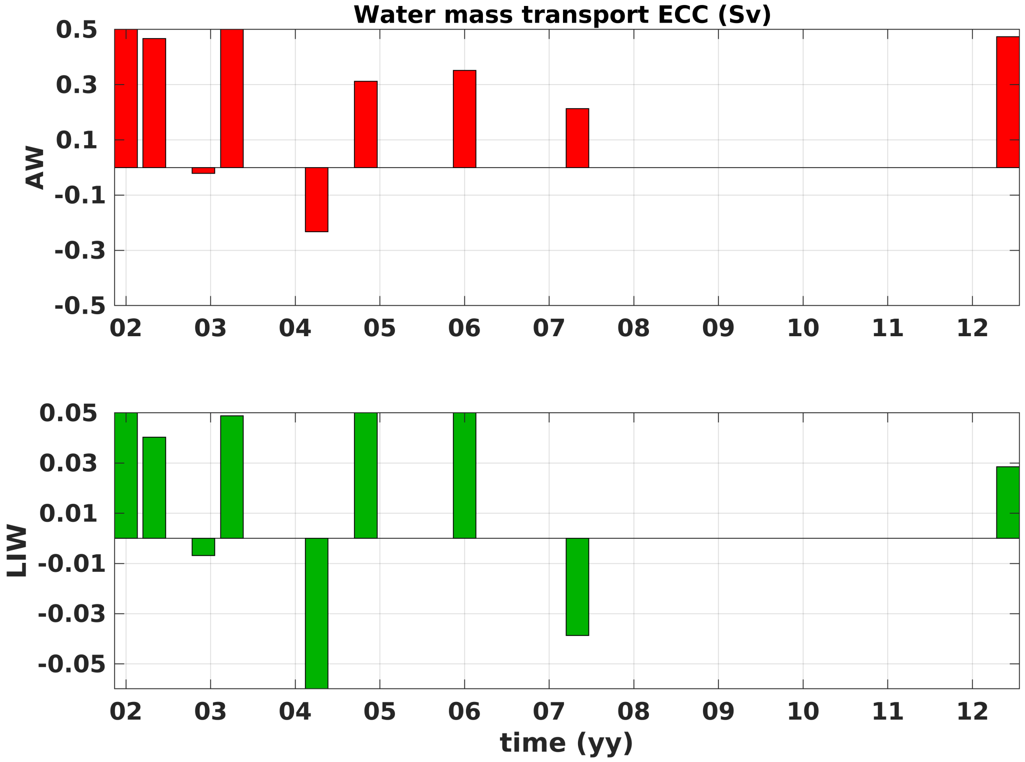

(b)

Figure 99: Eastern Corsica Channel time evolution for each water mass from inversions without the CL (99a) and considering the CL (99b). The total deep water transport includes Western Mediterranean Deep Water and new Western Mediterranean Deep Water. Positive transports are into the LS

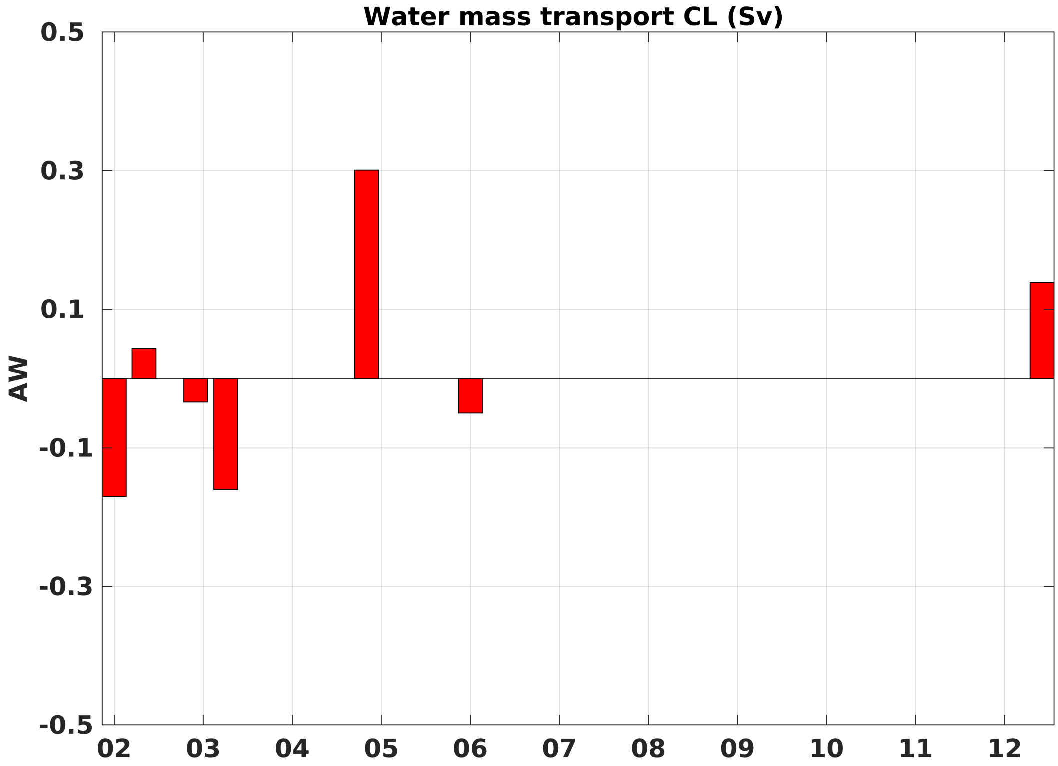

Figure 100: Capraia Channel time evolution for AW, the only water mass crossing the Capraia-Livorno Channel

The LPC's AW flow is directed westward (negative values in Figure 97). It oscillates between 1.2 Sv and 0.5 Sv. The minimum value being measured in 2005. The LIW transport varies from 0.45 Sv eastward (positive) and 0.32 Sv westward. The only positive transport happened in 2005, but MEDOCC05 has only 3 CTD stations in the CC and the circulation values need to be handled with care. It can be argued that 3 CTD stations in the centre of a channel are not enough to faithfully represent the geostrophic flow. Being the negative LPC's LIW value, measured in 2005, the only one, it is here considered erroneous. The abyssal layer transport (WMDW+nWMDW) ranges between 0.14 Sv westward and 0.29 eastward, neglecting data in 2005. The eastward flow has an abrupt increase in 2006 after the deep water formation event mentioned in CIESM Monographs (2009), the WMDW+nWMDW flow inside the box instead then outside might be linked in the eddy shaped paths that the newly formed water undertakes during the spreading phase (Marshall and Schott, 1999). When comparing Figure 97b and 97a, the main influence of the CL can be observed in 2005 (MEDOCC05), the LIW's flow aims in the same direction as layers above, westward, and the AW transport reaches approximately 0.9 Sv. MEDOCC05 is a good example to highlight the importance of monitoring the CL.

The AW carried by the WCC (Figure 98) goes from 0.25 Sv to 1.23 Sv, the intermediate layer oscillates between 0.03 Sv and 0.51 Sv, while the deep layer ranges from 0.34 Sv (eastward) to 1.61 Sv (westward). The CL flux influences the WCC and can be observed always in MEDOCC05 where the anomalous DW value is readjusted considering also the AW input across the CL.

In the ECC (Figure 99) the water flow is mainly directed into the LS, exception made for 2003 and 2004. In 2006 and 2007 the LIW only enters the TYS. When the CL contribution is taken into account the most evident change happens in in 2006 when the originally southward LIW flows is reversed and peaks to 0.5 Sv.

The CL (Figure 100) water transport is constituted by AW and it ranges between 0.17 Sv into the TYS and 0.3 entering the LS. Out of 7 cruises the CL flow is directed into the LS only 3 times, 2 of which happen in October 2002 and November 2012. It can be therefore stated that the CL current has the tendency to flow outside the LS.

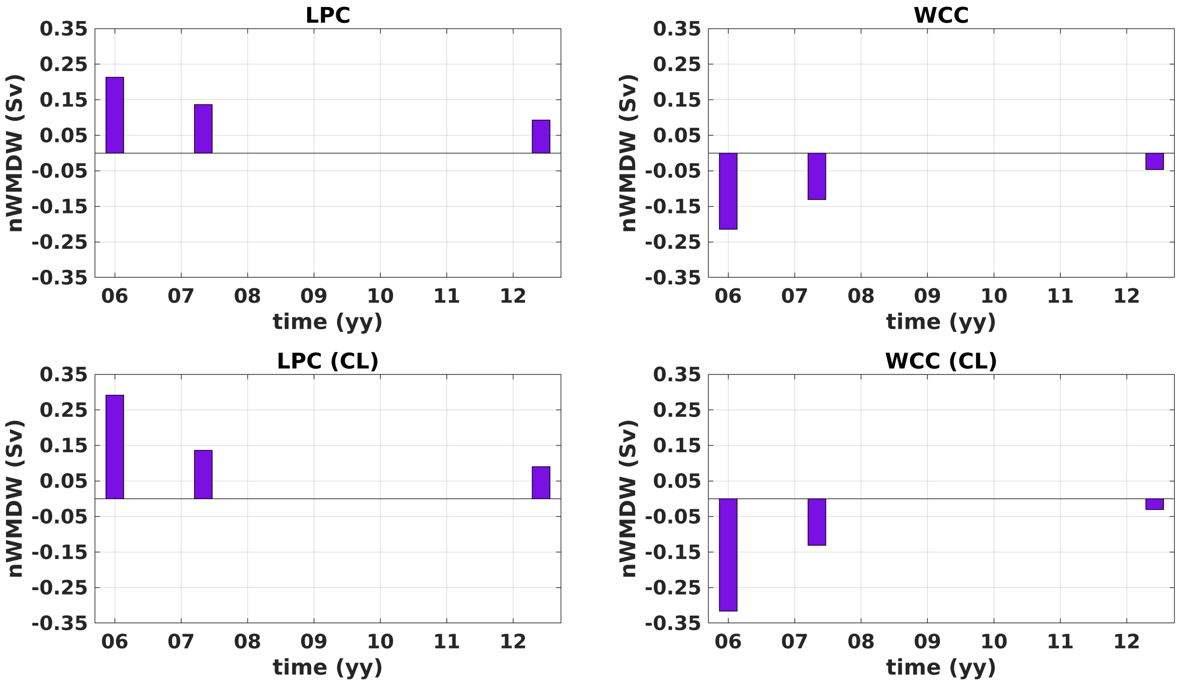

Figure 101: nWMDW time evolution for the three years when it has been measured, i.e during MEDOCC06 in June 2006, in MEDOCC07 in October 2007, in EUROFLEETS12 in November 2012, is here represented divided in each current (LPC and WCC) and for the two sets of analysis (with or without CL). Negative values are directed outside the box

In order to isolate the observations collected about the nWMDW, a separate plot has been produced and it shown in Figure 101. The nWMDW has been observed during MEDOCC06 in June 2006, MEDOCC07 in October 2007 and EUROFLEETS12 in November 2012. In 2006, the year after the WMT, the nWMDW shows its maximum, i.e $\sim$ 0.21 Sv ($\sim$ 0.29 with CL) in the LPC, then it diminishes to 0.14 and 0.09 (0.09) Sv. Similar transports can be observed in the WCC, but in the opposite direction: 0.21 (0.32) Sv during MEDOCC06, 0.13 Sv during MEDOCC07, 0.05 (0.03) Sv during EUROFLEETS12. The mean reference velocities averaged for the 9 cruises are reposted in Figure 102. These velocities represent the barotropic component of geostrophic velocities and they constitute the main output of the IBM. The values reported in Figure 102 have been obtained from inversions considering also the transect between Capraia and Livorno, as including the CL section renders the analysis complete and more accurate. In the north part of the NC section the reference velocities tend to be negative (westward) and can reach 0.01 m/s. In the south part of the NC, where the WCC crosses the section the reference velocities are directed mostly eastward, inside the box and can reach 0.015 m/s. In the CC at the borders of the channel the reference velocities tend to be directed southward reaching also 0.1 m/s, in the center instead the velocities point towards the LS reaching 0.025 m/s. In the CL on average the reference velocities are directed northwards and they reach 0.008 m/s.

When setting the IBM, the user has to balance various factors that will influence the result of the inversion. At first it is necessary to choose the density values that are going to constitute the interface value dividing different portions of the water column. It is good practice to choose the density interfaces in order to divide the different water masses characterising the defined box. In this way it is possible to investigate the budget of each water mass, diapycnal fluxes and water transformation. This study focuses on the water budget. The choice of different interfaces leads to the estimation of different barotropic velocities. DIABOX is set up in a way that the user can impose a maximum a priori error for each of the properties in each of the layers, plus a total layer encompassing the entire water column. The surface layer is normally considered the most variable, therefore DIABOX allows a bigger error for it. Consequently, the top-to-bottom layer, which comprises the surface waters, also allows for a larger error. This setting can be changed if the study area has, for instance, a considerable heat input from a ridge, in this case the bottom layer would allow for a larger error in comparison with the rest of the water column. The user can choose to use the climatology that suits the best the investigated area. It is worth mentioning that in this application, we used IMEDEA climatology for the ocean data. IMEDEAs dataset is still unpublished, but certainly adds value to the present study as it has been tailored for the Mediterranean Sea. The ocean data and the atmospheric data must have the same spatial resolution for the computation of the air sea interaction, so the IMEDEA dataset has been interpolated on the more coarse ERA-INTERIM reanalysis grid, used for the atmosphere. A future study might investigate the impact of using a new tailored climatology also for the atmospheric data. Another tuning aspect of the IBM regards embedding extra data, other than CTD, to constrain the model and better mirror our knowledge of the circulation. Here, a 30 years long time series was available for the transport across the Corsica Channel and the MERMAID floats provide the opportunity to constrain the deep circulation in the Nice-Calví transect. Figure 103 shows how changing the density layers choice and removing the extra constraint data will change the barotropic component of geostrophic velocities calculated through the IBM.

The strongest impact appears to be the layer choice. The data represented in Figure 103 are from MEDOCC06 (June 2006), used for extra sensitivity inversions. During all the inversions it is assumed that the state of the circulation remained stationary for the duration of the cruises. It is important to notice that the majority of the cruises happened in summer and that the resulting picture of the absolute geostrophic circulation is seasonally biased. In the study we did not use seasonal ancillary data, i.e. IMEDEA, ERA-INTERIM, etc, we used long term climatologies. Future studies might consider seasonal means instead of long term climatologies.

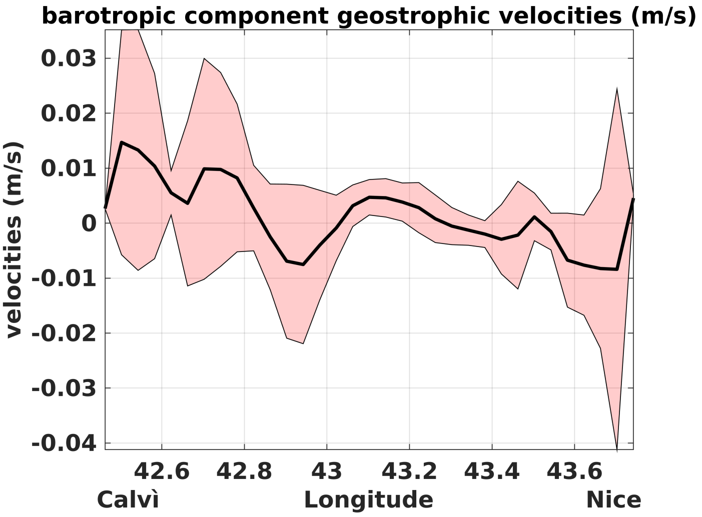

(a)

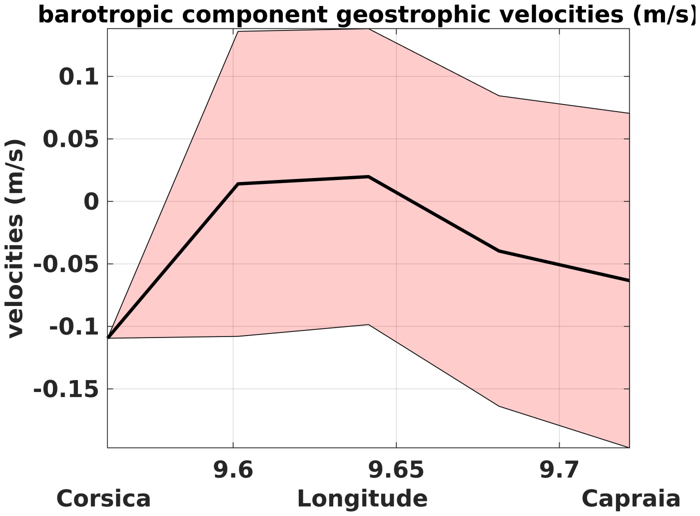

(b)

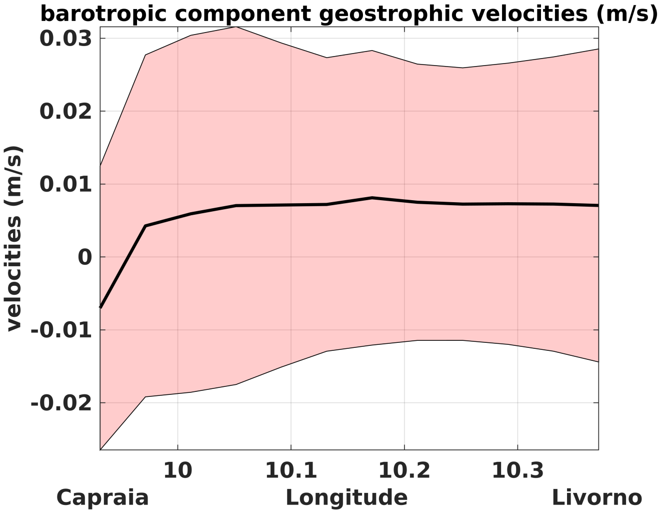

(c)

Figure 102: Reference velocities in the NC (102a), CC (102b) and CL (102c). The thin black line represents the mean barotropic component of geostrophic velocities, the coloured area shows the STD

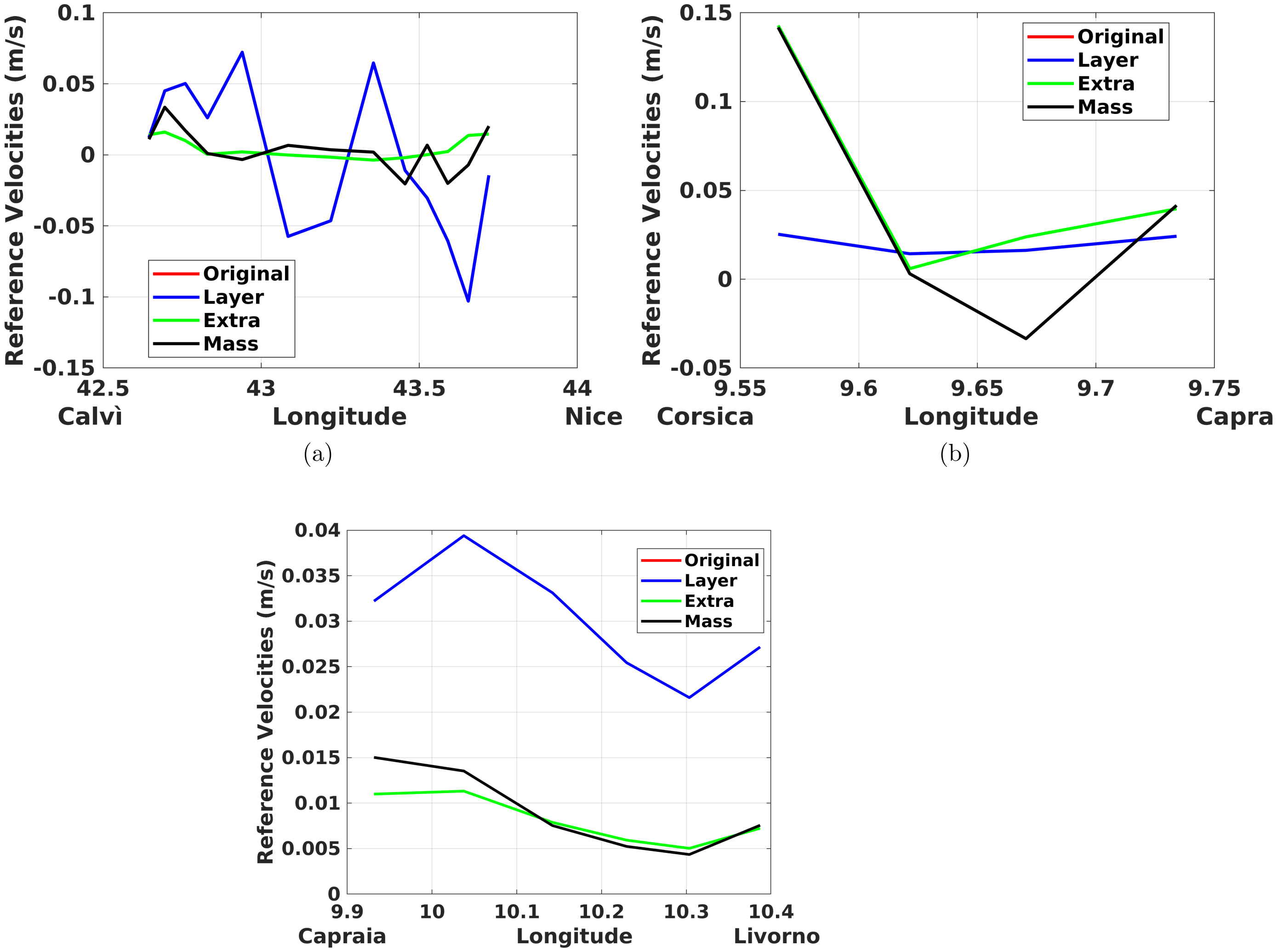

(a)

(b)

(c)

Figure 103: Reference velocities in the NC (103a), CC (103b) and CL (103c). The different lines represent the reference velocities obtained by changing the tuning parameters of the IBM, namely: density layer choice ('Layer' in legend), initial mass error estimate ('Mass' in legend), extra constraint data, i.e. Corsica Channel water velocities and MERMAID velocities ('Extra' in legend). Original data (red line), i.e. reference velocities used in the present study, coincide with the result obtained when changing the initial mass error estimate, because in the final phase of the inversion the extra observational data added to the study overwrite the initial guessing

6.5 Conclusion

Overall the WCC involves the whole water column although it weakens below 200 meters, it seems to be deeper than the LPC (∼250m). LPC and WCC mostly carry only AW in their shallow cores, but their influence extends deeper than the interface with the LIW, therefore the LPC and the WCC drag with them also the water masses located in the deeper layers, i.e. LIW, WMDW and nWMDW. The LIW-WMDW interface is generally situated at 470-500 m depth. In November 2012 the WMDW-nWMDW interface shows a clear slope, the isopycnal is shallower close to Calví (800 m) and deeper close to Nice (1800 m). Being aware of the fact that most of the data have been collected in summer it is not surprising to notice reversals in the ECC and in the CL, but it is a novelty the quantification flux current across the CL.

In general the presence of the CL attenuates the CC flow features. The absolute geostrophic velocities calculated through the IBM show that a southward component in the ECC is always present, often the CL and/or the CC sections are divided vertically (May 2003 -LIPRO2003-, September 2004 -MFSTEP2004-, November 2012 -EUROFLEETS12-). Anyhow in September 2003 the CC flow was fully northward and the CL flow was entirely southward. In November 2012 the CC water was all going into the LS, but the CL was divided as already mentioned above.

Although the flow rate across the CL section is never too high (maximum 0.3 Sv) and is always carrying AW, it seems to readjust the mass transport at surface and intermediate level. The CL has a more direct influence on the CC activity. The CL and the CC often share or balance the AW transport (October 2002 -LIGURE2002-, May and September 2003 -LIPRO2003 and LIGURE 2003-, November 2012 -EUROFLEETS2012-). Sometimes the DW in the NC transect flows westward in the south portion of the section and eastward close to Nice, this is the case in June 2002 (MODAS2002), April 2005 (MEDOCC05), June 2006 (MEDOCC06), October 2007 (MEDOCC07). In November 2012 (EUROFLEETS12) only the DW of the LPC is directed in opposite direction with respect to the upper layers. This behaviour has been observed before only by Le Floch (1963).

Here for the first time the evolution of the water masses located in the LS and their flux variability in time have been studied through an IBM application. The transport calculation presented in this study results in smaller water fluxes if compared with most of the historical values, this can be explained by the strong seasonal variability present in the LS. The majority of the CTD data were collected in summer, the season where the circulation of the basin is less active. Despite this our results agree with those found by Le Floch (1963), including the reverse abyssal circulation across the NC.

7 Conclusion and Future Work

In modern oceanography combining datasets from different platforms and spatial time resolution is a challenge. In this study a large variety of data have been brought together. Free floating devices, MERMAID, presented in Section 3 constitute an unusual, small dataset that gave an insight about the depth and behaviour of the Liguro Provençal current, which is generated in the eastern Ligurian Sea and flows across the entire north-western Mediterranean. Reanalysis data, measurements from moored rotor current meters, along track satellite altimetry data have been used in Section 4 to depict a clearer picture of the agents driving the water flow across the Corsica Channel especially to, but sometimes from, the Ligurian Sea. In the same context it has been possible to describe the annual and interannual variability emerging from the constituted datasets. In the last Section, 6, an Inverse Box Model has been applied to the Ligurian Sea. Nine inversions were performed thanks to in situ hydrographic data collected with a Conductivity Temperature Depth probe. None of the previous inverse box modelling studies in the western Mediterranean was repeated over time. From this study a detailed picture of the absolute geostrophic circulation arose.

The MERMAID floats, in Section 3 dive mostly below 800 m depth and 38% of the instruments reached 1500 m or deeper positions and travel at a velocity of 5 cm/s in more than 90% of the data, sometimes reaching more than 15 cm/s (3.8% of the measurements). The LPC appeared to involve the entire water column, as assessed by Taupier-Letage and Millot (1986), different from what was inferred by Bethoux et al. (1982) and Astraldi et al. (1994), and to imitate the behaviour of the surface current as described by Poulain et al. (2012). The deep Liguro-Provençal Current is weaker close to the Ligurian than in proximity of the Gulf of Lion and the Ibiza Channel. The considerable depths reached by the floats and their velocities make possible for the LPC to carry newly formed Western Mediterranean Deep Water, contributing to its spreading. One float remained trapped in an eddy feature in the central part of the Liguro-Provençal basin at roughly 1500 for almost a year from July 2014 to July 2015. From the pseudo-eulerian statistics the nature of the current results are mostly turbulent.

The Corsica Channel is a monitoring choke point in the north-western Mediterranean sea circulation and variability. Studying the dynamic of the channel can bring together a large variety of factors that drive the Liguro-Povençal basin circulation. The transport through the Corsica Channel has been related to the Ekman transport, Sea Surface Pressure, Sea Level Anomaly and wind stress in Section 4. The seasonal and spectral analyses highlighted how all the parameters contribute to making the winter flow more intense. The Ekman transport contribution to the total transport across the channel is on average 3%, but it can reach 25% during rare events. The Sea Level Anomaly calculated from along track data and retracked with ALES (Passaro et al., 2014) showed much better results in comparison with the gridded data from Copernicus Marine Service. For instance the correlation coefficient between Jason track 044, used also by Vignudelli et al. (2000), and the total water transport is 0.49, a similar analysis using gridded products resulted in a 0.016 correlation coefficient. Using ALES data also established a high correlation coefficient between along track Sea Level Anomaly and Sea Surface Pressure (0.4 in the Ligurian and 0.69 in the Tyrrhenian) that well compares with the value found by Fu and Pihos (1994) ($r = \sim 0.7$). The time-lag analysis evidenced how the transport of the Corsica Channel is rapidly responding (1 day delay) to Sea Surface Pressure variations. The Sea Surface Pressure configuration is generally higher over the Tyrrhenian than the Ligurian, therefore it favours almost constantly a northward flow across the Corsica Channel. The component of the wind stress linked to this Sea Surface Pressure configuration is the meridional wind stress. Time-lag analysis revealed a geostrophic flow across the Corsica Channel linked to the meridional component of the wind stress. A wind blowing along the coast induces an Ekman transport perpendicular to the coast, directed offshore. To replenish the volume of the water that moves away from the coast, deeper, denser waters upwell, tilting the isopycnals and the sea surface slope, which becomes higher offshore. In a rotating system, such as the Earth, the sea surface slope creates a pressure gradient, counter balanced by the Coriolis force. This configuration creates a geostrophic current along the coast, in the considered case, northward. The explained system takes three days to build up, which is the delay revealed by the time-lag analysis. The agent that resulted to have a constant influence on the Corsica Channel flow is the Sea Surface Pressure over the Ligurian and the Tyrrhenian. When exceptional winters occur in the total water transport across the Corsica Channel they well agree with the Sea Level Anomaly trend as seen by along track data.

The Western Mediterranean Deep Water transport across the northern part of Nice-Claví transect has been estimated thanks to MERMAID measurements and added as a constraint to the Inverse Box Model. MERMAID were deployed between 2012 and 2014. The Inverse Box Model investigation gave a new insight in the Western Corsica Current role in summer. This current has been neglected in previous studies, but here it results to be able to replenish the summer water export from the Ligurian Sea on its own. Overall the Western Corsica Current, as the Liguro-Provençal current, involves the whole water column, but it becomes weaker below 200 meters. The Liguro-Provençal current core is very well defined throughout all the cruises, moreover it is confined to the very north part of the Nice-Calví transect, supporting the statement by Astraldi and Gasparini (1992), i.e. the Western Corsica Current is compressed against the Corsica Island continental shelf during winter to early summer then it expands horizontally, confining the Liguro-Provençal current. The Atlantic Water constitutes the bulk of the circulation in the Ligurian Sea, but, although less intensely, the Levantine intermediate water and the (new) Western Mediterranean Deep Water are involved as well in the circulation. During this study for the first time it was possible to describe the variability of the Capraia-Livorno channel, which shares the transport normally attributed only to the Corsica Channel. Sometimes its contribution to the surface circulation (Atlantic Water) influences the estimated absolute geostrophic transport of other water masses as well. Some authors (Vignudelli et al., 1999) mentioned possible current reversals (southward) during summer in the Eastern Corsica Current. During the Inverse box Model, this happened to be the case in most of the considered years, partially because the data were generally collected in summer. Moreover the reversals were observed both in the Corsica Channel and in the Capraia-Livorno section. The deep water across the Nice - Calví sometimes showed an unusual behaviour flowing eastward in the northern part of the transect and westward in the southern part. This peculiarity was only mentioned by Le Floch (1963), with whom the final transport estimates agree the best.

The present investigation also laid the foundations for future work and improvement to strengthen the pseudo-eulerian statistic applied in the MERMAID study: further data below a thousand meters depth need to be collected. The study about the driving agents of the Corsica Channel dynamics might be enlarged in order to include also the Gulf of Lion, Astraldi et al. (1994) mention a possible role of the Corsica Channel in replenishing the water involved in Deep Water Formation processes the take place in the Gulf of Lion. The Inverse Box Model presented in this study resulted in an accurate picture of the absolute geostrophic circulation in the Ligurian Sea in summer. Future studies might include also winter observations. Given the difficulty of collecting in-situ hydrographic data in winter, especially in the surrounding of the Gulf of Lion and Ligurian Sea, alternative observing techniques need to be considered. One option might be to use autonomous profiling buoys as discussed in Aracri et al. (2016) or deep glider data. Remotely collected data, such as satellite data are not suitable yet to collect deep hydrographic data, as the entire water column needs to be sampled to apply the Inverse Box Model. Another option might be to implement model data to recreate a wintry scenario and estimate the winter absolute geostrophic circulation. Additional improvements could be made to the Inverse Box Model, such as using regional datasets with higher resolution to accurately estimate the air-sea interactions and the diapycnal velocities. The wind funnelled through the Strait of Bonifacio could be further investigated to be related to the Corsica Channel flux. Alongside the temporal evolution and hydrographic characteristics of the eddy formed east of the Strait of Bonifacio (Marullo et al., 1994) can be studied, as they constitute a potential proxy to asses water volume losses happening in the Liguro-Provençal Basin.

A vast variety of issues remain unresolved about the Ligurian Sea, as the water property evolution in recent years across the Corsica Channel, in the Liguro-Provençal

Current and the Western Corsica Current; the water mass modifications under the influence of a changing climate and their relationship with the deep water formation in one of the most active sites of the world: the Gulf of Lion. The study of the Mediterranean confirms the importance of the understanding of regional seas, stresses their linkage and rapid response to large scale air-sea dynamics such as North Atlantic Oscillation, as hypothesised in Section 5. From the present study also arises the importance of long time series and deep hydrographic data sets with a better temporal and spatial resolution, to tune the observational oceanography tools in order to add the missing pieces to our knowledge of the ocean.

References

Alberola, C., Millot, C., and Font, J. (1995). On the seasonal and mesoscale variabilities of the Northern Current during the PRIMO-0 experiment in the western Mediterranean Sea. *Oceanologica Acta*, 18(2):163–192.

Alvarez, A., Chiggiato, J., and Schroeder, K. (2013). Mapping sub-surface geostrophic currents from altimetry and a fleet of gliders. *Deep Sea Res. Part I Oceanogr. Res. Pap.*, 74:115–129.

Aracri, S., Borghini, M., Canesso, D., Chiggiato, J., Durante, S., Schroeder, K., Sparnocchia, S., Vetrano, A., Honda, T., Kitawaza, Y., Kawahara, H., and Nakamura, T. (2016). Trials of an autonomous profiling buoy system. *Journal of Operational Oceanography*, 9(sup1):s176–s184.

Aracri, S., Bryden, H. L., Chiggiato, J., McDonagh, E., Josey, S. A., Schroeder, K., and Borghini, M. (2015). Forty years of geostrophic currents in the Ligurian Sea. *Journal of the BLACK SEA / MEDITERRANEAN ENVIRONMENT. Proceedings of MedCLIVAR 2014 Conference Understanding Climate Evolution and Effects on Environment and Societies in the Old World Region, METU, ANKARA, TURKEY 23-25 JUNE 2014, (Special Issue 2015),* 58–61.

Astraldi, M. and Gasparini, G. P. (1986). Observation of pressure and wind fields over the Ligurian and Tyrrhenian seas (West Mediterranean). *Meteorol. Atmos. Phys.*, 148:139–148.

Astraldi, M. and Gasparini, G. P. (1992). The seasonal characteristics of the circulation in the north Mediterranean basin and their relationship with the atmospheric-climatic conditions. *Journal of Geophysical Research*, 97(1):9531–9540.

Astraldi, M., Gasparini, G. P., Manzella, G. M. R., and May, A. (1990). Temporal Variability of Currents in the Eastern Ligurian Sea. *J. Geophys. Res.*, 95(89):1515–1522.

Astraldi, M., Gasparini, G. P., and Sparnocchia, S. (1994). The seasonal and interannual variability in the Ligurian-Provençal Basin. *Seasonal and interannual variability of the Western Mediterranean sea*, 46:93–113.

Bethoux, J. P. and Prieur, L. (1978). Evaluation des Flux d'Eaux de la Circulation du Nord-Est du Bassin Occidental. *Ciesm Congress 1978,* 67–68.

Bethoux, J. P., Prieur, L., and Nyffeler, F. (1982). *Hydrodynamics of semi-enclosed seas,* 129–142, chapter The Water Circulation in the North-Western Mediterranean Sea, its Relations with Wind and Atmospheric Pressure. Elsevier.

Bonaduce, A., Pinardi, N., Oddo, P., Spada, G., and Larnicol, G. (2016). Sea-level variability in the Mediterranean Sea from altimetry and tide gauges. *Climate Dynamics*, 47(9):2851–2866.

Bosse, A., Testor, P., Mortier, L., Prieur, L., Taillandier, V., d'Ortenzio, F., and Coppola, L. (2015). Spreading of Levantine Intermediate Waters by submesoscale coherent vortices in the northwestern Mediterranean Sea as observed with gliders. *Journal of Geophysical Research: Oceans*, 120(3):1599–1622.

Bryden, H. L., Schroeder, K., Sparnocchia, S., Borghini, M., and Vetrano, A. (2014). Thermohaline staircases in the western Mediterranean Sea. *Journal of Marine Research*, 72.

Chiggiato, J., Bergamasco, A., Borghini, M., Falcieri, F. M., Falco, P., Langone, L., Miserocchi, S., Russo, A., and Schroeder, K. (2016). Dense-water bottom currents in the southern adriatic sea in spring 2012. *Marine Geology*, 375:134 – 145.

CIESM Monographs, W. (2009). Dynamics of Mediterranean deep waters. *CIESM Workshop Monographs*, N 38(MC-98000,):1–132.

Cipollini, P., Passaro, M., and Snaith, H. (2015). ALES Coastal Geophysical Data Records (CGDR) User Handbook, 1–13.

Civitarese, G., Gačić, M., Lipizer, M., and Eusebi Borzelli, G. L. (2010). On the impact of the Bimodal Oscillating System (BiOS) on the biogeochemistry and biology of the Adriatic and Ionian Seas (Eastern Mediterranean). *Biogeosciences*, 7(12):3987–3997.

Conan, P. and Millot, C. (1995). Variability of the northern current off Marseilles, western Mediterranean Sea, from February to June 1992. *Oceanologica Acta*, 18(2):193–205.

Dai, A. and Trenberth, K. E. (2002). Estimates of Freshwater Discharge from Continents: Latitudinal and Seasonal Variations. *Journal of Hydrometeorology*, 3(6):660–687.

Dee, D. P., Uppala, S. M., Simmons, A. J., Berrisford, P., Poli, P., Kobayashi, S., Andrae, U., Balmaseda, M. A., Balsamo, G., Bauer, P., Bechtold, P., Beljaars, A. C. M., van de Berg, L., Bidlot, J., Bormann, N., Delsol, C., Dragani, R., Fuentes, M., Geer, A. J., Haimberger, L., Healy, S. B., Hersbach, H., Hlm, E. V., Isaksen, L., Kllberg, P., Khler, M., Matricardi, M., McNally, A. P., Monge-Sanz, B. M., Morcrette, J.-J., Park, B.-K., Peubey, C., de Rosnay, P., Tavolato, C., Thpaut, J.-N., and Vitart, F. (2011). The era-interim reanalysis: configuration and performance of the data assimilation system. *Quarterly Journal of the Royal Meteorological Society*, 137(656):553–597.

Delworth, T. L., Rosati, A., Anderson, W., Adcroft, A. J., Balaji, V., Benson, R., Dixon, K., Griffies, S. M., Lee, H.-C., Pacanowski, R. C., Vecchi, G. A., Wittenberg, A. T., Zeng, F., and Zhang, R. (2012). Simulated climate and climate change in the gfdl cm2.5 high-resolution coupled climate model. *Journal of Climate*, 25(8):2755–2781.

Dumont, J. P., Rosmorduc, V., Carrere, L., Picot, N., Bronner, E., Couhert, A., Desai, S., Bonekamp, H., Figa, J., Lillibridge, J., and Scharroo, R. (2015). OSTM / Jason-2 Products Handbook, 1–74.

Durrieu de Madron, X., Houpert, L., Puig, P., Sanchez-Vidal, A., Testor, P., Bosse, A., Estournel, C., Somot, S., Bourrin, F., Bouin, M. N., Beauverger, M., Beguery, L., Calafat, A., Canals, M., Cassou, C., Coppola, L., Dausse, D., D'Ortenzio, F., Font, J., Heussner, S., Kunesch, S., Lefevre, D., Le Goff, H., Martn, J., Mortier, L., Palanques, A., and Raimbault, P. (2013). Interaction of dense shelf water cascading and open-sea convection in the northwestern mediterranean during winter 2012. *Geophysical Research Letters*, 40(7):1379–1385.

Emery, W. and Thomson, R. (2001). *Data Analysis Methods in Physical Oceanography*, page 624. Pergamon, Oxford, UK.

Font, J., Puig, P., Salat, J., and Palanques, A. (2007). Sequence of hydrographic changes in NW Mediterranean deep water due to the exceptional winter of 2005. *Sci. Mar.*, 71(June):339–346.

Fu, L.-L. and Pihos, G. (1994). Determining the response of sea level to atmospheric pressure forcing using topex/poseidon data. *Journal of Geophysical Research: Oceans*, 99(C12):24633–24642.

Ganachaud, A. S. (1999). Large Scale Oceanic Circulation and Fluxes of Freshwater, Heat, Nutrients and Oxygen. *Ph.D. Thesis*.

Gasparini, G. P., Zodiatis, G., Astraldi, M., Galli, C., and Sparnocchia, S. (1999). Winter intermediate water lenses in the Ligurian Sea. *J. Mar. Syst.*, 20(1-4):319–332.

Gačić, M., Schroeder, K., Civitarese, G., Cosoli, S., Vetrano, A., and Eusebi Borzelli, G. L. (2013). Salinity in the Sicily Channel corroborates the role of the Adriatic - Ionian Bimodal Oscillating System (BiOS) in shaping the decadal variability of the Mediterranean overturning circulation. *Ocean Sci.*, 9(1):83–90.

GLOBALSEIS (2015). Mermaid data. `https://www.geoazur.fr/GLOBALSEIS/Data.html`.

Gouretski, V. V. and Koltermann, K. P. (2004). WOCE global hydrographic climatology.

Grignon, L., Smeed, D. A., Bryden, H. L., and Schroeder, K. (2010). Importance of the variability of hydrographic preconditioning for deep convection in the Gulf of Lion , NW Mediterranean. *Ocean Sci.*, 6:573–586.

Grinsted, A., Moore, J. C., and Jevrejeva, S. (2004). Application of the cross wavelet transform and wavelet coherence to geophysical time series. *Nonlinear Processes in Geophysics*, 11(5/6):561–566.

Hello, Y., Og, A., Sukhovich, A., and Nolet, G. (2011). Modern mermaids: New floats image the deep earth. *Eos, Transactions American Geophysical Union*, 92(40):337–338.

Heslop, E., Ruiz, S., Allen, J., López-Jurado, J., Renault, L., and Tintoré, J. (2012). Autonomous underwater gliders monitoring variability at choke points in our ocean system: A case study in the Western Mediterranean Sea. *Geophysical Research Letters*, 39:L20604.

Josey, A. S., Gulev, S., and Yu, L. (2013). *Ocean Circulation and Climate A 21st Century Perspective*, volume 103, chapter Exchanges Through the Ocean Surface, pages 115–140. Academic Press.

Joubert, C., Nolet, G., Bonnieux, S., Deschamps, A., Dessa, J.-X., and Hello, Y. (2016). P-delays from floating seismometers (mermaid), part i: Data processing. *Seismological Research Letters*, 87(1):73–80.

Jullion, L., Garabato, A. C. N., Bacon, S., Meredith, M. P., Brown, P. J., Torres-Valds, S., Speer, K. G., Holland, P. R., Dong, J., Bakker, D., Hoppema, M., Loose, B., Venables, H. J., Jenkins, W. J., Messias, M.-J., and Fahrbach, E. (2014). The contribution of the weddell gyre to the lower limb of the global overturning circulation. *Journal of Geophysical Research: Oceans*, 119(6):3357–3377.

Jullion, L., Lumpkin, R., and Speer, K. (2017). *Using Diabox. Introduction to inverse modelling Physical Oceanography*, pages 1–23.

Katsumata, K. and Yoshinari, H. (2010). Uncertainties in global mapping of argo drift data at the parking level. *Journal of Oceanography*, 66(4):553–569.

Larnicol, G., Le Traon, P.-Y., Ayoub, N., and De Mey, P. (1995). Mean sea level and surface circulation variability of the Mediterranean Sea from 2 years of TOPEX / POSEIDON altimetry. *Journal of Geophysical Research*, 100:25.

Lascaratos, A., Roether, W., Nittis, K., and Klein, B. (1999). Recent changes in deep water formation and spreading in the Eastern Mediterranean Sea: A review. *Prog. Oceanogr.*, 44(1-3):5–36.

Le Floch, J. (1963). Sur les variations saisonnires de la circulation superficielle dans le secteur nord-est de la mediterranee occidentale. *Travaux du CREO.Tome V, fasc.1*, 5.

Le Traon, P.-Y. and Gauzelin, P. (1997). Response of the Mediterranean mean sea level to atmospheric pressure forcing. *Journal Of Geophysical Research-oceans*, 102(C1):973–984.

Manzella, G. M. R. (1985). Fluxes across the Corsica Channel and coastal circulation in the east Ligurian Sea-northwestern Mediterranean. *Oceanol. acta*, 8:29–35.

Marshall, J. and Schott, F. (1999). Open-Ocean Convection: observations, theory and models. *Reviews of Geophysics*, 37(98):1–64.

Marty, J. C. and Chiavérini, J. (2010). Hydrological changes in the Ligurian Sea (NW Mediterranean, DYFAMED site) during 19952007 and biogeochemical consequences. *Biogeosciences*, 7(7):2117–2128.

Marullo, S., Santoleri, R., and Bignami, F. (1994). *The Surface Characteristics of the Tyrrhenian Sea: Historical Satellite Data Analysis*, chapter 8, pages 135–154. American Geophysical Union (AGU).

MAST2-EU (1996). Final scientific report. Contract MAS2-CT92-0046.

McDonagh, E. L. and King, B. A. (2005). Oceanic Fluxes in the South Atlantic. *Journal of physical oceanography*, 35:109–122.

MEDOC-Group (1970). Observation of Formation of Deep Water in the Mediterranean Sea, 1969. *Nature*, 227(5262):1037–1040.

Menna, M. and Poulain, P. (2010). Mediterranean intermediate circulation estimated from Argo data in 2003-2010. *Ocean Science*, 6(1):331–343.

Millot, C. (1999). Circulation in the Western Mediterranean Sea. *Journal of Marine Systems*, 20(1-4):423–442.

Millot, C. and Taupier-Letage, I. (2005). *The Mediterranean Sea*, chapter Circulation in the Mediterranean Sea, pages 29–66. Springer Berlin Heidelberg, Berlin, Heidelberg.

Morgan, P. (1994). Box Inverse Modelling with Dobox 4.2. *Technical Report, CSIRO Marine Laboratory Report 225*, page 26.

Passaro, M., Cipollini, P., Vignudelli, S., Quartly, G. D., and Snaith, H. M. (2014). ALES: A multi-mission adaptive subwaveform retracker for coastal and open ocean altimetry. *Remote Sensing of Environment*, 145:173–189.

Picco, P., Cappelletti, a., Sparnocchia, S., Schiano, M. E., Pensieri, S., and Bozzano, R. (2010). Upper layer current variability in the Central Ligurian Sea. *Ocean Sci. Discuss.*, 6(4):445–475.

Pinot, J.-M. and Ganachaud, A. (1999). The role of winter intermediate waters in the spring-summer circulation of the Balearic Sea: 1. Hydrography and inverse box modeling. *Journal of Geophysical Research*, 104(C12):843–864.

Pond, S. and Pickard, G. (1983). *Introductory Dynamical Oceanography*, page 329. Butterworth-Heinemann, Oxford.

Ponte, R. M. and Gaspar, P. (1999). Regional analysis of the inverted barometer effect over the global ocean using topex/poseidon data and model results. *Journal of Geophysical Research: Oceans*, 104(C7):15587–15601.

Poulain, P.-M. (2001). Adriatic Sea surface circulation as derived from drifter data between 1990 and 1999. *Journal of Marine Systems*, 29:3–32.

Poulain, P.-M., Barbanti, R., Font, J., Cruzado, A., Millot, C., Gertman, I., Griffa, A., Molcard, A., Rupolo, V., Le Bras, S., and Petit de la Villeon, L. (2007). MedArgo: a drifting profiler program in the Mediterranean Sea. *Ocean Science*, 3(3):379–395.

Poulain, P.-M., Gerin, R., Rixen, M., Zanasca, P., Teixeira, J., Griffa, A., Molcard, A., de Marte, M., and Pinardi, N. (2012). Aspects of the surface circulation in the Liguro-Provenal basin and Gulf of Lion as observed by satellite-tracked drifters (2007-2009). *Bollettino di Geofisica Teorica ed Applicata,* 261–279.

Robinson, A. R., Leslie, W. G., Theocharis, A., and Lascaratos, A. (2001). Mediterranean sea circulation. *Ocean Currents: A Derivative of the Encyclopedia of Ocean Sciences,* 1689–1705.

Roether, W., Manca, B. B., Klein, B., Bregant, D., Georgopoulos, D., Beitzel, V., Kovacevic, V., and Luchetta, A. (1996). Recent Changes in Eastern Mediterranean Deep Waters. *Science*, 271(5247):333–335.

Sammari, C., Millot, C., and Prieur, L. (1995). Aspects of the seasonal and mesoscale variabilities of the Northern Current in the western Mediterranean Sea inferred from the PROLIG-2 and PROS-6 experiments. *Deep-Sea Research Part I*, 42(6):893–917.

Schroeder, K., Chiggiato, J., Bryden, H. L., Borghini, M., and Ben Ismail, S. (2016). Abrupt climate shift in the Western Mediterranean Sea. *Scientific Reports*, 6:23009.

Schroeder, K., Garcìa-Lafuente, J., Josey, S. a., Artale, V., Nardelli, B. B., Carrillo, A., Gačić, M., Gasparini, G. P., Herrmann, M., Lionello, P., Ludwig, W., Millot, C., Özsoy, E., Pisacane, G., Sánchez-Garrido, J. C., Sannino, G., Santoleri, R., Somot, S., Struglia, M., Stanev, E., Taupier-Letage, I., Tsimplis, M. N., Vargas-Yáñez, M., Zervakis, V., and Zodiatis, G. (2012). *The Climate of the Mediterranean Region*, chapter Circulation of the Mediterranean Sea and its variability, pages 187–256. Elsevier.

Schroeder, K., Josey, S. a., Herrmann, M., Grignon, L., Gasparini, G. P., and Bryden, H. L. (2010). Abrupt warming and salting of the Western Mediterranean Deep Water after 2005: Atmospheric forcings and lateral advection. *J. Geophys. Res.*, 115(C8):C08029.

Schroeder, K., Ribotti, A., Borghini, M., Sorgente, R., Perilli, A., and Gasparini, G. P. (2008a). An extensive western Mediterranean deep water renewal between 2004 and 2006. *Geophys. Res. Lett.*, 35(18):L18605.

Schroeder, K., Taillandier, V., Vetrano, A., and Gasparini, G. (2008b). The circulation of the western Mediterranean Sea in spring 2005 as inferred from observations and from model outputs. *Deep Sea Research Part I: Oceanographic Research Papers*, 55(8):947 – 965.

Simons, F. J., Nolet, G., Babcock, J. M., Davis, R. E., and Orcutt, J. A. (2006). A future for drifting seismic networks. *Eos, Transactions American Geophysical Union*, 87(31):305–307.

Simons, F. J., Nolet, G., Georgief, P., Babcock, J. M., Regier, L. A., and Davis, R. E. (2009). On the potential of recording earthquakes for global seismic tomography by low-cost autonomous instruments in the oceans. *J. Geophys. Res.*, 114(B05307).

Smith, R. O., Bryden, H. L., and Stansfield, K. (2008). Observations of new western Mediterranean deep water formation using Argo floats 20042006. *Ocean Sci.*, 4(2):133–149.

Soussi, B., Urien, S., Soulat, F., Muir, A., Roca, M., and Cotton, D. (2011). ENVISAT ALTIMETRY Level 2 User Manual, 1–165.

Sparnocchia, S., Picco, P., Manzella, G. M. R., Ribotti, A., Copello, S., and Brasey, P. (1995). Intermediate water formation in the Ligurian Sea. *Oceanol. Acta*, 18:151–162.

Sukhovich, A., Bonnieux, S., Hello, Y., Irisson, J.-O., Simons, F. J., and Nolet, G. (2015). Seismic monitoring in the oceans by autonomous floats. *Nature Communications*, 6:8027.

Tanhua, T., Hainbucher, D., Schroeder, K., Cardin, V., Álvarez, M., and Civitarese, G. (2013). The Mediterranean Sea system: a review and an introduction to the special issue. *Ocean Sci.*, 9(5):789–803.

Taupier-Letage, I. and Millot, C. (1986). General hydrodynamical features in the Ligurian Sea inferred from the Dyomé experiment. *Oceanol. Acta*, 9:119–131.

Testor, P. and Gascard, J. (2003). Large-scale spreading of deep waters in the Western Mediterranean Sea by submesoscale coherent eddies. *Journal of physical oceanography*, 33(1):75–87.

Testor, P. and Gascard, J.-C. (2006). Post-convection spreading phase in the Northwestern Mediterranean Sea. *Deep Sea Research Part I: Oceanographic Research Papers*, 53(5):869–893.

Testor, P., Send, U., Gascard, J.-C., Millot, C., Taupier-Letage, I., and Branger, K. (2005). The mean circulation of the southwestern Mediterranean Sea: Algerian Gyres. *Journal of Geophysical Research: Oceans*, 110(C11):C11017.

Torrence, C. and Compo, G. (1998). A practical guide to wavelet analysis. *Bams*, 79:61.

UNESCO (2010). *GTSPP Real-Time Quality Control Manual.* United Nations Educational.

Vetrano, a., Napolitano, E., Iacono, R., Schroeder, K., and Gasparini, G. P. (2010). Tyrrhenian Sea circulation and water mass fluxes in spring 2004: Observations and model results. *J. Geophys. Res.*, 115(C6):C06023.

Vignudelli, S., Cipollini, P., Astraldi, M., Gasparini, G. P., and Manzella, G. (2000). Integrated use of altimeter and in situ data for understanding the water exchanges between the Tyrrhenian and Ligurian Seas. *J. Geophys. Res.*, 105(C8):19649–19664.

Vignudelli, S., Gasparini, GP , Astraldi, M. and Schiano, M. E., Vignudelli S., Gasparini G.P., Astraldi M., Schiano, M. E., Vignudelli, S., and Gasparini, GP , Astraldi, M. and Schiano, M. E. (1999). A possible influence of the North Atlantic Oscillation on the circulation of the Western Mediterranean Sea. *Geophys. Res. Lett.*, 26(5):623–626.

Wunsch, C. (1996). *The Ocean Circulation Inverse Problem*, page 437. Cambridge U. Press.